Der Centrifugal Differential Mobility Analyzer - Konstruktion, Validierung und erste Messungen von zweidimensionalen Größenverteilungen

Dissertation zur Erlangung des akademischen Grades
DOKTOR DER INGENIEURWISSENSCHAFT (Dr.-Ing.)
an der Fakultät für Maschinenbau
der Universität Paderborn

genehmigte
DISSERTATION

von
Torben Norbert Rüther, M.Sc.
aus Brilon

Tag des Kolloquiums:	10. Februar 2026
Referent:	Prof. Dr.-Ing. Hans-Joachim Schmid
Korreferent:	Prof. Dr.-Ing. Einar Kruis

Vorwort

Mit großer Vorfreude, aber auch einem Hauch Wehmut endet meine Zeit am Lehrstuhl. Ich blicke auf viele wunderbare Momente zurück. Besonders unvergessen bleibt jener Abend in Madrid, als Hajo und ich spätabends zufällig eine charmante Weinbar entdeckten und wir es dennoch, na ja, mehr oder weniger pünktlich am nächsten Morgen zur Konferenz schafften. Oder die „Klassenfahrt“ nach Sevilla, bei der Steffen, Moritz[2] und ich eine unglaublich lustige und unvergessliche Zeit hatten. Apropos Ausflüge: Auch wenn es diesmal keine berufliche Konferenz war, darf der Skiausflug mit Janis, Steffen und seinen Kids nicht unerwähnt bleiben. Ich erinnere mich immer noch schmunzelnd – und mit einer Spur schlechtem Gewissen – daran, dass mein Wecker unerbittlich früh (um halb sechs!) klingelte. Besonders der Morgen, an dem ich aufgrund „mysteriöser Umstände“ nicht wachzukriegen war und Steffen mehrfach genervt den Wecker ausschalten musste, tut mir immer noch unglaublich leid.

Doch keine Sorge, wer jetzt denkt, unsere Zeit am Lehrstuhl bestand nur aus „Urlaub“, liegt falsch! Auch die Arbeit an der Uni war großartig – jeden einzelnen Tag habe ich genossen. Die fachspezifischen Diskussionen mit den Kollegen, die ein oder andere amüsante Anekdote über kleine Patzer von Studierenden und natürlich die Arbeit im Labor (von Norbert liebevoll „Jugend forscht“ genannt) haben mir unendlich viel Freude bereitet. Besonders die Freiheit, eigene Ideen auszuprobieren, und der Moment, wenn die Pläne tatsächlich aufgehen, sind einfach unbezahlbar. Selbst die längeren Kaffeepausen im Büro von Ilona, die oft einen harten Arbeitstag deutlich erleichterten, werde ich sehr vermissen.

Man merkt, wie viel mir diese Arbeit bedeutet hat und das lag nicht nur an den spannenden Themen, sondern vor allem an meinen großartigen Kolleginnen und Kollegen. Chapeau, Hajo und Steffen – eure Teamauswahl war wirklich hervorragend!

Auch wenn ich eigentlich niemanden hervorheben wollte, möchte ich doch zugeben, dass ich das Herumalbern und die sportlichen Mittagspausen mit Steffen am meisten vermissen werde. Vor allem dir, Steffen, gilt mein Dank für die schöne Zeit und die unermüdliche Unterstützung, auf die ich mich stets verlassen konnte.

Natürlich verdanke ich diese erfolgreiche Zeit nicht nur meiner Arbeit am Lehrstuhl. Im Hintergrund gab es viele Menschen, die mich stets unterstützt und ermutigt haben. Allen voran möchte ich meinen Eltern, Heike und Wolfram, danken, die immer an mich geglaubt haben. Ebenso gilt mein Dank meinen Freundinnen und Freunden, die mich in dieser Zeit begleitet haben – besonders Nils, der in den letzten Monaten wohl häufiger als ihm lieb war meine Klagen ertragen musste. Bitte verzeiht, dass ich hier nicht alle von euch namentlich erwähnen und unsere vielen gemeinsamen Erlebnisse ausführlich schildern kann – wobei, mal ehrlich, die meisten dieser Geschichten würden meine Seriosität sowieso in Rekordzeit über Bord werfen...

Vielen Dank euch allen!

Torben Rüther

Brilon, den 20. Februar 2026

Zusammenfassung

Das Interesse an komplex geformten Nanopartikeln wächst stetig. Für eine zuverlässige Prozessvorhersage und -optimierung ist eine detaillierte Charakterisierung erforderlich, die über die Bestimmung einer Äquivalentgröße hinausgeht. Klassische Methoden wie Tandem-Setups oder SEM/TEM-Bildgebung sind jedoch häufig durch hohen Zeit- und Kostenaufwand sowie begrenzte statistische Aussagekraft eingeschränkt. Zur Verbesserung und Vereinfachung der Charakterisierung nanoskaliger Partikel wurde der Centrifugal Differential Mobility Analyzer (CDMA) entwickelt, der die Prinzipien des Aerodynamic Aerosol Classifiers (AAC) und des Differential Mobility Analyzers (DMA) kombiniert. Damit ermöglicht er die simultane Bestimmung des Mobilitäts- und Stokesäquivalentdurchmessers sowie die Erfassung zweidimensionaler Partikelgrößenverteilungen. Im Rahmen dieser Arbeit wurde neben der Entwicklung eines Prototyps die zweidimensionale Transferfunktion unter verschiedenen Randbedingungen hergeleitet und diskutiert. Zudem kam der Algorithmus Projections onto Convex Sets (POCS) zum Einsatz, um das schlecht gestellte Inversionsproblem der zweidimensionalen Partikelcharakterisierung zu lösen. Der CDMA eröffnet damit einen effizienten und robusten Ansatz zur Nanopartikelanalyse und liefert zugleich Zugang zu erweiterten Kenngrößen wie effektiver Dichte und fraktaler Dimension, wodurch sich neue Einblicke in die Partikelmorphologie ergeben.

Abstract

The growing interest in complex-shaped nanoparticles requires a detailed characterization that goes beyond the determination of a single equivalent size to enable reliable process prediction and optimization. Conventional methods such as tandem setups or SEM/TEM imaging are often limited by high time and cost demands as well as restricted statistical significance. To address these limitations, the Centrifugal Differential Mobility Analyzer (CDMA) was developed, combining the principles of the Aerodynamic Aerosol Classifier (AAC) and the Differential Mobility Analyzer (DMA). This instrument enables the simultaneous determination of mobility and Stokes equivalent diameters, thereby providing access to two-dimensional particle size distributions. In this work, a prototype was designed and constructed, and the two-dimensional transfer function was derived and analyzed under various boundary conditions. Furthermore, the Projections onto Convex Sets (POCS) algorithm was applied to solve the ill-posed inversion problem inherent in two-dimensional particle characterization. The CDMA thus offers an efficient and robust approach for nanoparticle analysis, granting access to additional parameters such as effective density and fractal dimension, and thereby providing deeper insights into particle morphology.

Vorträge und Publikationen

Vorträge

[RJS22a] Torben Norbert Rüther, Steffen Jesinghausen und Hans-Joachim Schmid. *A novel correction method for the shear rate in a couette rheometer: Comparison between the corrections of Krieger/Elrod, Schümmer, Pawlowski and the novel correction*. Annual European Rheology Conference. Sevilla, 2022.

[RJS22b] Torben Norbert Rüther, Steffen Jesinghausen und Hans-Joachim Schmid. *New Correction Approaches for Determining the True Shear Rate in a Coaxial-Rheometer*. DRG Symposium. Online, 2022.

[RS23a] Torben Norbert Rüther und Hans-Joachim Schmid. *CDMA: Centrifugal Differential Mobility Analyzer: Ein Messprinzip zur Bestimmung von multidimensionalen Partikeleigenschaften*. DECHEMA Jahrestagung Partikelmesstechnik. Paderborn, 2023.

[RS24] Torben Norbert Rüther und Hans-Joachim Schmid. *CDMA: Centrifugal Differential Mobility Analyzer: Measurement of Transfer Functions, Theory and Data Inversion*. GAeF START. Wien, 2024.

[RS23b] Torben Norbert Rüther und Hans-Joachim Schmid. *CDMA: Centrifugal Differential Mobility Analyzer: Measurement Theory and Data Inversion*. International Congress on Particle Technology (PARTEC). Nürnberg, 2023.

Publikationen

[RRS25a] T. N. Rüther, D. B. Rasche und H.-J. Schmid. „The Centrifugal Differential Mobility Analyser – concept and initial validation of a new device for measuring 2D property distributions“. In: *Aerosol Research* 3.1 (2025), S. 65–79. DOI: 10.5194/ar-3-65-2025. URL: https://ar.copernicus.org/articles/3/65/2025/.

[RRS25b] Torben N. Rüther, David B. Rasche und Hans-Joachim Schmid. „The POCS-Algorithm—An effective tool for calculating 2D particle property distributions via data inversion of exemplary CDMA measurement data“. In: *Journal of Aerosol Science* 188 (2025), S. 106606. ISSN: 0021-8502. DOI: https://doi.org/10.1016/j.jaerosci.2025.106606. URL: https://www.sciencedirect.com/science/article/pii/S0021850225000837.

[RS25] Torben N. Rüther und Hans-Joachim Schmid. „Prediction of the transfer function for a centrifugal differential mobility analyzer by streamline functions“. In: *Aerosol Science and Technology* 59.9 (2025), S. 1108–1121. DOI: 10.1080/02786826.2025.2519092. eprint: https://doi.org/10.1080/02786826.2025.2519092. URL: https://doi.org/10.1080/02786826.2025.2519092.

[Rüt+25] Torben Norbert Rüther, Sebastian Gröne, Christopher Dechert und Hans-Joachim Schmid. „Centrifugal Differential Mobility Analysis—Validation and First Two-Dimensional Measurements“. In: *Powders* 4.2 (2025). ISSN: 2674-0516. DOI: 10.3390/powders4020011. URL: https://www.mdpi.com/2674-0516/4/2/11.

Weitere Publikationen

An dieser Stelle sind weitere Publikationen aufgeführt, die kein Bestandteil dieser Arbeit sind.

[Cla+20] Leander Claes, Elmar Baumhögger, Torben Rüther, Jan Gierse, Thomas Tröster und Bernd Henning. „Reduction of systematic measurement deviation in acoustic absorption measurement systems“. In: *Fortschritte der Akustik - DAGA 2020*. 2020, S. 1077–1080.

[Rüt+23] Moritz Rüther, Helge Klippstein, SathishKumar Ponusamy, Torben Rüther und Hans-Joachim Schmid. „Flowability of polymer powders at elevated temperatures for additive manufacturing“. In: *Powder Technology* 422 (2023), S. 118460. ISSN: 0032-5910. DOI: https://doi.org/10.1016/j.powtec.2023.118460.

Inhaltsverzeichnis

Abbildungsverzeichnis

Tabellenverzeichnis

Abkürzungen

AAC	Aerodynamic Aerosol Classifier
AMS	Aerosol Mass Spectrometer
APM	Aerosol Particle Mass Analyzer
APS	Aerodynamic Particle Sizer
CDMA	Centrifugal Differential Mobility Analyzer
CPC	Condensation Particle Counter
CPMA	Centrifugal Aerosol Particle Mass Analyzer
DLS	Dynamic Light Scattering
DMA	Dynamic Mobility Analyzer
ELPI	Electrical Low Pressure Impactor
LAS	Laser Aerosol Spectrometer
LPI	Low Pressure Impactor
lpm	Liters per minute
MFC	Mass Flow Controller
OPS	Optical Particle Sizer
SEM	Scanning Electron Microscope
TEM	Transmission Electron Microscope
Welas	Scattered Light Spectrometer System

Nomenklatur

d_m	Mobilitätsäquivalentdurchmesser	m
d_{ae}	Aerodynamischer Äquivalentdurchmesser	m
$d_{ae,vac}$	Aerodynamischer Äquivalentdurchmesser im Vakuum	m
d_{pr}	Äquivalentdurchmesser der Projektionsfläche	m
d_{st}	Stokes Äquivalentdurchmesser	m
d_v	Volumenäquivalentdurchmesser	m
d_{str}	Streulichtäquivalentdurchmesser	m
D	Diffusionskoeffizient	m^2/s
k	Boltzmann-Konstante	J/K
T	Temperatur	K
η	Dynamische Viskosität	Pas
n	Anzahl der Partikelladungen	–
ρ	Partikeldichte	kg/m^3
ρ_0	Einheitsdichte $1000\,kg/m^3$	kg/m^3
ρ_{eff}	Effektive Dichte	kg/m^3
χ_v	Formfaktor im freien molekularen Bereich	–
χ_v	Formfaktor im freien Übergangsbereich	–
D_f	Fraktale Dimension	–
Cu	Cunningham-Korrekturfaktor	–
w_s	Sedimentationsgeschwindigkeit	m/s
C'	Konstante	–
F_{el}	Elektrische Kraft	N
F_D	Widerstandskraft	N
F_z	Zentrifugalkraft	N
E	Elektrische Feldstärke	V/m
e	Elementarladung	C
U	Spannung	V
r_a	Außendurchmesser	m
r_i	Innendurchmesser	m
r_{ein}	Radius auf dem die Partikeln in den Klassierspalt eintreten	m
v	Partikeldriftgeschwindigkeit in radialer Richtung	m/s
u	Fluidgeschwindigkeit in axialer Richtung	m/s
τ	Partikelrelaxationszeit	s
τ^*	Mittlere Partikelrelaxationszeit	s
$\widetilde{\tau}$	Normierte Partikelrelaxationszeit	–
Z_p	Partikelmobilität	$m^2/(Vs)$
Z^*	Mittlere Partikelmobilität	$m^2/(Vs)$
$\widetilde{Z}$	Normierte Partikelmobilität	–
Q_a	Aerosolvolumenstrom	m^3/s

Q_{sh}	Hüllluftvolumenstrom	m^3/s
Q_s	Sample Volumenstrom	m^3/s
Q_{exh}	Abgasvolumenstrom	m^3/s
L	Klassierspaltlänge	m
β	Verhältnis von Q_a zu Q_{sh}	–
Ω	Transferfunktion	–
γ	Ladungsverteilung	–
η_{CPC}	Wirkungsgrad des CPC's	–
η_T	Penetrationseffizienz	–
n_0	Anzahldichteverteilung	$\#/m^3$
ω	Winkelgeschwindigkeit	1/s
y	Längenkoordinate in axialer Richtung	m
$\widetilde{h}$	Verhältnis der Spaltbreite zum mittleren Spaltradius	–
κ	Verhältnis von r_i zu r_a	–
x_o	Obere Grenze der Partikelklassen	m
x_u	Untere Grenze der Partikelklassen	m
M	Mehfachladungs-Korrekturmatrix	–
N_i	gemessene Anzahlkonzentration	$\#/m^3$
$\boldsymbol{N}$	Messwert-Vektor	$\#/m^3$
$\boldsymbol{N^s}$	Schätzwerte für die Partikelgrößenverteilung	$\#/m^3$
$\boldsymbol{\epsilon}$	Gewichtungsmatrix	–

1 Einleitung

Die Charakterisierung von Nanopartikeln ist für eine Vielzahl von wissenschaftlichen und industriellen Anwendungen von fundamentaler Bedeutung. Beispielsweise in den Materialwissenschaften, der Umwelttechnik und der Medizin, aber auch in der Energietechnologie, werden Nanopartikel aufgrund ihrer einzigartigen physikalischen und chemischen Eigenschaften immer häufiger eingesetzt. Diese Eigenschaften, wie eine verbesserte Reaktivität und die Möglichkeit, biologische Barrieren zu überwinden, sind das Ergebnis der geringen Partikelgröße und der damit verbundenen hohen spezifischen Oberfläche. Während traditionelle Methoden der Partikelcharakterisierung, wie die Messung des Mobilitäts-Äquivalentdurchmessers oder des aerodynamischen Äquivalentdurchmessers, für viele Anwendungen ausreichen, liefern diese Verfahren insbesondere bei komplexen Partikelstrukturen wie Agglomeraten oder anderen nicht sphärischen Formen, häufig unzureichende oder sogar verzerrte Informationen [Zha+22; Jin17; Toy+14; Kel+22]. So kann beispielsweise eine große, kugelförmige Partikel denselben Äquivalentdurchmesser aufweisen wie ein kleines, weit verzweigtes Agglomerat mit hoher spezifischer Oberfläche.

Eine Äquivalentgröße allein ist in der Regel nicht hinreichend für die vollständige Beschreibung der Eigenschaften von Nanopartikeln, da viele relevante physikalische Merkmale wie Partikelform, Struktur und Oberflächenbeschaffenheit erheblichen Einfluss auf das Verhalten und die Wechselwirkungen der Partikel haben. Aufgrund ihrer hohen Relevanz gibt es im Bereich der Forschung intensive Bestrebungen, Partikelsysteme anhand mehrerer Eigenschaften zu charakterisieren und zu trennen, um hochspezifische Partikelsysteme herzustellen. Ein Beispiel dafür ist das Schwerpunktprogramm SPP 2045: Hochspezifische mehrdimensionale Fraktionierung von technischen Feinstpartikelsystemen, das sich genau mit diesem Thema befasst. So wurde im Rahmen dieses Programms unter anderem der Einsatz von 3D-Röntgentechniken untersucht, wobei von multidimensionalen Verteilungen verschiedener Partikeleigenschaften ausgegangen wurde. Diese Verteilungen lassen sich mithilfe archimedischer Copulas beschreiben, die es ermöglichen, komplexe Zusammenhänge mit nur wenigen Parametern auszudrücken [Fur+19]. Eine weitere entwickelte Trennmethode basiert auf der Verwendung aerodynamischer Linsen, mit denen eine Separation der Partikeln nach Stokes-Durchmesser und Dichte möglich ist [Fur+20]. Darüber hinaus wurde die Nutzung stehender Ultraschallwellen untersucht, um disperse Partikelsysteme in Fein- und Grobanteile zu fraktionieren [SF23].

Um diese Herausforderungen zu meistern und ein umfassendes Verständnis für die komplexen Eigenschaften von Nanopartikelsystemen zu entwickeln, ist eine multidimensionale Partikelcharakterisierung erforderlich. Diese ermöglicht es, mehrere Eigenschaften von Nanopartikeln gleichzeitig zu messen und so ein vollständigeres Bild von der Partikelstruktur zu erhalten. Ein vielversprechender Ansatz für eine zweidimensionale Charakterisierung ist der Centrifugal Differential Mobility Analyzer (CDMA), ein neu entwickeltes Instrument, das die Messung von zwei äquivalenten Partikelgrößen, dem Aerodynamischen- und dem Mobilitäts-Äquivalentdurchmesser, in einer einzigen Messung ermöglicht [Ras25]. Diese gleichzeitige Messung der beiden Größen erlaubt es, eine zweidimensionale Verteilung

der beiden Partikeleigenschaften zu erstellen, die zur Berechnung weiterer wichtiger Parameter wie der effektiven Dichte oder des Formfaktors verwendet werden kann [Par+08]. Im Vergleich zu traditionellen Methoden, die meist nur eine einzige äquivalente Partikelgröße bestimmen, liefert der CDMA somit eine erheblich genauere und differenziertere Analyse von Nanopartikelsystemen. Dieses Wissen kann genutzt werden, um über die Partikeleigenschaften Verbrennungsprozesse genauer zu analysieren und zu verbesseren [OSC07] oder auch um weitere Korellationen beispielsweise zur spezifischen Oberfläche und somit zur Reaktivität der Partikeln zu bilden [TO13].

Die Anwendung des CDMA in der Partikelcharakterisierung bringt jedoch auch Herausforderungen mit sich. Besonders wichtig für die präzise Inversion der Messdaten ist ein fundiertes Verständnis der Transferfunktion des CDMA. In der vorliegenden Arbeit wird die Entwicklung dieser Transferfunktion vorgestellt, die zunächst auf einer Modellierung der Partikeltrajektorien basiert. Eine alternative Ableitung mit Hilfe der Streamline-Funktionen kommt zu einem identischen Ergebnis und kann somit als Validierung verstanden werden. Weiterhin erlaubt die Anwendung der Streamline-Funktionen eine genauere Beschreibung der Diffusionseffekte im Klassierspalt. Der Ansatz orientiert sich an den Methoden, die in früheren Arbeiten wie *Stolzenburg* [Sto88] verwendet wurden, und stellt sicher, dass die mathematische Beschreibung der Partikelbewegung innerhalb des CDMA realistische und präzise Rückschlüsse auf die Partikeleigenschaften zulässt. Zudem wird die Bedeutung der Randbedingungen am Einlass untersucht und deren Einfluss auf die Partikelklassierung sowie die daraus resultierenden Messwerte umfassend analysiert.

Diese Arbeit wurde in kumulativer Form verfasst. Die Abschnitte 2 und 3 dienen der Vermittlung der erforderlichen theoretischen Grundlagen und der Identifikation der bestehenden Forschungslücke. Abschnitt 4 umfasst die zugehörigen wissenschaftlichen Publikationen.

Die erste Veröffentlichung präsentiert eine initiale Validierung des CDMA. Aufbauend darauf werden in der zweiten Publikation die berechneten Transferfunktionen bestätigt und die zugrunde gelegten Randbedingungen näher untersucht. Die dritte Publikation widmet sich der theoretischen Fundierung sowie der praktischen Anwendung der Dateninversion. In der vierten Publikation wird der Einfluss des Strömungsfeldes im CDMA detailliert analysiert und erste experimentelle Messergebnisse werden vorgestellt.

2 Stand der Forschung

Im Folgenden werden die wesentlichen Techniken zur Messung von Aerosolen vorgestellt, woraus sich der Forschungs- und Entwicklungsbedarf ableitet. Diese Vorgehensweise dient der besseren Einordnung der nachfolgenden Publikationen sowie der Vermittlung des erforderlichen Vorwissens.

2.1 Aerosolmesstechnik

Ein Aerosol ist die Dispersion einer Flüssigkeit oder eines Feststoffes (disperse Phase) in einem Gas (kontinuierliche Phase)[Fri00]. Der Größenbereich der Aerosolpartikeln erstreckt sich von 1 nm über mehrere Größenordnungen bis zu etwa 100 μm [Col13]. Dies entspricht in etwa der Größe von großen Gasmolekülen bis hin zum Durchmesser eines menschlichen Haares. Aufgrund der immensen Spannbreite des zu untersuchenden Bereichs ist es erforderlich, auf eine Vielzahl von Methoden zurückzugreifen, um Aerosole adäquat charakterisieren zu können. Partikeln größer als etwa 250 nm lassen sich mit etablierten Streulicht- und optischen Methoden gut charakterisieren [Fri00]. Besonders bei Partikeln ab etwa 5 μm ist auch eine bildgebende optische Erfassung möglich. Unterhalb von etwa 250 nm nimmt jedoch die Streulichtintensität stark ab, und auch die optische Auflösung stößt an ihre Grenzen, was die direkte Bestimmung der Partikelgröße deutlich erschwert. Allerdings können über verschiedene Methoden Äquivalentgrößen bestimmt werden, welche in vielen Fällen eine zufriedenstellende, jedoch dennoch indirekte Maßangabe darstellen. Bei Methoden mit höherem Informationsgehalt kann allerdings aufgrund der geringen Probenmenge die Repräsentativität der gezogenen Probe für das gesamte Partikelkollektiv nicht immer gewährleistet werden. Tabelle 2.2 zeigt eine repräsentative Auswahl an Messmethoden, welche die Bestimmung von Äquivalentgrößen für Partikeln im Größenbereich bis 1000 nm ermöglichen.

Tabelle 2.2: Messmethoden zur Charakterisierung von Partikeln <1000 nm

Messmethode	Abk.	Äquiv.-größe	Messbereich
Aerodynamic Aerosol Classifier	AAC	d_{ae}	20 nm – 2.5 μm
Aerosol Particle Mass Analyzer	APM	d_v	14 nm – 1.3 μm
Centrifugal Aerosol Particle Mass Analyzer	CPMA	d_v	7 nm – 1.3 μm
Differential Mobility Analyzer	DMA	d_m	10 nm – 1 μm
Low Pressure Impactor	LPI	d_{ae}	30 nm – 10 μm
Electrical Low Pressure Impactor	ELPI	d_{ae}	6 nm – 10 μm
Aerodynamic Particle Sizer	APS	d_{ae}	500 nm – 20 μm
Aerosol Mass Spectrometer	AMS	$d_{ae,vac}$	40 nm – 1 μm
Laser Aerosol Spectrometer	LAS	d_{str}	90 nm – 7.5 μm
Scattered light spectrometer system	Welas	d_{str}	200 nm – 10 μm
Optical Particle Sizer	OPS	d_{str}	300 nm – 10 μm
Transmission Electron Microscope	TEM	d_{pr}	0.1 nm – 100 nm
Scanning Electron Microscope	SEM	d_{pr}	2 nm – 1 mm

In Bezug auf die genannten Messmethoden ist eine weitere Unterteilung in bildgebende

Verfahren, optische Verfahren und klassierende Verfahren möglich.

Zu den *bildgebenden Verfahren* zählen in erster Linie Elektronenmikroskope.Ihr Einsatz ist erforderlich, da die Größe von Nanopartikeln in der Größenordnung der Wellenlänge des sichtbaren Lichts liegt, wodurch eine hochauflösende Abbildung mittels lichtoptischer Mikroskopie nicht mehr realisierbar ist. In diesem Bereich wird das sogenannte Beugungslimit erreicht, das die maximal mögliche Winkelauflösung eines optischen Systems definiert. Eine präzise Abbildung und Unterscheidung einzelner Partikeln ist mit optischen Verfahren daher nicht mehr möglich. Im Gegensatz dazu wird bei einem Rasterelektronenmikroskop anstelle eines Lichtstrahls ein stark fokussierter Elektronenstrahl verwendet, welcher die Oberfläche der Probe abrastert. Die Detektion der rückgestreuten Elektronen erlaubt schließlich die Generierung eines Bildes [MZ11; Ale97]. Beim Transmissionselektronenmikroskop (TEM) basiert die Analyse auf dem durch die Probe transmittierten Elektronenstrahl. Daher ist eine ausreichende Durchlässigkeit des Materials erforderlich, was eine entsprechend geringe Probendicke voraussetzt. Dies ermöglicht beim TEM eine Auflösung bis zu wenigen Å [WC96]. Die bildgebenden Verfahren ermöglichen die Analyse der Projektionsfläche und somit der Partikelgeometrie. Außerdem kann mit Hilfe weiterer Sensoren auf die Materialzusammensetzung geschlossen werden.

Allerdings sind die Probenahme und -präparation sowie die Messung selbst sehr zeitaufwändig und erfordern ein hohes Maß an theoretischem Verständnis sowie praktischer Erfahrung. Da pro Messung lediglich eine begrenzte Anzahl an Partikeln analysiert wird, ist der Informationsgehalt zwar, wie zuvor beschrieben, sehr hoch. Allerdings erfordert ein statistisch belastbarer Rückschluss auf die Grundgesamtheit einen erheblichen experimentellen Aufwand.

Die Mehrzahl der *optischen Verfahren* zur Messung von Aerosolen mit geringen Konzentrationen basiert auf der Analyse einzelner Partikeln. Hierbei wird der Zusammenhang zwischen der Intensität des rückgestreuten Lichts und der Partikelgröße ausgenutzt. Da die Zuordnung insbesondere im Mie-Bereich nicht sehr eindeutig ist, nutzen beispielsweise der OPS (TSI) und auch das Welas (Palas) Weißlicht. Dies ermöglicht eine Integration über verschiedene Wellenlängen, was die Eindeutigkeit der Zuordnung erhöht. Des Weiteren wird die Eindeutigkeit der Zuordnung durch den Einsatz einer Weitwinkeloptik verbessert, wobei über eine Vielzahl von Rückstrahlwinkeln integriert wird [Szy02].

Laser-Aerosol-Spektrometer nutzen den Umstand, dass bei Detektion in einem engen Vorwärtswinkel sowohl die Zuordnung eindeutig ist als auch die rückgestreute Lichtintensität höher ist. Infolgedessen ist es mit Laser-Aerosol-Spektrometern möglich, kleinere Partikeln mit hoher Zuverlässigkeit zu messen [MC16].

Die Anwendung dieser Techniken ist unkompliziert, ein Nachteil ist jedoch, dass lediglich ein Streulichtäquivalentdurchmesser gemessen wird. Die Umrechnung in andere Größen ist nur mit sehr großem Aufwand möglich, da hierfür der genaue Brechungsindex sowie die Form der Partikel bekannt sein müssen. In der Praxis werden daher genormte Kalibrierpartikeln eingesetzt, um das Gerät zu kalibrieren. Es besteht jedoch die Möglichkeit, dass die tatsächlichen Partikelgrößen von den Messwerten abweichen [Jon99].

Klassierende Methoden stellen eine weitere Gruppe innerhalb der Aerosolmesstechnik

dar. Dabei wird auf die Partikel eine definierte Kraft ausgeübt, die ihre Trajektorie im Zylinderspalt von der ursprünglichen Bahn ablenkt. Das Ausmaß der Ablenkung hängt sowohl von der wirkenden Kraft als auch vom strömungsabhängigen Widerstand ab, dem das Partikel entgegenwirkt. Durch die Entnahme von Partikeln die spezifischen Stromlinien folgen, kann ein monomodales Aerosol mit definierter Äquivalentpartikelgröße gewonnen werden, dessen Größe und Eigenschaften durch die aufgebrachte Kraft definiert werden. Da die klassierten Partikeln oftmals eine geringe Größe aufweisen, erfolgt die Ermittlung der Partikelanzahl mittels eines Faraday-Cup-Elektrometers, welches die Ladungsanzahl der Partikeln misst, oder eines Condensation Particle Counters (CPC). In einem CPC fungieren die Partikeln als Kondensationskeime. Durch Sättigung der umgebenden Luft mit einem geeigneten Medium (z. B. Butanol, Wasser oder Isopropanol) und anschließende Abkühlung wird eine leichte Übersättigung erzeugt, die heterogenes Keimwachstum initiiert. Dadurch wachsen die Partikeln auf eine Größe an, die eine zuverlässige Detektion mittels optischer Verfahren ermöglicht.

Im Differential Mobility Analyzer (DMA) wird ein elektrisches Feld über einen Zylinderspalt aufgebracht. Unter Berücksichtigung der Ladung und der Lauflänge lässt sich der Mobilitätsdurchmesser d_m ableiten [KW75; Sto88].

Im Aerodynamic Aerosol Classifier (AAC) wird die Triebkraft durch Aufbringen einer Zentrifugalkraft auf den Zylinderspalt erzeugt. Dadurch werden Partikeln mit gleicher Sinkgeschwindigkeit klassiert. Die Sinkgeschwindigkeit ist dabei vom aerodynamischen Durchmesser d_{ae} abhängig [TO14].

Beim Aerosol Particle Mass Analyzer (APM) wirkt sowohl eine elektrische als auch eine Zentrifugalkraft. Anders als beim DMA und AAC werden hierbei die Partikeln allerdings nicht innen oder außen am Zylinderspalt aufgegeben, sondern über die gesamte Breite des Spalts. Die Partikeln, bei denen sich die Zentrifugalkraft und elektrische Kraft aufheben, erfahren keine radiale Partikelbewegung und können ebenso mittig gesampled werden. Hierdurch wird das Masse-Ladungs-Verhältnis gemessen. Sind die Partikeldichte ρ sowie die Ladung n bekannt, ergibt sich direkt der Volumenäquivalentdurchmesser [Taj+11].

Der Centrifugal Particle Mass Analyzer (CPMA) stellt eine Weiterentwicklung des APM dar. Der Antrieb des Außen- und Innenzylinders erfolgt mit unterschiedlichen Drehzahlen. Diese Vorgehensweise zielt darauf ab, die Zentrifugalkraft über den Zylinderspalt möglichst konstant zu halten. Während beim APM bereits geringe Abweichungen von der mittleren Stromlinie zur Abscheidung an den Wänden führen, ist die Partikelbewegung im CPMA stabil: Kleine Abweichungen resultieren in einer Rückführung zur mittleren Bahn, wodurch eine effektive Klassierung gewährleistet wird [Olf+06; OC05].

Die Klassierung in einem Niederdruckimpaktor (LPI) erfolgt mittels Trägheitsabscheidung, wodurch wiederum der aerodynamischen Durchmesser d_{ae} ermittelt wird. Im Rahmen dieses Prozesses erfolgt eine Beschleunigung eines Aerosolstroms in einer Düse. Im Anschluss wird der Luftstrom in einem definierten Abstand senkrecht zur Düse um eine angebrachte Platte herumgeleitet. Aufgrund ihrer Trägheit können Partikeln unterschiedlicher Größe der Fluid-Stromlinienbewegung unterschiedlich gut folgen, sodass größere Partikeln die Platte erreichen und abgeschieden werden. Diese Vorgehensweise erweist sich

insbesondere für Partikeln mit einer Größe von $> 300\,\text{nm}$ als sehr effektiv, während kleinere Partikeln aufgrund ihrer geringen Trägheit nur unzureichend abgeschieden werden. Aus diesem Grund wird der Druck hier abgesenkt, wodurch auch kleinere Partikeln effektiv abgeschieden werden können. Bei einer Kaskadierung mehrerer Impaktorstufen, wobei die abgeschiedene Partikelgröße mit jeder Stufe jeweils geringer wird, kann die Abscheidung an den einzelnen Stufen gemessen und somit die Partikelgrößenverteilung hinsichtlich des aerodynamischen Durchmessers d_{ae} bestimmt werden [HFF78; May75; HK91].

Der elektrische Niederdruckimpaktor (ELPI) stellt eine Weiterentwicklung des LPI dar. Im Rahmen dieses Verfahrens wird das Aerosol vorab mit einem Corona-Auflader unipolar aufgeladen. Sind nun die einzelnen Impaktorstufen elektrisch voneinander getrennt und an jeder Platte ein Elektrometer angeschlossen, ist eine direkte online-Messung der Ladung und (bei bekannter Ladungsverteilung) folglich die Bestimmung der Partikelanzahl möglich [KPL92; May75].

Die Messprinzipien des Aerodynamic Particle Sizer (APS) und Aerosol Mass Spectrometer (AMS) basieren auf der Messung der Flugzeit der Partikeln. Im Rahmen dieses Verfahrens wird ein Aerosolstrom in einer Düse beschleunigt. Im Bereich hinter der Düse herrscht ein Unterdruck. Die Ermittlung der Flugzeit erfolgt mittels zweier Laser, die in einem definierten Abstand angebracht sind (APS) oder über die Messung der Zeit von der Düse bis zur Detektion der Massenspektroskopie (AMS). Die Flugzeit ist dabei erneut von der Trägheit der Partikeln abhängig, sodass kleinere Partikeln stärker beschleunigt werden und folglich eine kürzere Flugzeit aufweisen. Dies liefert erneut Informationen über den aerodynamischen Durchmesser d_{ae} oder den aerodynamischen Durchmesser im Vakuum $d_{ae,vac}$. Darüber hinaus ermöglicht das APS die direkte Messung der Streulichtintensität, woraus sich der Streulichtäquivalentdurchmesser d_{str} bestimmen lässt [WJ87; WL80]. Das AMS liefert demgegenüber zusätzlich die Elementarzusammensetzung mittels Massenspektroskopie [All+04; Lee+13].

Wie aus dem vorliegenden Abschnitt ersichtlich wird, steht eine Vielzahl von Messsystemen zur Charakterisierung von Nanopartikeln zur Verfügung. Allerdings wird deutlich, dass mit den unterschiedlichen Methoden verschiedene Äquivalentgrößen gemessen werden. Der Mobilitätsäquivalentdurchmesser d_m beschreibt ein sphärisches Partikel, welches die gleiche Widerstandskraft erfährt wie das zu vermessende Partikel. Der aerodynamische Äquivalentdurchmesser beschreibt ein kugelförmiges Partikel mit einer Dichte von $1000\,\text{kg/m}^3$ und der Sinkgeschwindigkeit, die der zu vermessenden Partikel entspricht. Der Volumenäquivalentdurchmesser bezeichnet den Durchmesser einer sphärischen Partikel mit demselben Volumen [BKW11]. Der Streulichtäquivalentdurchmesser wird anhand des Streulichtdurchmessers des Kalibrieraerosols bestimmt. Dies bedeutet, dass das zu analysierende Partikel ein Streulichtverhalten aufweist, das mit dem einer bestimmten Partikelgröße der Kalibrierpartikel übereinstimmt [Szy02; MC16].

Es wird ersichtlich, dass eine Vielzahl von Messgrößen erfasst wird, die für sphärische Partikeln in vielen Fällen deckungsgleich sind. In der Praxis werden jedoch nur in den seltensten Fällen perfekt sphärische Teilchen untersucht, da insbesondere bei komplex geformten Agglomeraten Eigenschaften wie die spezifische Oberfläche und die Form

von großem Interesse sind. Diese spielen eine entscheidende Rolle hinsichtlich der Reaktionsgeschwindigkeit, der biologischen Verträglichkeit, der Adsorption oder auch bei der Katalyse.

Aufgrund dessen ist eine mehrdimensionale Partikelanalyse von großem Interesse [Jin17; Toy+14; Kel+22]. Die gezielte Trennung nach mehr als einer Partikeleigenschaft stellt ein vielversprechendes Forschungsfeld dar, dem sich bereits einige Einrichtungen mit innovativen Ansätzen widmen. Ziel ist die Herstellung hochspezifischer Partikelsysteme [RSN19; SF23; Fur+20; Fur+19].

2.2 Messung zweidimensionaler Eigenschaftsverteilungen

Wie aus dem vorherigen Abschnitt ersichtlich wird, liefern die vorgestellten Analysemethoden lediglich unzureichende Informationen und ein Vergleich verschiedener Verfahren ist nur begrenzt möglich.

Auch wenn eine Größe allein nicht ausreichend aussagekräftig ist, um einen Prozess hinsichtlich der Partikeleigenschaften zu optimieren, erlaubt die Ermittlung mehrerer unterschiedlicher Äquivalentdurchmesser die Ableitungen weiterer, komplexer Partikeleigenschaften.

Dies wird im allgemeinen durch Tandem-Setups realisiert. Hierbei werden zwei Messverfahren in Reihe geschaltet. *DeCarlo, Slowik, Worsnop, Davidovits und Jimenez* [DeC+04] stellen dar, welche Äquivalentgrößen gemessen werden und über welche Eigenschaften sie verknüpft sind. Dies zeigen sie in einer folgenden Veröffentlichung am Beispiel eines DMA-AMS-Tandem Setups zur Messung von Verbrennungsabgas [Slo+04]. Hierdurch sind sie in der Lage den Stokesdurchmesser d_{st} aus dem Volumenäquivalentdurchmesser d_v sowie dem Mobilitätsdurchmesser d_m oder auch aus dem aerodynamischen Durchmesser d_{ae} zu berechnen:

$$d_{st} = \sqrt{\frac{\rho_0}{\rho}} \cdot d_{ae} = \sqrt{\frac{d_v^3}{d_m}} \quad , \tag{1}$$

wobei ρ die Partikeldichte und ρ_0 die Einheitsdichte $1000\,\mathrm{kg/m^3}$ sind. Sind der Mobilitäts- und Volumenäquivalentdurchmesser bekannt, kann die fraktale Dimension D_f bestimmt werden.

$$d_v^3 = \log(C') \cdot d_m^{D_f} \tag{2}$$

Hierbei muss der Volumen- über dem Mobilitätsäquivalentdurchmesser aufgetragen werden. Durch anfitten der Exponentialfunktion aus Gleichung (2), kann sowohl die fraktale Dimension als auch die Konstante C' bestimmt werden. Des Weiteren kann mit Hilfe des Mobilitäts- und Volumenäquivalentdurchmessers die effektive Dichte bestimmt werden.

$$\rho_{eff} = \rho \cdot (d_m/d_v)^3 \tag{3}$$

Slowik, Stainken u. a. [Slo+04] zeigen durch die Bestimmung dieser Parameter, dass bei bestimmten Verbrennungsparametern weniger sphärische Teilchen und vielmehr stark agglomerierte Partikeln entstehen.

Ebenso verwendeten *Olfert, Symonds und Collings* [OSC07] eine DMA-CPMA Kombination, um ein Wertepaar aus Mobilitäts- und Volumenäquivalentdurchmesser zu bestimmen. Durch Klassierung mit einem DMA erhalten sie zunächst ein monomodales Aerosol. Wird nun eine konstante Drehzahl am CPMA eingestellt, kann die Spannung am CPMA so variiert werden, dass die maximale Partikelanzahlkonzentration gemessen wird. An diesem Punkt überlagern sich die Transferfunktionen des DMA und des CPMA, sodass sowohl der Mobilitätsäquivalentdurchmesser d_m, als auch die Partikelmasse m bekannt sind. Wird nun die Spannung am DMA verändert, kann so für verschiedene Partikelmobilitäten Z die zugehörige Partikelmasse m und somit auch der zugehörige Volumenäquivalentdurchmesser d_v bestimmt werden. Dies ermöglicht es, die fraktale Dimension und die effektive Dichte (vgl. Gleichungen 2 und 3) zu bestimmen, um den Einfluss von Sulfat auf die Verbrennung in Dieselmotoren zu untersuchen. Hierdurch konnten sie nicht nur den Agglomerationsgrad von Partikeln hinsichtlich ihrer Mobilität bestimmen, sondern auch feststellen, dass bei höheren Sulfatgehalten die effektive Dichte bei kleinen Partikeln deutlich steigt. Da hier die Agglomeration aber als sehr niedrig angesehen wird, stellen *Olfert, Symonds und Collings* [OSC07] die Vermutung der Kondensation von Schwefelsäure an diesen Partikeln auf.

Johnson, Symonds und Olfert [JSO13] verwenden ebenfalls ein CPMA-DMA Setup zur Bestimmung der Dichte oder der Ladungsverteilung. Hierzu werden DEHS-Partikeln verwendet, die unter Standardbedingungen in flüssiger Form vorliegen, jedoch aufgrund ihres geringen Dampfdrucks eine vergleichsweise lange Lebensdauer aufweisen. So beträgt die Standzeit von Partikeln mit einem Durchmesser von 100 nm etwa 80 min [Hin99]. Dadurch kann von einem stabilen Aerosol mit sphärischen Partikeln ausgegangen werden. Mit Hilfe der CPMA-DMA Kombination zeigen sie nun, dass sie die Dichte mit einer Abweichung von bis zu 12 % bestimmen können. Auch die Ladungsverteilung kann auf diesem Wege bestimmt werden und stimmt mit einer Abweichung von maximal 10 % mit der Ladungsverteilung nach *Wiedensohler* [Wie88] überein. *Shapiro, Vainshtein u. a.* [Sha+12] erweitern das Setup, indem sie Kombinationen aus DMA, APM und AMS zur Charakterisierung verwenden. Hierdurch ist zusätzlich der aerodynamische Durchmesser im Vakuum $d_{ae,vac}$ messbar. Diesen nutzen sie um den Formfaktor, die effektive Dichte und die fraktale Dimension zu bestimmen und vergleichen die unterschiedlichen Ergebnisse. Darüber hinaus zeigen sie Rasterelektronenmikroskopaufnahmen (SEM) von Partikeln, die bei einem aerodynamischen Äquivalentdurchmesser von 120 nm gesampled wurden (vgl. Abbildung 2.1). Hierbei wird deutlich, dass viele verschiedene Kombinationen aus Mobilitäts- und Stokesdurchmesser möglich sind. Diese ergeben sich aus unterschiedlichen Partikelformen, die somit einen maßgeblichen Einfluss auf die Partikeleigenschaften ausüben.

Eine weitere vielversprechende Kombination ist ein Setup aus DMA und AAC. Hierbei werden der Mobilitsäquivalentdurchmesser d_m sowie der aerodynamische Äquivalentdurchmesser d_{ae} gemessen. *Tavakoli und Olfert* [TO13] verwenden diese Kombination, um ebenfalls die effektive Dichte, den Formfaktor und die fraktale Dimension von Ruß und von DEHS zu bestimmen.

Diese Tandem-Messverfahren können nicht nur verwendet werden, um die effektive Dichte ρ_{eff}, den Formfaktor χ und die fraktale Dimension D_f zu berechnen, vielmehr ist

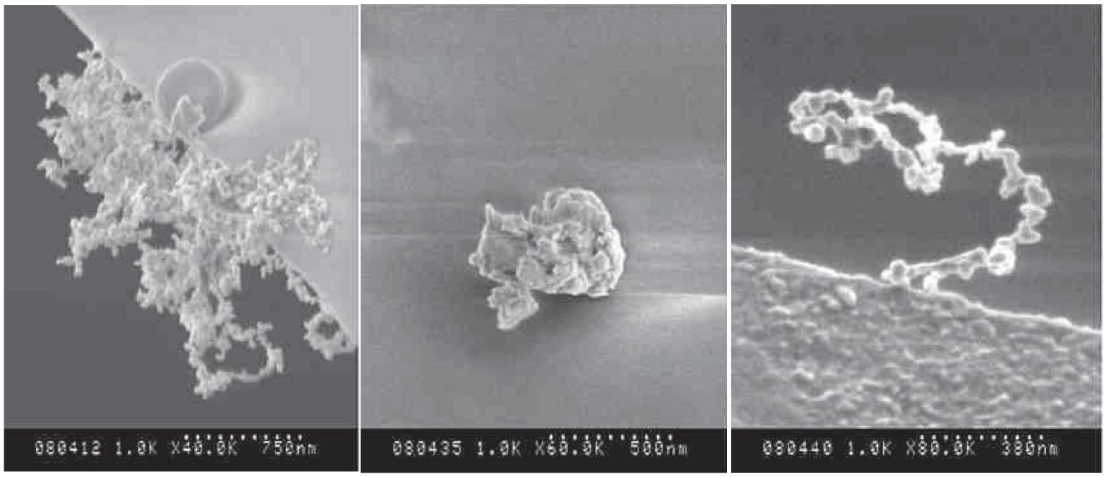

Abbildung 2.1: SEM Aufnahmen von Dieselabgas-Partikeln mit einem aerodynamischen Durchmesser von 120 nm [Sha+12].

es ebenfalls möglich, vollständige zweidimensionale Eigenschaftsverteilungen zu messen. Dies ist allerdings sehr aufwändig und benötigt umfassende Kenntnisse zur Dateninversion [SOR20].

Wie in diesem Kapitel dargelegt, ist die mehrdimensionale Analyse von Partikeln von großem wissenschaftlichen Nutzen. Auch *Park, Dutcher u. a.* [Par+08] verweisen in diesem Kontext auf weitere Studien.

Diese Untersuchungen verdeutlichen die neuen Möglichkeiten und Erkenntnisse, die sich durch die multidimensionale Charakterisierung von Partikelagglomeraten eröffnen. Dabei geht es nicht nur um den wissenschaftlichen Kontext, wie beispielsweise die Analyse der Ladungsverteilung in Abhängigkeit von der Partikelstruktur, sondern auch um die Optimierung industrieller Prozesse, etwa zur effizienteren Gestaltung von Katalysatoren. Vor diesem Hintergrund befasst sich diese Arbeit mit einem neuartigen Ansatz zur Bestimmung zweidimensionaler Eigenschaftsverteilungen.

Die Bestimmung von zwei unabhängigen Äquivalentdurchmessern in einem Gerät führt dabei zu einer wesentlichen Erleichterung hinsichtlich der Standardisierung der Messung sowie deren Rückrechnung. Gleichzeitig können die Kosten durch den geringeren apparativen Aufwand gegenüber Tandem-Setups deutlich reduziert werden. Auch messtechnisch ergeben sich Vorteile, da eine Partikel nicht zwei Messstrecken sowie zwei Klassierungen durchlaufen muss.

Für die Umsetzung dieses Vorhabens wurde eine Kombination aus DMA und AAC ausgewählt. Die beiden Geräte bestehen jeweils aus zwei konzentrischen Zylindern, wobei die Klassierung der Partikeln in dem Zylinderspalt erfolgt. In diesem Fall sind lediglich die elektrische Kraft (DMA) und die Zentrifugalkraft (AAC) für die jeweilige Klassierung ausschlaggebend. Dies führt dazu, dass sowohl der Stokes Äquivalentdurchmesser d_{st} als auch der Mobilitätsäquivalentdurchmesser d_m simultan gemessen werden können. Um die Funktion des CDMA besser verstehen zu können, werden in den Abschnitten 2.3 und 2.4

die Grundlagen für diese beiden einzelnen Messprinzipien vertieft dargestellt.

2.3 Differential Mobility Analyzer - DMA

Das Klassierprinzip des Differential Mobility Analyzer (DMA) basiert auf der Bewegung von geladenen Partikeln in einem elektrischen Feld. Der DMA besteht aus zwei konzentrisch angeordneten Zylindern, welche elektrisch isoliert sind, sodass eine Hochspannung angelegt werden kann, wodurch in dem Zylinderspalt ein elektrisches Feld entsteht. Der zu klassierende Aerosolstrom Q_a wird an der äußeren Elektrode aufgegeben, während an der inneren Elektrode gleichzeitig ein Hüllluftstrom Q_{sh} eingeleitet wird (vgl. Abbildung 2.2). Bei Anlegen eines negativen elektrischen Potentials an der inneren Elektrode, werden positiv geladene Partikeln, aufgrund der elektrischen Kraft F_{el}, von der äußeren Elektrode zur inneren Elektrode hin beschleunigt. Unter der Annahme der Stokes'schen Widerstandskraft F_D und trägheitsfreier Partikeln ergibt sich die Kräftebilanz für eine Partikel zu:

$$F_{el} = F_D \tag{4}$$

$$n \cdot e \cdot E = 3\pi\eta \cdot d_m \cdot v/Cu(d_m) \tag{5}$$

Mit: Ladungsanzahl n, Elementarladung $e = 1.6021{\cdot}10^{-19}$ C, elektrischer Feldstärke (raumladungsfrei, unendlicher Zylinderspalt) $E = \frac{U}{r \cdot \ln(r_a/r_i)}$, dynamische Viskosität η, Mobilitätsdurchmesser d_m, Partikeldriftgeschwindigkeit in radialer Richtung v, dem Cunningham Korrekturfaktor Cu [AR85] sowie Innen- bzw. Außenradius des Klassierspalts r_i, r_a.
Die Partikelmobilität ist definiert als [KW75]:

$$Z = \frac{v}{E} = \frac{n \cdot e \cdot Cu(d_m)}{3\pi\eta \cdot d_m} \tag{6}$$

Liegt nun im Messspalt ein laminares Strömungsprofil, also eine Schichtenströmung ohne Quervermischung, vor, kann die mittlere Fluidgeschwindigkeit in axialer Richtung u berechnet werden:

$$u = \frac{Q_{sh} + Q_a}{\pi(r_a^2 - r_i^2)} \tag{7}$$

Unter Vernachlässigung von Diffusion ergibt sich die Partikelbahn zu:

$$\frac{\mathrm{d}r}{\mathrm{d}y} = \frac{v}{u} = \frac{Z \cdot U \cdot (r_a^2 - r_i^2)}{r \cdot \ln(r_a/r_i) \cdot (Q_{sh} + Q_a)} \tag{8}$$

Wobei y die Position der Partikel in axialer Richtung ist. Umstellen und integrieren liefert:

$$r(y) = \sqrt{r_{ein}^2 + \frac{Z \cdot U \cdot (r_a^2 - r_i^2) \cdot y}{\ln(r_a/r_i) \cdot (Q_{sh} + Q_a)}} \tag{9}$$

Ist nun die Länge L vom Aerosoleinlass bis zum Sampling-Spalt bekannt, kann diese für y eingesetzt werden:

$$r(L) = \sqrt{r_{ein}^2 + \frac{Z \cdot U \cdot (r_a^2 - r_i^2) \cdot L}{\ln(r_a/r_i) \cdot (Q_{sh} + Q_a)}} \tag{10}$$

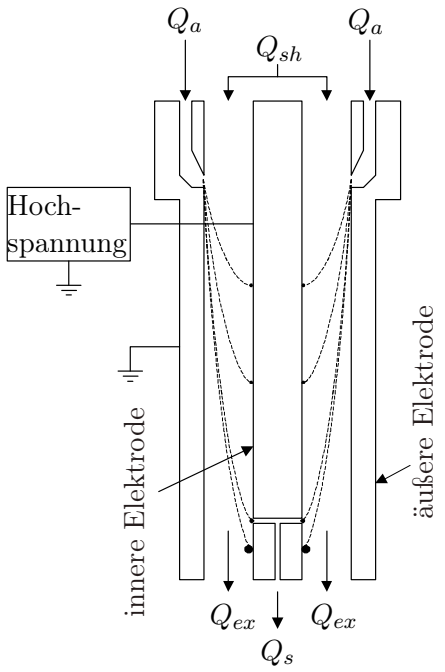

Abbildung 2.2: Schematische Darstellung eines DMA: Hüllluft Q_{sh}, Abluft Q_{exh}, Sampling-Volumenstrom Q_s, Aerosolvolumenstrom Q_a (nach [IT08]).

Dabei zeigt sich, dass der Eintrittsradius r_{ein}, an dem die Partikeln in den Klassierspalt gelangen, eine entscheidende Rolle für die Klassierung bzw. Abscheidung der Partikeln spielt. Allerdings besitzen sowohl der Einlass- als auch der Auslassspalt endliche Abmessungen, und das Verhältnis von Aerosol- zu Hüllluftstrom $\beta = Q_a/Q_{sh}$ kann nicht beliebig klein gewählt werden. Dies führt dazu, dass nicht ausschließlich eine einzelne Partikelgröße klassiert wird, sondern vielmehr ein definierter Größenbereich. Dieses Verhalten wird mit so genannten Transferfunktionen Ω abgebildet.
Stolzenburg [Sto88] leitete auf Basis von Stromlinenfunktionen eine analytische Gleichung zur Berechnung der Transferfunktion Ω ohne Partikeldiffusion her.

$$\Omega = \frac{1}{2 \cdot \beta} \cdot [\ |Z/Z^* - 1 - \beta| + |Z/Z^* - 1 + \beta| - 2 \cdot |Z/Z^* - 1|\ ] \tag{11}$$

Hierbei ist zu beachten, dass diese und folgende Gleichungen nur für die typische Betriebsbedingung ($Q_a = Q_s$, bzw. $Q_{sh} = Q_{ex}$) des DMA's gelten. Z^* stellt die Mobilität einer Partikel dar, welche der mittlere Partikelbahn folgt. Sie ergibt sich aus den Betriebsparametern:

$$Z^* = \frac{Q_{sh}}{2\pi \cdot L \cdot U} \cdot \ln\left(\frac{r_a}{r_i}\right) \tag{12}$$

Abbildung 2.3 zeigt eine Transferfunktion für ein Volumenstromverhältnis von $\beta = 0.1$. Hierbei ist auf der Abszisse die normierte Mobilität aufgetragen $\widetilde{Z} = Z/Z^*$. Die sich hieraus ergebende Dreiecksfunktion hat ihr Maximum bei 1, startet bei $1 - \beta$ und endet bei $1 + \beta$. Folglich wird die Auflösung über das Verhältnis von Aerosol- zu Hüllluftvolumenstrom β

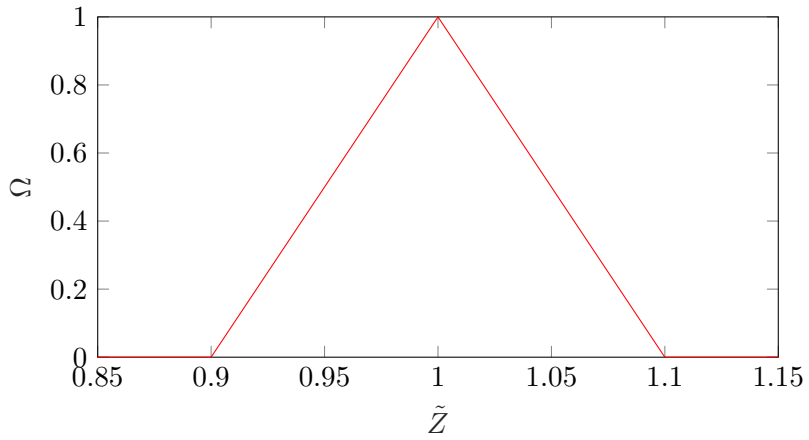

Abbildung 2.3: Ideale DMA Transferfunktion für $\beta = 0.1$.

definiert.

Um die gesamte Größenverteilung des Aerosols zu messen werden in der Praxis mehrere Spannungen eingestellt, sodass verschiedene Partikelgrößen klassiert und anschließend typischerweise mit einem CPC gezählt werden können. Stellt nun jede eingestellte Spannung U einen Betriebspunkt i dar, ergibt sich die gemessene Partikelanzahlkonzentration $N_i(U_i)$ aus [LLC06]:

$$N_i(U_i) = \sum_n \int_0^{+\infty} \eta_{CPC}(d_m) \cdot \eta_T(d_m) \cdot n_0(d_m) \cdot \gamma(d_m, n) \cdot \Omega(d_m) \, \mathrm{d}d_m \tag{13}$$

Wobei $\eta_{CPC}(d_m)$ und $\eta_T(d_m)$ die Wirkungsgrade des CPC's und die Penetrationseffizienz der Rohrleitungen darstellen, $\gamma(d_m, n)$ die Ladungsverteilung und $n_0(d_m)$ die Anzahldichteverteilung. Die Anzahldichteverteilung ist definiert als die Ableitung der Partikelanzahlkonzentration c_0 nach dem Mobilitätsdurchmesser d_m.

$$n_0(d_m) = \frac{\mathrm{d}c_0}{\mathrm{d}d_m} \tag{14}$$

Wird das Aerosol durch einen Neutralisator geleitet, bevor es in den DMA gelangt, kann eine definierte Ladungsverteilung aufgebracht werden. Typische Neutralisatoren sind radioaktive Quellen, wobei hier die Ladungsverteilung nach *Wiedensohler* [Wie88] berechnet werden kann, oder Röntgenquellen, wo die Ladungsverteilung nach *Tigges, Jain und Schmid* [TJS15] berechnet werden kann.
Im forliegenden Fall ist $N_i(U_i)$ die Messgröße und $n_0(d_m)$ die Zielgröße. Dies stellt natürlich zunächst ein mathematisches Problem dar, da $n_0(d_m)$ für die Lösung des Integrals bekannt sein müsste. Hierdurch kann nicht von der Messgröße auf die Zielgröße geschlossen werden. Es ergibt sich ein inverses mathematisches Problem, welches mit verschiedenen Inversionsverfahren gelöst werden kann. Die Dateninversion wird in Abschnitt 2.5 genauer diskutiert. Ist die maximale Partikelgröße bekannt, kann dieses Gleichungssystem direkt gelöst werden. Dies wird im allgemeinen erreicht, indem ein Impaktor eingesetzt wird.

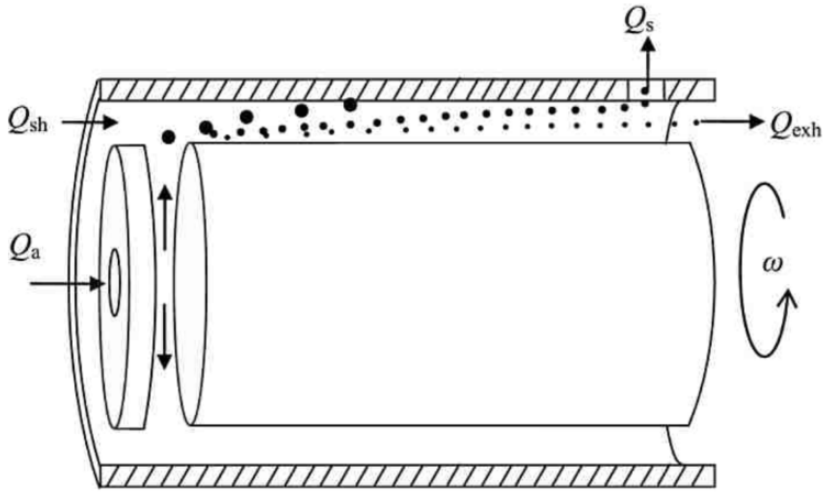

Abbildung 2.4: Schematische Darstellung eines AAC: Hüllluft Q_{sh}, Abluft Q_{exh}, Sampling-Volumenstrom Q_s, Aerosolvolumenstrom Q_a, Winkelgeschwindigkeit ω (nach [TO14]).

2.4 Aerodynamic Aerosol Classifier - AAC

Der Aerodynamic Aerosol Classifiers (AAC) ist wie der DMA ebenfalls aus zwei konzentrisch angeordneten Zylindern aufgebaut. Bei dem AAC wird der Aerosolvolumenstrom Q_a an dem inneren Zylinder aufgegeben und ein Hüllluftstrom Q_{sh} am Außenzylinder (vgl. Abbildung 2.4). Werden nun beide Zylinder in Rotation versetzt, entsteht eine Zentrifugalkraft F_z, die auf die Partikeln wirkt. Unter Annahme der Stokes'schen Widerstandskraft F_D und bei Vernachlässigung der Partikelträgheit ergibt sich die Kräftebilanz über eine Partikel zu:

$$F_z = F_D \tag{15}$$

$$\rho \cdot \pi \cdot \frac{d_v^3}{6} \cdot a_z = 3\pi\eta \cdot d_m \cdot v/Cu(d_m) \tag{16}$$

Mit der Dichte ρ und der Zentrifugalbeschleunigung $a_z = \omega^2 r$. Das Klassiermerkmal des AAC ist der aerodynamische Äquivalentdruchmesser. Dieser kann grundlegend durch die Partikelrelaxationszeit ausgedrückt werden, welche durch folgende Formel definiert wird:

$$\tau = \frac{v}{\omega^2 r} = \frac{\rho \cdot d_v^3 \cdot Cu(d_m)}{18 \cdot d_m \cdot \eta} = \frac{\rho \cdot d_{st}^2 \cdot Cu(d_{st})}{18\eta} = \frac{\rho_0 \cdot d_{ae}^2 \cdot Cu(d_{ae})}{18\eta} \tag{17}$$

Wie aus Gleichung (1) ersichtlich ist, stehen die unterschiedlichen Äquivalentdurchmesser in einer Abhängigkeitsbeziehung zueinander. Eine Umrechnung ist dabei prinzipiell möglich. In seiner Definition wird der Äquivalentdurchmesser als die Größe beschrieben, die ein sphärisches Partikel mit der gleichen Eigenschaft wie das betrachtete Partikel hätte. Dies impliziert, dass bei der Umrechnung zwischen den Äquivalentgrößen die Cunningham-Korrektur unverändert bleiben sollte. Die Prämisse, dass die Cunningham-Korrektur vom Mobilitätsäquivalentdurchmesser abhängt (vgl. Gleichung (16)), ist bereits fragwürdig. Diese Fragestellung ist allerdings noch nicht vollends geklärt und bedarf weiterer Untersuchungen sowie Vereinheitlichungen bezüglich der exakten Verwendung der Cunningham-Korrektur

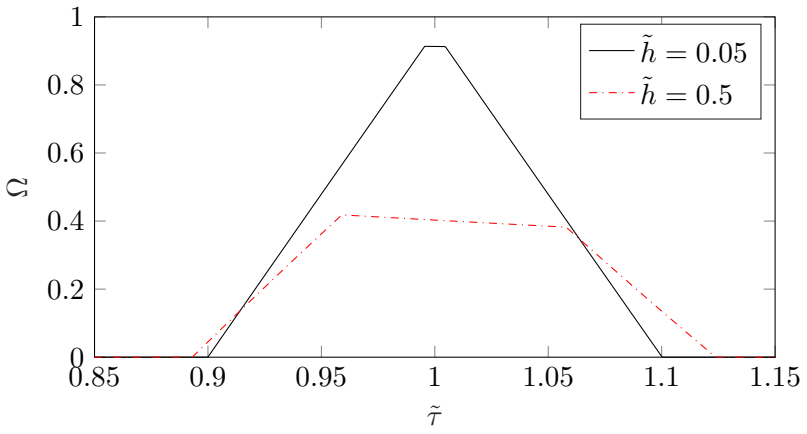

Abbildung 2.5: Ideale AAC Transferfunktion für $\beta = 0.1$.

der einzelnen Äquivalentgrößen. Hierzu wurde in der ersten hier gezeigten Veröffentlichung des Autors (vgl. Abschnitt 4.1) ein umfassender Kommentar verfasst [RRS25a].
Da der aerodynamische Durchmesser d_{ae} gemäß der vorliegenden Literatur die klassierte Äquivalentgröße darstellt [TO14] und bei fehlender Kenntnis der Partikeldichte die einzige zugängliche Äquivalentgröße ist, wird für die folgende Herleitung der aerodynamische Äquivalentdurchmesser als Größe für die Cunningham-Korrektur verwendet.
Nimmt man an, im Messspalt liegt eine uniforme Geschwindigkeit (Plugflow-Strömungsprofil) vor (vgl. Gleichung (7)) und wird der Einfluss von Diffusion vernachlässigt, kann die Partikelbahn direkt berechnet werden:

$$\frac{\mathrm{d}r}{\mathrm{d}y} = \frac{v}{u} = \frac{\tau \cdot \omega^2 \cdot r \cdot \pi \cdot (r_a^2 - r_i^2)}{Q_{sh} + Q_a} \tag{18}$$

Wobei y die Position der Partikel in axialer Richtung ist. Umstellen, integrieren und einsetzen von $y = L$ liefert:

$$r(L) = r_{ein} \cdot \exp\left\{ \frac{\tau \cdot \omega^2 \cdot \pi \cdot (r_a^2 - r_i^2)}{Q_{sh} + Q_a} \cdot L \right\} \tag{19}$$

Analog zum DMA zeigt sich hier eine Abhängigkeit der Partikeltrajektorie vom Startpunkt des Partikels. Da auch hier nur endliche Abmessungen für Aerosoleintritt und Aerosolaustritt sowie ein nicht unendlich kleines β realisiert werden können, ergibt sich ein Bereich klassierter Partikelgrößen. Dieser Bereich wird durch eine Transferfunktion Ω repräsentiert.
Unter der Annahme einer konstanten Zentrifugalkraft über den Spalt zeigen *Tavakoli und Olfert* [TO14] eine Methode zur Kalkulation der Transferfunktionen für den AAC. Diese Annahme trifft jedoch insbesondere bei einem großem Spalt nicht zu, weshalb die Methodik entsprechend weiterentwickelt werden musste. In Abschnitt 4.1 wird die Entwicklung der erweiterten Theorie über ein Partikeltrajektoriemodell diskutiert und schließlich in 4.2 über eine alternative Ableitung aus dem Streamline-Modell validiert. Eine Transferfunktion, bei

der Diffusion nicht berücksichtigt wird, kann somit dargestellt werden durch:

$$\Omega = \frac{1}{2\beta(1+A)} \cdot \left[-\left|-1-\frac{\beta+\kappa^2}{\kappa^2-1}\cdot A\right| + \left|-1-\beta-\frac{\kappa^2+\beta\kappa^2}{\kappa^2-1}\cdot A\right| + \left|-1+\beta-\frac{\beta+\kappa^2}{\kappa^2-1}\cdot A\right| - \left|-1-\frac{\kappa^2+\beta\kappa^2}{\kappa^2-1}\cdot A\right| \right] \tag{20}$$

Mit:

$$A = \exp\left\{\frac{2\tau\omega^2 L}{u}\right\} - 1 = \exp\left\{\frac{\tau}{\tau^*}\cdot\frac{2\widetilde{h}}{1+\beta}\right\} - 1 \tag{21}$$

und dem Radienverhältnis κ:

$$\kappa = \frac{r_i}{r_a} = \frac{1-\widetilde{h}/2}{1+\widetilde{h}/2} \tag{22}$$

wobei:

$$\tau^* = \frac{Q_{sh}+Q_{ex}}{\pi\omega^2(r_i+r_a)^2 L} \tag{23}$$

die Partikelrelaxationszeit ist, die eine Partikel hat, welche die mittlere Partikelbahn beschreibt.
In Abbildung 2.5 werden zwei Transferfunktionen für verschiedene Werte von $\widetilde{h} = 2\cdot\frac{r_a-r_i}{r_a+r_i}$ dargestellt. $\widetilde{h}$ entspricht dem Verhältnis der Spaltbreite zum mittleren Spaltradius und ist somit ein Maß für die Änderung der Zentrifugalkraft bezogen auf den Radius. Ist $\widetilde{h}$ klein, kann in guter Näherung die Zentrifugalkraft im Spalt als konstant angenommen werden. Auf der Abszisse ist die normierte Partikelrelaxationszeit $\widetilde{\tau} = \tau/\tau^*$ aufgetragen. Es entsteht eine abgeschnittene Dreiecksfunktion, wobei mit größeren Werten für $\widetilde{h}$ die Funktion immer weiter abgeschnitten und verzerrt wird. Eine detaillierte Erklärung wird in Abschnitt 4.1 gegeben.
Die gemessene Partikelanzahlkonzentration N_i für einen Betriebspunkt ergibt sich analog zu Abschnitt 2.3 zu:

$$N_i(\omega_i) = \int_0^{+\infty} \eta_{CPC}(d_{ae})\cdot\eta_T(d_{ae})\cdot n_0(d_{ae})\cdot\Omega(d_{ae})\,\mathrm{d}d_{ae} \tag{24}$$

Auch hier muss die Zielgröße $n_0(d_{ae})$ mit Hilfe einer Dateninversion berechnet werden, welche im folgenden Abschnitt erläutert wird.

2.5 Dateninversion

2.5.1 DMA Rückrechnung

Der Ladungszustand spielt bei der Klassierung in einem elektrischen Feld eine wichtige Rolle. Im ersten Schritt zur Berechnung der Partikelgrößenverteilung wird zunächst angenommen, dass lediglich einfach geladene Partikeln vorliegen. Der CPC-Wirkungsgrad $\eta_{CPC}(d_m)$ und Wirkungsgrad die Penetrationseffizienz der Rohrleitungen $\eta_T(d_m)$ werden an dieser Stelle der Übersichtlichkeit halber zunächst nicht mit berücksichtigt, können aber

später leicht in die Gleichung integriert werden. Der mittlere Mobilitätsdurchmesser d_i bei der jeweiligen Spannung U_i[1] ist wie folgt definiert.

$$d_i = \frac{2}{3} \cdot \frac{n \cdot e \cdot L \cdot U}{\eta \cdot Q_{sh} \cdot \ln(r_a/r_i)} \cdot Cu(d_i) \tag{25}$$

Mit d_i ergibt sich aus Gleichung (13):

$$N_i(U_i) = \int_0^{+\infty} n_0(d) \cdot \gamma(d_i, n = 1) \cdot \Omega(d_i) \, \mathrm{d}d \tag{26}$$

Unter Annahme einer dreieckigen Transferfunktionen (vgl. Abschnitt 2.3) können die Intervallgrenzen beschränkt werden:

$$N_i(U_i) = \int_{d_{i,u}}^{d_{i,o}} n_0(d) \cdot \gamma(d_i, n = 1) \cdot \Omega(d_i) \, \mathrm{d}d \tag{27}$$

wobei die Klassengrenzen:

$$d_{i,u} = \frac{Cu(d_{i,u})}{(1+\beta) \cdot \frac{Cu(d_i)}{d_i}} \tag{28}$$

$$d_{i,o} = \frac{Cu(d_{i,o})}{(1+\beta) \cdot \frac{Cu(d_i)}{d_i}} \tag{29}$$

berechnet werden müssen. Da die Cunningham-Korrektur selbst vom Partikeldurchmesser abhängt, muss die Lösung iterativ erfolgen.
Nun wird der Ergebnisvektor $\boldsymbol{N^*}$ (die gemessenen Werte) in k logarithmisch skalierte Klassen aufgeteilt, wobei erneut eine untere Klassengrenze $d_{j,u}$, obere Klassengrenze $d_{j,o}$ und eine Klassenmitte d_j für jede Klasse $j = 1, ...k$ erzeugt werden.
Für die Festlegung der Integrationsgrenzen ist entscheidend, ob die Transferfunktion vollständig innerhalb der Klassengrenzen liegt oder diese überschreitet. Liegt die untere Klassengrenze $d_{j,u}$ oberhalb des unteren Endes der Transferfunktion $d_{i,u}$, wird $d_{j,u}$ als untere Integrationsgrenze gewählt; andernfalls wird $d_{i,u}$ verwendet. Die obere Integrationsgrenze wird in entsprechender Weise bestimmt.
Das heißt, Gleichung (27) muss für jede Klasse erneut berechnet werden. Anschließend werden die Ergebnisse jeder Klasse summiert:

$$N_i(U_i) = \sum_{j=1}^{k} \left[\int_{x_u}^{x_o} n_0(d_j) \cdot \gamma(d_i, n = 1) \cdot \Omega(d_i) \, \mathrm{d}d \right] \tag{30}$$

Die neuen Klassengrenzen ergeben sich aus:

$$x_u = \begin{cases} d_{j,u}, & d_{j,u} \geq d_{i,u} \\ d_{i,u}, & d_{j,u} < d_{i,u} \end{cases} \tag{31}$$

[1] An dieser Stelle wurde der 'Mobilitäts'-Index m weg gelassen, sodass d_m lediglich durch d dargestellt wird, um eine bessere Lesbarkeit mit Hilfe der Indizierung zu ermöglichen.

$$x_o = \begin{cases} d_{i,o}, & d_{j,o} \geq d_{i,o} \\ d_{j,o}, & d_{j,o} < d_{i,o} \end{cases} \tag{32}$$

Unter der Annahme, dass $n_0(d_j)$ konstant über der Klasse ist, kann die Partikelanzahl pro Klasse N_j berechnet werden:

$$n_0(d_j) = \frac{N_j^*}{(x_o - x_u)} \tag{33}$$

Da diese nun unabhängig von der Partikelgröße ist, kann sie vor das Integral gezogen werden. Da sich die Ladungsverteilung bei kleinen Änderungen in der Partikelgröße ebenfalls nur sehr wenig ändert $\mathrm{d}\gamma(d_i, n)/\mathrm{d}d \approx 0$, kann über dem betrachteten Intervall die Ladungsverteilung ebenfalls als konstant angenommen und somit vor das Integral gezogen werden.

$$N_i(U_i) = \sum_{j=1}^{k} \left[\frac{N_{j,i}^*}{(x_o - x_u)} \cdot \gamma(d_i, n = 1) \cdot \int_{x_u}^{x_o} \Omega(d_i)\ \mathrm{d}d \right] \tag{34}$$

Um die Summierung aufzulösen kann nun jede Klasse einzeln betrachtet werden. Anschaulich heißt dies, wenn die Transferfunktion innerhalb einer Klasse liegt, werden alle klassierten Partikeln in diese Klasse im Klassierspalt abgeschieden. Ist die Transferfunktion allerdings breiter als die Klasse oder greift in eine andere Klasse über, muss der Anteil der Partikeln, die in einer anderen Klasse sind, korrigiert werden.

$$N_i(U_i) = \frac{N_{j,i}^*}{(x_o - x_u)} \cdot \gamma(d_i, n = 1) \cdot \int_{x_u}^{x_o} \Omega(d_i)\ \mathrm{d}d \ \cdot \frac{(d_{i,o} - d_{i,u})}{\int_{x_u}^{x_o} \Omega(d_i)\ \mathrm{d}d} \tag{35}$$

Hieraus folgt:

$$N_i(U_i) = N_{j,i}^* \cdot \frac{d_{i,o} - d_{i,u}}{x_o - x_u} \cdot \gamma(d_i, n = 1) \tag{36}$$

Das heißt, zu jedem Messwert $N_i(U_i)$ erhält man einen Vektor $N_{j,i}^*$ über alle Klassen j. Da die Einträge des Vektors $N_{j,i}^*$ nicht gleich wahrscheinlich sind, kann nicht nicht ohne weitere Schritte ein Mittelwert gebildet werden. Daher wird ein Schätzwert N_j^s für jede Partikelklasse gebildet. Hierbei wird angenommen, dass, je größer der Flächenanteil der Transferfunktion an der Messung ist, desto größer ist der Anteil des jeweiligen Wertes von $N_{j,i}^*$ Schätzwert N_j^s.

$$N_j^s = \frac{\sum_i N_{j,i}^* \cdot \epsilon_{j,i}}{\sum_i \epsilon_{j,i}} \tag{37}$$

Wobei:

$$\epsilon_{j,i} = \frac{x_o - x_u}{d_{j,o} - d_{j,u}} \cdot \int_{x_u}^{x_o} \Omega(d_i)\ \mathrm{d}d \tag{38}$$

Dieses hier dargestellte Ergebnis ist äquivalent zu dem von *Brunner* [Bru07].

Die bisherigen Berechnungen haben lediglich die Verteilung für einfach geladene Teilchen berücksichtigt. Um die korrekte Verteilung zu berechnen, müssen die Messwerte korrigiert werden. Für diese Mehrfachladungskorrektur wird eine Korrekturmatrix erzeugt:

$$M(i,j) = \begin{cases} 0, & i < j \\ \gamma(d_i, n=1), & i = j \\ \sum_{n=2}^{p} \left[\gamma(d_i, n) \cdot \frac{\int_{x_u}^{x_o} \Omega_n(d_i)}{\int_{d_{i,u}}^{d_{i,o}} \Omega_n(d_i)} \right], & i > j \end{cases} \tag{39}$$

Wobei Ω_n nun die Transferfunktion bei der jeweiligen Mehrfachladung ist. Die Ladungsverteilung $\gamma(d_i, n)$ kann für radioaktive Quellen [Wie88] und für Röntgenquellen [TJS15] berechnet werden. Der Schätzwert, falls nur einfach geladene Partikeln gemessen werden N_j^s, setzt sich nun zusammen aus [Bru07]:

$$N_j^s = N_j \cdot M(j,j) + \sum_i N_i \cdot C_i \tag{40}$$

Dieses ergibt ein Gleichungssystem. Ist die maximale Partikelgröße, z. B. durch einen vorgeschalteten Impaktor, bekannt, folgt daraus, dass auch keine mehrfachgeladenen größeren Partikeln in dieser Klasse sind, sondern nur einfach geladene Partikeln. Dies kann dazu verwendet werden, um das Gleichungssystem (vgl. Gleichung (40)) durch Rückwärtseinsetzen zu lösen, sodass der korrigierte Lösungsvektor N_j entsteht (vgl. [Bru07]).

2.5.2 AAC Rückrechnung

Die Dateninversion des AAC verläuft analog zu der Inversionsroutine des DMA (vgl. Abschnitt 2.5.1), nur dass hierbei die Ladungsverteilung der Partikeln keinen Einfluss hat sondern das gesamte Partikelkollektiv nur durch die Zentrifugalkraft beeinflusst wird.
Für den mittleren Durchmesser der Transferfunktion d_i gilt[2]:

$$d_i = \frac{36 \cdot \eta \cdot Q_{sh}}{\pi \cdot \omega^2 \cdot (r_a + r_i)^2 \cdot L \cdot Cu(d_i) \cdot \rho_0} \tag{41}$$

Auch hier werden der Übersichtlichkeit halber analog zu Abschnitt 2.5.1 die Wirkungsgrade η_{CPC} und η_T weg gelassen. Es ergibt sich die gemessene Partikelanzahl pro Drehzahl aus (vgl. Gleichung (24)):

$$N_i(\omega_i) = \int_{d_{i,u}}^{d_{i,o}} n_0(d) \cdot \Omega(d_i)\, \mathrm{d}d \tag{42}$$

Mit:

$$d_{i,u} = d_i \cdot \sqrt{(1-\beta) \cdot \frac{Cu(d_{i,u})}{Cu(d_i)}} \tag{43}$$

$$d_{i,o} = d_i \cdot \sqrt{(1+\beta) \cdot \frac{Cu(d_{i,o})}{Cu(d_i)}} \tag{44}$$

[2]Aus Gründen der Übersichtlichkeit wird in diesem Abschnitt ebenfalls auf den Index *ae* verzichtet.

Nun wird der Ergebnisvektor $\boldsymbol{N^*}$ in k logarithmisch skalierte Klassen aufgeteilt, wobei erneut eine untere Klassengrenze $d_{j,u}$, eine obere Klassengrenze $d_{j,o}$ und eine Klassenmitte d_j für jede Klasse $j = 1, ...k$ erzeugt werden.
Das heißt, Gleichung (42) muss für jede Klasse erneut ausgeführt und summiert werden, wobei sich die Klassengrenzen erneut anpassen:

$$N_i(\omega_i) = \sum_{j=1}^{k} \left[\int_{x_u}^{x_o} n_0(d_j) \cdot \Omega(d_i) \, \mathrm{d}d \right] \tag{45}$$

Mit:

$$x_u = \begin{cases} d_{j,u}, & d_{j,u} \geq d_{i,u} \\ d_{i,u}, & d_{j,u} < d_{i,u} \end{cases} \tag{46}$$

$$x_o = \begin{cases} d_{i,o}, & d_{j,o} \geq d_{i,o} \\ d_{j,o}, & d_{j,o} < d_{i,o} \end{cases} \tag{47}$$

Unter der Annahme, dass $n_0(d_j)$ konstant über der Klasse ist, kann die Partikelanzahl pro Klasse N_j berechnet werden:

$$n_0(d_j) = \frac{N_j^*}{(x_o - x_u)} \tag{48}$$

Hieraus folgt analog zu Abschnitt 2.5.1:

$$N_i(\omega_i) = N_{j,i}^* \cdot \frac{d_{i,o} - d_{i,u}}{x_o - x_u} \tag{49}$$

Um nun gute Schätzwerte für die Verteilung N_j^s zu erhalten, werden die Werte des Ergebnisvektors $N_{j,i}^*$ entsprechend der Flächenanteile gewichtet. Das bedeutet, dass eine Transferfunktion, die überwiegend innerhalb einer bestimmten Partikelgrößenklasse liegt, einen größeren Einfluss auf die Gewichtung erhält als eine Transferfunktion, die nur zu einem geringen Anteil in dieser Klasse enthalten ist.

$$N_j^s = \frac{\sum\limits_i N_{j,i}^* \cdot \epsilon_{j,i}}{\sum\limits_i \epsilon_{j,i}} \tag{50}$$

Wobei:

$$\epsilon_{j,i} = \frac{x_o - x_u}{d_{j,o} - d_{j,u}} \cdot \int_{x_u}^{x_o} \Omega(d_i) \, \mathrm{d}d \tag{51}$$

2.6 Centrifugal Differential Mobility Analyzer - CDMA

Das Messprinzip des Centrifugal Differential Mobility Analyzer (CDMA) verbindet die grundlegenden Prinzipien des Differential Mobility Analyzer (DMA) und des Aerodynamic Aerosol Classifier (AAC).
Diese Kombination eröffnet neue Möglichkeiten in der Partikelmesstechnik, insbesondere bei der Analyse von komplexen Partikelsystemen. Die simultane Nutzung verschiedener

physikalischer Prinzipien ermöglicht es, eine vollständige zweidimensionale Partikelgrößenverteilung hinsichtlich des Stokes Äquivalentdurchmessers und Mobilitäsäquivalentdurchmessers aufzunehmen. Dies ist ein entscheidender Fortschritt, da in vielen Anwendungen – etwa in der Aerosolforschung, Materialwissenschaft oder Umwelttechnik – eine einfache Äquivalentgröße nicht ausreicht, um die Systeme hinreichend gut zu beschreiben.
Der CDMA bietet zudem die Möglichkeit, die Ladungsverteilungen von Partikeln sowie die Cunningham-Korrektur zu bestimmen, vorausgesetzt, die Form der Partikeln ist bekannt. Diese Berechnungen sind in der Literatur typischerweise auf sphärische Partikeln beschränkt. Treten hingegen Agglomerate auf, ändern sich deren Eigenschaften signifikant, was zu Unsicherheiten bei der Berechnung der Ladungsverteilung sowie der Cunningham-Korrektur führt. Zudem ist nicht abschließend geklärt, welcher gemessene Äquivalentdurchmesser für deren Berechnung verwendet werden sollte.
Darüber hinaus könnte die zweidimensionale Charakterisierungsmethode durch das Hinzufügen weiterer Parameter zu einer multidimensionalen Analyse erweitert werden. So wäre es beispielsweise möglich, die Streulichtintensität nach der Klassierung zu messen oder mittels Massenspektroskopie die Elementzusammensetzung sowie den aerodynamischen Äquivalentdurchmesser im Vakuum $d_{ae,vac}$ zu bestimmen. Diese Ansätze würden die Analyse um eine dritte Dimension ergänzen und eine noch detailliertere Charakterisierung der Partikelsysteme erlauben.
Die Auswertung solcher multidimensionaler Verteilungen könnte durch den Einsatz von datenbasierten Algorithmen, insbesondere solcher auf Basis künstlicher Intelligenz, erheblich verbessert werden. Diese Algorithmen könnten komplexe Zusammenhänge in den Daten erkennen und eine effizientere Inversion der Messsignale ermöglichen.
Insgesamt eröffnet der CDMA, kombiniert mit den beschriebenen Weiterentwicklungen, neue Möglichkeiten für die Untersuchung und Analyse von Partikelsystemen. Diese Ansätze könnten nicht nur die Grundlagenforschung vorantreiben, sondern auch praktische Anwendungen in Industrie und Medizin verbessern. Die damit einhergehende Erweiterung des wissenschaftlichen Verständnisses und der technischen Möglichkeiten birgt das Potenzial, die Partikelanalyse auf ein völlig neues Niveau zu heben.
Für eine detaillierte Beschreibung der theoretischen Grundlagen sowie der praktischen Umsetzung wird auf die entsprechenden Veröffentlichungen verwiesen (vgl. Abschnitt 4.1 bis 4.4).

3 Forschungsbedarf

Die Vorhersage des Partikelverhaltens ist für zahlreiche Anwendungen essenziell, etwa zur Optimierung funktioneller Eigenschaften, zur Effizienzsteigerung von Prozessen und Produkten oder zur Bewertung der biologischen Verträglichkeit in Medizin und Umwelttechnik. Besonders Nanopartikel ($< 1000\,\mathrm{nm}$) stellen hierbei eine Herausforderung dar, da ihre Analyse mit erheblichem Messaufwand und komplexer Datenauswertung verbunden ist.
Zur Vereinfachung werden meist Äquivalentgrößen bestimmt (siehe Abschnitt 2), die eine Reduktion auf eine vergleichbare Größe erlauben. Bei Agglomeraten und komplexen Strukturen, wie Rußpartikeln, führt dies jedoch häufig zu Fehlinterpretationen.
Eine detailliertere Charakterisierung solcher Systeme kann mithilfe sogenannter Tandem-Aufbauten erfolgen. Diese erfassen zwei unterschiedliche Äquivalentgrößen und erlauben dadurch eine differenziertere Analyse. Die Anwendung dieser Technik ist jedoch durch hohe Investitionskosten sowie den erheblichen Bedarf an spezifischem Fachwissen für die Dateninversion eingeschränkt, da standardisierte Aufbauten bislang nicht verfügbar sind.
Um die mit Tandem-Setups verbundenen Einschränkungen – insbesondere die Faltung der Transferfunktionen, den hohen Erfahrungs- und Kenntnisbedarf des Anwenders sowie die erheblichen Investitionskosten – zu überwinden, wurde am Lehrstuhl für Partikelverfahrenstechnik das Konzept des Centrifugal Differential Mobility Analyzer (CDMA) entwickelt. Dieses, von Rasche entwickelte Messkonzept ermöglicht die Erfassung zweidimensionaler Eigenschaftsverteilungen von Partikeln in einem einzigen Messvorgang mit einem kompakten Gerät und wurde in einer vorangegangenen Arbeit beschrieben [Ras25].
Durch die Standardisierung der Messung kann ein Dateninversionsverfahren direkt implementiert werden, sodass die Bedienung durch Anwender mit weniger Fachwissen ermöglicht wird. Ein wesentlicher Vorteil dieses Ansatzes besteht darin, dass lediglich eine einzige Transferfunktion berücksichtigt werden muss. Dies reduziert insbesondere in den Randbereichen der zweidimensionalen Verteilung statistische Unsicherheiten, da in Tandem-Setups durch die Faltung mehrerer Transferfunktionen viele Partikeln abgeschieden werden. Im Gegensatz dazu führt die Anwendung einer einzelnen Transferfunktion im CDMA zu einem höheren Messsignal und damit zu einer verbesserten statistischen Auswertung. Diese Eigenschaften machen den CDMA zu einem vielversprechenden Instrument, insbesondere für die Grundlagenforschung. Rasche lieferte bereits wertvolle Erkenntnisse zur Optimierung der Auslegungsparameter und entwickelten Berechnungsansätze für die Transferfunktionen auf Basis eines Partikeltrajektorienmodells.
Ziel dieser Arbeit ist es, die theoretischen Grundlagen in die Entwicklung und experimentelle Validierung eines ersten funktionsfähigen Prototyps zu überführen. Auf Grundlage des bereits erarbeiteten Konzepts, werden Auslegungs- und Konstruktionskriterien des Messaufbaus erarbeitet sowie die geometrischen Abmessungen des CDMA bestimmt. Diese Dimensionierung des Systems hängt dabei unmittelbar vom gewählten Messbereich ab und ist bedingt durch ein tiefgehendes Verständnis der zugrunde liegenden physikalischen Prozesse, um eine zuverlässige Funktionsweise zu gewährleisten.
Zur Erlangung dieses Verständnisses werden mehrere komplementäre Untersuchungen durch-

geführt, die sowohl numerische als auch analytische Methoden umfassen. Ein zentraler Bestandteil ist die Simulation des elektrischen Feldes, welche Aufschluss über die Ladungsverteilung und die Feldhomogenität im CDMA gibt. Parallel dazu wird das Strömungsfeld numerisch analysiert, um die resultierenden Strömungsverhältnisse und deren Einfluss auf die Partikeltrajektorien zu erfassen. Die Kombination dieser Untersuchungen erlaubt nicht nur eine präzise Vorhersage des Partikeltransports, sondern auch eine erste quantitative Abschätzung der Partikelverluste innerhalb des Systems. Ergänzend hierzu wird die Transferfunktion des Prototyps berechnet. Dabei werden verschiedene Randbedingungen und Modellannahmen berücksichtigt, sodass unterschiedliche Szenarien abgebildet und deren Einfluss auf die Messergebnisse bewertet werden können. Diese Ergebnisse bilden die Grundlage für eine detaillierte Charakterisierung des Prototyps und stellen zugleich die notwendige Voraussetzung für die Durchführung von Vorwärtsrechnungen sowie die darauf aufbauende Dateninversion dar.
Die numerischen Ergebnisse werden im nächsten Schritt durch gezielte experimentelle Untersuchungen überprüft. Hierzu zählen insbesondere die Bestimmung der Transferfunktion sowie die experimentelle Erfassung von Partikelverlusten, um die Validität der Modellannahmen und die Qualität des Aufbaus experimentell abzusichern. Auf dieser Basis wird der von Rasche entwickelte Dateninversionsalgorithmus an die spezifischen Eigenschaften des Prototyps angepasst und mithilfe der gemessenen Transferfunktionen validiert. Durch diese Adaption ist es möglich, erste zweidimensionale Eigenschaftsverteilungen von Aerosolen im CDMA zu bestimmen und somit das Potenzial der Methode im praktischen Einsatz zu demonstrieren.
Abschließend wird der entwickelte Prototyp mit Aerosolen unterschiedlicher, idealerweise bekannter Partikelform getestet. Diese Messungen dienen nicht nur der Überprüfung der Robustheit des entwickelten Systems, sondern ermöglichen auch eine umfassende Bewertung der Aussagekraft der Methode. Damit wird ein durchgängiger Entwicklungsprozess realisiert, der von der konzeptionellen Erarbeitung über die numerische Simulation und experimentelle Validierung bis hin zur prototypischen Anwendung reicht und die Grundlage für weiterführende Optimierungen und eine mögliche Standardisierung des Verfahrens schafft.

4 Publikationen

Die vorliegenden Publikationen beschäftigen sich umfassend mit der Konstruktion, Inbetriebnahme und Validierung des Centrifugal Differential Mobility Analyzers (CDMA).
In der ersten Publikation (vgl. Abschnitt 4.1) werden das grundlegende Konzept und die Theorie des CDMA ausführlich erläutert. Darauf aufbauend wurde ein erster Prototyp des Geräts konstruiert und einer initialen Fehlerabschätzung unterzogen. Ein zentrales Ergebnis dieser Arbeit war die Berechnung einer zweidimensionalen Transferfunktion basierend auf einem Partikeltrajektorienmodell, was die Grundlage für erste Messungen bietet. Um die Funktionalität zu validieren, wurde ein Tandem-Setup bestehend aus einem DMA und dem CDMA aufgebaut. Ein derartiger Aufbau ermöglicht die Bestimmung der Transferfunktion in den Randbereichen des CDMA ($U = 0$ und $\omega = 0$). Die Berechnung der Transferfunktionen wurde durch eine neu entwickelte Methode durchgeführt. Diese Ansätze lieferten erste wichtige Abschätzungen der Geräteparameter, weisen jedoch noch Einschränkungen hinsichtlich ihrer Genauigkeit auf.
Die zweite Publikation (vgl. Abschnitt 4.2) fokussiert sich stark auf theoretische Aspekte und dient der Validierung der in der ersten Arbeit berechneten Transferfunktion. Durch eine alternative Herleitung der Transferfunktion mithilfe von Stromlinienfunktionen wurde die Korrektheit der vorigen Berechnungen untermauert. Darüber hinaus erlaubt es der neu präsentierte Ansatz, die Berechnungen um Effekte der Diffusion zu erweitern. Die Annahme eines homogenen Partikelstroms am Aerosoleinlass wurde kritisch hinterfragt. Eine Analyse zeigte, dass bei einem laminaren Strömungsprofil mit homogener Konzentration über den Querschnitt, der Partikelstrom in der Mitte des Einlassspalts höher ist als an den Rändern. Es scheint sogar möglich, dass am Rand gar keine Partikeln vorhanden sind. Eine Berücksichtigung dieser Randbedingungen verändert die Form der Transferfunktion erheblich und ermöglicht eine präzise Annäherung, beispielsweise durch eine Gaußfunktion, auch für größere Partikeln.
Die dritte Publikation (vgl. Abschnitt 4.3) widmet sich der Thematik der Dateninversion. Hierbei wurde der POCS-Algorithmus (Projection onto Convex Sets) eingeführt, implementiert und unter festgelegten Randbedingungen auf Messdaten angewendet. Zur Validierung des Algorithmus wurden ideale, virtuelle Partikelkollektive simuliert. Diese Daten wurden mit künstlichem Rauschen versehen, um reale Messbedingungen zu imitieren. Die Abweichungen zwischen den Ausgangsdaten und rekonstruierten Daten liegen dabei unter 10 %, was auf eine hohe Genauigkeit des Algorithmus hinweist. Abschließend wurde der Algorithmus auf reale Messdaten angewendet, wobei die Ergebnisse zeigen, dass der POCS-Algorithmus auch hier plausible Verteilungen liefert.
In der vierten Publikation (vgl. Abschnitt 4.4) steht die numerische Simulation des Strömungsverhaltens im CDMA mittels CFD (Computational Fluid Dynamics) im Mittelpunkt. Die gewonnenen Daten wurden genutzt, um den Einfluss realer Strömungsbedingungen auf die Transferfunktion zu untersuchen. Ergänzend dazu wurden umfangreiche Messreihen durchgeführt, um die tatsächliche Transferfunktion des CDMA zu bestimmen. Diese experimentellen Daten dienten als Basis für die Anwendung des POCS-Algorithmus

zur Messung realer Verteilungen. Als Anwendungsbeispiel wurde ein Silberaerosol bei unterschiedlichen Sinterstufen analysiert. Die gemessenen Verteilungen wurden anschließend in verschiedene weitere Parameter umgerechnet und die Ergebnisse ausführlich diskutiert. Die vier Publikationen zeigen die kontinuierliche Weiterentwicklung und Validierung des CDMA in Theorie, Simulation und Praxis. Beginnend mit der Konzeptentwicklung und der ersten Umsetzung eines Prototypen, über die theoretische Verfeinerung und Dateninversion bis hin zur praktischen Anwendung und Messung realer Verteilungen bildet diese Arbeit die Grundlage für die Anwendung des CDMA in der Partikelanalyse und weitere Optimierungen des Verfahrens.

4.1 The Centrifugal Differential Mobility Analyser - concept and initial validation of a new device for measuring 2D property distributions

Torben N. Rüther, David B. Rasche, Hans-Joachim Schmid,
Aerosol Research 3.1 (2025), S. 65–79. doi: 10.5194/ar-3-65-2025.
Nachdruck aus Aerosol Reserach (2025) mit Erlaubnis von Aerosol Research.

Der Autor dieser Dissertation hat das von David Rasche und Prof. Hans-Joachim Schmid entwickelte Grundkonzept des CDMA verwendet um einen Prototypen auszulegen, zu konstruieren und aufzubauen sowie die Berechnung der zweidimensionalen Transferfunktion zu erweitern. Eine neue Methode zur Messung von Transferfunktionen wurde entwickelt und es wurden erste reale Messungen durchgeführt und zu analysiert. Prof. Hans-Joachim Schmid hat den Autor während der gesamten Arbeit betreut und an der Revision des Manuskripts mitgewirkt.

Aerosol Res., 3, 65–79, 2025
https://doi.org/10.5194/ar-3-65-2025

AEROSOL Research Open Access

The Centrifugal Differential Mobility Analyser – concept and initial validation of a new device for measuring 2D property distributions

Torben N. Rüther[1], David B. Rasche[1,2], and Hans-Joachim Schmid[1]

[1]Particle Technology Group, Mechanical Engineering, Paderborn University, Paderborn 33098, Germany
[2]REMBE GmbH Safety+Control, Brilon 59929, Germany

Correspondence: Hans-Joachim Schmid (hans-joachim.schmid@uni-paderborn.de)

Received: 17 October 2024 – Discussion started: 25 October 2024
Revised: 9 December 2024 – Accepted: 15 December 2024 – Published: 28 January 2025

Abstract. Usually for the characterization of nanoparticles, an equivalent property is measured, e.g. the mobility-equivalent diameter. In the case of non-spherical, complex-shaped nanoparticles, one equivalent particle size is not sufficient for a complete characterization. Most of the methods utilized to gain deeper insight into the morphology of nanoparticles are very time-consuming and costly or have bad statistics (such as tandem setups or TEM (transmission electron microscopy)/SEM (scanning electron microscopy) images). To overcome these disadvantages, a prototype of a new compact device, the Centrifugal Differential Mobility Analyser (CDMA), was built, which can measure the full 2D distribution of mobility-equivalent and Stokes equivalent diameters by classification in a cylinder gap through electrical and centrifugal forces. An evaluation method to determine the transfer probabilities is developed and used in this work to compare the measurement results with the theory for the pure rotational behaviour (like the Aerodynamic Aerosol Classifier) and the pure electrical behaviour (like the Dynamic Mobility Analyser). In addition, the ideal 2D transfer function was derived using a particle trajectory approach. This 2D transfer function is a prerequisite for obtaining the full 2D particle size distribution from measurements by inversion.

1 Introduction

A common feature of many techniques is that, for non-spherical particles, they measure an equivalent particle size. For example, the Differential Mobility Analyser (DMA) (Knutson and Whitby, 1975) measures the mobility-equivalent diameter. The Aerodynamic Aerosol Classifier (AAC) (Tavakoli and Olfert, 2013), the Low Pressure Impactor (LPI) (Fernandez de la Mora et al., 1989), and the Aerodynamic Particle Sizer (APS) (Mitchell et al., 2003) measure the aerodynamic-equivalent diameter. The Centrifugal Particle Mass Analyser (CPMA) (Olfert and Collings, 2005) measures the mass–charge ratio. However, this information alone is not sufficient to determine the actual particle properties comprehensively, especially in the case of large agglomerates, which may have significantly different shapes than spherical particles. Therefore, numerous studies have focused on this topic. In particular, the influence of particle shape on bio-availability and toxicity (Jindal, 2017; Toy et al., 2014) as well as on environmental aerosols is a topic of great scientific interest (Kelesidis et al., 2022). The effects of particle shape on the mechanical stability and reaction rates of batteries have also been investigated (Zhang et al., 2022). Due to its relevance, many research institutions are focusing on separation by more than one particle property to produce highly specific particle systems (Rhein et al., 2019; Sandmann and Fritsching, 2023; Furat et al., 2020, 2019).

In order to design and control these processes effectively, it is essential to develop techniques to assess the particle structure and dimensions. Scanning electron microscopy (SEM) studies at least offer full shape information in 2D for this purpose, but imaging the full particle size distribution requires a significant number of images, which can be both time-consuming and costly. An alternative approach is tandem se-

tups, i.e. a serial arrangement of two different classification systems, allowing the determination of two different equivalent particle sizes. This can provide more comprehensive information and can be used to derive enhanced, more specific structure information, e.g. the effective density or fractal dimension (Park et al., 2008; Slowik et al., 2004; Tavakoli and Olfert, 2013).

The CDMA (Centrifugal Differential Mobility Analyser) is a recently developed compact device that has been designed to address the limitations of existing tandem setups, particularly the high costs of equipment and the complexity of the associated measurement procedures. Furthermore, the measurement and evaluation can be conducted directly with the CDMA, which significantly reduces the analytical burden and the user's required knowledge for calculating such measurements.

The objective is to obtain a complete 2D particle size distribution expressed in terms of the Stokes equivalent and mobility-equivalent diameters. The combination of these two properties allows us to draw conclusions about the particle geometry. That is, a complete 2D property distribution of the effective density or fractal dimension can be calculated, thus facilitating an even more precise and comprehensive investigation of the distribution shape. Additionally, the large number of examined particles enhances the statistical reliability of the findings, exceeding SEM examinations. Furthermore, additional examinations can be conducted using this approach. For example, it may be possible to measure the charge distribution of specific particles or to investigate the influence of particle shape on charge distribution.

2 Concept and fundamental theory

The newly developed principle of the CDMA combines the concepts of the DMA and AAC. In general, the CDMA consists of two concentric cylinders between which high voltage can be applied. Both of them can be rotated at the same angular speed. This means that both the voltage and the speed can be superimposed, whereas in the DMA only the voltage can be varied and, in the AAC, only the speed. This means that, with the CDMA, particles can be classified according to their drag force and mass. In the DMA particles are usually characterized by their mobility diameter d_m (i.e. the diameter of a spherical particle experiencing the same drag force for a given relative velocity as the actual particle) (Friedlander, 2000). The AAC typically uses the aerodynamic diameter d_{ae} to characterize particles (i.e. the diameter of a sphere with unit density and the same settling velocity), which has the advantage that all particles of the same settling velocity in the centrifugal field will have the same equivalent diameter (Tavakoli and Olfert, 2014). However, particles with exactly the same shape but a different material density will show different aerodynamic diameters. Since in our instrument the 2D characterization mainly aims to characterize the particle shape, we suggest using the Stokes diameter d_{St} instead (i.e. the diameter of a sphere of the same density with the same settling velocity w_S as the actual particle) for characterization (Colbeck, 2013; Reist, 1993). Although both equivalent sizes are closely related, the Stokes diameter only depends on the particle shape, e.g. characterized by the volume- and mobility-equivalent diameters d_v and d_m, respectively (Baron et al., 2011).

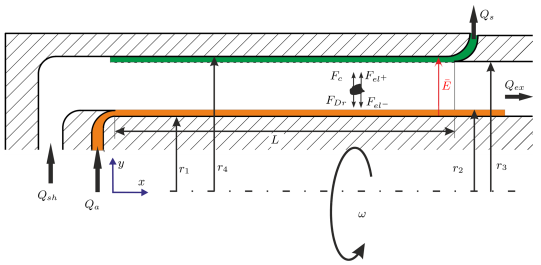

Figure 1. Schematic drawing of the classification zone of the CDMA: sheath air Q_{sh}, exhaust air Q_{ex}, sample air Q_s, aerosol air Q_a, electrical field magnitude E, rotational speed ω, electrical force F_{el}, centrifugal force F_c, drag force F_{Dr}, length of the transfer path L, inner radius r_1, maximum radius at which the particles enter r_2, minimum radius at which the particles are still classified r_3, and outer radius r_4.

$$d_{St} = \sqrt{\frac{18\eta}{\rho_S \cdot b \cdot \mathrm{Cu}(d_m)} \cdot w_s} = \sqrt{\frac{\rho_0}{\rho_S}} \cdot d_{ae} = \sqrt{\frac{d_v^3}{d_m}} \quad (1)$$

η is the dynamic viscosity, ρ_S the solid density of the particle material, ρ_0 the unit density of $1000\,\mathrm{kg\,m^{-3}}$, b the centrifugal or gravitational acceleration, and w_S the settling velocity. In particular, the Stokes and mobility diameters become identical in the case of a perfect sphere. However, the calculation of the Stokes diameter from classification according to the settling velocity in the CDMA centrifugal field requires knowledge of the particle density. Therefore, if the density is not known with sufficient accuracy or an aerosol consisting of different materials is analysed, the aerodynamic diameter should be used as in classical AAC theory. This can easily be adapted in the inversion algorithm. However, if the density of the particles is unknown, the shape information will no longer be accessible. By measuring all voltage–speed combinations, a full 2D particle size distribution in terms of d_{st} and d_m can be calculated by data inversion.

When an aerosol volume flow Q_a is the inner cylinder, the particles are displaced by electrical forces and centrifugal forces which always drive the particles towards the outer cylinder (Fig. 1). Particles pass through the sheath airflow Q_{sh} and are classified and counted in the sample flow Q_s if they meet the specified characteristics.

Because inertial forces are typically negligible, the quasi-static particle drift velocity w_{Dr} can be obtained from a force

balance. Assuming Stokes' drag then leads to

$$Q_P \cdot E + m_P \cdot a_c = 3\pi\eta d_m w_{Dr}/Cu, \quad (2)$$

with particle charge Q_P, electrical field magnitude E (as defined like in Fig. 1), particle mass m_P, centrifugal acceleration $a_c = \omega^2 r$, dynamic viscosity η, mobility diameter d_m, particle drift velocity w_{Dr}, and Cunningham correction factor Cu (Allen and Raabe, 1985).

The limiting cases $E = 0$ and $\omega = 0$ in Eq. (2) lead to the equations from the derivations of the DMA (Stolzenburg, 1988) and AAC (Tavakoli and Olfert, 2014), respectively.

Using the same assumptions as in the boundary cases – i.e. no diffusion, plug flow, and no perturbations of the E field (ideal geometry, no room charges, and no inertial forces) – the deterministic description of the particle's path is achieved by rearranging and integrating Eq. (2).

$$r(y) = \sqrt{\frac{\left(\tau\cdot\omega^2\cdot r_{in}^2 + \frac{Z\cdot U}{\ln\left(\frac{r_4}{r_1}\right)}\right)\cdot\exp\left\{2\cdot\tau\cdot\omega^2\cdot y\cdot\frac{\pi\cdot(r_4^2-r_1^2)}{Q_{sh}+Q_a}\right\} - \frac{Z\cdot U}{\ln\left(\frac{r_4}{r_1}\right)}}{\tau\cdot\omega^2}}, \quad (3)$$

with the voltage U, the rotational velocity ω, the inner r_1 and outer r_4 radii, the actual radius at which the particle enters r_{in}, the length of the classifying gap L, the position of the particle in the streamwise direction y, the particle relaxation time τ (Tavakoli and Olfert, 2014)[1], and the particle mobility Z (Stolzenburg, 1988).

$$\tau = \frac{\rho\cdot d_v^3\cdot Cu(d_m)}{18\cdot d_m\cdot\eta} = \frac{\rho\cdot d_{st}^2\cdot Cu(d_m)}{18\eta}, \quad (4)$$

$$Z = \frac{n\cdot e\cdot Cu(d_m)}{3\pi\cdot\eta\cdot d_m}, \quad (5)$$

where ρ is the particle density, d_{st} is the Stokes equivalent diameter, d_v is the volume-equivalent diameter, n is the number of charges carried by a particle, e is the elementary charge, and Q_{ex} is the exhaust gas volume flow.

The dimensionless, normalized mobility or particle relaxation time is obtained as follows:

$$\tilde{Z} = Z/Z^*; \tilde{\tau} = \tau/\tau^*, \quad (6)$$

where Z^* is the mobility required for a particle entering at the centre of the aerosol inlet to be sampled at exactly the centre of the outlet (Stolzenburg, 1988). τ^* describes the same behaviour but for the relaxation time (Tavakoli and Olfert, 2014).

$$Z^* = \frac{Q_{sh}+Q_{ex}}{4\cdot\pi\cdot L\cdot U}\cdot\ln\left(\frac{r_4}{r_1}\right) \quad (7)$$

[1]See the short comment on the definition of the particle relaxation time in Appendix A.

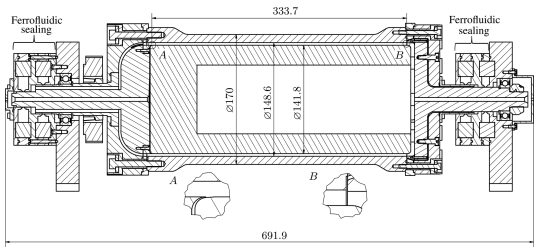

Figure 2. Cross section of the CDMA prototype.

$$\tau^* = \frac{Q_{sh}+Q_{ex}}{\pi\omega^2(r_1+r_4)^2 L} \quad (8)$$

For typical operating conditions ($Q_s = Q_a$), a dimensionless form of Eq. (3) can be derived, where $\bar{r} = \frac{r_1+r_4}{2}$ is the average of the outer and inner radii, $\beta = \frac{Q_a}{Q_{sh}}$ is the ratio of the aerosol-to-sheath airflow, and $\tilde{h} = \frac{r_4-r_1}{\bar{r}}$ is the ratio of the gap height to $\bar{r}$.

$$r(y) = \sqrt{r_{in}^2\cdot\exp\left\{\frac{y}{L}\cdot\tilde{\tau}\cdot\frac{2\tilde{h}}{1+\beta}\right\} + \bar{r}^2\cdot\frac{\tilde{Z}}{\tilde{\tau}}\cdot\left[\exp\left\{\frac{y}{L}\cdot\tilde{\tau}\cdot\frac{2\tilde{h}}{1+\beta}\right\} - 1\right]} \quad (9)$$

3 CDMA prototype

To validate the functional principle, a prototype was designed and built. As a boundary condition, this prototype should be able to measure particle sizes ranging from 50 to 1000 nm for both the mobility-equivalent diameter and the Stokes equivalent diameter. In addition, the speed should not exceed 6000 rpm, because the ferrofluid sealing has only been tested in this range (with higher angular speeds, the sealing could evaporate much more quickly and produce particles itself) and to prevent unbalanced forces on the bearings.

3.1 Design

Figure 2 shows the cross section of the CDMA prototype and its dimensions.

At flow rates of $Q_a = 0.3$ lpm and $Q_{sh} = 3$ lpm, and assuming a particle density of 1000 kg m^{-3}, these dimensions enable the characterization of particles in the size range from 50 to 1000 nm, where the maximum speed is 6000 rpm and the maximum voltage is limited to 1000 V[2].

One difficulty was in achieving a suitable seal against the environment. Friction seals are not an option, as either the

[2]A maximum gap distance of 3 kV mm^{-1} can be applied with optimally dry air and smooth flat surfaces (). As there are corners, particularly at the inlet and outlet, a maximum voltage of 300 V mm^{-1} is chosen for safety reasons.

sealing of the system is difficult or the seal heats up strongly due to high friction, generating particles, or abrasion occurs in general. Therefore, a ferrofluid seal was designed and tested. A ring magnet is used. On the outside of the ring magnet there are iron components that create a pole shoe on the inside of the ring. This pole shoe has a tolerance of approximately +0.1 mm of the shaft passing through it. The ferrofluid is injected into the pole shoe. This creates a virtually frictionless seal that does not generate particles.

The aerosol is fed into the long bore on the left, entering the classifying gap at point A. The sheath air is fed between the two ferrofluid sealings (this drilling is not visible in Fig. 2), entering the CDMA through eight axial holes and finally also the classifying gap via a bend. At the end of the classifying gap (point B), the sample flow is diverted outwards so that the particles are directed through narrow gaps towards the ferrofluid sealing and released at the centre of the seal. The sampled particles can then be counted by a CPC or similar instrument. The excess gas flow is sucked in towards the centre and directed through the long bore to the right, where it is purified for return to the inlet of the CDMA as the sheath airflow.

A toothed belt is used to transmit the forces of the motor to the rotating cylinder. A negative high potential is applied to the centre of the outer cylinder. This area is electrically isolated from the rest of the CDMA by insulators (outside between points A and B). The other components, like the inner electrode and all kinds of bearings, sealings, and housings, are connected to Earth so that there is mass potential, creating a voltage and thus an electrical field between the electrodes. This leads the electrical force of positively charged particles to be in the direction of the centrifugal force.

3.2 Particle losses

Particle losses occur due to the classification principle in the inlet and outlet areas of the CDMA. This occurs, in particular, during rotation, as the centrifugal force then acts on the particles in all the rotating feed and discharge pipes. This movement pushes the particles further towards the respective outer wall, where they are separated. Walls with a large radius running parallel to the axis of rotation are particularly susceptible because of the higher exerting centrifugal forces.

Separation can be calculated individually for each part. Dividing the radial distance s the particles move in each part by the distance between the walls $s_{\max}$ gives the degree of separation, assuming a laminar flow profile and a uniform concentration across the flow cross section[3].

$$T = s/s_{\max} \tag{10}$$

[3]This only affects the measured number concentration and therefore only the maximum height of the transfer function, as neither the width nor the position is affected: $\Omega_{\max} = \frac{\Omega_{\max,\text{measured}}}{(1-T)}$.

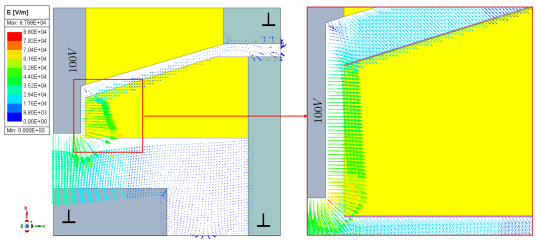

Figure 3. Electrostatic simulation of the outlet using Ansys Electronics at an applied voltage of 100 V.

In addition, losses occur when the voltage is applied. Since a polymeric material (yellow regions in Fig. 3) was used to insulate the high-voltage outer electrode directly in the input and output regions, an electrical field is even generated in the input and output gaps due to the insulating properties of the air. Figure 3 shows a simulation with the Ansys Electronics software, which was used to simulate the field strengths at an applied voltage of 100 V. It can be seen that the field strength is partly as high as in the classifying gap. Hence, the simulation can also be used to calculate a theoretical deposition analogous to rotation.

4 The transfer function

The transfer function Ω describes the probability of a particle with certain properties (relaxation time τ and mobility Z) being successfully classified under given operating conditions (voltage U and angular velocity ω).

4.1 Two-dimensional transfer function based on the particle trajectory calculation

Since in CDMA, as in DMA and AAC, the ratio of aerosol volume flow to sheath air volume flow cannot be infinitely small and the inlet and sample gaps are also finite, the classified aerosol is not completely monomodal, but a distribution exists.

Assuming a constant particle flux density at the inlet, stratified plug flow, a homogeneous E field in the classifying gap, and non-inertial and diffusion-free particles, this distribution can be calculated analytically. The assumption of a plugflow profile is justified, since, for classifying a particle, the mean velocity is mainly relevant, since the particle path crosses the whole flow domain. Stolzenburg (1988) proved this with the derivation of transfer functions based on a streamline approach for diffusing particles. The derivation of the 2D transfer function is given in Appendix B.

Therefore, the transfer function Ω can be calculated as follows:

$$\Omega_{\text{CDMA}} = \max\left[\min\left(f_1, f_2, 1\right), 0\right], \tag{11}$$

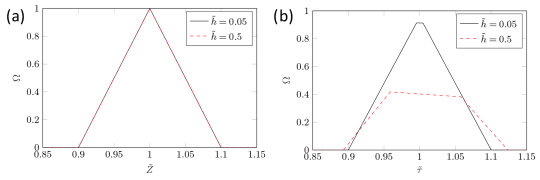

Figure 4. Transfer functions for $\tilde{\tau} = 0$ **(a)** and $\tilde{Z} = 0$ **(b)** at $\beta = 0.1$ for different ratios of radii.

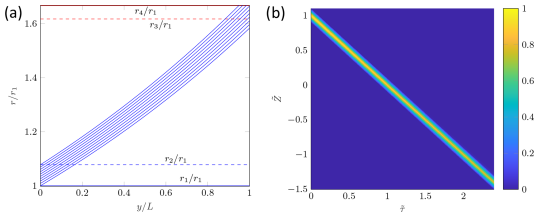

Figure 5. Exemplary particle trajectories for $\tilde{Z} = 0$, $\tilde{\tau} = 1$, and $\tilde{h} = 0.5$ **(a)** and 2D transfer functions $\beta = 0.1$ and $\tilde{h} = 0.05$.

with

$$f_1 = \frac{\frac{\beta+\kappa^2}{1+\beta} - (\frac{1/\beta+\kappa^2}{1/\beta+1} + \frac{(\kappa+1)^2}{4} \cdot \frac{\tilde{Z}}{\tilde{\tau}}) \cdot \exp\left\{-\tilde{\tau} \cdot \frac{2\tilde{h}}{1+\beta}\right\} + \frac{(\kappa+1)^2}{4} \cdot \frac{\tilde{Z}}{\tilde{\tau}}}{\frac{\beta+\kappa^2}{1+\beta} - \kappa^2} - \max\left(\frac{\frac{\beta+\kappa^2}{1+\beta} - (1 + \frac{(\kappa+1)^2}{4} \cdot \frac{\tilde{Z}}{\tilde{\tau}}) \cdot \exp\left\{-\tilde{\tau} \cdot \frac{2\tilde{h}}{1+\beta}\right\} + \frac{(\kappa+1)^2}{4} \cdot \frac{\tilde{Z}}{\tilde{\tau}}}{\frac{\beta+\kappa^2}{1+\beta} - \kappa^2}, 0\right), \tag{12}$$

$$f_2 = \frac{(1 + \frac{(\kappa+1)^2}{4} \cdot \frac{\tilde{Z}}{\tilde{\tau}}) \cdot \exp\left\{-\tilde{\tau} \cdot \frac{2\tilde{h}}{1+\beta}\right\} - \frac{(\kappa+1)^2}{4} \cdot \frac{\tilde{Z}}{\tilde{\tau}} - \kappa^2}{\frac{\beta+\kappa^2}{1+\beta} - \kappa^2} - \max\left(\frac{\left(\frac{1/\beta+\kappa^2}{1/\beta+1} + \frac{(\kappa+1)^2}{4} \cdot \frac{\tilde{Z}}{\tilde{\tau}}\right) \cdot \exp\left\{-\tilde{\tau} \cdot \frac{2\tilde{h}}{1+\beta}\right\} - \frac{(\kappa+1)^2}{4} \cdot \frac{\tilde{Z}}{\tilde{\tau}} - \kappa^2}{\frac{\beta+\kappa^2}{1+\beta} - \kappa^2}, 0\right), \tag{13}$$

$$\kappa = \frac{r_1}{r_4} = \frac{1 - \tilde{h}/2}{1 + \tilde{h}/2}, \tag{14}$$

$$\beta = Q_a / Q_{sh}. \tag{15}$$

4.2 Theoretical transfer functions for $\tau = 0$ and $Z = 0$

Figure 4 presents the transfer functions for $\tilde{\tau} = 0$ and $\tilde{Z} = 0$ of the CDMA. For $\tilde{\tau} = 0$ (Fig. 4a), the transfer function becomes that of a normal DMA. This is indicated by the typical triangular shape, where the FWHM (full width at half maximum) value also corresponds to the value for β. It can also be seen that there is no dependence on the slit geometry, because the curves for both $\tilde{h} = 0.05$ and $\tilde{h} = 0.5$ are identical.

The transfer function for $\tilde{Z} = 0$ (Fig. 4b) exhibits pure AAC behaviour. In contrast to traditional AAC theory (Tavakoli and Olfert, 2014), the transfer function does not have a triangular shape. This is due to the assumption of a mean centrifugal force acting on the particles throughout the whole classification gap, which has been used thus far. However, as described in the previous section, increased particle deposition occurs because the centrifugal force increases with an increasing radius. This means that, if particles with $\tilde{\tau} = 1$ are fed over the inlet, all particle trajectories should only be shifted parallel. However, as the centrifugal force increases with radius, particles entering the classifier gap at a larger radius are directly affected by a higher centrifugal force. Thus, if the particles are close to r_2, they are already located at a larger radius compared to the centre radius of the aerosol inlet when they enter the transfer zone, so they experience a higher centrifugal force. Figure 5a shows individual particle trajectories (with $\tilde{\tau} = 1$ and $\tilde{Z} = 0$) for particles fed between r_1 and r_2 (blue dashed line) and sampled between r_3 and r_4 (the two red dashed lines) after transfer length L.

It can be seen that the particle trajectories are widened to such an extent that particles are deposited both before and after the sampling gap – particle trajectories which do not end between the red lines at L are deposited on the walls before or after the sampling outlet. This phenomenon is, of course, due to the way in which the AAC works and therefore occurs mainly when the particle relaxation time is relevant. This is also why the ideal transfer function for an AAC is a truncated triangular function. This increases as the $\tilde{h}$ value increases, so the shape of the transfer function becomes increasingly distorted and values for Ω decline.

4.3 Theoretical 2D transfer function

Equation (11) can be used to calculate the transfer probability for each combination of $\tilde{\tau}$ and $\tilde{Z}$. If $\beta = 0.1$ and $\tilde{h} = 0.05$, the 2D transfer function shown in Fig. 5b is obtained. Here, the influence of the widening particle trajectories increases with decreasing $\tilde{Z}$ and increasing values of $\tilde{\tau}$, and the height of the transfer function decreases. It should be noted that, in contrast to $\tilde{\tau}$, there are also negative values for $\tilde{Z}$. This is due to the presence of both positively and negatively charged particles. For $\tilde{Z} > 0$, the direction of the electrical force is on the particles with the centrifugal force. For $\tilde{Z} < 0$, it acts in the opposite direction. Using the 2D transfer function, the classification probabilities can be calculated for each operating point, providing a matrix for data inversion, which is required for back-calculation.

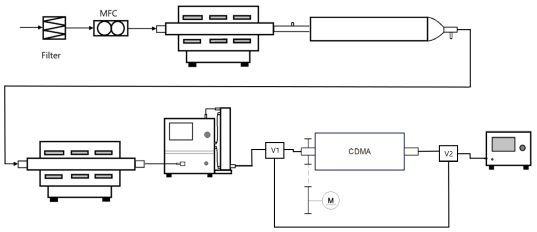

Figure 6. Schematic of the entire experimental setup: test aerosol production with two tube furnaces (Nabertherm) and an agglomeration tube, together with the consecutive setup consisting of a classifier (TSI 3080) with a DMA (TSI 3081), CDMA (TSI 3775), and CPC (TSI 3775) for the measurement of a transfer function.

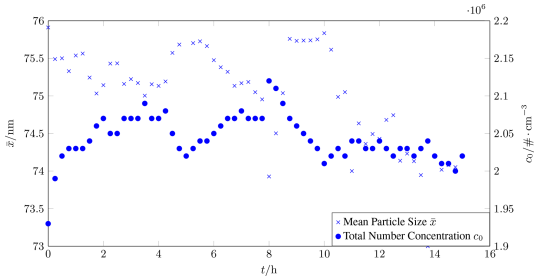

Figure 7. Mean particle diameter and total concentration measured by the SMPS over time.

5 Measurement of the transfer functions for the DMA and AAC operating modes

To validate the instrument functionality, the transfer functions for $\tilde{\tau} = 0$ and $\tilde{Z} = 0$ (DMA mode, i.e. $\omega = 0$; AAC mode, i.e. $U = 0$) should first be determined experimentally. To measure a DMA–AAC transfer function, a tandem setup consisting of two instruments was used, where the first instrument continuously provides a mono-mobile aerosol while the second instrument scans the whole measuring range step by step.

In this case, a classifier (TSI 3080) with a DMA (TSI 3081) and a Kr-85 neutralizer (TSI 3077a) was used as the first instrument in the tandem setup, providing the mono-mobile aerosol. The voltage and desired volume flows are set there. To investigate the different operation parameters, Q_a was set to 0.3 or 1.5 lpm and Q_{sh} was varied between 1.5 lpm and about 20 lpm, resulting in different values for β. The second device was the CDMA, to which the same volume flows are applied via another classifier (TSI 3080). The used classifiers include a negative voltage power supply, so that both devices sample positively charged particles. To measure the transfer function, the measuring range of the CDMA is scanned step by step. That is, the voltage or speed is increased discretely and the resulting concentration n_2 is measured. As the concentration after the first unit (n_1) is also important for the calculation, the second unit can be bypassed using two valves. For the aerosol production, two tube furnaces and an agglomeration tube are used. Figure 6 shows a scheme of this complete setup.

5.1 Production of a test aerosol

To obtain meaningful measurements, it is also important to produce a stable and constant test aerosol. This is achieved by heating silver to 1150 °C in a hot-wall reactor. During this process, some of the silver evaporates into the gas phase. When the temperature is lowered at the outlet of the hot-wall reactor, silver vapor nucleates to form nanoparticles. Larger agglomerates are formed in the agglomeration tube.

These agglomerates can be heated to approximately 700 °C in a second hot-wall reactor in order to thermally round them into spherical particles. Figure 7 shows the mean particle diameter of the test aerosol after agglomeration. It can be seen that the mean particle size and total number concentration remain very stable over a long period of time, allowing us to measure transfer functions, which typically takes about 30 min. Figure 8a shows the roundness of the particles and thus underscores their suitability for the first CDMA evaluation.

5.2 Calculating a transfer function from measurement data assuming a Gaussian shape

If the tubing length from the first valve (V1) to the second instrument plus the tubing length from the second instrument to the second valve (V2) is equal to the length of the tubing, which is the bypass of the second instrument, the tubing loss term is eliminated (Li et al., 2006). The efficiency of the condensation particle counter (CPC) is also eliminated if exactly the same CPC is used to measure n_1 and n_2 (see Fig. 6 and Sect. 5).

Since the first instrument is a DMA, the determination of the transfer function for the DMA mode (i.e. $\omega = 0$) is done in the following. For the quotient n_2/n_1, the following formula applies (Li et al., 2006)[4]:

$$n_2/n_1 = \frac{\int_{-\infty}^{+\infty} \Omega_1\left(\tilde{Z}\right) \cdot \Omega_2\left(\tilde{Z}\right) \mathrm{d}\tilde{Z}}{\int_{-\infty}^{+\infty} \Omega_1\left(\tilde{Z}\right) \mathrm{d}\tilde{Z}}. \quad (16)$$

Here, Ω_1 and Ω_2 represent the transfer functions of the first and second measurement devices.

Deviating from the ideal type assumption of the previously discussed triangular transfer function, a Gaussian function

[4]The dimensionless form of n_2/n_1 as given in Eq. (16) can be derived from the dimensioned equation given by Li et al. (2006).

is now assumed for the shape of the transfer function. This approach is sensible for considering the effects of diffusion or the lack of a plugflow profile in the inlet gap. Moreover, the convolution of two Gaussian functions is also a Gaussian function, which fits very well with the measurement data (Fig. 8b).

A Gaussian transfer function can be described by

$$\Omega_1 = a \cdot \exp\left\{-\frac{(\tilde{Z}-\tilde{\mu}_1)^2}{c^2}\right\},$$
$$\Omega_2 = d \cdot \exp\left\{-\frac{(\tilde{Z}-\tilde{\mu}_2)^2}{e^2}\right\}, \tag{17}$$

where a and d are transfer function height fit parameters, $\tilde{\mu}_2$ is a transfer function position fit parameter, and e is a transfer function width fit parameter. In the normalized case, the position fit parameters $\tilde{\mu}_1$ and $\tilde{\mu}_2$ should be 1, but for real measurements there are some minor errors or inaccuracies that can be determined by these parameters. Since the position of the function on the abscissa is inconsequential when integrating from $-\infty$ to $+\infty$, the abscissa can be displaced arbitrarily. If the abscissa is now displaced so that the centre of the first transfer function is zero, the following equation is obtained:

$$n_2/n_1 = \frac{\int_{-\infty}^{+\infty} a \cdot \exp\left\{-\frac{\tilde{Z}^2}{c^2}\right\} \cdot d \cdot \exp\left\{-\frac{(\tilde{Z}-\tilde{\mu}_2+\tilde{\mu}_1)^2}{e^2}\right\} \mathrm{d}\tilde{Z}}{\int_{-\infty}^{+\infty} a \cdot \exp\left\{-\frac{\tilde{Z}^2}{c^2}\right\} \mathrm{d}\tilde{Z}}. \tag{18}$$

Solving these integrals,

$$\int_{-\infty}^{+\infty} a \cdot \exp\left\{-\frac{\tilde{Z}^2}{c^2}\right\} \cdot d \cdot \exp\left\{-\frac{(\tilde{Z}-\tilde{\mu}_2+\tilde{\mu}_1)^2}{e^2}\right\} \mathrm{d}\tilde{Z}$$
$$= \sqrt{\frac{\pi}{c^2+e^2}} \cdot a \cdot d \cdot |c| \cdot |e| \cdot \exp\left\{-\frac{(\tilde{\mu}_2-\tilde{\mu}_1)^2}{c^2+e^2}\right\}, \tag{19}$$

$$\int_{-\infty}^{+\infty} a \cdot \exp\left\{-\frac{\tilde{Z}^2}{c^2}\right\} \mathrm{d}\tilde{Z} = \sqrt{\pi} \cdot a \cdot |c|. \tag{20}$$

If the transfer function, i.e. a and c, of the first instrument is known, with the help of

$$n_2/n_1 = \sqrt{\frac{1}{c^2+e^2}} \cdot d \cdot |e| \cdot \exp\left\{-\frac{(\tilde{\mu}_2-\tilde{\mu}_1)^2}{c^2+e^2}\right\} \tag{21}$$

it is possible to fit a Gaussian function to the measurement values and calculate the remaining parameters by comparison of the coefficients. Figure 8b presents the real measured values and the corresponding approximation of a Gaussian function.

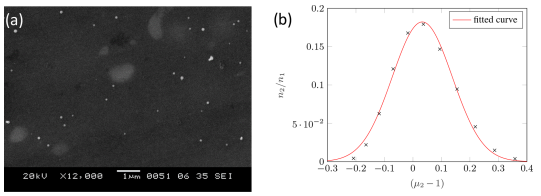

Figure 8. SEM image of silver particles **(a)** and a fitted Gaussian function of the ratio of the measured number concentration at the exit of the second device of the tandem setup n_2 to the number concentration at the inlet of the second device n_1, for different relative shifts of the CDMA transfer function to the fixed transfer function of the pre-classifying DMA **(b)**.

The proposed method is easy to use and does not require a complex minimum search for all measurement points. In addition, the error caused by the influence of the start parameters on a minimum value search is eliminated. From Eq. (21), one can see that the height of the transfer function of the pre-classifying DMA is eliminated and therefore has no influence on the measurement.

Since the pre-classifying instrument is a DMA, the determination of the transfer function of the CDMA with $U = 0\,\mathrm{V}$ must be adopted, so that the following equations can be applied:

$$\Omega_1 = a \cdot \exp\left\{-\frac{(\tilde{\tau}-\tilde{\mu}_1)^2}{c^2}\right\},$$
$$\Omega_2 = d \cdot \exp\left\{-\frac{(\tilde{\tau}-\tilde{\mu}_2)^2}{e^2}\right\}. \tag{22}$$

Therefore, the transfer function for the first DMA must be determined first. This is done in Appendix C.

5.3 Measurement results

In general, three different particle sizes (50, 100, and 200 nm) of spherical silver particles were analysed. Because the measured values were very similar for all the particle sizes, only the results for a particle size of 100 nm are presented here. The other sizes are shown in Appendix D. The transfer functions were determined over the full range of possible operating parameters. The aerosol flow rate was kept constant for each series of measurements, and the sheath airflow rate was varied so that the parameters could be determined for different values of β. Both the Scanning Mobility Particle Sizer (SMPS) DMA and the CDMA were operated at the same ratio of aerosol to sheath air volume flow. The points on the red lines show comparative measurements of a DMA–DMA configuration as a reference. It should also be noted that the corrections explained in Sect. 3.2 have already been applied

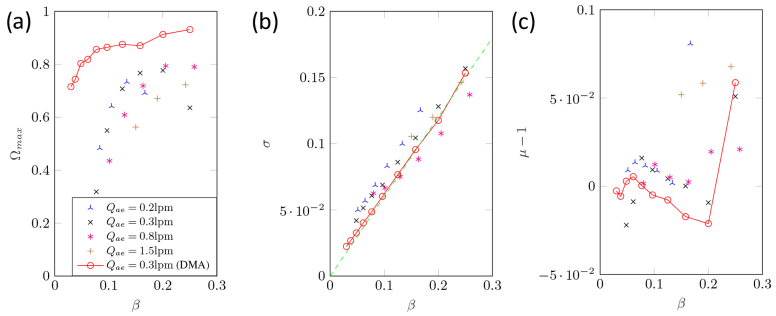

Figure 9. Measured transfer function parameters: maximum height **(a)**, width **(b)**, and shift **(c)** of the CDMA in DMA mode for $d_p = 100\,\text{nm}$.

here, so that the unwanted separation due to voltage or speed has already been eliminated.

To determine the transfer function of the pre-classifying DMA from the SMPS system, two identical DMAs were first measured in a tandem configuration. Assuming that they are equal regarding their classification properties, it is possible to determine the relevant parameters for the pre-classifying DMA for DMA measurements by

$$\mu_1 = 1.00319; c = 0.5868 \cdot \beta \tag{23}$$

and for AAC measurements by

$$\mu_1 = 1.00319; c = 0.6468 \cdot \beta. \tag{24}$$

5.3.1 DMA mode

Figure 9a plots the measured height of the transfer function against the aerosol-to-sheath air volume flow ratio. Comparing the measured values of the CDMA in DMA mode with the measurement values of a commercial DMA (TSI 3081), it is noticeable that the height is significantly lower. This is not surprising because the CDMA requires significantly more deflections and a longer travel distance during which particles are deposited on the walls by impaction or diffusion, respectively. The scatter of the measured values can be explained by random variations in the operation of the CDMA. For example, at low aerosol volume flows and high values of β, only very small sheath airflows occur, which are outside the normal operating range of recirculation technology and do not guarantee a reliable and uniform volume flow. A very strong drop in the height of the transfer function from $\beta = 0.1$ to $\beta = 0.05$ is observed. There is also a slight drop in the height of the DMA transfer function due to the increasing influence of diffusion as the transfer functions become narrower. However, this phenomenon does not explain the sharp decrease in the CDMA curves. In particular, for other particle sizes, exactly the same drop can be observed. This leads to the conclusion that there is no relevant particle loss due to diffusion or impaction, as a similar curve can be observed for all the volume flows. This indicates that further particle losses are present, but the source could not be identified yet. To investigate this problem, a new prototype with significantly shortened inlet and outlet regions of the aerosol and sample volume flow is required.

Figure 9b shows the standard deviation of the transfer function, which corresponds to the width of the transfer function. The green dashed line represents the ideal relationship between standard deviation and β. This can also be observed in the measured values, as they too exhibit a linear dependence on β. When the measured values are compared with the DMA reference values, it is noticeable that the width of the transfer function is generally slightly larger. This can be explained by the narrower gap of the CDMA at approximately the same length (the applied voltage is therefore significantly lower and there is a lower Peclet number in the CDMA, and hence diffusion plays a greater role) and also by the assembly and tolerances of the prototype (especially in combination with the short travelling distances of the particles in the radial direction).

Figure 9c shows the shift of the transfer function on the x axis. It can be seen that there is no significant difference with the DMA comparison values. Larger deviations can be observed only for large β values. This was again due to the control range of the sheath airflow.

5.3.2 AAC mode

It should be noted that the AAC measurements have already been corrected for charge distribution. This was performed by measuring the particle size distribution available directly at the outlet of the sintering furnace. As the charge distribution is assumed to be known (Wiedensohler, 1988), it is possible to deduce the proportion of multiply charged particles that pass through the pre-classification. This fraction can then be subtracted from n_1 to obtain the actual number concentration of singly charged particles at the CDMA inlet.

Figure 10a shows the height of the transfer function for the AAC mode. Unlike the DMA mode, there is no plateau where the height remains constant. However, the transfer functions

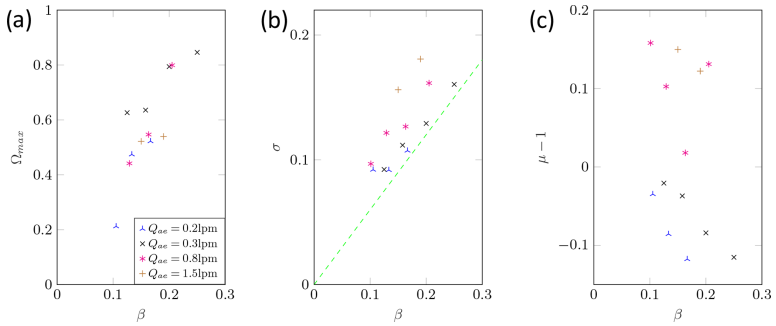

Figure 10. Measured transfer function parameters: maximum height **(a)**, width **(b)**, and shift **(c)** of the CDMA in AAC mode for $d_p = 100$ nm.

reach very high values. It can also be seen that the decrease is analogous to the heights shown for the DMA. At low β values, however, no measurement is possible, because at $\beta < 0.1$ almost all particles are separated by the centrifugal force at the inlet and outlet of the CDMA.

Figure 10b again shows the standard deviation of the transfer function. There are still linear dependence on the β values and fluctuation around the ideal value. However, the scattering of the measured values was significantly larger compared to the DMA mode. This is due to the more difficult flow control as the flows take a longer distance to fully develop, i.e. due to the rotation the walls have to take with all the air in the rotation too. By changing for example the sheath air, CFD simulations have shown that the development of the flow profile is delayed in the axial direction. This effect becomes stronger as the sheath airflow rate increases. One potential improvement is the installation of vanes at the point at which the sheath radius changes. Moreover, higher angular velocities lead to a higher pressure difference at the inlet, and hence some flow disturbances may occur there. This can affect the classification zone and explains the larger variations in the results. In addition, the strong separation in the inlet and outlet areas results in very high correction factors, especially for small β values.

Figure 10c shows a similar picture to Fig. 10b. Again, the deviation is significantly greater than that in the DMA mode, which, as in Fig. 10b, is due to the flow field in CDMA. However, except for one outlier, in Fig. 10c there seems to be a linear dependence on the β values for each aerosol volume flow. In addition, the curves were all parallel, with the curves shifting in the positive direction as the aerosol volume flow increased. Again, this can be explained by the difficulty in the flow adaptation at higher speeds, i.e. higher flow velocities (or volume flows). The deviation might also be caused by manufacturing tolerances or imperfectly aligned system components. As the deviation for the other particle sizes is also very similar to this result, a calibration for the CDMA could be performed during further validation.

6 Conclusions

As described in the previous section, the transfer functions of the CDMA for $\tilde{\tau} = 0$ and $\tilde{Z} = 0$ agreed well with the theory and reference values of a DMA–DMA configuration. For $\beta < 0.2$, the height of the transfer function decreased much more than for $\beta > 0.2$, but the cause has not yet been clarified conclusively. In order to find the cause, a new prototype needs to be designed and built that significantly reduces the depositions in the inlet and outlet areas and minimizes the electrical fields outside the classification zone. The superposition of these effects makes it difficult to determine the cause in the current arrangement. As one operating point is sufficient for the initial investigations, further investigations will be conducted for $\beta = 0.2$. For this purpose, this operating point needs to be measured again in detail, and a calibration of the CDMA possibly needs to be carried out. Furthermore, a validation for particle sizes larger than 200 nm is necessary in order to be able to fully describe the CDMA for those larger particles. The ideal 2D transfer function can be calculated using the particle trajectory method. However, an extension to the streamline model is highly recommended for validation, because diffusion in the classifier gap can be considered. Furthermore, a new robust method of measuring transfer functions was presented, which made it possible to draw conclusions about the transfer function simply by measuring the number concentrations. If these results agree with the theoretical values for different particle types, the final step is to develop an algorithm that can be used to calculate a 2D distribution with respect to d_m and d_{st} from the measured values.

Appendix A: Comment on the definition of the particle relaxation time

In contrast to Tavakoli and Olfert (2014), the Stokes equivalent diameter was used instead of the aerodynamic-equivalent diameter. Furthermore, the argument of the Cun-

ningham slip correction should be mentioned here. The equations for calculating the slip correction are derived only for spherical particles. There are many studies in the literature dealing with the slip correction for non-spherical particles. For example, Cheng et al. (1988) and Dahneke (1973) proposed the introduction of a new equivalent diameter for non-spherical particles with the same slip correction. However, these methods are mostly limited to specific particle shapes and apply only to the free molecular or continuum region but not to the transition region. However, we consider the aerodynamic-equivalent diameter to be inappropriate for calculating the slip correction as done by Tavakoli and Olfert (2014), since the aerodynamic diameter depends on the particle density as well. That is, two particles with identical shapes but different densities would experience the same drag force and thus slip correction while having different aerodynamic diameters. Therefore, we suggest using the mobility-equivalent diameter instead. This is in accordance with a number of studies in the literature, such as Knutson and Whitby (1975) and Sorensen (2011). Moreover, slip correction experimental investigations have typically been performed using the Millikan apparatus, where the particles are moved in an electrical field (Buckley and Loyalka, 1989; Rader, 1990; Allen and Raabe, 1985).

Appendix B: Derivation of the 2D transfer function using particle trajectory calculation

In accordance with the specified operating parameters (i.e. voltage U and speed ω), a multitude of combinations of the equivalent particle sizes d_m and d_{st} or combinations of τ and Z can be derived analytically from the geometry and the volume flow conditions. The aforementioned combinations are subject to a probability of classification. A characteristic combination, for instance, exhibits the property that, if a particle is introduced at the centre of the inlet gap, it will also be collected at the centre of the classifying gap. In the case of edge transfer functions, the following relationships are observed: $\tau = \tau^*$ or $\tilde{\tau} = 1$ (for $Z^* = 0$) and $Z = Z^*$, or $\tilde{Z} = 1$ (for $\tau^* = 0$). The results are presented in Sect. 4.2 of this article.

Two characteristic classification properties are the limiting particle trajectories, hereafter called the maximum and minimum particle paths. All particles that traverse the classifying section at a shorter distance than the particle on the minimum path are no longer classified. This minimum path is defined by substituting $r_{in} = r_2$ and $r(L) = r_3$ into Eq. (9). In contrast, the maximum particle trajectory represents the boundary from which particles traversing a greater distance are deposited at the inner electrode ($r_{in} = r_1$ and $r(L) = r_4$). Equation (9) may be employed to ascertain the transfer probability for each τ–Z combination. If two critical radii (r_c) are defined where $r_1 < r_c < r_{c2} < r_2$ and a constant particle flux density at the inlet is assumed, the transfer probability can be determined by the following equations:

$$\Omega_{CDMA} = \max\left[\min(f_1, f_2, 1), 0\right], \tag{B1}$$

$$f_1 = \frac{r_2^2 - r_c^2}{r_2^2 - r_1^2} - \max\left(\frac{r_2^2 - r_{c2}^2}{r_2^2 - r_1^2}, 0\right), \tag{B2}$$

$$f_2 = \frac{r_{c2}^2 - r_1^2}{r_2^2 - r_1^2} - \max\left(\frac{r_c^2 - r_1^2}{r_2^2 - r_1^2}, 0\right). \tag{B3}$$

In other words, if we assume that the minimum particle path is limiting (as is the case for f_1 with the DMA transfer function; Wang and Flagan, 1990), a lower critical radius can be defined so that all particles entering at $r < r_c$ are no longer classified but are separated behind the classifying gap or discharged with the sheath air.

Therefore, r_c is defined by

$$r_3 = \sqrt{r_c^2 \cdot \exp\left\{\tilde{\tau} \cdot \frac{2\tilde{h}}{1+\beta}\right\} + \bar{r}^2 \cdot \frac{\tilde{Z}}{\tilde{\tau}} \cdot \left[\exp\left\{\tilde{\tau} \cdot \frac{2\tilde{h}}{1+\beta}\right\} - 1\right]}. \tag{B4}$$

As a consequence of the speed-controlled operating mode, it is possible that not all particles entering at r_2 will be classified. Because of the elevated feed radius, a higher drift velocity is observed at the outlet of the transfer section, thereby enabling the separation of particles at the outer electrode or excess air (for further details, please refer to Sect. 4.2). In order to accommodate this phenomenon, a second critical radius, designated as r_{c2}, is introduced, situated between r_c and r_2; the calculation is performed in accordance with the following formula:

$$r_4 = \sqrt{r_{c2}^2 \cdot \exp\left\{\tilde{\tau} \cdot \frac{2\tilde{h}}{1+\beta}\right\} + \bar{r}^2 \cdot \frac{\tilde{Z}}{\tilde{\tau}} \cdot \left[\exp\left\{\tilde{\tau} \cdot \frac{2\tilde{h}}{1+\beta}\right\} - 1\right]}. \tag{B5}$$

Once the flow ratio β has been established, it can be subtracted from the initial value in order to prevent the value r_{c2} from exceeding r_2. The minimum value for this term is set to 0.

In light of the continuously increasing probability of transfer in the direction of r_1, a new parameter (f_2) is introduced. It is important to note that the maximum particle path represents a limiting quantity too. The same procedure is applied as for f_1, but now r_{c2} is used as the critical radius for the first term, while r_c is used for the second term. This implies that all particles entering the transfer section with a radius greater than r_{c2} are separated at the outer electrode before the classification gap. As a consequence of the reduction in radius, particles entering the transfer section at $r_{in} > r_1$ are again subjected to separation. A second critical radius is defined at which the particles are classified. The area ratio can once more be subtracted from the first term. Since the case

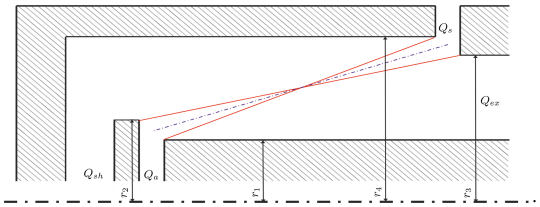

Figure B1. Characteristic particle paths: minimal and maximal particle paths (solid red lines) and the centred particle path (dash-dotted blue line) for combinations of τ and Z

$r_c < r_1$ cannot occur, a value of zero is also defined here as the minimum.

The probability of a τ–Z combination being classified is now the smaller of f_1 or f_2. This is due to the fact that both the maximum and minimum particle paths were taken into account. Furthermore, it should be noted that the transfer function can assume a maximum value of 1. It is also necessary to ensure that the transfer function does not become smaller than 0. This implies that the minima of f_1, f_2, and 1 must not become smaller than 0 (Eq. 11).

Upon substituting Eqs. (B4) and (B5) into Eqs. (B2) and (B3), the following result is obtained:

$$f_1 = \frac{r_2^2 - \left(r_3^2 + \bar{r}^2 \cdot \frac{\tilde{Z}}{\tilde{\tau}}\right) \cdot \exp\left\{-\tilde{\tau} \cdot \frac{2\tilde{h}}{1+\beta}\right\} \bar{r}^2 \cdot \frac{\tilde{Z}}{\tilde{\tau}}}{r_2^2 - r_1^2} - \max\left(\frac{r_2^2 - \left(r_4^2 + \bar{r}^2 \cdot \frac{\tilde{Z}}{\tilde{\tau}}\right) \cdot \exp\left\{-\tilde{\tau} \cdot \frac{2\tilde{h}}{1+\beta}\right\} + \bar{r}^2 \cdot \frac{\tilde{Z}}{\tilde{\tau}}}{r_2^2 - r_1^2}, 0\right), \quad \text{(B6)}$$

$$f_2 = \frac{\left(r_4^2 + \bar{r}^2 \cdot \frac{\tilde{Z}}{\tilde{\tau}}\right) \cdot \exp\left\{-\tilde{\tau} \cdot \frac{2\tilde{h}}{1+\beta}\right\} - \bar{r}^2 \cdot \frac{\tilde{Z}}{\tilde{\tau}} - r_1^2}{r_2^2 - r_1^2} - \max\left(\frac{(r_3^2 + \bar{r}^2 \cdot \frac{\tilde{Z}}{\tilde{\tau}}) \cdot \exp\left\{-\tilde{\tau} \cdot \frac{2\tilde{h}}{1+\beta}\right\} - \bar{r}^2 \cdot \frac{\tilde{Z}}{\tilde{\tau}} - r_1^2}{r_2^2 - r_1^2}, 0\right). \quad \text{(B7)}$$

Assuming a constant flux density at the inlet, the radii can be set in relation to each other. This yields the following relationships:

$$u = \frac{Q_{sh} + Q_a}{\pi(r_4^2 - r_1^2)} = \frac{Q_{sh}}{\pi(r_4^2 - r_2^2)} = \frac{Q_a}{\pi(r_2^2 - r_1^2)} = \frac{Q_{ex}}{\pi(r_3^2 - r_1^2)} = \frac{Q_s}{\pi(r_4^2 - r_3^2)}. \quad \text{(B8)}$$

Using these relations for the typical operation conditions ($Q_a = Q_s$ and subsequently $Q_{sh} = Q_{ex}$) and $\beta = Q_a/Q_{sh}$ can lead to

$$\left(\frac{r_2}{r_4}\right)^2 = \frac{\beta + \kappa^2}{1+\beta}, \quad \left(\frac{r_3}{r_4}\right)^2 = \frac{1/\beta + \kappa^2}{1/\beta + 1}, \quad \left(\frac{\bar{r}}{r_4}\right)^2 = \frac{(\kappa+1)^2}{4}, \quad \text{(B9)}$$

with

$$\kappa = \frac{r_1}{r_4} = \frac{1 - \tilde{h}/2}{1 + \tilde{h}/2}. \quad \text{(B10)}$$

In order to insert the ratios from Eqs. (9) and (10), it is necessary to expand the denominator and numerator with r_4^2 in Eqs. (7) and (8). From this follows, for f_1 and f_2,

$$f_1 = \frac{\frac{\beta+\kappa^2}{1+\beta} - \left(\frac{1/\beta+\kappa^2}{1/\beta+1} + \frac{(\kappa+1)^2}{4} \cdot \frac{\tilde{Z}}{\tilde{\tau}}\right) \cdot \exp\left\{-\tilde{\tau} \cdot \frac{2\tilde{h}}{1+\beta}\right\} + \frac{(\kappa+1)^2}{4} \cdot \frac{\tilde{Z}}{\tilde{\tau}}}{\frac{\beta+\kappa^2}{1+\beta} - \kappa^2} - \max\left(\frac{\frac{\beta+\kappa^2}{\beta+1} - \left(1 + \frac{(\kappa+1)^2}{4} \cdot \frac{\tilde{Z}}{\tilde{\tau}}\right) \cdot \exp\left\{-\tilde{\tau} \cdot \frac{2\tilde{h}}{1+\beta}\right\} + \frac{(\kappa+1)}{4} \cdot \frac{\tilde{Z}}{\tilde{\tau}}}{\frac{\beta+\kappa^2}{1+\beta} - \kappa^2}, 0\right), \quad \text{(B11)}$$

$$f_2 = \frac{\left(1 + \frac{(\kappa+1)^2}{4} \cdot \frac{\tilde{Z}}{\tilde{\tau}}\right) \cdot \exp\left\{-\tilde{\tau} \cdot \frac{2\tilde{h}}{1+\beta}\right\} - \frac{(\kappa+1)^2}{4} \cdot \frac{\tilde{Z}}{\tilde{\tau}} - \kappa^2}{\frac{\beta+\kappa^2}{1+\beta} - \kappa^2} - \max\left(\frac{\left(\frac{1/\beta+\kappa^2}{1/\beta+1} + \frac{(\kappa+1)^2}{4} \cdot \frac{\tilde{Z}}{\tilde{\tau}}\right) \cdot \exp\left\{-\tilde{\tau} \cdot \frac{2\tilde{h}}{1+\beta}\right\} - \frac{(\kappa+1)^2}{4} \cdot \kappa^2}{\frac{\beta+\kappa^2}{1+\beta} - \kappa^2}, 0\right). \quad \text{(B12)}$$

Appendix C: Calculation of the transfer functions of the pre-classifying DMA

To determine the transfer function of the pre-classifying DMA, two identical DMAs are measured first. It is assumed that the transfer functions are identical, which means that

$$d = a \text{ and } e = c. \quad \text{(C1)}$$

Also assuming that the shift $\tilde{\mu}$ of the DMA is the same as $\tilde{\mu}_1$ and $\tilde{\mu}_2$, the shift of the pre-classifying DMA can be calculated as $\tilde{\mu} = (\tilde{\mu}_2 - \tilde{\mu}_1)/2$. In the DMA mode (i.e. $\omega = 0$), Eq. (21) can be simplified:

$$n_2/n_1 = \sqrt{\frac{1}{2}} \cdot d \cdot \exp\left\{-\frac{(\tilde{\mu}_2 - \tilde{\mu}_1)^2}{2 \cdot e^2}\right\}. \quad \text{(C2)}$$

The parameters can now be extracted by fitting a Gaussian function to the measurement data and comparing the coefficients of the fitted curve and Eq. (C2).

As already explained in Sect. 5.2, a validation of the AAC mode (i.e. $\omega = 0$) is only possible if the transfer function of the DMA can be expressed as a function of the particle relaxation time. For the measurement results n_2/n_1, the mobility

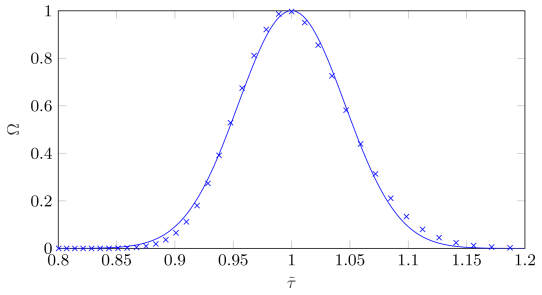

Figure C1. Fit of a Gaussian function to the Ω–$\tilde{\tau}$ domain, based on the mobility measurements.

must be converted into the particle relaxation time, assuming a particle shape. A renewed application of a Gaussian function enables the parameters for $\Omega(\tilde{\tau})$ to be determined in the same way as for the DMA mode.

An alternative approach is to plot $\Omega(\tilde{Z})$, convert the mobilities into particle relaxation times, and approximate a Gaussian function using the values in the $\Omega(\tilde{\tau})$ diagram. The resulting approximation is shown in Fig. C1. As illustrated in the figure, there are inconsistencies between the fitting function and the generated values, particularly in the marginal areas, since the measured distribution appears to be slightly skew. Nevertheless, the shape is relatively similar, allowing for an approximation of the curve. With the assistance of the parameters from Sect. 5.3, the width of the curve is determined to be $\sigma_{U=0} = 0.06468$ ($\sigma_{\omega=0} = 0.05868$). However, for an exact calculation, the aforementioned method should be employed.

These approaches for the determination of $\Omega(\tilde{\tau})$) are only valid for spherical particles.

Appendix D: Measurement values for the determination of the pre-classifying DMA parameters

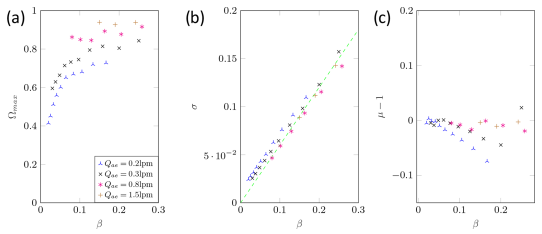

Figure D1. Measured transfer function parameters: maximum height **(a)**, width **(b)**, and shift **(c)** of the pre-classifying DMA for $d_p = 50\,\text{nm}$.

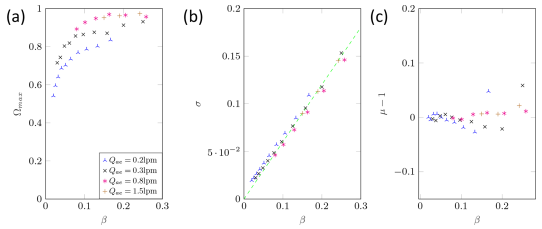

Figure D2. Measured transfer function parameters: maximum height **(a)**, width **(b)**, and shift **(c)** of the pre-classifying DMA for $d_p = 100\,\text{nm}$.

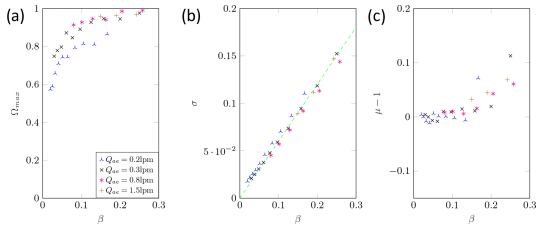

Figure D3. Measured transfer function parameters: maximum height **(a)**, width **(b)**, and shift **(c)** of the pre-classifying DMA for $d_p = 200\,\text{nm}$.

Appendix E: Measurement values for 50 and 200 nm

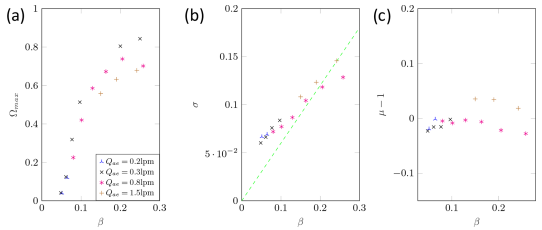

Figure E1. Measured transfer function parameters: maximum height **(a)**, width **(b)**, and shift **(c)** of the CDMA in DMA mode for $d_p = 50\,\text{nm}$.

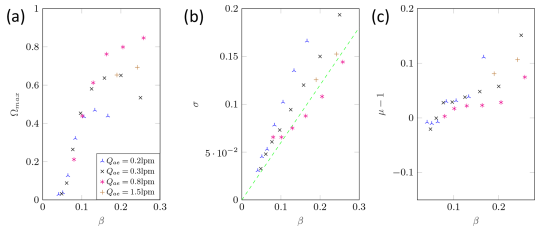

Figure E2. Measured transfer function parameters: maximum height **(a)**, width **(b)**, and shift **(c)** of the CDMA in DMA mode for $d_p = 200\,\mathrm{nm}$.

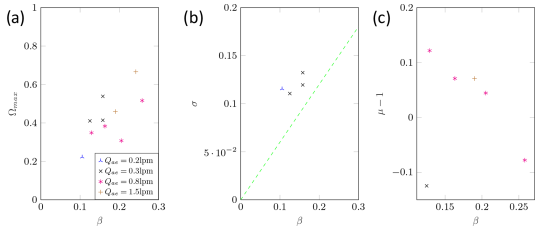

Figure E3. Measured transfer function parameters: maximum height **(a)**, width **(b)**, and shift **(c)** of the CDMA in AAC mode for $d_p = 50\,\mathrm{nm}$.

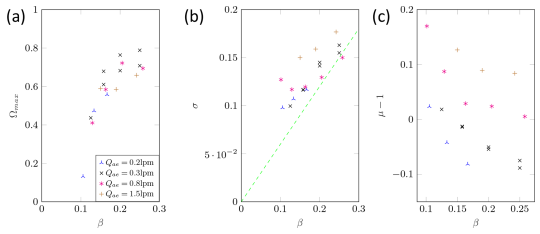

Figure E4. Measured transfer function parameters: maximum height **(a)**, width **(b)**, and shift **(c)** of the CDMA in AAC mode for $d_p = 200\,\mathrm{nm}$.

Appendix F: Nomenclature

a, d	Fit parameters for the height of a Gaussian function	–
a_c	Centrifugal acceleration	$\mathrm{m\,s^{-2}}$
c, e	Fit parameters for the width of a Gaussian function	–
Cu	Cunningham slip correction factor	–
c_0	Total number concentration	$\#\,\mathrm{m^{-3}}$
d_m	Mobility-equivalent diameter	m
d_{ae}	Aerodynamically equivalent diameter	m
d_{st}	Stokes equivalent diameter	m
d_v	Volume-equivalent diameter	m
E	Electrical field magnitude	$\mathrm{V\,m^{-1}}$
F_c	Centrifugal force	N
F_{el}	Electrical force	N
F_{Dr}	Drag force	N
L	Length of the CDMA transfer path	m
m_P	Particle mass	kg
n_1	Particle number concentration after the first device in a tandem setup	$\#\,\mathrm{m^{-3}}$
n_2	Particle number concentration after both devices in a tandem setup	$\#\,\mathrm{m^{-3}}$
Q_a	Aerosol volume flow	$\mathrm{m^3\,s^{-1}}$
Q_s	Sample volume flow	$\mathrm{m^3\,s^{-1}}$
Q_{sh}	Sheath air volume flow	$\mathrm{m^3\,s^{-1}}$
Q_{ex}	Excess air volume flow	$\mathrm{m^3\,s^{-1}}$
Q_P	Particle charge	As
r_1	Inner radius	m
r_2	Maximum radius at which the particles enter	m
r_3	Minimum radius at which the particles are still classified	m
r_4	Outer radius	m
r_{in}	Actual radius at which the particle enters	m
$\overline{r}$	Average of the outer and inner radii	–
s	Radial distance	m
s_{max}	Maximum radial distance	m
T	Truncation factor	–
u	Velocity of the air	$\mathrm{m\,s^{-1}}$
U	Voltage	V
w_{Dr}	Particle drift velocity	$\mathrm{m\,s^{-1}}$
$\overline{x}$	Mean particle size	m
y	Position of the particle in the streamwise direction	m
Z_p	Particle mobility	$\mathrm{m^2\,(Vs)^{-1}}$
Z^*	Nominal particle mobility	$\mathrm{m^2\,(Vs)^{-1}}$
$\tilde{Z}$	Normalized particle mobility	–
$\tilde{h}$	Ratio of the gap width to the mean radius	–

ρ	Particle density	$\mathrm{kg\,m^{-3}}$
β	Ratio of Q_a to Q_{sh}	–
η	Dynamic viscosity	Pas
κ	Ratio of r_1 to r_4	–
τ	Particle relaxation time	s
τ^*	Nominal particle relaxation time	s
$\tilde{\tau}$	Normalized particle relaxation time	–
$\tilde{\mu_2}, \tilde{\mu_1}$	Fit parameters for the shift of a Gaussian function	–
$\tilde{\mu}$	Shift of the transfer function	–
Ω_{max}	Maximum height of the transfer function	–
σ	Width of the transfer function	–
ω	Angular speed	$1\,\mathrm{s^{-1}}$
Ω	Transfer function	–

Code and data availability. The data that support the findings of this study are openly available in GitHub at https://git.uni-paderborn.de/pvt/cdma, reference number 11577 (CDMA, 2025).

Author contributions. TR: software, validation, formal analysis, investigation, data curation, writing – original draft, visualization. DR: conceptualization, methodology, formal analysis, writing – review and editing, funding acquisition. H-JS: resources, writing – review and editing, supervision, project administration, funding acquisition.

Competing interests. The contact author has declared that none of the authors has any competing interests.

Financial support. This research has been supported by the Deutsche Forschungsgemeinschaft (grant no. SPP2045).

Review statement. This paper was edited by Attila Nagy and reviewed by two anonymous referees.

References

Allen, M. D. and Raabe, O. G.: Slip correction measurements for aerosol particles of doublet and triangular triplet aggregates of spheres, J. Aerosol Sci., 16, 57–67, https://doi.org/10.1016/0021-8502(85)90020-5, 1985.

Baron, P. A., Kulkarni, P., and Willeke, K.: Aerosol measurement: Principles, techniques, and applications, Wiley, Hoboken N.J., 3rd Edn., ISBN 9780470387412, 2011.

Buckley, R. L. and Loyalka, S. K.: Cunningham correction factor and accommodation coefficient: Interpretation of Millikan's data, J. Aerosol Sci., 20, 347–349, https://doi.org/10.1016/0021-8502(89)90009-8, 1989.

CDMA: MatLab Codes CDMA, Gitlab [data set], https://git.uni-paderborn.de/pvt/cdma (last access: 20 December 2024), reference number 11577, 2025.

Cheng, Y.-S., Allen, M. D., Gallegos, D. P., Yeh, H.-C., and Peterson, K.: Drag Force and Slip Correction of Aggregate Aerosols, Aerosol Sci. Technol., 8, 199–214, https://doi.org/10.1080/02786828808959183, 1988.

Colbeck, I.: Aerosol Science: Technology and Applications, Wiley, Hoboken, 2. Edn., ISBN 978-1-119-97792-6, 2013.

Dahneke, B. E.: Slip correction factors for nonspherical bodies – I Introduction and continuum flow, J. Aerosol Sci., 4, 139–145, https://doi.org/10.1016/0021-8502(73)90065-7, 1973.

Fernandez de la Mora, J., Hering, S. V., Rao, N., and McMurry, P. H.: Hypersonic impaction of ultrafine particles, J. Aerosol Sci., 21, 169–187, https://doi.org/10.1016/0021-8502(90)90002-F, 1989.

Friedlander, S. K.: Smoke, dust, and haze: Fundamentals of aerosol dynamics, Topics in chemical engineering, Oxford Univ. Press, New York, 2. Edn., ISBN 978-0195129991, 2000.

Furat, O., Leißner, T., Bachmann, K., Gutzmer, J., Peuker, U., and Schmidt, V.: Stochastic Modeling of Multidimensional Particle Properties Using Parametric Copulas, Microscopy and microanalysis: the official journal of Microscopy Society of America, Microbeam Analysis Society, Microscopical Society of Canada, 25, 720–734, https://doi.org/10.1017/S1431927619000321, 2019.

Furat, O., Masuhr, M., Kruis, F. E., and Schmidt, V.: Stochastic modeling of classifying aerodynamic lenses for separation of airborne particles by material and size, Adv. Powder Technol., 31, 2215–2226, https://doi.org/10.1016/j.apt.2020.03.014, 2020.

Hong, A.: The Physics Factbook: Dielectric Strength of Air, https://hypertextbook.com/facts/2000/AliceHong.shtml (last access: 24 July 2024), 2000.

Jindal, A. B.: The effect of particle shape on cellular interaction and drug delivery applications of micro- and nanoparticles, Int. J. Pharmaceut., 532, 450–465, https://doi.org/10.1016/j.ijpharm.2017.09.028, 2017.

Kelesidis, G. A., Neubauer, D., Fan, L.-S., Lohmann, U., and Pratsinis, S. E.: Enhanced Light Absorption and Radiative Forcing by Black Carbon Agglomerates, Environ. Sci. Technol., 12, 8610–8618, https://doi.org/10.1021/acs.est.2c00428, 2022.

Knutson, E. O. and Whitby, K. T.: Aerosol classification by electric mobility: apparatus, theory, and applications, J. Aerosol Sci., 6, 443–451, https://doi.org/10.1016/0021-8502(75)90060-9, 1975.

Li, W., Li, L., and Chen, D.-R.: Technical Note: A New Deconvolution Scheme for the Retrieval of True DMA Transfer Function from Tandem DMA Data, Aerosol Sci. Technol., 40, 1052–1057, https://doi.org/10.1080/02786820600944331, 2006.

Mitchell, J. P., Nagel, M. W., Wiersema, K. J., and Doyle, C. C.: Aerodynamic particle size analysis of aerosols from pressurized

metered-dose inhalers: comparison of Andersen 8-stage cascade impactor, next generation pharmaceutical impactor, and model 3321 Aerodynamic Particle Sizer aerosol spectrometer, AAPS PharmSciTech, 4, E54, https://doi.org/10.1208/pt040454, 2003.

Olfert, J. S. and Collings, N.: New method for particle mass classification – the Couette centrifugal particle mass analyzer, J. Aerosol Sci., 36, 1338–1352, https://doi.org/10.1016/j.jaerosci.2005.03.006, 2005.

Park, K., Dutcher, D., Emery, M., Pagels, J., Sakurai, H., Scheckman, J., Qian, S., Stolzenburg, M. R., Wang, X., Yang, J., and McMurry, P. H.: Tandem Measurements of Aerosol Properties – A Review of Mobility Techniques with Extensions, Aerosol Sci. Technol., 42, 801–816, https://doi.org/10.1080/02786820802339561, 2008.

Rader, D. J.: Momentum slip correction factor for small particles in nine common gases, J. Aerosol Sci., 21, 161–168, https://doi.org/10.1016/0021-8502(90)90001-E, 1990.

Reist, P. C.: Aerosol science and technology, McGraw-Hill, New York, 2. Edn., ISBN 0-07-051882-3, 1993.

Rhein, F., Scholl, F., and Nirschl, H.: Magnetic seeded filtration for the separation of fine polymer particles from dilute suspensions: Microplastics, Chem. Eng. Sci., 207, 1278–1287, https://doi.org/10.1016/j.ces.2019.07.052, 2019.

Sandmann, K. and Fritsching, U.: Acoustic separation and fractionation of property-distributed particles from the gas phase, Adv. Powder Technol., 34, 104270, https://doi.org/10.1016/j.apt.2023.104270, 2023.

Slowik, J. G., Stainken, K., Davidovits, P., Williams, L. R., Jayne, J. T., Kolb, C. E., Worsnop, D. R., Rudich, Y., DeCarlo, P. F., and Jimenez, J. L.: Particle Morphology and Density Characterization by Combined Mobility and Aerodynamic Diameter Measurements. Part 2: Application to Combustion-Generated Soot Aerosols as a Function of Fuel Equivalence Ratio, Aerosol Sci. Technol., 38, 1206–1222, https://doi.org/10.1080/027868290903916, 2004.

Sorensen, C. M.: The Mobility of Fractal Aggregates: A Review, Aerosol Sci. Technol., 45, 765–779, https://doi.org/10.1080/02786826.2011.560909, 2011.

Stolzenburg, M. R.: An ultrafine aerosol size distribution measuring system, Disseratation, University of Minnesota, Minnesota, 1988.

Tavakoli, F. and Olfert, J. S.: An Instrument for the Classification of Aerosols by Particle Relaxation Time: Theoretical Models of the Aerodynamic Aerosol Classifier, Aerosol Sci. Technol., 47, 916–926, https://doi.org/10.1080/02786826.2013.802761, 2013.

Tavakoli, F. and Olfert, J. S.: Determination of particle mass, effective density, mass–mobility exponent, and dynamic shape factor using an aerodynamic aerosol classifier and a differential mobility analyzer in tandem, J. Aerosol Sci., 75, 35–42, https://doi.org/10.1016/j.jaerosci.2014.04.010, 2014.

Toy, R., Peiris, P. M., Ghaghada, K. B., and Karathanasis, E.: Shaping cancer nanomedicine: the effect of particle shape on the in vivo journey of nanoparticles, Nanomedicine (London, England), 9, 121–134, https://doi.org/10.2217/nnm.13.191, 2014.

Wang, S. C. and Flagan, R. C.: Scanning Electrical Mobility Spectrometer, Aerosol Sci. Technol., 13, 230–240, https://doi.org/10.1080/02786829008959441, 1990.

Wiedensohler, A.: An approximation of the bipolar charge distribution for particles in the submicron size range, J. Aerosol Sci., 19, 387–389, https://doi.org/10.1016/0021-8502(88)90278-9, 1988.

Zhang, J., Qiao, J., Sun, K., and Wang, Z.: Balancing particle properties for practical lithium-ion batteries, Particuology, 61, 18–29, https://doi.org/10.1016/j.partic.2021.05.006, 2022.

4.2 Prediction of the transfer function for a centrifugal differential mobility analyzer by streamline functions

Torben N. Rüther, Hans-Joachim Schmid,
Aerosol Science and Technology, 0, (2025) 1-14, https://doi.org/10.1080/02786826.2025.2519092

Der Autor dieser Dissertation hat das von *Stolzenburg* [Sto88] entwickelte Streamlinemodell verwendet, um eine zweidimensionale Transferfunktion für den CDMA zu berechnen. Des weiteren wurde Diffusion sowie ein laminares Strömungsprofil am Aerosoleinlass mit berücksichtigt und in die Berechnung mit eingearbeitet. Prof. Hans-Joachim Schmid hat den Autor während der gesamten Arbeit betreut und an der Revision des Manuskripts mitgewirkt.

Aerosol Science and Technology

Taylor & Francis
Taylor & Francis Group

ISSN: 0278-6826 (Print) 1521-7388 (Online) Journal homepage: www.tandfonline.com/journals/uast20

Prediction of the transfer function for a centrifugal differential mobility analyzer by streamline functions

Torben N. Rüther & Hans-Joachim Schmid

To cite this article: Torben N. Rüther & Hans-Joachim Schmid (15 Jul 2025): Prediction of the transfer function for a centrifugal differential mobility analyzer by streamline functions, Aerosol Science and Technology, DOI: 10.1080/02786826.2025.2519092

To link to this article: https://doi.org/10.1080/02786826.2025.2519092

AEROSOL SCIENCE AND TECHNOLOGY
https://doi.org/10.1080/02786826.2025.2519092

Prediction of the transfer function for a centrifugal differential mobility analyzer by streamline functions

Torben N. Rüther and Hans-Joachim Schmid

Particle Technology Group, Mechanical Engineering, Paderborn University, Paderborn, Germany

ABSTRACT

For complexly shaped aerosol particles a single equivalent diameter is often not sufficient for comprehensive characterization. The newly developed Centrifugal Differential Mobility Analyzer (CDMA) allows the simultaneous assessment of two equivalent sizes, e.g., mobility and aerodynamic diameter. However, determining the full two-dimensional particle size distribution using the CDMA requires precise knowledge of the transfer function. Thus, the derivation of the ideal transfer function *via* streamline functions, as proposed by Stolzenburg (2008), is adapted to the two-dimensional framework of the CDMA and compared to the calculation of the transfer function using particle trajectories. Both methods yield identical results for an idealized situation, which strongly indicates validity. Subsequently, the streamline method is extended to calculate the transfer function by applying different inlet boundary conditions, namely the common assumption of constant particle flux density versus the assumption of a given velocity profile and constant particle concentration. This appears to be a more realistic assumption in case of a laminar flow profile at the inlet. Furthermore, diffusion is considered, leading to realistic transfer functions down to ultrafine particle sizes. The results demonstrate that the inlet boundary condition significantly affects the transfer function and that diffusion has a considerable impact on the shape of the transfer function, particularly for smaller particles. Consequently, the assumption of a Gaussian transfer function can be deemed to be valid even for larger particles.

GRAPHICAL ABSTRACT

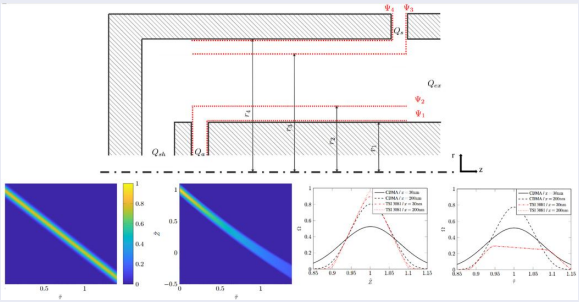

ARTICLE HISTORY
Received 28 October 2024
Accepted 6 May 2025

EDITOR
Kihong Park

1. Introduction

In actual processes, the particle properties cannot be described comprehensively by a single particle size, although typical measurement setups deliver only one equivalent particle size. Properties such as particle shape, structure, and surface may also have a significant influence. To obtain a deeper understanding of complexly shaped particle ensembles, multidimensional particle characterization is necessary. Therefore, a new device called centrifugal differential mobility analyzer (CDMA) has been developed which is described in detail by Rüther, Rasche, and Schmid (2025). This

CONTACT Hans-Joachim Schmid hans-joachim.schmid@uni-paderborn.de Particle Technology Group, Mechanical Engineering, Paderborn University, Warburger Straße 100, NRW, 33098 Paderborn, Germany.

Supplemental data for this article can be accessed online at https://doi.org/10.1080/02786826.2025.2519092.

CDMA is a classifier based on the classification of submicron particles in a cylindrical gap by simultaneously acting electrical and centrifugal forces, i.e. the gap is formed by two concentrically arranged cylinders with a voltage applied to the outer cylinder to create an electrical force on charged aerosol particles. Simultaneously, the entire can be rotated to induce a centrifugal force. As the aerosol is introduced at the inner cylinder, a radial velocity develops due to the combined effects of electrical and centrifugal forces. These forces drive the aerosol particles through a sheath air flow within the gap toward the outer cylinder. This leads to a defined trajectory over the classification gap, depending on the respective particle mass and electrical mobility. Particles with a trajectory ending at the sample outlet will be classified and counted subsequently. Effectively, the new device combines the principles of an AAC-Aerodynamic Aerosol Classifier (Tavakoli and Olfert 2013) and a DMA-Dynamic Mobility Analyzer (Knutson and Whitby 1975) in one single instrument. Consequently, from a full measurement, the complete two-dimensional distribution regarding mobility and aerodynamic equivalent diameter can be derived and used to calculate other quantities such as the effective density or the shape factor (Park et al. 2008). However, precise knowledge of the CDMA transfer function is required for the back-calculation of the measured data.

Since the calculation of the transfer function is of significant importance, numerous approaches have been pursued to derive it. For instance, in the case of an APM (Aerosol Particle Mass Analyzer), the ideal transfer function was calculated based on the streamline functions proposed by Hagwood et al. (1995) and on a Lagrangian approach for diffusion-affected transfer functions as introduced by Hagwood, Coakley, and Ehara (1996), which were experimentally validated by Olfert et al. (2006). Leveraging this knowledge, Olfert et al. (2006) applied the theory to a CPMA (Centrifugal Particle Mass Analyzer) and calculated both diffusive and non-diffusive transfer functions, employing methods such as finite difference schemes. Sipkens, Olfert, and Rogak (2020) used a Crank-Nicholson algorithm to implement a finite difference scheme for transfer function calculations. They also employed Taylor series expansions to derive an analytical transfer function, where a first-order expansion was found to be both robust and sufficiently accurate. Notably, they demonstrated that applying a single angular velocity to both electrodes also yields a completely analytical solution.

For DMAs (Differential Mobility Analyzers), various approaches for calculating transfer functions have also been developed. Knutson and Whitby (1975) proposed a method based on the particle trajectory model. Stolzenburg (1988) introduced an approach grounded in streamline calculations, which allowed the analytical extension of ideal transfer functions to diffusion-affected transfer functions. These were later confirmed through Monte Carlo simulations (Hagwood 1999), which observed nearly identical transfer functions, as well as experimentally validated by Hummes et al. (1996).

This methodology was similarly employed by Tavakoli and Olfert (2013) in the development of the AAC (Aerosol Particle Classifier). They derived diffusion-free transfer functions based on particle trajectories and streamline functions and extended the latter approach to diffusion-affected transfer functions. However, their derivations assumed a constant centrifugal force across the entire measurement gap. They also used an Eulerian diffusion model to derive diffusion-affected transfer functions, observing only minimal deviations from the streamline-based model.

It becomes apparent that streamline-based calculations play a crucial role in describing these kinds of devices, especially due to their simplicity, expandability, and good agreement with other simulation results. Consequently, this paper delves into the derivation of two-dimensional transfer functions for the CDMA (Centrifugal Differential Mobility Analyzer). In contrast to a previous study (Rüther, Rasche, and Schmid 2025), which employed an idealized particle trajectory model, the first step in this work applies the streamline model to the case of the CDMA to obtain the 2D transfer function under the same idealized conditions. This approach includes demonstrating the equivalence of streamline-based derivations to those based on particle trajectories. As a result, the commonly assumed approximation of a constant centrifugal force, previously used for the AAC, could be replaced by the actual force. Since the 2D transfer function reduces to AAC theory when no voltage is applied, this extension of the existing framework may have a significant impact on certain geometric configurations, leading to markedly different transfer functions even for the AAC setup (cf. Chapters 2 and 3).

Additionally, the streamline model is employed to assess the influence of the inlet boundary condition. Until now, a plug flow with a constant concentration has been universally assumed at the inlet. As an alternative, we derive the transfer function under the more realistic assumption of a laminar flow profile with a constant concentration, resulting in a non-uniform particle flux at the inlet. This modification leads to a

substantial change in the transfer function, deviating from its conventional triangular shape (cf. Chapter 4).

Finally, the streamline theory for the CDMA is extended to account for diffusion-affected transfer functions, which still exhibit significant broadening for particles as large as 200 nm. Overall, these improvements in the 2D transfer function are crucial for obtaining accurate approximations of the real transfer functions across various particle sizes. This is essential for the reliable application of the CDMA as a precise measuring instrument (cf. Chapter 5).

2. Non-diffusing transfer function

Figure 1 provides a sketch of the key streamlines within a Centrifugal Differential Mobility Analyzer (CDMA), illustrating the relevant radii and volume flows associated with the classification process. However, it is important to notice, that this illustration is not a technical description of the real classifier geometry. Rather, it represents the location of the respective streamlines in the classification gap without depicting their exact paths at the inlet and outlet. In fact, the trajectories of the streamlines are determined primarily by the corresponding flow rates rather than the precise geometry of the inlet and outlet. In this configuration, the aerosol is introduced into the system between streamlines Ψ_1 and Ψ_2 defining the aerosol volume flow Q_a. Particles that are located between streamlines Ψ_3 and Ψ_4 at the end of the classification gap are subsequently directed into the sampling volume flow Q_s. Additionally, the sheath air (Q_{sh}) and excess air (Q_{ex}) contribute to the overall flow configuration, ensuring precise particle classification.

The streamline functions Ψ, describes the flow paths of the air and can be calculated using the following equation (Stolzenburg 1988):

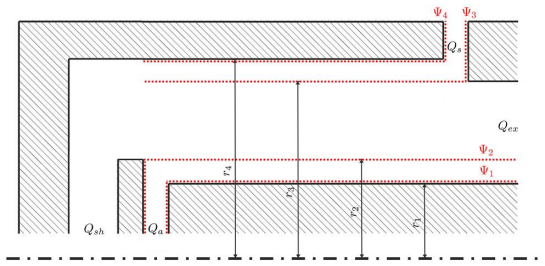

Figure 1. Representative streamlines of a CDMA with corresponding radii and volume flows: aerosol volume flow Q_a; Sheath air Q_{sh}; Exhaust air Q_{ex}; Sample air Q_s. The Sketch of the classification gap does not represent the exact geometry of in- and outlet.

$$\Psi(r,z) = \int^{r,z} [ru_r\,\mathrm{d}z - ru_z\,\mathrm{d}r], \tag{1}$$

Here, r and z denote the radial and axial coordinate, u_r and u_z the radial and axial components of the airflow velocity, respectively. In this study a plug flow is assumed in the classification gap, i.e., $u_r = 0$ and $u_z = const$. This assumption appears to be valid, as the flow profile would have no impact on particles that traverse all streamlines, i.e., particles entering the classification gap at Ψ_1 and exiting at Ψ_4. As demonstrated by Stolzenburg (1988), the influence of the flow profile on other particles is generally minimal. In particular, the smaller the parameter β, the less significant the effect of the flow profile will be. This streamline function therefore provides a continuous and smooth representation of the airflow within the CDMA, which is essential for predicting particle behavior.

In addition to the airflow, the motion of particles under the influence of external forces, such as electrical and centrifugal forces, is described by the particle stream function Φ :

$$\Phi(r,z) = \int^{r,z} [rw_r\,\mathrm{d}z - rw_z\,\mathrm{d}r], \tag{2}$$

In this equation, w_r and w_z represent the radial and axial components of the particle velocity. These functions allow for the precise calculation of particle trajectories based on the operating parameters and particle properties[1].

The radial velocity of particles, w_r, can be determined if the particle mobility (Z), relaxation time (τ), and the CDMA's operating parameters, such as applied voltage (U) and angular velocity (ω), are known. Assuming no radial fluid velocity ($u_r = 0$), the radial particle velocity is given by Rüther, Rasche, and Schmid (2025):

$$w_r = \frac{Z \cdot U}{r \cdot \ln(r_4/r_1)} + \tau\omega^2 r, \tag{3}$$

The radii r_4 and r_1 are depicted in Figure 1. This equation incorporates both the electrical force (first term) and the centrifugal force (second term) acting on the particles. In the axial direction, it is assumed that the particle velocity matches the fluid velocity, i.e., $w_z = u_z$. This simplification is valid due to very small particle relaxation times of submicron particles considered in this work. The transmission probability Ω is a measure of the likelihood that a particle entering the system is classified. This overall probability is calculated integrating over the inlet and outlet section, using the following integral (Stolzenburg and McMurry 2008):

[1]See Appendix S1.

$$\Omega = \int_{\Psi_1}^{\Psi_2} \left[\int_{\Psi_3}^{\Psi_4} f_{trans}(\Psi_{out}, \Psi_{in}) \mathrm{d}\Psi_{out} \right] \cdot f_{in}(\Psi_{in}) \mathrm{d}\Psi_{in}, \tag{4}$$

In this equation, $f_{trans}(\Psi_{out}, \Psi_{in})\, d\Psi_{out}$ represents the transfer probability, describing the likelihood that particles entering the classification path on streamline Ψ_{in} exit the system on streamline $\Psi_{out} + d\Psi_{out}$.

$$f_{trans}(\Psi_{out}, \Psi_{in}) = \delta_D(\Psi_{out} - \Psi_{in} - \Phi_{out} + \Phi_{in}), \tag{5}$$

Here, δ_D is the Dirac delta function, which ensures that only particles for which the difference in streamline functions equals the difference in flux functions are classified. This condition implies that particles must travel the given radial distance to satisfy the classification criterion.

When integrating over the Dirac delta function, the result is one, indicating successful classification for particles meeting this criterion. The integral bounds, Ψ_3 and Ψ_4 further define the streamline range of the sample flow Q_S. For particles entering on a specific streamline Ψ_{in} with a trajectory ending at the outlet the integral $\int_{\Psi_3}^{\Psi_4} f_{trans}(\Psi_{\mathrm{in}}, \Psi_{\mathrm{out}}) \mathrm{d}\Psi_{out}$ equals unity and zero otherwise.

This calculation ensures an accurate representation of the classification efficiency and its dependence on the systems' parameters and particle properties. This detailed explanation provides a comprehensive understanding of the flow dynamics, particle behavior, and mathematical framework used in the CDMA for particle classification.

After this probability is multiplied by the probability $f_{in}(\Psi_{in})\mathrm{d}\Psi_{in}$ of a particle entering the transfer path at point $\Psi_{in} + \mathrm{d}\Psi_{in}$, it is possible to integrate over Ψ_{in} with the integration limits Ψ_1, Ψ_2. Assuming no concentration gradients and a perfect plug flow, the probability of a particle entering the classification gap within the interval Ψ_1, Ψ_2 is constant over the height, corresponding to a constant particle flux density at the inlet:

$$f_{in}(\Psi_{in}) = \frac{1}{\Psi_1 - \Psi_2}, \tag{6}$$

If Equation (3) is inserted into the particle stream function (Equation (2)), $\Delta\Phi = \Phi_{out} - \Phi_{in}$ can be calculated, considering the whole classifying length L:

$$\Delta\Phi = \int_0^L r w_r dz = \frac{Z \cdot U}{\ln(r_4/r_1)} \cdot \int_0^L \mathrm{d}z + \tau\omega^2 \cdot \int_0^L r^2(z) \mathrm{d}z, \tag{7}$$

It should be noted that the first term, resulting from the electrical drift, is independent of the particle's position. This is because the electrical drift velocity is inversely proportional to the radius. As a result, in the term $rw_{r,el}$ the radius r cancels out. Here, an ideal electrical field for an infinitely long cylindrical gap is assumed. However, the centrifugal term is strongly dependent on the actual radial position.

If normalized forms of the electrical mobility and the particle relaxation time are used, results will be more generally valid. Furthermore, the relevant equations become more compact. These dimensionless forms, i.e., normalized mobility $\tilde{Z}$ and particle reaction time $\tilde{\tau}$, read:

$$\tilde{Z} = Z/Z^*; \quad \tilde{\tau} = \tau/\tau^*, \tag{8}$$

where Z^* is the mobility required for a particle entering at the center of the aerosol inlet to be sampled exactly at the center of the outlet in the absence of centrifugal force. Likewise, τ^* represents the analogous behavior for the relaxation time in the absence of the electrical force.

$$Z^* = \frac{Q_{sh} + Q_{ex}}{4 \cdot \pi L U} \cdot \ln\left(\frac{r_4}{r_1}\right), \tag{9}$$

$$\tau^* = \frac{Q_{sh} + Q_{ex}}{\pi\omega^2 (r_1 + r_4)^2 L}, \tag{10}$$

With the behavior of the particle trajectory (based on the volume flows, centrifugal force, and electrical force), which is derived in Rüther, Rasche, and Schmid (2025):

$$r(z) = \sqrt{r_{\mathrm{in}}{}^2 \cdot \exp\left\{\frac{z}{L} \cdot \tilde{\tau} \cdot \frac{2\tilde{h}}{1+\beta}\right\} + \overline{r^2} \cdot \frac{\tilde{Z}}{\tilde{\tau}} \cdot \left[\exp\left\{\frac{z}{L} \cdot \tilde{\tau} \cdot \frac{2\tilde{h}}{1+\beta}\right\} - 1\right]}, \tag{11}$$

concerning, that $\tilde{h}$ is the ratio of the gap width to the mean radius, and β is the ratio of the aerosol volume flow Q_a to the sheath air Q_{sh}:

$$\tilde{h} = 2 \cdot \frac{r_4 - r_1}{r_4 + r_1}, \tag{12}$$

$$\beta = Q_a/Q_{sh}, \tag{13}$$

the following equation can be obtained:

$$\Delta\Phi = -\Psi_{in} A + \frac{Q_{sh}}{4\pi} \cdot \frac{\tilde{Z}}{\tilde{\tau}} \cdot \frac{1+\beta}{\tilde{h}} \cdot A. \tag{14}$$

Here, A can be expressed as follows:

$$A = \exp\left\{\frac{2\tau\omega^2 L}{u}\right\} - 1 = \exp\left\{\tilde{\tau} \cdot \frac{2\tilde{h}}{1+\beta}\right\} - 1, \tag{15}$$

A comprehensive derivation of Equation (14) can be found in Appendix A2.

Using the solution of the integral of a Dirac delta function δ_D (Stolzenburg 1988):

$$2\int_0^x \delta_D(u)\mathrm{d}u = \begin{matrix} +1, x > 0 \\ 0, x = 0 \\ -1, x < 0 \end{matrix} \equiv H^+(x), \tag{16}$$

Equation (4) can be solved as follows:

$$\Omega = \frac{1}{2}\int_{\psi_1}^{\psi_2}\left[H^+\left(\psi_4 - \psi_{\mathrm{in}} + \frac{\tilde{Z}}{\tilde{\tau}}\cdot\frac{Q_{\mathrm{sh}}}{4\pi}\cdot\frac{1+\beta}{\tilde{h}}\cdot A - \psi_{\mathrm{in}}\cdot A\right) - H^+\left(\psi_3 - \psi_{\mathrm{in}} + \frac{\tilde{Z}}{\tilde{\tau}}\cdot\frac{Q_{\mathrm{sh}}}{4\pi}\cdot\frac{1+\beta}{\tilde{h}}\cdot A - \psi_{\mathrm{in}}\cdot A\right)\right]\cdot f_{\mathrm{in}}\, d\psi_{\mathrm{in}}. \tag{17}$$

Here, H^+ is a modified version of a Heaviside step function, whose definite integral can be calculated using:

$$\int_0^x H^+(u)\mathrm{d}u = \begin{matrix} x, & x \geq 0 \\ -x, & x < 0 \end{matrix} = |x|, \tag{18}$$

Inserting Equation (18) into (17) results in:

$$\Omega = \frac{1}{2(\Psi_2 - \Psi_1)(1+\mathrm{A})}\left[-\left|\Psi_4 - \Psi_2 - \Psi_2 A + \frac{Q_{sh}}{4\pi}\cdot\frac{\tilde{Z}}{\tilde{\tau}}\cdot\frac{1+\beta}{\tilde{h}}A\right| + \left|\Psi_4 - \Psi_1 - \Psi_1 A + \frac{Q_{sh}}{4\pi}\cdot\frac{\tilde{Z}}{\tilde{\tau}}\cdot\frac{1+\beta}{\tilde{h}}A\right| + \left|\Psi_3 - \Psi_2 - \Psi_2 A + \frac{Q_{sh}}{4\pi}\cdot\frac{\tilde{Z}}{\tilde{\tau}}\cdot\frac{1+\beta}{\tilde{h}}A\right| - \left|\Psi_3 - \Psi_1 - \Psi_1 A + \frac{Q_{sh}}{4\pi}\cdot\frac{\tilde{Z}}{\tilde{\tau}}\cdot\frac{1+\beta}{\tilde{h}}A\right|\right]. \tag{19}$$

Using the mean particle stream function

$$\overline{\Delta\Phi} = \frac{Q_{sh}}{2\pi}, \tag{20}$$

and the following substitutions

$$\frac{\Psi_4 - \Psi_1}{\overline{\Delta\Phi}} = -\beta - 1, \quad \frac{\Psi_4 - \Psi_2}{\overline{\Delta\Phi}} = -1, \tag{21}$$

$$\frac{\Psi_3 - \Psi_2}{\overline{\Delta\Phi}} = \beta - 1, \quad \frac{\Psi_3 - \Psi_1}{\overline{\Delta\Phi}} = -1, \tag{22}$$

Equation (19) can be modified to a dimensionless representation of the ideal transfer function for a CDMA:

$$\Omega = \frac{1}{2\beta(1+A)}\left[-\left|-1 - \frac{\beta+\kappa^2}{\kappa^2-1}\cdot A + \frac{\tilde{Z}}{\tilde{\tau}}\cdot\frac{1+\beta}{2\tilde{h}}\cdot A\right| + \left|-1-\beta - \frac{\kappa^2+\beta\kappa^2}{\kappa^2-1}\cdot A + \frac{\tilde{Z}}{\tilde{\tau}}\cdot\frac{1+\beta}{2\tilde{h}}\cdot A\right| + \left|-1+\beta - \frac{\beta+\kappa^2}{\kappa^2-1}\cdot A + \frac{\tilde{Z}}{\tilde{\tau}}\cdot\frac{1+\beta}{2\tilde{h}}\cdot A\right| - \left|-1 - \frac{\kappa^2+\beta\kappa^2}{\kappa^2-1}\cdot A + \frac{\tilde{Z}}{\tilde{\tau}}\cdot\frac{1+\beta}{2\tilde{h}}\cdot A\right|\right], \tag{23}$$

κ being the substitution

$$\kappa = \frac{r_1}{r_4} = \frac{1-\tilde{h}/2}{1+\tilde{h}/2}. \tag{24}$$

It should be noted that to simplify the calculation, the typical operation condition $Q_a = Q_s$ and consequently $Q_{sh} = Q_{ex}$ is assumed. The derivation of the ratios of the streamline and particle stream functions are shown in Appendix A3. Moreover, it can be shown analytically, that Equation (23) is equal to the derivation of Stolzenburg and McMurry (2008) for no rotation ($\tilde{\tau} = 0$). Nevertheless, for $\tilde{Z} = 0$ the derivation of Equation (23) differs from the results presented by Tavakoli and Olfert (2013), as they apply the simplifying assumption of a mean centrifugal force over the entire classification gap. This has a significant impact on the shape of the transfer function, which will be discussed in detail in Section 4.

Figure 2a shows the two-dimensional transfer function without diffusion for the plug flow velocity profile. Because both, positively and negatively charged particles are present, the normalized mobility can also be positive or negative. However, the normalized relaxation time of the particles must be positive.

In general, the transfer function presented here is very similar to the transfer function from (Rüther, Rasche, and Schmid 2025). To confirm this, the

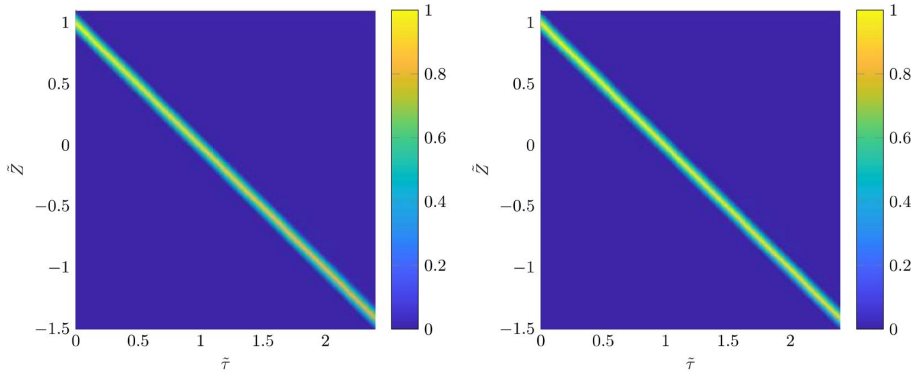

(a) Non diffusing transfer function

(b) Transfer function with a laminar velocity profile at the inlet

Figure 2. Non-diffusing two-dimensional transfer functions for $\beta = 0.1$ and $\tilde{h} = 0.05$.

equivalence of the transfer functions without diffusion is discussed in the next section based on the streamline consideration and particle trajectory calculation.

3. Equivalence of derivations based on streamline and particle trajectory assumptions

A derivation of the CDMA transfer function based on particle trajectory considerations has already been presented in Rüther, Rasche, and Schmid (2025). Following, the equivalence of the equations derived from the particle trajectories (PT) (Rüther, Rasche, and Schmid 2025) and from the streamlines (S) (see Chapter 2) is then discussed. For better readability, Equation (25) was inserted into Equation (22).

$$a = -1 - \frac{\kappa^2 + \kappa^2\beta}{\kappa^2 - 1} \cdot A + \frac{\tilde{Z}}{\tilde{\tau}} \cdot \frac{1+\beta}{2\tilde{h}} \cdot A, \tag{25}$$

where a can take any value from $-\infty$ to $+\infty$, depending on the operating conditions.

This results in a simplified representation of the transfer function as a function of $a, \beta,$ and A.

$$\Omega_{\mathrm{S}} = -\frac{1}{2\beta(1+A)} \cdot [-|a+\beta A| - |a| + |a-\beta| + |a+\beta+\beta A|], \tag{26}$$

By rearranging and inserting the placeholders defined above into Equations (21) and (22) of Rüther, Rasche, and Schmid (2025), the following equation can be used to calculate the transfer function based on particle trajectory considerations.

$$\Omega_{\mathrm{PT}} = \max\left[\min\left(f_1, f_2, 1\right), 0\right], \tag{27}$$

$$f_1 = \frac{1}{\beta(A+1)}\left[a + \beta + \beta A - \max\left(a + \beta A, 0\right)\right], \tag{28}$$

$$f_2 = \frac{1}{\beta(A+1)}\left[-a + \beta - \max\left(-a, 0\right)\right], \tag{29}$$

Comparing the equations Ω_{S} and Ω_{PT}, they appear very similar.

Since an analytical transformation from one equation into the other is very difficult due to the nested maximum and minimum functions, the different boundary cases should be considered. In addition, the fact that both A and β can only assume positive values is also employed in this context.

Forming these boundary cases, both equations yield the same results.

$$\Omega = \frac{1}{\beta(1+A)} \begin{cases} 0, & (a<0)\ \ (a<-\beta A)\ \ (a<-\beta-\beta A) \\ \beta+\beta A+a, & (a<0)\ \ (a<-\beta A)\ \ (a>-\beta-\beta A) \\ \beta, & (a<0)\ \ (a>-\beta A) \\ \beta-a, & (a>0)\ \ (a<\beta) \\ 0, & (a>0)\ \ (a>\beta) \end{cases}, \tag{30}$$

The equivalence of the results obtained from both methods justifies the use of the stream function approach for calculating the transfer function under varying inlet boundary conditions or when accounting for particle diffusion. In these cases, the stream

function approach is considerably easier to implement than the corresponding particle trajectory method.

4. Laminar flow profile at the inlet gap

The derivations of Stolzenburg (1988) (DMA) and Tavakoli (Tavakoli and Olfert 2013) (AAC) always assume a constant homogenous particle flux density at the inlet of the measurement device. However, assuming, that the particle concentration c is constant throughout the inlet gap, the particle flux density distribution $\overrightarrow{j} = c \cdot \overrightarrow{w}$ at the inlet is completely dependent on the flow profile $u(r)$. Given a laminar flow profile (Reynolds number at the inlet of the CDMA: $Re_{\mathrm{CDMA}} = 42$) and neglecting particle migration due to the small size and flow length, a parabolic profile mirroring the velocity profile should be a good representation of the true situation.

By integrating a second-order polynomial for a parabolic normalized flux density profile with the specified boundary conditions (i.e., zero flux density at the walls and a total integral equal to one) and applying the desired probability distribution, the following expression can be obtained for f_{in}.

$$f_{\mathrm{in}} = \frac{6}{(\psi_2 - \psi_1)^3} \cdot \left(-\psi_{\mathrm{in}}^2 + \psi_{\mathrm{in}}(\psi_1 + \psi_2) - \psi_1\psi_2\right), \tag{31}$$

Inserting this into Equation (17) yields:

$$\Omega = \frac{3}{(\psi_2 - \psi_1)^3}\left[\int_{\psi_1}^{\psi_2}\left[H^+\left(\psi_4 - \psi_{\mathrm{in}} + \frac{\tilde{Z}}{\tilde{\tau}} \cdot \frac{Q_{\mathrm{sh}}}{4\pi} \cdot \frac{1+\beta}{\tilde{h}} \cdot A - \psi_{\mathrm{in}} \cdot A\right) - H^+\left(\psi_3 - \psi_{\mathrm{in}} + \frac{\tilde{Z}}{\tilde{\tau}} \cdot \frac{Q_{\mathrm{sh}}}{4\pi} \cdot \frac{1+\beta}{\tilde{h}} \cdot A - \psi_{\mathrm{in}} \cdot A\right)\right]\right.$$
$$\left.\left(-\psi_{\mathrm{in}}^2 + \psi_{\mathrm{in}}(\psi_1 + \psi_2) - \psi_1\psi_2\right) d\psi_{\mathrm{in}}\right]. \tag{32}$$

With the solutions of the integrals (where k is a constant term and C is the integration constant)[2]:

$$\int H^+\left(k - \psi_{in}(1+A)\right) d\psi_{in} = \psi_{in} \cdot H^+\left(k - \psi_{in}(1+A)\right) + \mathrm{H}\left(\psi_{in}(1+A) - k\right) \cdot 2k + C, \tag{33}$$

$$\int H^+\left(k - \psi_{in}(1+A)\right)\psi_{in} d\psi_{in} = \frac{{\psi_{in}}^2}{2} \cdot H^+\left(k - \psi_{in}(1+A)\right) + H\left(\psi_{in}(1+A) - k\right) \cdot \frac{k^2}{(1+A)^2} + C, \tag{34}$$

$$\int H^+\left(k - \psi_{in}(1+A)\right)\psi_{in}^2 dx = \frac{{\psi_{in}}^3}{3} \cdot H^+\left(k - \psi_{in}(1+A)\right) + \mathrm{H}\left(\psi_{in}(1+A) - k\right) \cdot \frac{2k^3}{3(1+A)^3} + C, \tag{35}$$

and applying the procedure of Section 2 we obtain the following equation:

[2] $\int H^+\left(k - \psi_{in}(1+A)\right) d\psi_{in} = -\frac{1}{1+A}\left|k - \psi_{in}(1+A)\right|$ is valid only for a defined integral.

$$\Omega=\frac{3}{\beta}\cdot\left\{\left[-\frac{{B_2}^2C_2}{3}\cdot H^+(D_4-C_2(1+A))-H(C_2(1+A)-D_4)\cdot\frac{2{E_4}^2D_4}{3(1+A)^3}+\frac{{B_1}^2C_1}{3}\cdot H^+(D_4-C_1(1+A))+H(C_1(1+A)-D_4)\cdot\frac{2{E_4}^2D_4}{3(1+A)^3}\right]\right.$$
$$+(B_1+B_2)\left[\frac{B_2C_2}{2}H^+(D_4-C_2(1+A))+H(C_2(1+A)-D_4)\frac{E_4D_4}{(1+A)^2}-\frac{B_1C_1}{2}H^+(D_4-C_1(1+A))-H(C_1(1+A)-D_4)\frac{E_4D_4}{(1+A)^2}\right]$$
$$+B_1B_2\left[\frac{1}{1+A}|D_4-C_2(1+A)|-\frac{1}{1+A}|D_4-C_1(1+A)|\right]$$
$$+\left[\frac{{B_2}^2C_2}{3}H^+(D_3-C_2(1+A))+H(C_2(1+A)-D_3)\frac{2{E_3}^2D_3}{3(1+A)^3}-\frac{{B_1}^2C_1}{3}H^+(D_3-C_1(1+A))-H(C_1(1+A)-D_3)\frac{2{E_3}^2D_3}{3(1+A)^3}\right]$$
$$-(B_1+B_2)\left[\frac{B_2C_2}{2}H^+(D_3-C_2(1+A))+H(C_2(1+A)-D_3)\frac{E_3D_3}{(1+A)^2}-\frac{B_1C_1}{2}H^+(D_3-C_1(1+A))-H(C_1(1+A)-D_3)\frac{E_3D_3}{(1+A)^2}\right]$$
$$\left.+\frac{B_1B_2}{1+A}\left[-|D_3-C_2(1+A)|+|D_3-C_1(1+A)|\right]\right\},\tag{36}$$

whereby[3]:

$$B_1=\left(\kappa^2/\beta+\kappa^2\right)/(1-\kappa^2)\quad;\quad B_2=\left(1+\kappa^2/\beta\right)/(1-\kappa^2)B_3=\left(1/\beta+\kappa^2\right)/(1-\kappa^2)\quad;\quad B_4=(1/\beta+1)/(1-\kappa^2)\tag{37}$$

$$C_1=-\left(\kappa^2+\kappa^2\beta\right)/(1-\kappa^2)\quad;\quad C_2=-\left(\beta+\kappa^2\right)/(1-\kappa^2)\quad C_3=-\left(1+\beta\kappa^2\right)/(1-\kappa^2)\quad;\quad C_4=-(1+\beta)/(1-\kappa^2)\tag{38}$$

$$D_3=C_3+\cdot\frac{\tilde{Z}}{\tilde{\tau}}\cdot\frac{1+\beta}{2\tilde{h}}\cdot A\quad;\quad D_4=C_4+\cdot\frac{\tilde{Z}}{\tilde{\tau}}\cdot\frac{1+\beta}{2\tilde{h}}\cdot A\tag{39}$$

$$E_3=B_3-(B_4-B_2)\cdot\frac{\tilde{Z}}{\tilde{\tau}}\cdot\frac{1+\beta}{2\tilde{h}}\cdot A\quad;\qquad E_4=B_4-(B_4-B_2)\cdot\frac{\tilde{Z}}{\tilde{\tau}}\cdot\frac{1+\beta}{2\tilde{h}}\cdot A\tag{40}$$

and where $H(x)$ is the real step function with its definition:

[3]Also, Appendix A3 for additional information.

$$H(x) = \begin{matrix} 0, & x < 0 \\ +1, & x > 0 \end{matrix}. \tag{41}$$

The derivation of the CDMA transfer function results in a lengthy and intricate equation, as demonstrated by the previous example. Figure 2 shows the two-dimensional transfer functions for a diffusion-less flow profile with a plug-flow velocity profile (Figure 2a) and with a laminar velocity profile at the inlet (Figure 2b). Since the two-dimensional representation does not allow for a simple quantitative comparison, Figure 3 shows a direct comparison of the transfer functions for both inlet boundary conditions of the cases $\tilde{\tau} = 0$ and $\tilde{Z} = 0$ and different values of $\tilde{h}$.

Looking at the transfer function at $\tilde{\tau} = 0$ (Figure 3a), it can be clearly observed that both inlet conditions give distinct shapes of the transfer function, with the laminar velocity profile leading to a significantly rounder curve. However, the dimensionless slit width had no effect on the transfer function.

For the marginal distribution at $\tilde{Z} = 0$ (Figure 3b), the assumed plug flow at the inlet results in a 'truncated' triangle for the transfer function. This is in contrast to the triangular-shaped transfer function derived by Tavakoli. This discrepancy is due to his assumption of a mean centrifugal force throughout the classification gap which was abandoned in our derivation. As the gap becomes larger relative to the mean radius (i.e., $\tilde{h}$ becoming larger), the difference in the centrifugal forces becomes greater. I.e. particles entering at r_1 experience a lower initial centrifugal force than particles entering at r_2. The higher force is amplified further over the entire particle trajectory. Thus, the original triangle is further truncated and slightly deformed. Again, the laminar velocity profile has the effect of creating a smooth, continuous transfer function with no kinks, i.e., the function remains differentiable across the entire range. In addition, the transfer function is higher because the concentration profile releases more particles at the center of the gap and fewer or no particles at the edges of the inlet gap. This results in a less pronounced truncation of the transfer function in this case.

When examining the transfer functions of the AAC and DMA, the question of their shape becomes particularly relevant, as it must be assumed to be known for accurate measurement. For large particles, a triangular function is often assumed, while for small particles, a Gaussian function is typically used (Stolzenburg 1988). However, if the theoretical transfer functions are analyzed under the assumption of a laminar flow profile at the inlet,

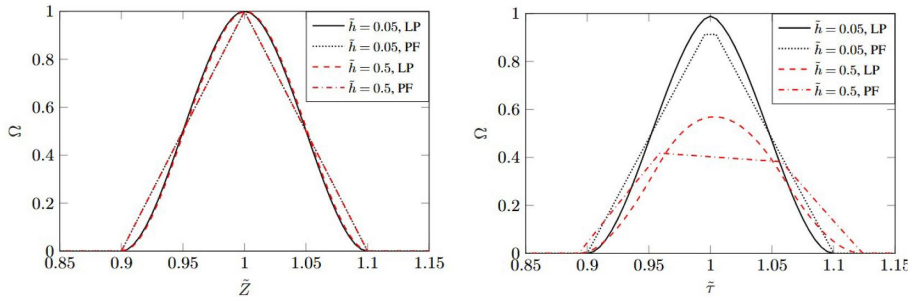

(a) $\tilde{\tau} = 0$ (b) $\tilde{Z} = 0$

Figure 3. Transfer functions for $\tilde{\tau} = 0$ and $\tilde{Z} = 0$ at $\beta = 0.1$ for different ratios of radii (PF: plug flow/LP: laminar velocity profile).

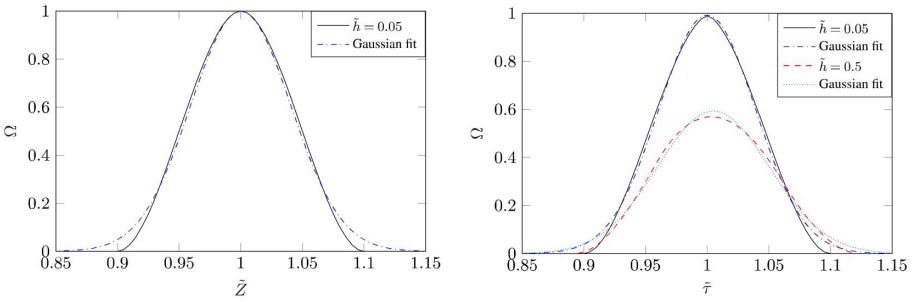

(a) $\tilde{\tau} = 0$ (b) $\tilde{Z} = 0$

Figure 4. Fit of a Gaussian function to the transfer functions with $\tilde{\tau} = 0$ and $\tilde{Z} = 0$ at $\beta = 0.1$ for a laminar velocity profile and different ratios of radii.

$$\Omega_d = \frac{1/2}{\Psi_2 - \Psi_1} \cdot \int_{\Psi_1}^{\Psi_2} \left[\mathrm{erf}\left\{ \frac{\Psi_4 - \Psi_{\mathrm{in}}(1+A) + \frac{\tilde{Z}}{\tilde{\tau}} \frac{Q_{\mathrm{sh}}}{4\pi} \frac{(1+\beta)}{\tilde{h}} A}{\sqrt{2}\sigma_\Gamma} \right\} - \mathrm{erf}\left\{ \frac{\Psi_3 - \Psi_{\mathrm{in}}(1+A) + \frac{\tilde{Z}}{\tilde{\tau}} \frac{Q_{\mathrm{sh}}}{4\pi} \frac{(1+\beta)}{\tilde{h}} A}{\sqrt{2}\sigma_\Gamma} \right\} \right] d\Psi_{\mathrm{in}}, \quad (43)$$

they closely resemble a Gaussian profile—even in the absence of diffusion effects. To address this, a Gaussian function was fitted to the transfer functions (see Figure 4). In general, a Gaussian function appears to describe a transfer function quite well. However, the maximum value appears to be slightly too high, the FWHM (full width at half maximum) slightly smaller, and the edges flatten out more slowly. Nevertheless, this shape is much closer to reality than the typically assumed triangular transfer function. Especially in real systems, the diffusion is still superimposed and thus supports the Gaussian behavior of the transfer function (c.f. Section 5).

5. Diffusing transfer function

To obtain further information about the behavior of the transfer functions, Stolzenburg's derivation for calculating a diffusing transfer function is extended to the CDMA principle. Equation (42) describes the diffusive transfer function, where σ_Γ represents the standard deviation of the Gaussian distribution of the diffusion path perpendicular to the direction of the particle trajectory.

$$\Omega_d = \frac{1}{\Psi_1 - \Psi_2} \cdot \int_{\Psi_1}^{\Psi_2} \left[\int_{\Psi_3}^{\Psi_4} \frac{1}{\sqrt{2\pi}\sigma_\Gamma} \cdot \exp\left\{ -\frac{1}{2} \left(\frac{\Psi_{\mathrm{out}} - \Psi_{\mathrm{in}}(1+A) + \frac{\tilde{Z}}{\tilde{\tau}} \cdot \frac{Q_{\mathrm{sh}}}{4\pi} \cdot \frac{(1+\beta)}{\tilde{h}} \cdot A}{\sigma_\Gamma} \right)^2 \right\} d\Psi_{\mathrm{Out}} \right] d\Psi_{\mathrm{in}}, \quad (42)$$

The integration of the inner integral provides:

The solution of the integral of the error function follows:

$$\epsilon(x) = \int^x erf\{u\} \mathrm{d}u = x \cdot \mathrm{erf}\{x\} + \frac{1}{\sqrt{\pi}} \cdot \exp\{-x^2\}, \quad (44)$$

Inserting this behavior into Equation (43) yields:

$$\Omega_{\mathrm{d}} = \frac{\sigma_\Gamma/\sqrt{2}}{\Psi_1 - \Psi_2} \cdot \frac{1}{1+\mathrm{A}} \left[-\epsilon\left(\frac{\Psi_4 - \Psi_2(1+\mathrm{A}) + \frac{\tilde{Z}}{\tilde{\tau}} \frac{Q_{\mathrm{sh}}}{4\pi} \frac{(1+\beta)}{\tilde{h}} \mathrm{A}}{\sqrt{2}\sigma_\Gamma} \right) + \epsilon\left(\frac{\Psi_4 - \Psi_1(1+\mathrm{A}) + \frac{\tilde{Z}}{\tilde{\tau}} \frac{Q_{\mathrm{sh}}}{4\pi} \frac{(1+\beta)}{\tilde{h}} \mathrm{A}}{\sqrt{2}\sigma_\Gamma} \right) \right.$$
$$\left. + \epsilon\left(\frac{\Psi_3 - \Psi_2(1+\mathrm{A}) + \frac{\tilde{Z}}{\tilde{\tau}} \frac{Q_{\mathrm{sh}}}{4\pi} \frac{(1+\beta)}{\tilde{h}} \mathrm{A}}{\sqrt{2}\sigma_\Gamma} \right) - \epsilon\left(\frac{\Psi_3 - \Psi_1(1+\mathrm{A}) + \frac{\tilde{Z}}{\tilde{\tau}} \frac{Q_{\mathrm{sh}}}{4\pi} \frac{(1+\beta)}{\tilde{h}} \mathrm{A}}{\sqrt{2}\sigma_\Gamma} \right) \right], \quad (45)$$

Replacing σ_Γ with a dimensionless diffusion spread parameter σ yields the final form of the diffusive transfer function.

$$\Omega_d = \frac{\sigma}{\sqrt{2}\beta} \cdot \frac{1}{1+A}\left[-\epsilon\left(\frac{-1 - B_2A + \frac{\tilde{Z}}{\tilde{\tau}}\frac{(1+\beta)}{2\tilde{h}}A}{\sqrt{2}\sigma}\right) + \epsilon\left(\frac{-(1+\beta) - B_1A + \frac{\tilde{Z}}{\tilde{\tau}}\frac{(1+\beta)}{2\tilde{h}}A}{\sqrt{2}\sigma}\right) + \epsilon\left(\frac{-(1\text{-}\beta) - B_2A + \frac{\tilde{Z}}{\tilde{\tau}}\frac{(1+\beta)}{2\tilde{h}}A}{\sqrt{2}\sigma}\right) - \epsilon\left(\frac{-1 - B_1A + \frac{\tilde{Z}}{\tilde{\tau}}\frac{(1+\beta)}{2\tilde{h}}A}{\sqrt{2}\sigma}\right)\right], \tag{46}$$

This dimensionless diffusion spread parameter depends on the flow field, the electrical field, the centrifugal field, and the particle size. Assuming all particles behave like the particles at the mean particle trajectory (i.e., $\tilde{h}$ and β are small) σ can be calculated from the geometry, the particle diffusion coefficient Dp, and operating parameters.[4]

$$\sigma = \sqrt{4 \cdot \frac{(1+\beta)^2}{1-\kappa^2} \cdot \frac{4 \cdot \pi \cdot L \cdot D_p}{Q_{sh} + Q_{ex}} \cdot \left[\frac{1+\kappa^2}{2} + \frac{1-\kappa^2}{4 \cdot (1+\beta)^2 \cdot \left(\frac{L}{r_4}\right)^2}\right]}, \tag{47}$$

Figure 5 shows an examplary transfer function for the geometries shown in Table 1, once for the CDMA and once for the DMA (TSI 3081) commercially available from TSI. The curve for the CDMA (Figure 5a) is very similar to the figures in Section 4. The only difference is that the maximum values are about 0.8, which is due to diffusion losses. This is more apparent in Figure 5b. Here, the height of the transfer function decreases significantly with increasing values of $\tilde{\tau}$, becomes broader and is no longer linear[5], although the transfer function at $\tilde{\tau} = 0$ is still higher than that for the CDMA. This behavior can be explained by the large gap width. To classify particles of given properties with a larger gap (but constant classifier length and constant flow rates), the radial drift velocity must increase while the residence time remains unchanged. I.e. for larger gap widths particles are classified at higher voltages or rotational speeds, respectively. Consequently, the relevance of particle transport in the radial direction in relation to diffusional transport increases, meaning that diffusion has a diminishing effect as gap width increases. However, for higher values of $\tilde{h}$, the effect of the truncated triangular function increases for larger values of $\tilde{\tau}$ (cf. Section 4).

In order to provide a more quantitative comparison, Figure 6 shows the transfer functions for $\tilde{\tau} = 0$ and $\tilde{Z} = 0$ associated with the two-dimensional distribution for the dimensions of the actual CDMA prototype (Rüther, Rasche, and Schmid 2025) and for the commercially available DMA (TSI 3081), respectively.

A comparison of the two devices at $\tilde{\tau} = 0$ reveals a notable discrepancy in the extent of diffusion between the two devices. This is attributable to the markedly narrower gap width of the CDMA prototype, which results in reduced applied voltages and, consequently decreased Peclet number (Flagan 1999). This indicates that the CDMA experiences a discernible influence on diffusion even at a particle size of 200 nm, which intensifies further with decreasing particle size.

For the CDMA prototype at $\tilde{Z} = 0$, there is an increased influence of diffusion as well, particularly for small particle sizes, which leads to a significant broadening of the curve. Moreover, a smoothing effect is observed, whereby the corners lose their sharpness. Nevertheless, when a CDMA at $\tilde{Z} = 0$ with the geometric dimensions of a TSI 3081 is considered, the truncated triangular function can still be discerned in pure rotation mode. In addition, considering this geometry, the impact of particle size i.e., the impact of diffusion is markedly diminished. This result is attributed to the larger gap width of a standard DMA again, which would require much higher angular velocities to classify particles in a manner analogous to that observed for narrower gaps as realized in the CDMA prototype. Similar to the electrical classification, a higher angular velocity corresponds to a higher Peclet

[4]The complete derivation can be found in Stolzenburg (1988).

[5]The non-linearity is a consequence of the normalization with τ^* (Equation (10)), which was adopted from Tavakoli and Olfert. However, this definition corresponds only approximately to the actual mean streamline $\Delta\Psi^*$. The correct $\tau' *$ can be calculated as follows:

$$\tau' * = \frac{Q_{sh}}{2\pi(r_4^2 - r_2^2)\omega^2 L} \cdot \ln\left(\frac{r_4^2 + r_3^2}{r_2^2 + r_1^2}\right)$$

However, since this requires additional data to compute, we relied in our approach on the τ^* definition provided by Tavakoli and Olfert (Tavakoli, 2013). This simplification is acceptable because τ^* is only used for normalization. It should be noted that the deviation of the transfer function from linearity increases for increasing values of $\tilde{h}$.

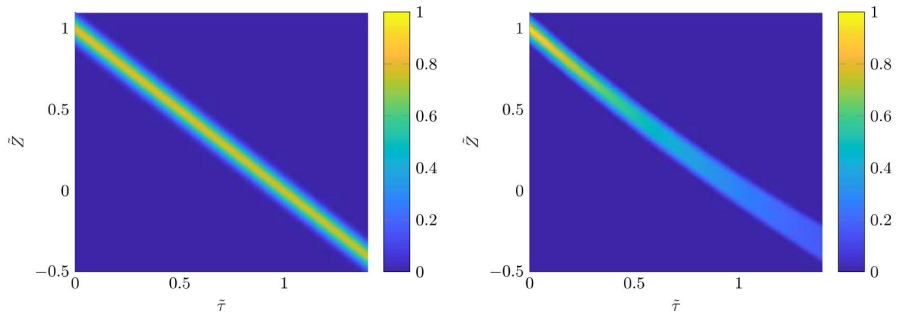

(a) Diffusing two-dimensional transfer function for DMA (TSI 3081) dimensions.

(b) Diffusing two-dimensional transfer function for the dimensions of the CDMA prototype.

Figure 5. Diffusing two-dimensional transfer functions for DMA (TSI 3081) and CDMA dimensions (geometry data is provided in Table 1) at a particle size of $x = 200\,\text{nm}$.

Table 1. Geometric properties of the DMA (TSI 3081) and the CDMA prototype used for the calculations in this section.

Measurement system	r_4 in mm	r_1 in mm	$\tilde{h}$	L in mm	β	Q_{sh} in l/min
DMA (TSI 3081)	19.61	9.37	0.7067	443.69	0.1	3
CDMA prototype	74.3	70.9	0.0486	334	0.1	3

number, i.e., a significantly smaller influence of diffusion for higher gap widths as used in a standard DMA. However, realizing the rotation of the CDMA without inducing vibrations limits the realizable angular velocity. Therefore, the geometry of a CDMA is a compromise between the smallest measurable particle size and the diffusional broadening of the transfer function.

Figure 7 illustrates the influence of diffusion on the transfer functions with respect to particle size in detail. In Figure 7a, the FWHM (Full Width at Half Maximum) is depicted, representing a measure of the width of the transfer function. For the mobility margin function a value of 0.1 is expected in the limiting case of neglectable diffusion. It can be seen that both geometries (CDMA and commercial DMA) approximate to this limiting value for large particle sizes. However, due to the small gap of the CDMA prototype diffusion is relevant up to particle sizes even above 250 nm. For the relaxation time margin transfer function the limiting value is strongly depending on the geometry due to the truncated shape. For the CDMA prototype, the FWHM curve is very similar to the mobility curve. However, for the commercial DMA a much larger value of FWHM occurs even without diffusion due to the large $\tilde{h}$ value while the transfer function shows almost negligible further broadening by diffusion even for ultrafine particles.

Figure 7b illustrates the peak values $\Omega_{\max}$ of the respective transfer functions. As can be seen, $\Omega_{\max}$ approaches unity in case that diffusion is negligible. Here again, the much stronger diffusion in the CDMA is reflected in decreasing peak values for decreasing particle sizes. Only the peak value for the relaxation time margin transfer function shows an almost constant value of around 0.3 due to the strongly truncated transfer function in this case.

Obviously, in the case of diffusion, the influence of the inlet boundary condition is much less pronounced since the diffusion and inlet flow profile both have a similar effect, namely broadening and smearing of the transfer function.

6. Conclusions

This paper presents the derivation of a two-dimensional transfer function based on the streamline model (Stolzenburg and McMurry 2008) for the newly developed Centrifugal Differential Mobility Analyzer (CDMA). It is demonstrated analytically, that both the particle trajectory model and streamline model provide identical results over the whole domain in case of the ideal transfer function, i.e., assuming a constant particle flux density at the inlet and neglecting diffusion (cf. Section 3, Equation (30)). However, the streamline function approach can be extended much easier to non-idealities. Namely, the more realistic assumption at the aerosol inlet cross-section of a laminar flow profile and a constant particle concentration shows significant discrepancies in the transfer function. Moreover, the consideration of diffusion leads to a significant broadening of the transfer function, particularly for smaller particles. This broadening results from the smaller gap width in the CDMA prototype compared to a standard DMA which in turn results from a limited angular velocity.

Given the satisfactory approximation of the transfer function by a Gaussian function in the case of a laminar flow profile at the inlet and considering that diffusion further enhances the broadening of the transfer

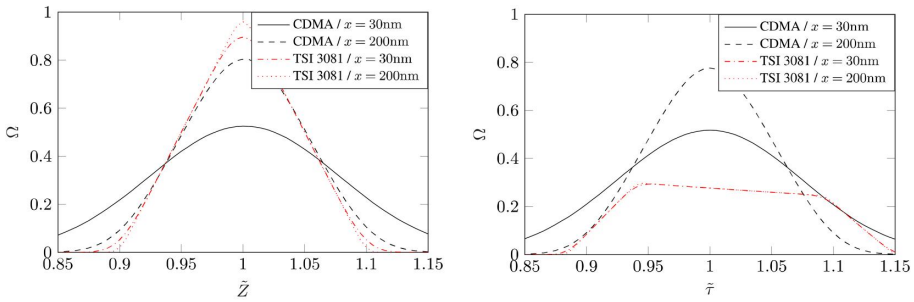

(a) $\tilde{\tau} = 0$ (b) $\tilde{Z} = 0$

Figure 6. Margin transfer functions with Diffusion, for a CDMA prototype (Rüther, Rasche, and Schmid 2025) and a DMA TSI 3081 (geometry data is provided in Table 1) at different particle sizes d_p and ambient temperature and pressure.

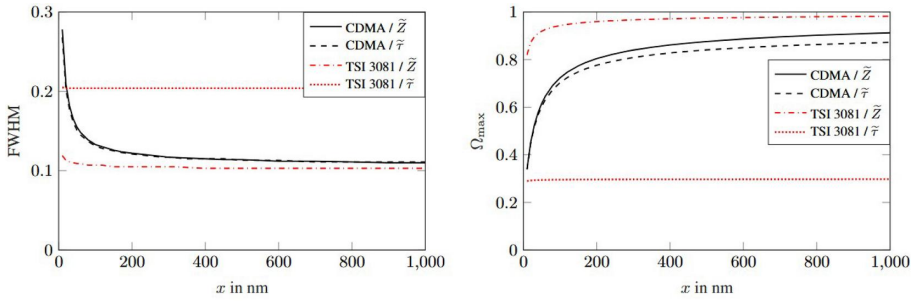

(a) FWHM of the transfer function. (b) Maximum height of the transfer function.

Figure 7. Parameter full width at half maximum and maximum height of margin transfer functions with diffusion, for a CDMA prototype (Rüther, Rasche, and Schmid 2025) and a DMA TSI 3081 (geometry data is provided in Table 1) depending on particle size d_p at ambient temperature and pressure.

function, it becomes evident that a Gaussian function can accurately approximate the transfer function with good precision, even for larger particles.

The analytical solutions presented here can be employed to develop a comprehensive solution for operational modes of the CDMA in which the conditions $Q_a \neq Q_s$ and $Q_{sh} \neq Q_{ex}$ are met.

The solutions developed in this paper are important for understanding the CDMA classification behavior and the influence of the discussed operational parameters. However, to re-calculate two-dimensional size distributions from measurements, additional effects, namely losses, in the inlet and outlet must also be assessed and determined as precisely as possible.

Disclosure statement

No potential conflict of interest was reported by the authors.

Funding

This work was supported by the German Research Foundation under the SPP 20245 MehrDimPart (GZ: SCHM 1429/19–1).

ORCID

Torben N. Rüther http://orcid.org/0000-0002-2766-1656

References

Flagan, R. C. 1999. On differential mobility analyzer resolution. *Aerosol Sci. Technol.* 30 (6):556–70. doi: 10.1080/027868299304417.

Hagwood, C., K. Coakley, and K. Ehara. 1996. Novel method to classify aerosol particles according to their mass-to-charge-ratio—Aerosol particle mass analyzer. *Journal of Aerosol Science* 27 (2):217–34. doi: 10.1016/0021-8502(95)00562-5.

Hagwood, C., K. Coakley, A. Negiz, and K. Ehara. 1995. Stochastic modeling of a new spectrometer. *Aerosol Sci. Technol.* 23 (4):611–27. doi: 10.1080/02786829508965342.

Hagwood, C. 1999. The DMA transfer function with Brownian motion a trajectory/Monte-Carlo approach. *Aerosol Sci. Technol.* 30 (1):40–61. doi: 10.1080/027868299304877.

Hummes, D., S. Neumann, H. Fissan, and F. Stratmann. 1996. Experimental determination of the transfer function of a differential mobility analyzer (DMA) in the nanometer size range. *Part. Part. Syst. Charact.* 13 (5):327–32. doi: 10.1002/ppsc.19960130513.

Knutson, E. O., and K. T. Whitby. 1975. Aerosol classification by electric mobility: Apparatus, theory, and applications. *Aerosol Sci. Technol.* 6 (6):443–51. doi: 10.1016/0021-8502(75)90060-9.

Olfert, J. S., K. S. Reavell, M. G. Rushton, and N. Collings. 2006. The experimental transfer function of the Couette centrifugal particle mass analyzer. *Aerosol Science* 37 (12): 1840–52. doi: 10.1016/j.jaerosci.2006.07.007.

Park, K., D. Dutcher, M. Emery, J. Pagels, H. Sakurai, J. Scheckman, S. Qian, M. R. Stolzenburg, X. Wang, J. Yang, et al. 2008. Tandem measurements of aerosol properties—A review of mobility techniques with extensions. *Aerosol Sci. Technol.* 42 (10):801–16. doi: 10.1080/02786820802339561.

Rüther, T. N., D. B. Rasche, and H.-J. Schmid. 2025. The centrifugal differential mobility analyzer - concept and initial validation of a new device for measuring 2D property distributions. *Aerosol Research*. 3 (1):65–79. doi: 10.5194/ar-2024-29.

Sipkens, T. A., J. S. Olfert, and S. N. Rogak. 2020. New approaches to calculate the transfer function of particle mass analyzers. *Aerosol Sci. Technol.* 54 (1):111–27. doi: 10.1080/02786826.2019.1680794.

Stolzenburg, M. R. 1988. An ultrafine aerosol size distribution system. PhD Diss., University of Minnesota.

Stolzenburg, M. R., and P. H. McMurry. 2008. Equations governing single and tandem DMA configurations and a new lognormal approximation to the transfer function. *Aerosol Sci. Technol.* 42 (6):421–32. doi: 10.1080/02786820802157823.

Tavakoli, F., and J. S. Olfert. 2013. An instrument for the classification of aerosols by particle relaxation time: Theoretical models of the aerodynamic aerosol classifier. *Aerosol Sci. Technol.* 47 (8):916–26. doi: 10.1080/02786826.2013.802761.

4.3 The POCS-Algorithm - An effective tool for calculating 2D particle property distributions via Data Inversion of exemplary CDMA measurement data

Torben N. Rüther, David B. Rasche, Hans-Joachim Schmid,
Aerosol Science, 188, (2025), https://doi.org/10.1016/j.jaerosci.2025.106606

Der Autor dieser Dissertation hat den von David Rasche entwickelten Algorithmus zur Dateninversion leicht angepasst und auf ideale Messdaten, mit statistischem Rauschen überlagerte Messdaten sowie reale Messdaten angewendet und die Ergebnisse diskutiert. Prof. Hans-Joachim Schmid hat den Autor während der gesamten Arbeit betreut. Er und David Rasche haben an der Erstellung und Revision des Manuskripts mitgewirkt.

Journal of Aerosol Science 188 (2025) 106606

Contents lists available at ScienceDirect

Journal of Aerosol Science

journal homepage: www.elsevier.com/locate/jaerosci

The POCS-Algorithm—An effective tool for calculating 2D particle property distributions via data inversion of exemplary CDMA measurement data

Torben N. Rüther [a,*], David B. Rasche [a,b], Hans-Joachim Schmid [a]

[a] Particle Technology Group, Department of Mechanical Engineering, Paderborn University, Warburger Straße 100, Paderborn, 33098, NRW, Germany
[b] REMBE GmbH Safety+Control, Gallbergweg 21, Brilon, 59929, NRW, Germany

ARTICLE INFO

Dataset link: https://git.uni-paderborn.de/pvt/cdma

Keywords:
POCS
Projection onto convex sets
Data inversion
2D distribution
CDMA
Centrifugal Differential Mobility Analyzer

ABSTRACT

In many cases particle characterization is not trivial, so that data inversion routines are needed in order to determine particle size distributions from measurement data. In particular, determination of two-dimensional particle property distributions, which are very valuable for analyzing complex shaped particles, results in large ill-posed systems of equations which are challenging to be solved. In this paper the Projections onto Convex Sets (POCS) method is implemented for solving such problems in particle characterization for the first time. The POCS method is an iterative algorithm which allows the use of all available information about the distribution to significantly reduce the number of potential solutions. Here, the application of this method is shown for the example of a Centrifugal Differential Mobility Analyzer (CDMA), which measures the number concentration of a nanoscaled aerosol after classification in a gap between two concentric cylinders with a combination of different voltages and angular speeds, i.e. controlled electrical and centrifugal forces. The application of the POCS algorithm to this problem comprising the formulation of appropriate boundary conditions and projection operators to include all available information, is described in detail. Further on, the implementation of the algorithm is explained. The algorithm is then used to invert constructed ideal data and constructed data with superimposed noise. It is demonstrated that the POCS algorithm in either case is well suited to obtain a stable and efficient inversion of the measurement data and to obtain highly accurate 2-dimensional particle property distributions with respect to mobility equivalent diameter and Stokes diameter, respectively. Finally, the algorithm is applied to real measurement data obtained from a prototype of the new device to derive real 2D density distributions.

1. Introduction

The applications of nanotechnology get more diverse and complex. The analysis of the structure of nanoparticles is becoming a crucial aspect of research in various fields, including battery technology (Zhang et al., 2022) and medicine (Jindal, 2017; Toy et al., 2014). Consequently, the current literature demonstrates considerable interest in the highly specific characterization of disperse systems based on multidimensional particle properties (Masuhr & Kruis, 2024; Rhein et al., 2019; Sandmann & Fritsching, 2023) and in methods of particle characterization (DeCarlo et al., 2004; Shapiro et al., 2012; Slowik et al., 2004).

* Corresponding author.
E-mail address: hans-joachim.schmid@uni-paderborn.de (T.N. Rüther).

https://doi.org/10.1016/j.jaerosci.2025.106606
Received 12 December 2024; Received in revised form 28 April 2025; Accepted 5 May 2025
Available online 20 May 2025

Nomenclature

Greek Symbols

β	Ratio of Q_a to Q_{sh} (–)
δ	Permitted deviation (–)
η	Dynamic viscosity (Pa s)
η_{CPC}	CPC counting efficiency (–)
η_{V}	Experimentally determined loss term (–)
Γ	Weighting factors for construction of noise data (–)
γ	Charge distribution (–)
μ	Expected value of the normal distribution (#/cm^3)
Ω	Transfer function (–)
ω	Angular speed $\omega = 2\pi \cdot n$ (1/s)
ρ	Particle density (kg/m^3)
ρ_0	Virtual assumed density of (1000 kg/m^3) (kg/m^3
ρ_{eff}	Effective density (kg/m^3)
σ	Constructed virtual measurement noise (#/m^3)
σ_{g}	Geometrical standard deviation (–)
σ_{l}	Logarithmic standard deviation (–)
τ	Particle relaxation time (s)
τ^*	Nominal particle relaxation time (s)
$\widetilde{\tau}$	Normalized particle relaxation time (–)

Indices

$i\omega$	Component of the measurement vector regarding to the angular speed
iU	Component of the measurement vector regarding to the voltage
j	Component of $\boldsymbol{d}_m$
k	Number of mobility diameter classes
l	Component of $\boldsymbol{d}_{st}$
low	Upper interval limit
m	Mobility
o	Number of stokes diameter classes
st	Stokes
up	Upper interval limit

Arabic Symbols

$\dot{V}$	Volume flow though the CPC (m^3/s)
$\widetilde{h}$	Ratio of the gap width to the mean radius (–)
$\widetilde{Z}$	Normalized particle mobility (–)
Cu	Cunningham slip correction factor (–)
d_m	Mobility equivalent diameter (m)
d_v	Volume equivalent diameter (m)
d_{ae}	Arodynamic equivalent diameter (m)
d_{st}	Stokes equivalent diameter (m)
F_D	Drag force (N)
K	Kernel matrix (–)
L	Length of the CDMA transfer path (m)
N	Measured number concentration (#/m^3)
n	Particle charge (–)
N_{tot}	Total number concentration (#/m^3)
q_0	Number density distribution (1/m)
Q_a	Aerosol volume flow (m^3/s)
q_o	Number density distribution (#/m^3)
Q_P	Particle charge (A s)

Q_{sh}	Sheath air volume flow (m^3/s)
r_{in}	Inner radius (m)
r_{out}	Maximum radius at which the particles enter (m
t	time (s)
w_s	Settling velocity (m/s)
Z^*	Nominal particle mobility ($m^2/(V\ s)$)
Z_p	Particle mobility ($m^2/(V\ s)$)

Vector Symbols

$\boldsymbol{b}$	Measured frequency ($\#/cm^3$)
$\boldsymbol{b}_0$	Measured particle number (#)
$\boldsymbol{C}$	Boundary condition (–)
$\boldsymbol{e}$	Potential measurement error (–)
$\boldsymbol{P}$	Projection operator (–)
$\boldsymbol{q}$	Solution vector (1/m)
$\boldsymbol{R}$	Vector of normal distributed random numbers ($\#/cm^3$)
$\boldsymbol{r}$	Residuum (–)
$\boldsymbol{U}$	Voltage (V)
$\boldsymbol{z}$	Set of operating and geometry parameters (–)
$\underline{\boldsymbol{A}}$	Auxiliary matrix (–)
$\underline{\boldsymbol{K}}$	Kernel matrix (–)

The simultaneous measurement of several particle properties is currently a challenging task. One approach to the multidimensional measurement of nanoparticles is to use available measurement systems, such as the DMA (Dynamic Mobility Analyzer) (Stolzenburg, 1988) or AAC (Aerodynamic Aerosol Classifier) (Tavakoli & Olfert, 2014), in tandem setups. Using a DMA and an AAC in a serial connection two different equivalent properties are characterized by each instrument, namely the mobility equivalent and the Stokes equivalent diameter (Rüther et al., 2024). From these, other particle properties such as effective density or fractal dimension can be derived (Park et al., 2008; Slowik et al., 2004; Tavakoli & Olfert, 2014). It should be noted, however, that this requires sophisticated inversion routines and extensive knowledge on the part of the user.

The CDMA (Centrifugal Differential Mobility Analyzer) has been developed to measure a two-dimensional distribution with a single instrument, allowing for a smaller footprint and a standardized measurement setup, which is particularly advantageous for cost and handling reasons. The CDMA combines the features of a DMA and an AAC in one single instrument. The operation principle is based on the classification within a cylindrical gap, whereby both a voltage and a rotational speed can be applied to influence the particle path simultaneously and enables the sampling of particles with corresponding properties at a specific position within the cylinder gap. This allows a two-dimensional scan of both variables (Rüther et al., 2024). The resulting two-dimensional distribution of the number of classified particles with respect to applied voltage and angular speed show however some ambiguity concerning the particle properties. Therefore, the data inversion for obtaining the 2D particle density distribution with respect to mobility and Stokes diameter is much more complex than in the aforementioned sequential approaches.

This means that the transfer function is not only dependent on one property but on two independent properties, thereby becoming two-dimensional. Consequently, the direct back-calculation routines used for DMA or AAC are no longer applicable [Rüther, forthcoming2]. In general, there are different methods for data inversion of ill-posed mathematical systems, which are regularization methods (Markowski, 1987; Twomey, 1975), the Tikhonov method (Kenneth Wolfenbarger & Seinfeld, 1990; Wang et al., 2006), maximum entropy method (Wang, 2008; Yee, 1989), statistical methods (Voutilainen et al., 2001), iterative methods (Stark & Olsen, 1992; Worlitschek et al., 2005) or evolutionary methods (Lienert et al., 2003). Recent approaches use neuronal networks and artificial intelligence to solve these problems, too (Adler & Öktem, 2017).

The routines for the tandem arrangements of conventional instruments are also not transferable directly, as they can only perform direct back-calculation by connecting both devices in series. Park et al. (2003) show a good measurement back transformation for a DMA-APM (Aerosol Particle Mass Analyzer) combination, which is confirmed by specific measurements (Rawat et al., 2016). Based on these works (Buckley et al., 2017) introduced a revised Twomey algorithm, which seemingly performs very well.

Sipkens et al. (2020b) present a comparative analysis of various inversion algorithms for a DMA-CPMA (Centrifugal Particle Mass Analyzer) combination. Their findings indicate that an unregularized minimum squared error approach yields suboptimal performance. In contrast, the Twomey–Markowski method refined by Buckley (Buckley et al., 2017), which represents the current state-of-the-art, accurately reconstructs the pre-specified virtual distributions across the entire range of input distributions. Notably, Tikhonov regularization demonstrates even superior performance compared to the Twomey–Markowski approach. Meanwhile, MART (Multiplicative Algebraic Reconstruction Technique) algorithms, despite delivering comparably strong results, exhibit higher computational demands, reduced stability, and a tendency towards divergence.

Sipkens et al. (2020a) propose that these inversion algorithms can be effectively applied to a variety of tandem measurement setups. For instance, Broda et al. (2018) demonstrate the use of the Twomey algorithm in a CPMA - SP2 (Single Particle Soot Photometer) -CPC (Condensation Particle counter) configuration, highlighting its applicability in resolving two dimensional particle mass distributions. Similarly, Naseri et al. (2021) explore alternative inversion methods for the same combination, reporting that the MART algorithms exhibit the fastest convergence, while Tikhonov regularization yields the highest accuracy when benchmarked against the established Twomey–Markowski approach. Morán et al. (2023) extend these methodologies by employing a minimum squared error method to infer particle characteristics in a two-dimensional framework using a wire-plate electrostatic precipitator in conjunction with a tandem DMA-APM system. Their results, validated through simulation, exhibit strong agreement, further underscoring the robustness of these inversion techniques.

Building upon these advances, Chen, et al. (2018) applies the refined Twomey–Markowski approach developed by Buckley et al. (2017) to a DMA-APM system for characterizing nanoparticle agglomeration in non-equilibrium plasma synthesis environments. Their findings reveal excellent agreement with Langevin dynamic simulations, demonstrating that this methodology can be extended to different synthesis conditions and reactor geometries. This, in turn, provides valuable insights into the morphological evolution of synthesized nanoparticles and their corresponding growth dynamics. Furthermore, Sipkens et al. (2023) consolidate these advancements in a comprehensive review paper, wherein they systematically evaluate the capabilities of various measurement techniques for soot particle analysis. Their work critically discusses different tandem setups and associated data evaluation algorithms, offering a thorough assessment of their respective advantages and limitations.

Despite the considerable number of inversion methods explored thus far, the Projections onto Convex Sets (POCS) algorithm has received only little attention in data inversion applications. POCS is an iterative approach designed to solve ill-posed systems of equations and is generally recognized for its robustness, particularly in the fields of tomography and image reconstruction (Gubin et al., 1967). To date, the method has been employed in the field of characterization only by Mehler et al. (2002) who derive surface charge densities for the characterization of adsorption processes across a range of substances, while Schürer and Peukert (2005) have leveraged the algorithm for the prediction of adsorption equilibria.

In this study, we present the application of the Projections onto Convex Sets (POCS) algorithm to data inversion, highlighting its significant advantages in incorporating prior knowledge directly into the inversion process. Being aware of promising work involving the POCS algorithm (Mehler et al., 2002; Schürer & Peukert, 2005), we aimed to explore its potential within our specific research context. One of its key strengths lies in its ability to enforce known constraints, such as predefined marginal distributions – an aspect previously discussed by Naseri – as well as the fundamental requirement that the cumulative distribution function converges to one. In contrast to incorporate any prior knowledge, the utilization of inherent constraints significantly enhances the stability and reliability of the inversion process when applied within the framework of the POCS algorithm. Consequently, this approach expands the repertoire of available methodologies, providing a robust and flexible alternative to well-established techniques. Given its adaptability and theoretical soundness, the POCS algorithm holds promise for improving inversion accuracy across a wide range of applications. However, benchmarking against existing algorithms which would be of great interest as well is out of scope of the present paper.

2. Concept of the data inversion

The objective of data inversion is to reconstruct the true distribution of properties from the distribution of measured signal values. In the present case, the measured values comprise the measured particle numbers, $N_{iU,i\omega}(U_{iU},\omega_{i\omega})$, as a function of the voltage U_{iU} and the rotational speed, $\omega_{i\omega}$. The objective of the inversion is to derive the two-dimensional number density distribution, i.e.

$$q_0(\log(d_m),\log(d_{st})) = \frac{\mathrm{d}N(d_m,d_{st})}{N_{\mathrm{tot}}\cdot \mathrm{dlog}(d_m)\mathrm{dlog}(d_{st})} \tag{1}$$

which is dependent on the mobility equivalent diameter d_m, i.e. a spherical particle of this diameter experiences the same drag force in a continuum fluid for a given relative velocity as the actual particle and the Stokes equivalent diameter d_{st}, i.e. the size of a spherical particle which has the same settling velocity, while having the same density (Colbeck, 2013; Reist, 1993), therefore depending on drag force and mass.[1] With $\mathrm{d}N(d_m,d_{st})$ being the number of particles in a given 2D size interval of width $\mathrm{dlog}(d_m)$ and $\mathrm{dlog}(d_{st})$, respectively, N_{tot} being the total number of assessed particles. However, since particle distributions are broad, it is advantageous to scale the arguments of number density distribution $q_0(\log(d_m),\log(d_{st}))$ lognormally. The measurement signal, i.e. the number of classified particles $\Delta N(U_{iU},\omega_{i\omega})$ for a given combination of voltage U_{iU} and rotational speed $\omega_{i\omega}$ can result from any different combination of mobility equivalent diameter and Stokes equivalent diameter, that satisfy the correct particle trajectory. This results in a highly complex relationship between the target (c.f. Eq. (2)) and the measured variable, so that reconstructing the true property distribution from the measurement signal, or the measured value distribution is a challenging task.

The measured number concentration of particles for a given combination of voltage and speed can be calculated for a given particle size distribution $q_0\left(\log\left(d_m\right),\log\left(d_{st}\right)\right)$ by integrating the two-dimensional number density distribution multiplied with a

[1] If the particle density is not known with sufficient accuracy, the aerodynamic equivalent diameter d_{ae} could be used instead of the Stokes diameter $d_{st} = d_{ae}\sqrt{\rho_0/\rho}$. Here, ρ is actual particle density and ρ_0 is the particle density of $1\,\mathrm{g/cm^3}$. However, this leads to an equivalent inversion problem (Rüther et al., 2024).

Kernel function $K(d_m, d_{st}, n, z)$ over all possible combinations of mobility and Stokes diameters. Additionally, a potential measurement error $e_{iU,i\omega}$ must be considered as well. Therefore, the measured frequency $b_{iU,i\omega}$ can be calculated as follows:

$$b_{iU,i\omega} = \frac{\Delta N_{iU,i\omega}(U_{iU}, \omega_{i\omega})}{N_{\text{tot}}} = \int_0^\infty \int_0^\infty K(d_m, d_{st}, z) \cdot q(\log(d_m), \log(d_{st})) \cdot \text{dlog}(d_m)\text{dlog}(d_{st}) + e_{iU,i\omega} \tag{2}$$

where **b** is the target vector of the calculation and **z** are the operating parameters (flow rates, voltage, rotational speed, pressure, temperature, gas species, etc.) as well as the geometry of the CDMA.

The Kernel function K is derived from the transfer function of the device $\Omega(n, d_m, d_{st}, z)$. Furthermore, the charge distribution $\gamma(n, d_m)$ must be considered also, with the particle charge n. This Kernel function and the respective parameters are discussed in greater detail in Sections 3.2 and 3.3.

Since neither the solution vector nor the measured values are continuous, Eq. (2) must be represented in discrete form:

$$b_{iU,i\omega} = \frac{\Delta N_{iU,i\omega}(U_{iU}, \omega_{i\omega})}{N_{\text{tot}}} = \sum_{j=1}^{k} \sum_{l=1}^{o} K_{j,l,iU,i\omega} \cdot q_{j,l} \cdot \Delta \log(d_{m,j}) \cdot \Delta \log(d_{st,l}) + e_{iU,i\omega} \tag{3}$$

Discretization transforms the Kernel function K into a Kernel matrix $\underline{\boldsymbol{K}}$ (cf. Section 3.3). Hence, this equation can be represented in matrix notation:

$$\boldsymbol{b} = \underline{\boldsymbol{A}} \cdot \boldsymbol{q} + \boldsymbol{e} \tag{4}$$

where

$$\underline{\boldsymbol{A}} = \langle \underline{\boldsymbol{K}} \mid \langle \Delta \log(\boldsymbol{d_m}) | \Delta \log(\boldsymbol{d_{st}})^T \rangle \rangle \tag{5}$$

$$q_{j,l} = q(\log(d_{m,j}), \log(d_{st,l})) \tag{6}$$

The aim of data inversion is to solve this system of equations in such a way that a unique solution, in this case the number density distribution $\boldsymbol{q}$, for a measured frequency number distribution $\boldsymbol{b}$ is found. The main difficulty is that this inverse problem represents a mathematically ill-posed system of equations. This means that there are several or an infinite number of possible mathematical approximate solutions to the problem. A promising approach is the POCS method, which can solve ill-posed systems of equations robustly and efficiently.

3. Projections onto convex sets (POCS)

The POCS method is based upon the utilization of prior knowledge regarding the solution, which can be integrated into an iterative algorithmic process through the implementation of boundary conditions $(C_1, C_2, \ldots, C_n)$. The incorporation of this knowledge allows for a significant reduction in the number of potential solutions. Accordingly, the algorithm identifies a solution that is consistent with all underlying boundary conditions, provided that the boundary conditions can be represented by projections onto closed and convex sets in a Hilbert space (Hocker et al., 2001). The method is founded upon a procedure in which a solution vector is iteratively projected onto all boundary conditions C with the assistance of projection operators P (Gubin et al., 1967; Stark & Yang, 1998).

If all boundary conditions are consistent and have a non-empty intersection C_0, the iteration scheme converges to a possible solution on the boundary of the intersection (Gubin et al., 1967).

If the boundary conditions are inconsistent and therefore an empty intersection exists, a solution will still be found with a high probability (Stark & Yang, 1998). It should be noted that this method can never lead to a unique and exact solution for non-trivial systems. The higher the number of boundary conditions, the smaller the space of possible solutions and the higher the expected accuracy. Therefore, to solve a linear system of equations of the form (4) robustly, it is necessary to find as many boundary conditions as possible that constrain the problem.

3.1. Boundary conditions

3.1.1. Non-negativity of the density distribution

Negative values of the number density distribution are physically impossible and can therefore be excluded. Mathematically, this boundary condition can be interpreted as follows

$$C_{\text{nonNeg}} = \left\{ \boldsymbol{q} \ \epsilon \ R : \quad q_{j,l} \geq 0; \quad j = 1, \ldots, k \wedge l = 1, \ldots, o \right\} \tag{7}$$

The projection operator of non-negativity P_{nonNeg} is therefore (Stark & Yang, 1998):

$$P_{\text{nonNeg}} : \ q_{j,l} = \begin{cases} q_{j,l}, & q_{j,l} \geq 0 \\ 0, & q_{j,l} < 0 \end{cases}; \qquad j = 1, \ldots, k \wedge l = 1, \ldots, o \tag{8}$$

This means, that all values that are less than zero are rendered zero, while all other values remain unaltered.

3.1.2. Normalization of the density distribution

A further significant characteristic of particle size density distributions is that due to normalization by N_{tot} (cf. Eq. (2)), the integral of the density distribution over the complete two-dimensional size range, is always equal to one.

$$\int_0^\infty \int_0^\infty q(\log(d_m), \log(d_{st})) \cdot \mathrm{dlog}(d_m)\mathrm{dlog}(d_{st}) = 1 \tag{9}$$

In the discrete representation, this can be formulated as follows:

$$\sum_{j=1}^{k} \sum_{l=1}^{o} q_{j,l} \cdot \Delta \log(d_{m,j}) \cdot \Delta \log(d_{st,l}) = 1 \tag{10}$$

This representation may be transformed into the form of a scalar product.

$$\langle\langle \boldsymbol{q} | \boldsymbol{g} \rangle\rangle = \sum_{j=1}^{k} \sum_{l=1}^{o} q_{j,l} \cdot g_{j,l} = 1 \tag{11}$$

where:

$$\boldsymbol{g} = \langle \Delta \log(\boldsymbol{d_m}) | \Delta \log(\boldsymbol{d_{st}})^T \rangle \tag{12}$$

In defining a boundary condition that accounts for the characteristics of a particle size distribution, it is important to recognize that even minor inaccuracies, e.g. due to limited numerical resolution, can prevent that this condition may be completely satisfied. Accordingly, for the normalization boundary condition C_{norm} a discrepancy δ_{norm} from the specified value of one is permitted for the sum. This category of boundary conditions is designated as 'soft-linear' (Stark & Yang, 1998).

$$C_{\text{norm}} = \left\{ \boldsymbol{q} \ \epsilon \ R: \quad |\langle\langle \boldsymbol{q} | \boldsymbol{g} \rangle\rangle - 1| \leq \delta_{\text{norm}} \right\} \tag{13}$$

A scaling projection operator for the specified boundary condition can be represented as follows:

$$P_{\text{norm}}: \ \boldsymbol{q} = \begin{cases} \boldsymbol{q}, & \boldsymbol{q} \quad \epsilon \ C_{\text{norm}} \\ \frac{\boldsymbol{q}}{\langle\langle \boldsymbol{q} | \boldsymbol{g} \rangle\rangle}, & \langle\langle \boldsymbol{q} | \boldsymbol{g} \rangle\rangle < 1 - \delta_{\text{norm}} \\ \frac{\boldsymbol{q}}{\langle\langle \boldsymbol{q} | \boldsymbol{g} \rangle\rangle}, & \langle\langle \boldsymbol{q} | \boldsymbol{g} \rangle\rangle < 1 + \delta_{\text{norm}} \end{cases} \tag{14}$$

3.1.3. Marginal distributions

The marginal distributions represent the frequency distribution with respect to just one of the considered properties, irrespective of the other property, i.e. $q(d_m)$ or $q(d_{st})$, respectively. They can be calculated by integrating or, in the discrete case, summing over the other property:

$$q_{\text{margMob}}(d_m) = \int_0^\infty q(\log(d_m), \log(d_{st})) \ \ \mathrm{dlog}(d_{st}) \tag{15}$$

and discretized:

$$q_{\text{margMob,j}} = \sum_{l=1}^{o} q_{j,l} \ \cdot \Delta \log(d_{st,l}) \tag{16}$$

Analogously, the marginal distribution of the Stokes equivalent diameter is obtained:

$$q_{\text{margSt}}(d_{st}) = \int_0^\infty q(\log(d_m), \log(d_{st})) \ \ \mathrm{dlog}(d_m) \tag{17}$$

as well as:

$$q_{\text{margSt,l}} = \sum_{j=1}^{k} q_{j,l} \ \cdot \Delta \log(d_{m,j}) \tag{18}$$

These marginal distributions are identical to measurements results obtained with a DMA (Knutson & Whitby, 1975) or an AAC (Tavakoli & Olfert, 2014), respectively. Thus, for the CDMA, the two marginal distributions can be determined for the cases $\omega = 0$ and $U = 0$, respectively, by applying the common data inversion theories of the DMA and AAC, accordingly. Therefore, the resulting distributions $\boldsymbol{q}_{\text{DMA}}$ (corresponding to $\boldsymbol{q}_{\text{margMob}}$) and $\boldsymbol{q}_{\text{AAC}}$ (corresponding to $\boldsymbol{q}_{\text{margSt}}$) can be determined prior to inversion of the two-dimensional data and can be assumed to be known upon inversion with the POCS algorithm. If a deviation δ_{marg} is permitted again, the soft-linear boundary conditions are defined as follows:

$$C_{\text{margMob}} = \left\{ \boldsymbol{q}_{\text{margMob}} \ \epsilon \ R: \quad | \ \langle \boldsymbol{q} | \Delta \log(\boldsymbol{d}_{st}) \rangle - \boldsymbol{q}_{\text{DMA}} \ | \leq \delta_{\text{marg}} \right\} \tag{19}$$

$$C_{\text{margSt}} = \left\{ \boldsymbol{q}_{\text{margSt}} \ \epsilon \ R: \quad | \ \langle \boldsymbol{q} | \Delta \log(\boldsymbol{d}_m) \rangle - \boldsymbol{q}_{\text{AAC}} \ | \leq \delta_{\text{marg}} \right\} \tag{20}$$

The two corresponding soft-linear projection operators can be defined as follows:

$P_{\mathrm{margMob,j}}$ for any fixed value of $j;\ l = 1, \dots, o$:

$$q_{\mathrm{j,l}} = \begin{cases} q_{\mathrm{j,l}}, & q_{\mathrm{margMob,j}} \ \epsilon \ C_{\mathrm{margMob}} \\ q_{\mathrm{j,l}} + \frac{q_{\mathrm{DMA,j}} - \delta_{\mathrm{marg}} - q_{\mathrm{margMob,j}}}{\|\Delta \log(\boldsymbol{d}_{st})\|^2} \cdot \Delta \log(d_{st,l}), & q_{\mathrm{margMob,j}} < q_{\mathrm{DMA,j}} - \delta_{\mathrm{marg}} \\ q_{\mathrm{j,l}} + \frac{q_{\mathrm{DMA,j}} + \delta_{\mathrm{marg}} - q_{\mathrm{margMob,j}}}{\|\Delta \log(\boldsymbol{d}_{st})\|^2} \cdot \Delta \log(d_{st,l}), & q_{\mathrm{margMob,j}} < q_{\mathrm{DMA,j}} + \delta_{\mathrm{marg}} \end{cases} \tag{21}$$

$P_{\mathrm{margSt,l}}$ for any fixed value of $l;\ j = 1, \dots, k$:

$$q_{\mathrm{j,l}} = \begin{cases} q_{\mathrm{j,l}}, & q_{\mathrm{margSt,l}} \ \epsilon \ C_{\mathrm{margSt}} \\ q_{\mathrm{j,l}} + \frac{q_{\mathrm{AAC,l}} - \delta_{\mathrm{marg}} - q_{\mathrm{margSt,l}}}{\|\Delta \log(\boldsymbol{d}_{m})\|^2} \cdot \Delta \log(d_{m,j}), & q_{\mathrm{margSt,l}} < q_{\mathrm{AAC,l}} - \delta_{\mathrm{marg}} \\ q_{\mathrm{j,l}} + \frac{q_{\mathrm{AAC,l}} + \delta_{\mathrm{marg}} - q_{\mathrm{margSt,l}}}{\|\Delta \log(\boldsymbol{d}_{m})\|^2} \cdot \Delta \log(d_{m,j}), & q_{\mathrm{margSt,l}} < q_{\mathrm{AAC,l}} + \delta_{\mathrm{marg}} \end{cases} \tag{22}$$

3.1.4. Agreement with measurement data

While Eq. (4) requires that the size distribution perfectly describes the measurement data, in reality a measurement error $e_{iU,i\omega}$ can occur at every measurement point $U_{iU},\ \omega_{i\omega}$. If the residuum $r_{iU,i\omega}$, i.e. the deviation between the measurement values and the target vector, has an acceptable deviation $\delta_{\mathrm{measVal}}$, the boundary condition becomes:

$$C_{\mathrm{measVal,iU,i\omega}} = \left\{ \boldsymbol{q} \ \epsilon \ R : \quad |r_{iU,i\omega}| \leq \delta_{\mathrm{measVal}} \right\} \tag{23}$$

Here, the residuum $\boldsymbol{r}$ is defined as follows:

$$\boldsymbol{r} = \boldsymbol{b} - \langle \underline{\boldsymbol{A}} | \boldsymbol{q} \rangle \tag{24}$$

The corresponding projection operators $P_{\mathrm{measVal,i}}$ for any measurement point $U_{iU},\ \omega_{i\omega}$ yields the following result:

$P_{\mathrm{measVal,i}}$:

$$\boldsymbol{q} = \begin{cases} \boldsymbol{q}, & |r_{iU,i\omega}| \leq \delta_{\mathrm{measVal}} \\ \boldsymbol{q} + \frac{r_{iU,i\omega} - \delta_{\mathrm{measVal}}}{\|\underline{\boldsymbol{A}}_{iU,i\omega}\|^2} \cdot \underline{\boldsymbol{A}}_{iU,i\omega}, & r_{iU,i\omega} < -\delta_{\mathrm{measVal}} \\ \boldsymbol{q} + \frac{r_{iU,i\omega} + \delta_{\mathrm{measVal}}}{\|\underline{\boldsymbol{A}}_{iU,i\omega}\|^2} \cdot \underline{\boldsymbol{A}}_{iU,i\omega}, & r_{iU,i\omega} > +\delta_{\mathrm{measVal}} \end{cases} \tag{25}$$

3.1.5. Relation between mobility d_m and Stokes diameter d_{st}

A particle of any shape always experiences a higher drag force than the volume-equivalent sphere:

$$F_D \geq F_{D,vol.eq.sphere} \tag{26}$$

This leads to the inequality:

$$d_m \geq d_v \tag{27}$$

so that for any particle the mobility equivalent diameter is larger than or equal to the volume equivalent diameter. From the force equilibrium over the particle, which leads to the settling velocity w_{s}, the Stokes equivalent diameter d_{st} is defined as (Baron et al., 2011; Rüther et al., 2024):

$$w_{\mathrm{s}} = \frac{\rho \omega^2 r \cdot d_v^3}{18\eta \cdot \frac{1}{Cu(d_m)} \cdot d_m} = \frac{\rho \omega^2 r \cdot d_{St}^2}{18\eta \cdot \frac{1}{Cu(d_m)}} \tag{28}$$

Hence:

$$d_{St} := \sqrt{\frac{d_v^3}{d_m}} \tag{29}$$

Inserting this in Eq. (27) yields the following inequality (DeCarlo et al., 2004):

$$d_m \geq d_{st} \tag{30}$$

Consequently, the boundary condition becomes:

$$C_{\mathrm{d_{st} \leq d_m}} = \left\{ \boldsymbol{q} \ \epsilon \ R : \quad d_{m,j} \geq d_{st,l}; \quad j = 1, \dots, k \wedge l = 1, \dots, o \right\} \tag{31}$$

The projection operator is therefore:

$$P_{\mathrm{d_{st} \leq d_m}} : \ q_{j,l} = \begin{cases} q_{j,l}, & d_{m,j} \geq d_{st,l} \\ 0, & d_{m,j} < d_{st,l} \end{cases} \qquad j = 1, \dots, k \wedge l = 1, \dots, o \tag{32}$$

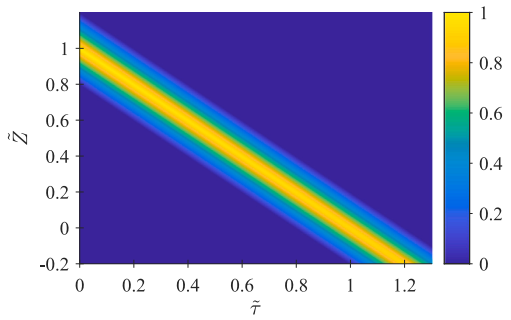

Fig. 1. Two dimensional transfer function for the CDMA prototype properties (c.f. Table 1).

Table 1
Classifying gap properties of the CDMA prototype (Rüther et al., 2024).

Aerosol volume flow	Sheath air volume flow	Inner radius	Outer radius	Length	$2 \cdot \frac{r_{out}-r_{in}}{r_{out}+r_{in}}$	Q_a/Q_{sh}
Q_a in lpm	Q_{sh} in lpm	r_{in} in mm	r_{out} in mm	L in mm	$\tilde{h}$	β
0.3	1.5	70.9	74.3	334	0.0486	0.2

3.2. The ideal kernel matrix

As described in Section 2, the ideal Kernel matrix generally depends on the ideal transfer function $\Omega_{id}(U_{iU}, \omega_{i\omega}, \tilde{\tau}, n \cdot \tilde{Z}, z)$ and the charge distribution $\gamma(d_m, n)$, which is assumed to be known (Wiedensohler, 1988 in case of radioactive sources and Tigges et al., 2015 in case of X-ray sources). Ideal in this context means a CDMA without any secondary effects, like diffusion, losses in the in- and outlet, etc.

The ideal two-dimensional transfer function for the CDMA can be calculated in accordance with the methodology outlined in Rüther et al. (2024) through the utilization of the particle trajectory model. Fig. 1 illustrates the two-dimensional transfer function, wherein $\tilde{\tau}$ represents the normalized particle relaxation time and $\tilde{Z}$ denotes the normalized mobility (see Appendix A). The transfer function presented here describes the probability of classifying particles within a particle collective. The number of classified particles is determined by the double integral of the transfer function weighted by the particle size distribution. Consequently, all particles are classified in proportion to their respective properties. Note that the normalized values for particle mobility $\tilde{Z}$ and relaxation time $\tilde{\tau}$ are used in this analysis. A change in voltage and speed also affects the normalization parameters, resulting in the same normalized transfer function for each voltage and rotational speed.

In order to calculate a Kernel element for a specific two-dimensional size interval, the interval limits $d_{st,\mathrm{up}}$ and $d_{st,\mathrm{low}}$ are employed to calculate the limiting particle relaxation time τ_{up} and τ_{low}, while the interval limits $d_{m,\mathrm{up}}$ and $d_{m,\mathrm{up}}$ are used to calculate the limiting mobilities Z_{up} and Z_{low} (see Appendix A).

The values $d_{St,\mathrm{up}}$, $d_{St,\mathrm{low}}$ and $d_{m,\mathrm{up}}$, $d_{m,\mathrm{low}}$ are the limits of the discretized bins of the sought two dimensional distribution. Combining these limits with the charge distribution[2] $\gamma(d_m, n)$ as well as the transfer function $\Omega_{id}(U_{iU}, \omega_{i\omega}, \tilde{\tau}, n \cdot \tilde{Z}, z)$, the Kernel matrix for each two-dimensional size class is defined as:

$$K_{iU,i\omega,j,l} = \sum_{n=n_{\min}}^{n_{\max}} \frac{\gamma(d_m, n)}{(\tilde{\tau}_{\mathrm{up}} - \tilde{\tau}_{\mathrm{low}})(\tilde{Z}_{\mathrm{up}} - \tilde{Z}_{\mathrm{low}})} \int_{\tilde{\tau}_{\mathrm{low}}}^{\tilde{\tau}_{\mathrm{up}}} \int_{\tilde{Z}_{\mathrm{low}}}^{\tilde{Z}_{\mathrm{up}}} \Omega_{id}(\tilde{\tau}, n \cdot \tilde{Z})\, \mathrm{d}\tilde{Z}\, \mathrm{d}\tilde{\tau} \tag{33}$$

Fig. 2(a) shows an exemplary ideal Kernel matrix at $U = 54.8\,\mathrm{V}$ and $\omega = 12.24\,\mathrm{s}^{-1}$ for the typical dimensions and operating parameters (c.f. Table 1) for the CDMA prototype, built in our lab, which was thoroughly described in Rüther et al. (2024). Considering the boundary condition described in Section 3.1.5, only data for $d_{st} \leq d_m$ is presented here, ensuring that no data appears above the dashed line. Uncharged particles are only influenced by the Stokes diameter. The resulting matrix assigns multiple particle sizes to a given setpoint, yielding a highly ill-posed system of equations. This inverse problem is subsequently addressed using the POCS algorithm.

3.3. The complete kernel matrix

As further losses occur in the measuring device, such as diffusion losses or general particle losses in supply lines and sample lines due to centrifugal or electrical forces, as well as the CPC counting efficiency $\eta_{\mathrm{CPC}}(d_m)$, it is necessary to subject the Kernel matrix to account for these influences.

[2] Here, the charge distribution is assumed to be constant over a size interval.

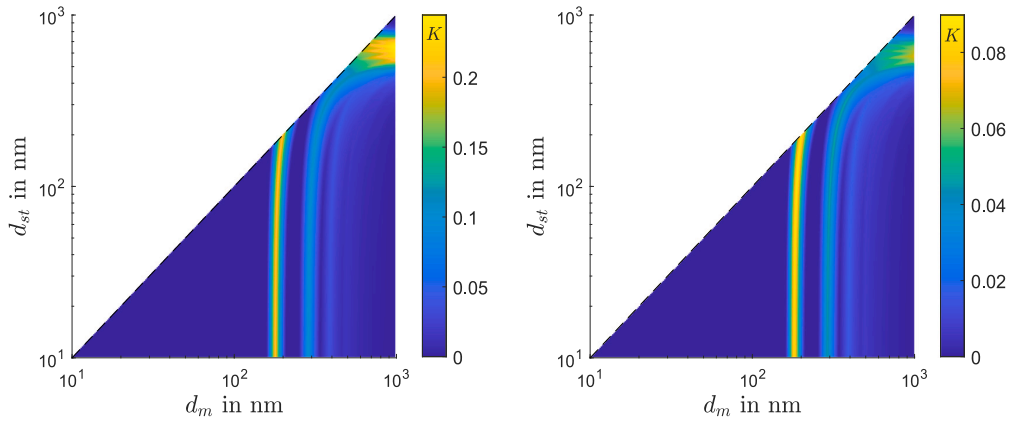

(a) Ideal Kernel matrix (b) Complete Kernel matrix

Fig. 2. Exemplary Kernel matrices, for dimensions of the CDMA prototype and operation parameters (c.f. Table 1) at $U = 54.8\,\mathrm{V}$ and $\omega = 12.24\,\mathrm{s}^{-1}$.

Instead of an ideal transfer function, for example, the analytical transfer function, which takes diffusion losses into account, can be used as an alternative (Rüther, forthcoming2). Furthermore, particle losses resulting from centrifugal and electrical forces, i.e. losses due to undesired electrical and centrifugal fields in the in- and outlet region, can be calculated and thus the transfer function can be corrected accordingly (Rüther et al., 2024). Finally, all other losses can be summarized in a loss term η_V, which was determined experimentally (Rüther et al., 2024). When these aspects are considered, the Kernel matrix results in:

$$K_{iU,i\omega,j,l} = \frac{1}{\eta_V \cdot \eta_{\mathrm{CPC}}(d_m)} \cdot \sum_{n=n_{\min}}^{n_{\max}} \frac{\gamma(d_m,n)}{(\widetilde{\tau}_{\mathrm{up}} - \widetilde{\tau}_{\mathrm{low}})(\widetilde{Z}_{\mathrm{up}} - \widetilde{Z}_{\mathrm{low}})} \int_{\widetilde{\tau}_{\mathrm{low}}}^{\widetilde{\tau}_{\mathrm{up}}} \int_{\widetilde{Z}_{\mathrm{low}}}^{\widetilde{Z}_{\mathrm{up}}} \Omega(\widetilde{\tau}, n \cdot \widetilde{Z}, d_m, d_{st}, U, \omega, z)\, \mathrm{d}\widetilde{Z}\, \mathrm{d}\widetilde{\tau} \tag{34}$$

Fig. 2(b) shows the corresponding complete Kernel matrix. Once again, values above the dashed line are excluded due to the constraint $d_{st} \leq d_m$. The influence of the losses results in a general height reduction to approximately 30% of the original kernel matrix height (compare Figs. 2(a) and 2(b)). Particles with larger Stokes diameters are more dominantly influenced by the centrifugal force, which results in a higher degree of deposition at the sampling outlet.

These losses occurred in this first CDMA prototype due to unforeseen separations in the inlet and outlet regions. These will be significantly reduced in a subsequent prototype.

3.4. Initial condition

To enable the algorithmic calculations, an initial guess concerning the particle sizes must be made. Here, the initial guess assumes that the 2D distribution is a pointwise multiplication of the marginal particle distributions (i.e. the two properties are assumed to be independent as a first guess):

$$\underline{q}_{\mathrm{init}} = \langle \boldsymbol{q}_{marg\,Mob} | \boldsymbol{q}_{marg\,St}{}^{T} \rangle \tag{35}$$

Since additionally the condition $d_{st} \leq d_m$ has to be considered, the values, not satisfying this condition are set to zero to avoid unphysical initial values. Finally, a normalization of the integral to 1 i.e. projection according to Eq. (14) leads to the initial guess.

3.5. Inversion scheme

The mathematical model described this far has been implemented as an algorithmic program, using the software MATLAB. Fig. 3 illustrates the structure of the data-inversion program. Firstly, certain data inputs and calculations must be performed to obtain the required data for the POCS-algorithm. This includes the calculation of the marginal distributions, Kernel matrices and so forth. Subsequently, the POCS-algorithm initiates a verification and recalculation of the conditions outlined in Section 3.1. If the residuum $|\boldsymbol{r}^2|$ converges to a constant value, the iteration is terminated manually. Then, the POCS-algorithm terminates and the back-transformation to the two-dimensional density distribution is completed in accordance with the output of the result.

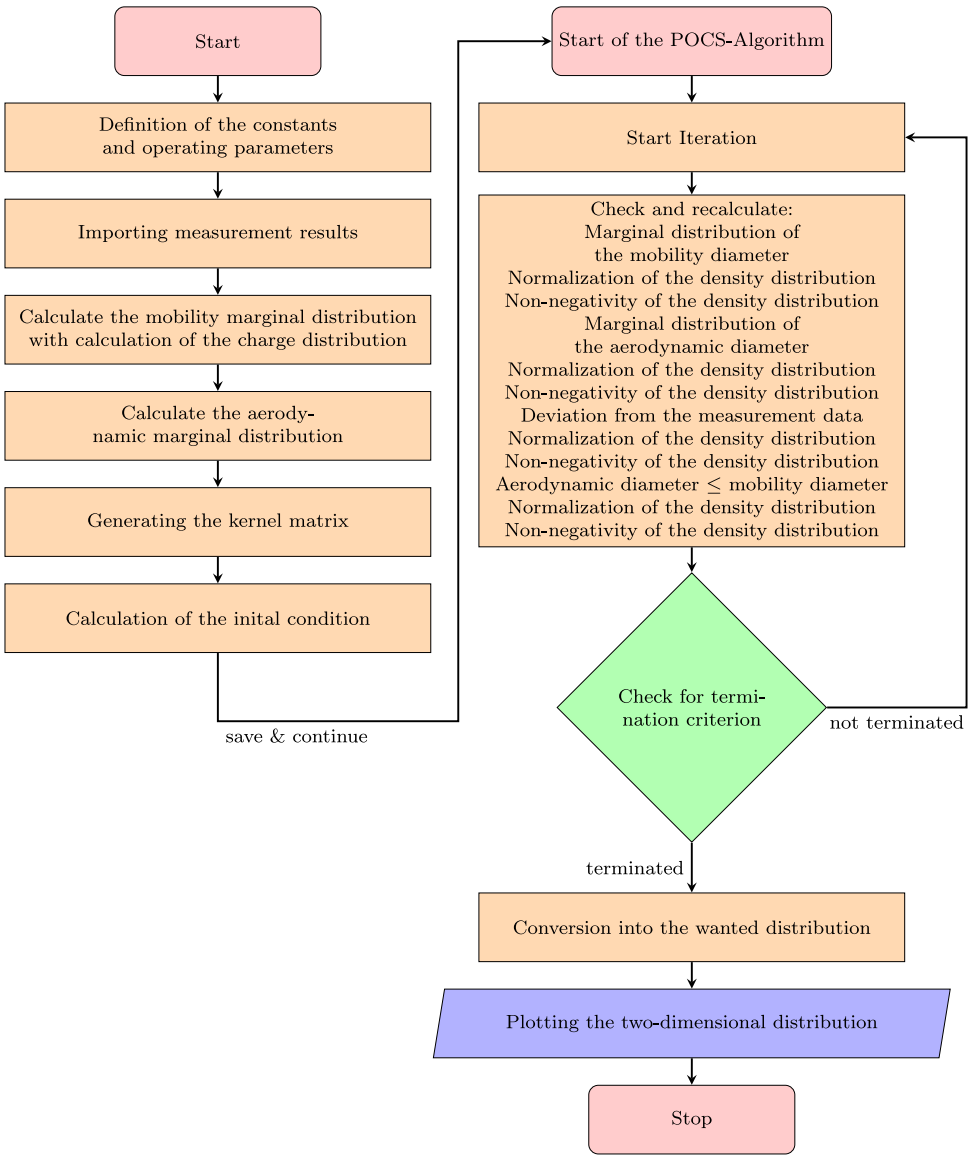

Fig. 3. Flow chart of the data-inversion program.

4. Test of the POCS-algorithm

In this section, the functionality and accuracy of the algorithm are thoroughly examined. Initially, ideal data are used to demonstrate the general functionality of the algorithm, allowing for a clear understanding of its behavior under optimal conditions. For these ideal data, a simulated kernel is employed, which closely resembles the kernel used for inversion (c.f. Section 4.1). Following this, idealized measurement data is corrupted with statistical noise, specifically Poisson noise and Gaussian noise, to simulate real measurement conditions (c.f. Section 4.2). Lastly, the applicability of the algorithm to real measurement data is assessed, demonstrating its practical relevance and effectiveness in handling more complex, noise-affected real-world data sets (c.f. Section 4.3).

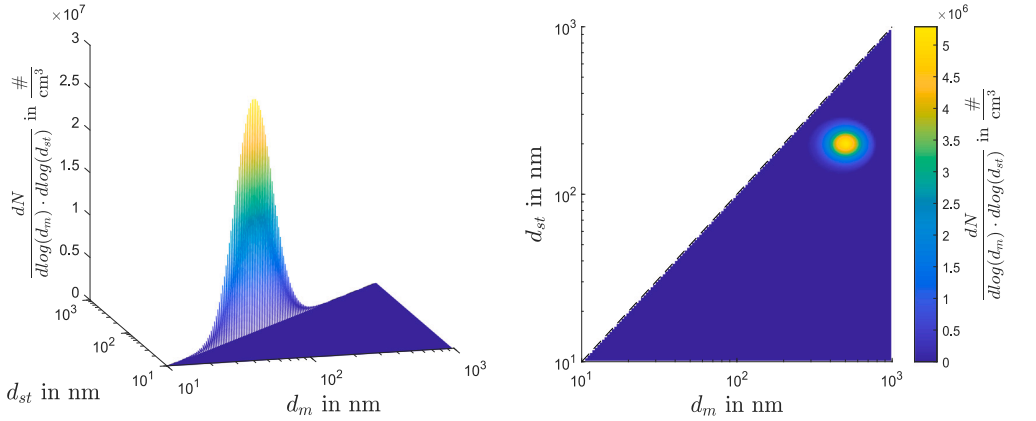

(a) Ensemble of spherical particles with $68\,\mathrm{nm}/\sigma = 30\,\mathrm{nm}$.

(b) Ensemble of particles with $d_m = 500\,\mathrm{nm}/\sigma_m = 100\,\mathrm{nm}$ and $d_{st} = 200\,\mathrm{nm}/\sigma_{st} = 30\,\mathrm{nm}$.

Fig. 4. Assumed ideal two-dimensional distributions for particle ensembles of differently shaped virtual silver particles.

4.1. Performance with ideal data

For validation purposes, two particle size distributions are used to test the data inversion algorithm. As a first test case, an ensemble of perfectly spherical particles is considered with a log-normally distributed particle size distribution and a mean diameter of $\mu = 68\,\mathrm{nm}$ and logarithmic standard deviation $\sigma_l = 0.422$ (c.f. Fig. 4(a)). As second test case an ensemble of complex shaped particles is considered with a 2D-size distribution comprised of two log-normal distributions with regard to the mobility diameter d_m ($\mu_m = 500\,\mathrm{nm}$, $\sigma_{l,m} = 0.198$) and the Stokes diameter d_{st} ($\mu_{st} = 200\,\mathrm{nm}$, $\sigma_{l,st} = 0.149$), respectively (c.f. Fig. 4(b)).

Since silver is the first material under investigation and centrifugal forces play a key role in classification, the density of silver particles ($\rho = 10490\,\mathrm{kg/m^3}$) is assumed in all test cases. This assumption leads to the generation of virtual silver particles with different shapes, specifically spherical particles and large particle agglomerates. For test purposes, the expected measurement signal resulting from an 'ideal' CDMA scan of the respective ensemble is calculated (c.f. Section 4.1.1). Subsequently, the inversion with the POCS algorithm is applied to the simulated measurement data and the resulting 2D particle size distribution compared to the original size distribution (c.f. Sections 4.1.2 and 4.1.3).

4.1.1. Forward calculation

In order to test the performance of the POCS-algorithm, ideal data sets are constructed, in which the target particle properties are prescribed. An imaginary set of approximately a million particles is produced, in such a way that each particle has the three parameters: mobility equivalent diameter (d_m), Stokes equivalent diameter (d_{st}) according to the prescribed size distribution (c.f. Figs. 4(a) and 4(b)) and charge (n) (Wiedensohler, 1988).

For every particle (having a special combination of mobility and Stokes diameter), the particle trajectories are calculated starting from 50 different, homogeneously distributed positions at the aerosol inlet. Here, for calculating the particle trajectory, diffusion and inertia are neglected. Doing this for every operating point of the CDMA (i.e. every combination of voltage U and rotational velocity ω) and counting the successfully traversed particles, results in the vector containing the number of classified particles for each examined operational condition $\boldsymbol{b}_0$. In real measurements, the particle concentration is measured. To get this, a volume flow $\dot{V} = 0.3\,\mathrm{lpm}$ (that is the volume flow of a CPC 3775 from TSI) and a time difference $\Delta t = 100\,\mathrm{s}$ are chosen to calculate the concentration:

$$\boldsymbol{b}_{id} = \frac{\boldsymbol{b}_0}{\dot{V} \cdot \Delta t} \tag{36}$$

The measurement values are lognormally distributed in both directions. To reduce the computational effort, the measuring of voltages and rotational speeds are limited to the relevant ranges. These relevant ranges can be easily determined from a full scan of the marginal distributions and then limiting the operational parameters to the respective interval of interest, i.e. measurement areas where the marginal distributions are already zero are excluded. For future investigations, it would be advantageous to implement this functionality in the software, such that higher voltages and rotational speeds are excluded until a specific threshold – such as 0.1% of the maximum value – is reached in the marginal cases. This consideration is not only important for the time required for calculations but also for the real measurement time, which, under current conditions, could exceed 20 h for a full scan. In particular, when a scanning mode is implemented, this consideration becomes less critical due to the faster measurement times. However, it could still be beneficial for systems with less stable processes, where fast measurement and a good control over the process conditions are crucial.

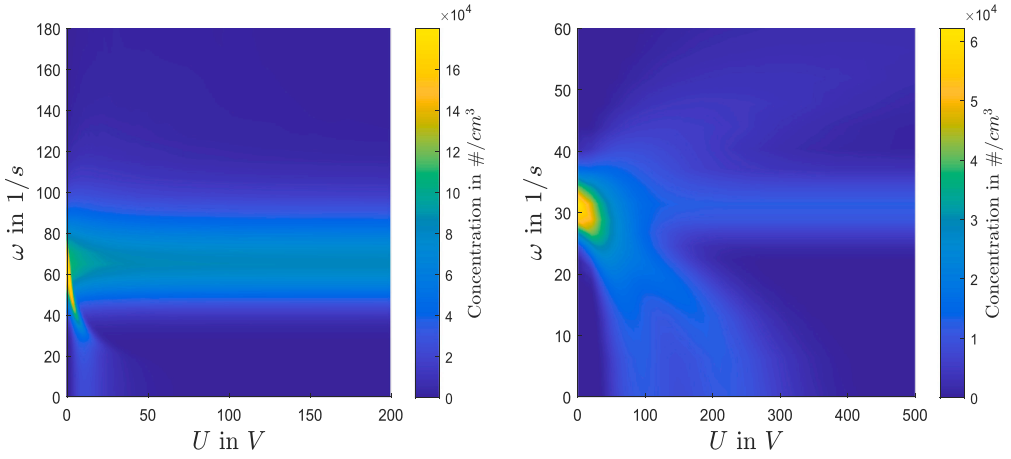

(a) Particle ensemble of figure 4a. (b) Particle ensemble of figure 4b.

Fig. 5. Ideal measurement values for CDMA prototype dimensions for two different particle ensembles.

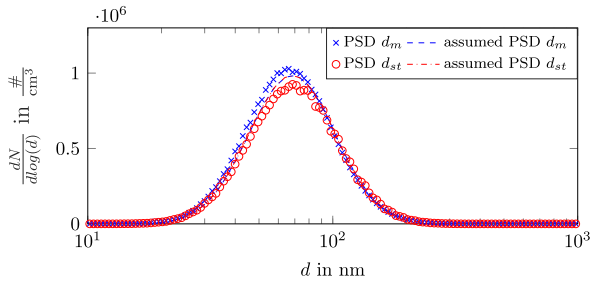

Fig. 6. One-dimensional data inversion of the marginal distributions for the data set of spherical particles.

Therefore, Fig. 5(a) has different range then Fig. 5(b). Hence, for the particle ensemble of spherical particles (Fig. 4(a)), the measurement vector is calculated at 36 different voltages and 31 different rotational velocities (Fig. 5(a)). The particle ensemble of agglomerated silver particles (Fig. 4(b)) has a measurement vector of 33 different voltages and 23 different rotational velocities (Fig. 5(b)). Fig. 5 presents the typical measurement signals for a monomodal aerosol. A distinct peak appears at $U = 0$, while multiple peaks may emerge at $\omega = 0$ due to the presence of multiply charged particles, particularly for larger particle sizes. These additional peaks arise solely as a consequence of multiple charging. Furthermore, non-charged particles are unaffected by the electric field, leading to a particle classification at a specific rotational speed but irrespective of the applied voltage. In contrast, the classification of charged aerosol fractions are strongly influenced by the respective combination of voltage and rotation. Therefore, a particle ensemble will give a characteristic classification pattern for each parameter setpoint.

This data set $\boldsymbol{b}_{id}$ can be achieved from the multiplication of the given ideal distribution with the Kernel matrix, too.[3]

$$\boldsymbol{b}_{id} = \langle \underline{\boldsymbol{A}} | \boldsymbol{q}_{id} \rangle \tag{37}$$

4.1.2. Inversion for an ensemble of spherical particles

Fig. 4(a) depicts the particle distribution, which is the input for the forward calculation. Fig. 6 illustrates the outcomes of common data inversion routines (i.e. for the DMA or AAC) for a one-dimensional particle size distribution, i.e. the inversion of measurement results obtained with the CDMA with $U = 0$ and $\omega = 0$, respectively. It can be demonstrated that the inversion routine for the marginal distribution for pure electric operation and for pure rotation are essentially identical. Only minor discrepancies are observed, which can be attributed to the discretization involved in generating the ideal particle ensemble. As described in Section 4.1.1, the process of generating the ensemble involves discretization at each step, leading to small inaccuracies.

[3] The deviation between the forward calculation and Eq. (37) was ≤0.1%.

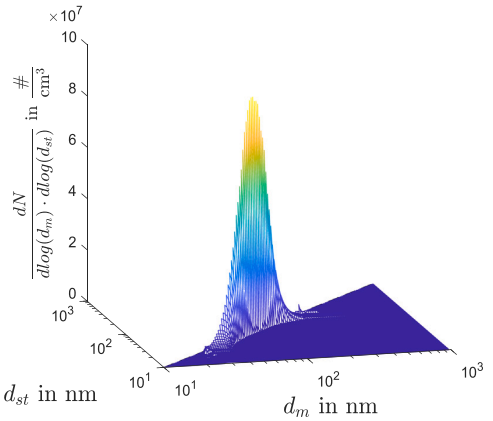

(a) Reconstructed two-dimensional density distribution.

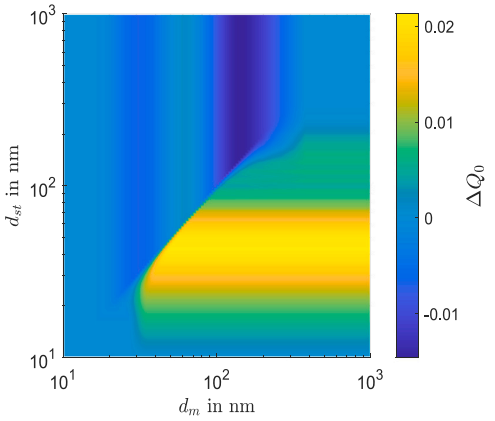

(b) Difference of cumulative distributions ΔQ_0 as obtained from inversion and as specified.

Fig. 7. Results of inversion for simulated measurement data obtained for an ensemble of spherical particles (c.f. Fig. 4(a)).

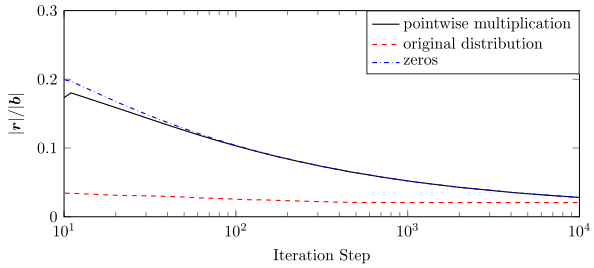

Fig. 8. Convergence of the POCS-Algorithm for different initial conditions.

For the calculation of the two-dimensional distribution, 32×32 geometrically scaled size classes per decade are considered. To start the data inversion, the initial condition of pointwise multiplication, described in chapter 3.4, is prescribed. The result of the POCS algorithm is illustrated in Fig. 7. The position of the resulting two-dimensional distribution (c.f. Fig. 7) agrees very well with that of the distribution originally prescribed in the forward calculation, so that even the modal value is identical (c.f. Fig. 4(a)). The height of the distribution is slightly lower, as the classification of a two-dimensional size distribution is more challenging, particularly for ideal spherical particles, where only the bisecting interval is occupied, i.e. an infinite gradient in normal direction exists for the original two-dimensional size distribution. Consequently, misclassifying a particle in a lower interval significantly reduces the height, especially at high resolutions of the particle size distribution. It should be noted, that we did not apply any artificial smoothing which might lead to a decrease in the peak value as well. This can be seen in the difference of the 2D cumulative distributions shown in Fig. 7(b). Here a pointwise comparison of the cumulative distributions as obtained from POCS $Q_{0,\mathrm{POCS}}$ inversion and as specified in the forward calculation $Q_{0,\mathrm{ForwardCalc}}$ is considered. Which is:

$$\Delta Q_0 = Q_{0,\mathrm{POCS}} - Q_{0,\mathrm{ForwardCalc}} \tag{38}$$

Based on Eq. (10) the cumulative distributions are defined as follows:

$$Q_{0,s,t} = \sum_{j=1}^{s} \sum_{l=1}^{t} q_{j,l} \cdot \Delta \log(d_{m,j}) \cdot \Delta \log(d_{st,l}); \qquad s = 1, \ldots, k \wedge t = 1, \ldots, o \tag{39}$$

It can be seen, that only small differences not exceeding ±2.5% (typically less than ±1%) are occurring.

To ascertain the impact of the initial condition, two further distinct initial conditions are subjected to analysis. For this second initial condition, no knowledge of the marginal distribution is assumed, hence all elements of the initial particle size distribution are set to zero. The third initial condition is to utilize the correct solution for the particle size distribution as the initial condition. Of course, this is only possible for the theoretical test cases and no option for the inversion of real measurement data. Fig. 8 illustrates the convergence of the various initial conditions. It becomes obvious that for all initial conditions the results are converging but have not reached their final value already, even after 10^4 iterations. The initial conditions of point-wise multiplication and the array

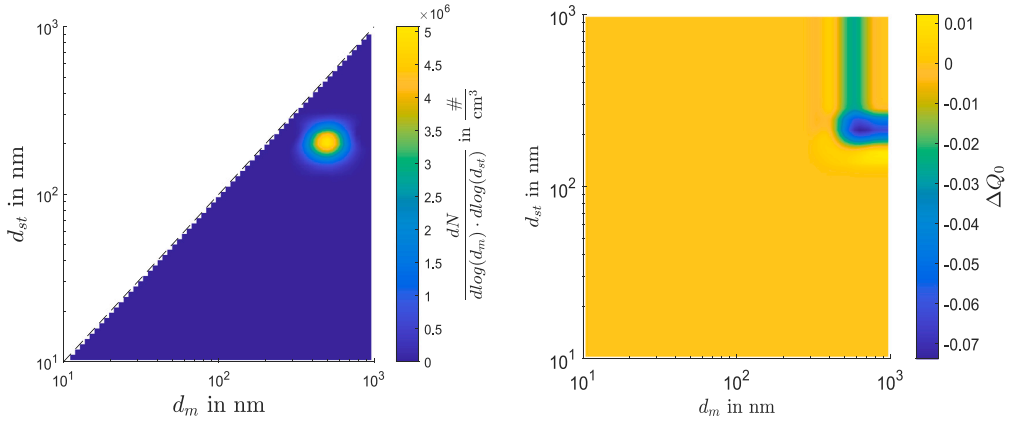

(a) Reconstructed two-dimensional density distribution.

(b) Difference of cumulative distributions ΔQ_0 as obtained from inversion and as specified.

Fig. 9. Results of inversion for simulated measurement data obtained for an ensemble of non-spherical particles (c.f. Fig. 4(b)).

of zeros exhibit a comparable progression in convergence, except for the first 100 iteration steps. A comparison of the differences of the cumulative distribution from the original distribution ΔQ_0 shows a similar error in all cases (for quantitative comparisons the respective figures are included in the Appendix B). However, if the correct solution is used in the first iteration step the deviation is slightly smaller. Nevertheless, increasing the number of iteration steps further (100.000 instead of 10.000) leads to a similar result even if the standard initial condition (product of marginal distributions) is used. This emphasizes that even though the solution shows already good agreement after 10^4 iterations, for full convergence even higher numbers of 10^5 iterations are advisable.

4.1.3. Inversion for an ensemble of non-spherical particles

To test the algorithm for non-spherical particles, a collective of particles with a mean mobility diameter of 500 nm and a mean Stokes diameter of 200 nm is considered. A comparison between the given particle size distribution (Fig. 4(b)) and the reconstructed distribution (Fig. 9(a)) reveals that, as in the previous section, the position is identical and the height is 3.1% smaller. Furthermore, the marginal distributions show a good agreement to the original data (cf. Fig. B.19(b)), too.

Comparing the difference in the cumulative distribution (c.f. Fig. 9(b)) it appears that the maximum difference is twice as high (i.e. less than 6% at any point) as for the spherical particles, but also in a good agreement to the original data.

4.2. Performance with ideal data superimposed with statistical errors

To assess the efficacy of the algorithm in a realistic setting, ideal data (c.f. Section 4.1) is used as a baseline onto which noise is superimposed. In this study, a combination of the Poisson and Gaussian noise approaches is employed.

The number of particles in a given volume can be described by a Poisson distribution (Raasch & Umhauer, 1984). For particle numbers exceeding 30, the Poisson distribution can be approximated by a normal distribution (Papula, 2011). In a Poisson distribution, the variance of the number of particles σ_0^2 is equal to the expected value μ_0. As the number concentrations $\boldsymbol{N}$ are typically quantified in a CPC, the number of particles is given by the concentration multiplied with the volume flow $\dot{V}$ and measurement time Δt. Hence:

$$\boldsymbol{\sigma}_0^2 = \boldsymbol{\mu}_0 = \boldsymbol{N} \cdot \dot{V} \cdot \Delta t \tag{40}$$

The following therefore applies to the expected values:

$$\boldsymbol{\mu}_N = \frac{\boldsymbol{\mu}_0}{\dot{V} \cdot \Delta t} \tag{41}$$

And therefore for the variances:

$$\boldsymbol{\sigma}_N^2 = \frac{\boldsymbol{\sigma}_0^2}{(\dot{V} \cdot \Delta t)^2} \tag{42}$$

Inserting this relation into Eq. (40) yields:

$$\boldsymbol{\sigma}_N = \sqrt{\frac{\boldsymbol{N}}{\dot{V} \cdot \Delta t}} \tag{43}$$

Using the values from Section 4.1.1 (i.e. $\dot{V} = 0.3$ lpm and $\Delta t = 1$ s) gives direct access to the variance for every measured value.

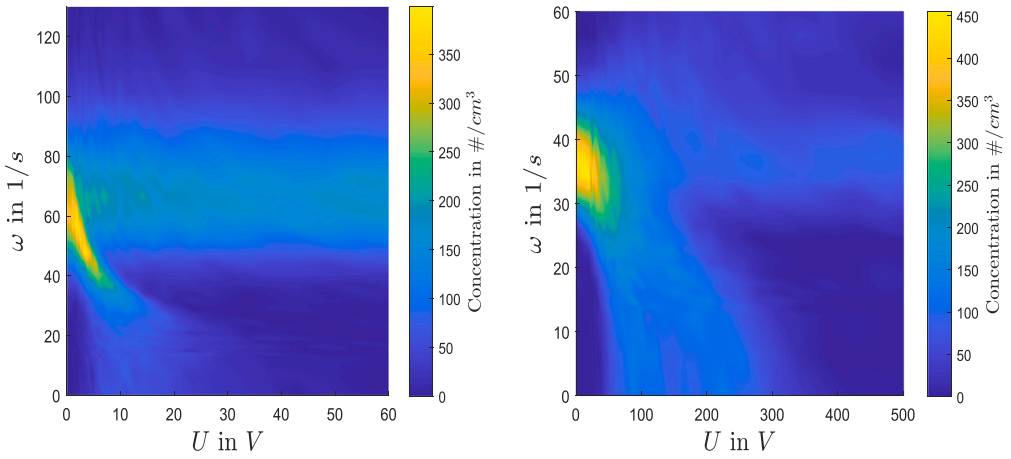

(a) Spherical particle ensemble (c.f. 4a). (b) Non-spherical particle ensemble (c.f. 4b).

Fig. 10. Ideal noise-laden measurement values for CDMA-prototype dimensions for the two different particle collectives.

In order to get reasonable total measuring times, for each measurement point a measurement duration of just 1 s is assumed (c.f. Figs. 5 and 10). Such a short measurement time can be considered to represent an upper limit to the Poisson noise resulting from counting statistics.

In addition to the Poisson noise, some Gaussian noise is superimposed. For this a relative Gaussian noise which should describe relative measurement errors like fluctuations in the aerosol, are assumed with about 5% from the respective measurement value.

$$\boldsymbol{\sigma}_{\text{Gauss,rel}} = \boldsymbol{N} \cdot 5\% \tag{44}$$

Moreover, an absolute Gaussian noise is added, to describe errors which are based on fluctuations in the setup, like the false count rate of the CPC. The absolute Gaussian noise is assumed to be 1% of the maximum measurement value.

$$\sigma_{\text{Gauss,abs}} = \max(\boldsymbol{N}) \cdot 1\% \tag{45}$$

Since all three types of error may be assumed to be independent, the variances can be amalgamated as follows (Papula, 2011):

$$\boldsymbol{\sigma}^2_{\text{tot}} = \boldsymbol{\sigma}^2_{N} + \boldsymbol{\sigma}^2_{\text{Gauss,rel}} + \sigma^2_{\text{Gauss,abs}} \tag{46}$$

Accounting for the physical condition of non-negative concentrations, the measured particle concentration $\boldsymbol{N}$, affected by noise, results in the noise-laden concentration $\boldsymbol{N}_{\text{noise}}$:

$$\boldsymbol{N}_{\text{noise}} = \begin{cases} \boldsymbol{N} + \boldsymbol{R}, & \boldsymbol{N} + \boldsymbol{R} > 0 \\ 0, & \boldsymbol{N} + \boldsymbol{R} \leq 0 \end{cases} \tag{47}$$

Because for large concentrations, the Poisson distribution can be described by a Gaussian distribution, $\boldsymbol{R}$ is a vector of normal distributed random numbers with an expected value $\mu = 0$ and variance $\boldsymbol{\sigma}^2_{\text{tot}}$. Fig. 10 shows the constructed noise-laden measurement data sets, which are used to test run the algorithm of Section 3 again. The noise added here is clearly visible and is assumed to rather exceed errors found in typical real-world measurements. However, it should be noted that the noise is smoothed by the interpolation of the values upon visualization.

4.2.1. *Noise-laden measurement data for an ensemble of spherical particles*

Fig. 10(a) shows the used ideal measurement data superimposed with statistic noise. When using this measurement signal as input for the POCS-algorithm, the data inversion leads to the result represented in Fig. 11(a). This result is significantly more unsteady, which may be caused by the marginal distribution being also significantly more affected by errors (Fig. B.20(a)). Even more iterations (here again 10^4 iterations were used) will not lead to further improvements. Nevertheless, the position of the distribution remains identical to the initial distribution. The height is also 10.8% lower, but this is again due to the minimal broadening of the distribution in normal direction, resulting in considerable changes in the total height. This can be seen in the difference of the sum distributions in Fig. 11(b). The differences are significantly higher as in the ideal case, but still always lower than ±5% despite the high amount of superimposed statistical noise.

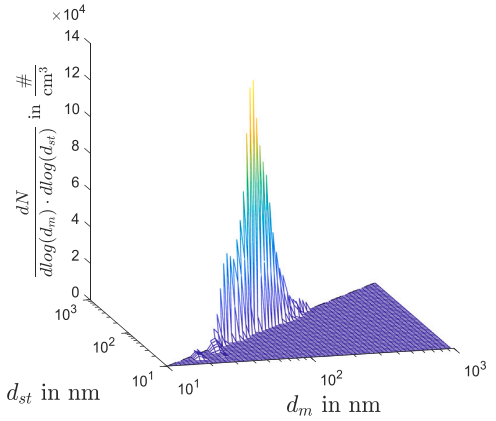

(a) Reconstructed two-dimensional density distribution.

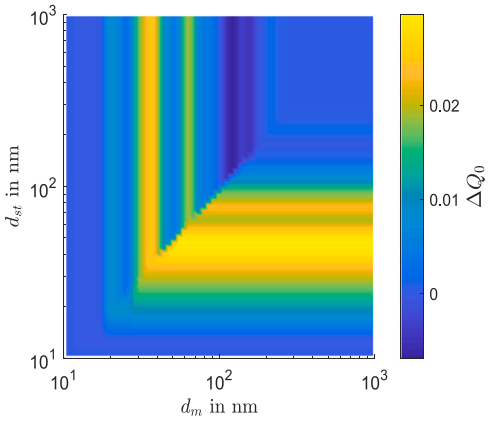

(b) Difference of cumulative distributions ΔQ_0 as obtained from inversion and as specified.

Fig. 11. Results of inversion for noise-laden simulated measurement data obtained for an ensemble of spherical particles (c.f. Figs. 4(a) and 10(a)).

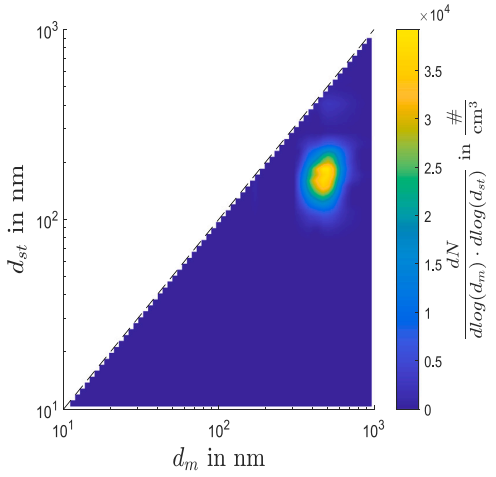

(a) Reconstructed two-dimensional density distribution.

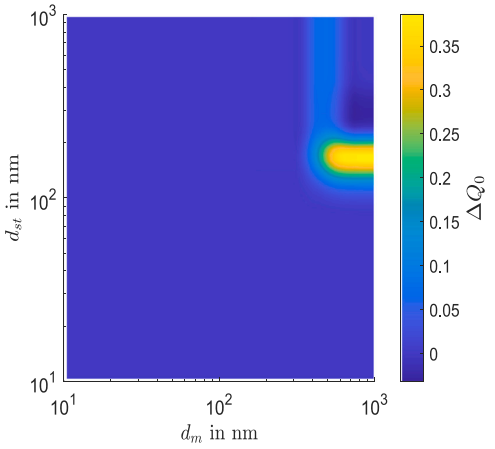

(b) Difference of cumulative distributions ΔQ_0 as obtained from inversion and as specified.

Fig. 12. Results of inversion for noise-laden simulated measurement data obtained for an ensemble of non-spherical particles (c.f. Figs. 4(b) and 10(b)).

4.2.2. Noise-laden measurement data for an ensemble of non-spherical particles

The solution obtained through the POCS-algorithm from the contaminated measurement data (c.f. Fig. 10(b)) as input is illustrated in Fig. 12(a). Both marginal distributions are adequately mapped (c.f. Fig. B.20(b)). Furthermore, the marginal distributions are also depicted with remarkable clarity. The absolute error in the cumulative distribution in case of noise acting on the measurement signal is only slightly larger compared to the case without noise (c.f. Figs. 9(b) and 12(b)). However, it is to be expected that the result would be significantly inferior with a smaller number of measuring points. Overall, it can be demonstrated that the algorithm inverts the measurement data with remarkable stability and precision, even when strong disturbances act on the measurement signal.

4.3. Application to real measurement data

The applicability of the algorithm to real measurement data is evaluated using measurement data from various experiments. As it is only possible to check the accuracy to a limited extent, sine the real distribution is not known anymore, the plausibility of the resulting distributions is checked and analyzed using comparative measurements.

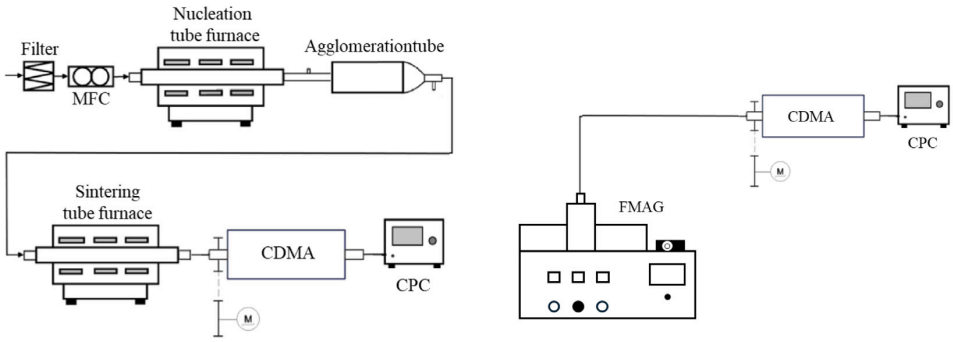

(a) Measurement setup for silver nanoparticles. (b) Measurment setup for DEHS droplets.

Fig. 13. Schematic of the measurement setups for measuring spherical/agglomerated silver and DEHS (Di-Ethyl-Hexyl-Sebacat) particles.

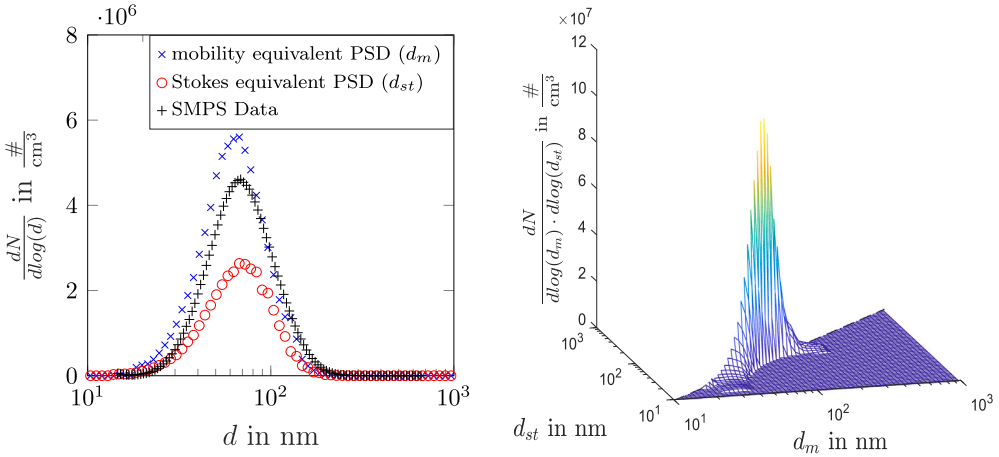

(a) One-dimensional data inversion. (b) Two-dimensional data inversion.

Fig. 14. Results of the data inversion for the measurement of spherical silver particles.

4.3.1. Measurement setups

Fig. 13 presents a schematic representation of the experimental setup used for measuring the particle size distributions of silver and DEHS (Di-Ethyl-Hexyl-Sebacate) aerosols. The silver aerosol is generated by placing solid silver in a nucleation tube furnace, which is heated to 1150 °C. A controlled airflow, regulated by a mass flow controller (MFC), transports air saturated with silver vapor from the tube furnace to a cooling region, where the supersaturation leads to the nucleation of silver nanoparticles. The aerosol subsequently passes through an agglomeration tube ($V = 10\,\mathrm{l}$), promoting the formation of silver agglomerates. To obtain spherical silver particles, a second tube furnace is maintained at 750 °C, facilitating the sintering process and yielding rounded particles.

For the generation of a DEHS aerosol, a flow focusing aerosol generator (TSI FMAG 1520) is employed. This device produces droplets with a highly monodisperse size distribution.

Prior to measurement, the aerosol is passed through a krypton-85 source to establish a well-defined charge distribution on the particles. The particles are subsequently classified in a centrifugal differential mobility analyzer (CDMA) according to their aerodynamic and mobility diameters. The sheath air flow rate is set to $Q_{sh} = 1.5\,\mathrm{l/min}$, while the aerosol flow rate is maintained at $Q_a = 0.3\,\mathrm{l/min}$.

Finally, the classified aerosol is analyzed by counting particles for each combination of applied voltage and rotational speed. The resulting data are processed using an inversion algorithm, as described in Sections 3.3 and 3.5 to determine the particle size distribution.

4.3.2. Measurement of spherical silver particles

Almost spherical silver particles were used as a first test-aerosol. A comparison between the one-dimensional data inversion routines on the CDMA measurement of marginal distributions and standard DMA measurement (SMPS Data) reveals a notable

Table 2
Characteristic values for the one-dimensional data inversion routines for measurements of spherical silver particles.

Inversion routine	Mode in nm	d_g in nm	σ_g	max $\left[\frac{dN}{dlog(d)}\right]$ in $10^6 \frac{\#}{cm^3}$
CDMA, $\omega = 0$	67.32	61.62	1.519	5.60
CDMA, $U = 0$	67.32	64.59	1.533	2.64
SMPS	68.50	68.24	1.507	4.61

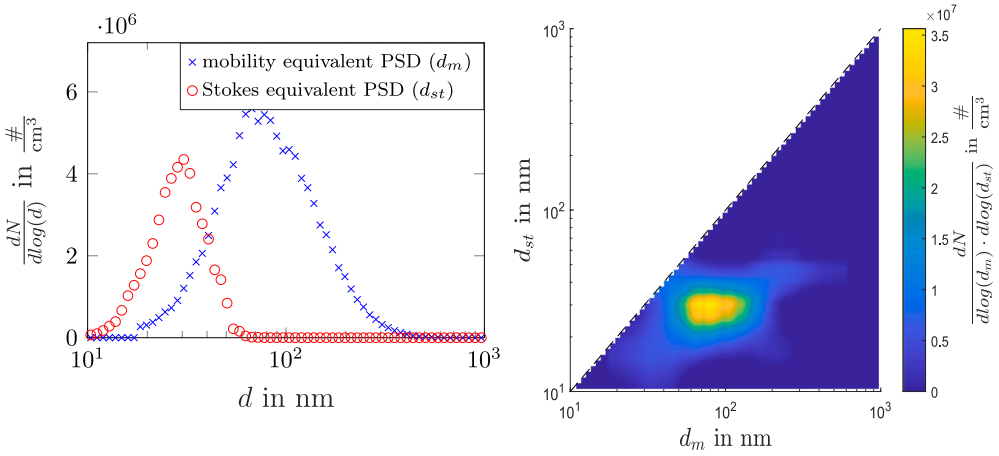

(a) One-dimensional data inversion. (b) Two-dimensional data inversion.

Fig. 15. Results of the data inversion for the measurement of agglomerated silver particles.

discrepancy. Table 2 shows characteristic values of the different size distributions. It can be seen that the modal values are in a quite good agreement, while the geometric mean diameter d_g differs slightly, which is due to the slight asymmetry of the distribution for the CDMA measurements (c.f. 14(a)). Nevertheless, the geometric standard deviation again only has minor deviations. Only the heights of the marginal distributions obtained from the CDMA differ significantly, to the SMPS results. This is likely a result from over- and underestimation of the loss coefficients upon determination of the Kernel function, particularly for losses due to rotation (Rüther et al., 2024). Due to the generally high particle losses and the substantial correction factors required, it is not possible to determine an exact cause of this discrepancy. However, future investigations using a new prototype with an improved design should allow for a more accurate analysis. Nevertheless, the POCS-algorithm provides a two-dimensional size distribution that indicates very spherical particles and possesses the expected modal value (Fig. 14(b)).

4.3.3. Measurement of agglomerated silver particles

The subsequent stage of the process involved the removal of the sintering process (Rüther et al., 2024), thus allowing for the measurement of agglomerated silver particles. This revealed unequivocally disparate equivalent diameters, as depicted in the marginal distributions (cf. Fig. 15(a)). However, since we have no access to a proper reference measurement method it is unclear whether the actual particle size distribution corresponds exactly to the calculated one (c.f. Fig. 15(b)).

4.3.4. Round DEHS-particles

The final stage of the present study was the generation of a monodisperse aerosol from DEHS (Di-Ethyl-Hexyl-Sebacat). A flow-focusing monodisperse aerosol generator (TSI FMAG 1520) was employed. The FMAG can generate particles within a very narrow size interval. DEHS was chosen because of its property to form near-perfect spherical particles with monodisperse particle sizes. In the experiment, the FMAG generates DEHS droplets with the settings to produce mean diameters between 800–1000 nm. The one-dimensional back-calculation routines depicted in Fig. 16(a) demonstrate that the particles produced exceed the measurement range of the instrument. Regarding the mobility diameter, the presence of particles larger than 1000 nm appears to be a reasonable assumption, given the observation of a multiple charge peak. The application of the POCS-algorithm to the aforementioned measurement data yielded the results depicted in Fig. 16(b). As with the previous data set, the particles are at the upper limit of the measurement range. However, the initial gradient of the curve is higher, indicating a highly monodisperse aerosol. Furthermore, the distribution lies precisely on the bisector between Stokes equivalent diameter and mobility diameter, suggesting that the particles are highly spherical. This was confirmed even at significantly higher resolutions of up to 128×128 size classes per decade.

Since the measurements presented here lie at the edge of the instrument's detection range, they are subject to increased uncertainty. This particularly affects the multiple charge correction, but also influences the overall recalculation. Nevertheless, the

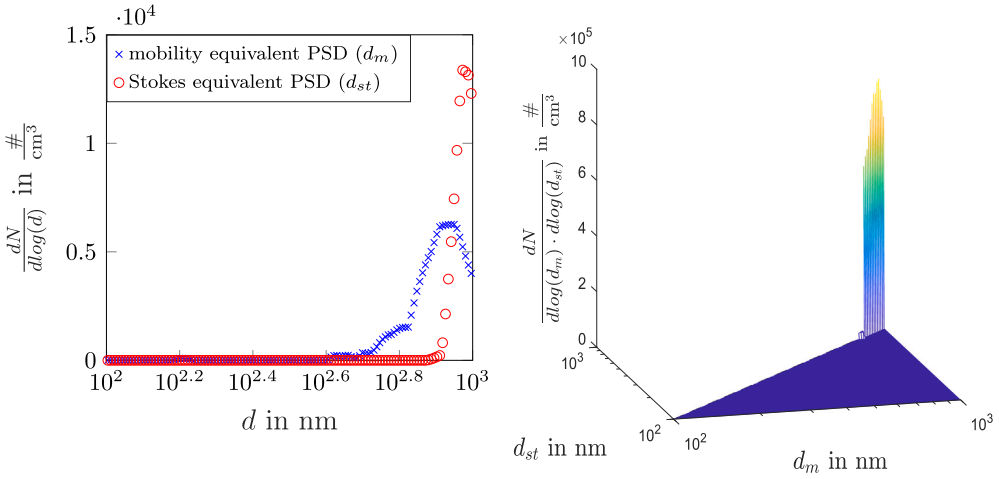

(a) One-dimensional data inversion. (b) Two-dimensional data inversion.

Fig. 16. Results of the data inversion for the measurement DEHS-particles produced with an FMAG.

inversion demonstrates that the algorithm yields consistent results, even when applied to a material other than silver and under boundary conditions of the measurement range—i.e., maintaining spherical parity within the correct size range.

4.4. Stability of the POCS algorithm when solving for other disperse properties

In the preceding data inversion algorithm, the back calculation to the two-dimensional distribution was always considered with regard to the Stokes and the mobility diameter. However, since the relationship between mobility and volume equivalent diameter is often necessary, particularly for deriving information on particle shape, it should also be possible to determine the two-dimensional distribution $q(d_v, d_m)$ with respect to volume equivalent diameter d_v and mobility diameter d_m.

On the one hand, this can be calculated using the two-dimensional distribution $q(d_m, d_{st})$ obtained from inversion as discussed above and using the relation (c.f. Eq. (A.3)):

$$d_v = \sqrt[3]{d_{st}^2 \cdot d_m} \tag{48}$$

Since the Stokes diameter d_{st} and mobility diameter d_m are known at any point, the volume equivalent diameter d_v can be calculated for each combination of the two-dimensional density distribution. If the classes for the volume equivalent diameter are chosen like the classes for d_m and d_{st}, the number of particles which belongs to the respective class must be re-assigned. This leads to data losses, especially if large size intervals are used.

Therefore, it could be beneficial, to alternatively perform the data inversion to the desired properties d_m and d_v in order to directly obtain the two-dimensional distribution $q(d_v, d_m)$. In this case however, the projection operator for the marginal distribution from the AAC-Mode $P_{\text{margSt,l}}$ is not valid anymore and cannot be used.

Fig. 17(a) shows the difference in the sum distributions ΔQ_0 for using the 'standard' algorithm and a conversion afterwards compared to the direct inversion to the d_m/d_v-distribution for the ideal data given from Fig. 4(a). It can be seen that there are differences of about 10%. This is because misclassifying into a neighbored class leads directly to a difference. Since for the round ideal particles, the distribution is very narrow the likelihood for misclassified particles is very high.

Fig. 17(b) further shows the difference of the sum distributions for real measurements of spherical silver nanoparticles. Here, the difference is much smaller. This is, because the distribution calculated of the real measurement data is a bit broader. This shows, that especially for very narrow distributions, it is sensible to address the equivalent diameters of interest directly upon inversion.

5. Conclusions and outlook

In summary, the here presented POCS algorithm has the potential to perform data inversion for CDMA measurements and to be applied to further applications in data inversion. Both, ideal data with and without noise as well as the application to real measurements showed very good results, especially concerning the position of the mode and the spread of the distribution. The algorithm demonstrates a high degree of robustness, even in the presence of substantial noise. However, as this assessment was limited to a single Gaussian noise scenario, a systematic investigation into the correlation between noise level and reconstruction quality would be a valuable subject for future studies.

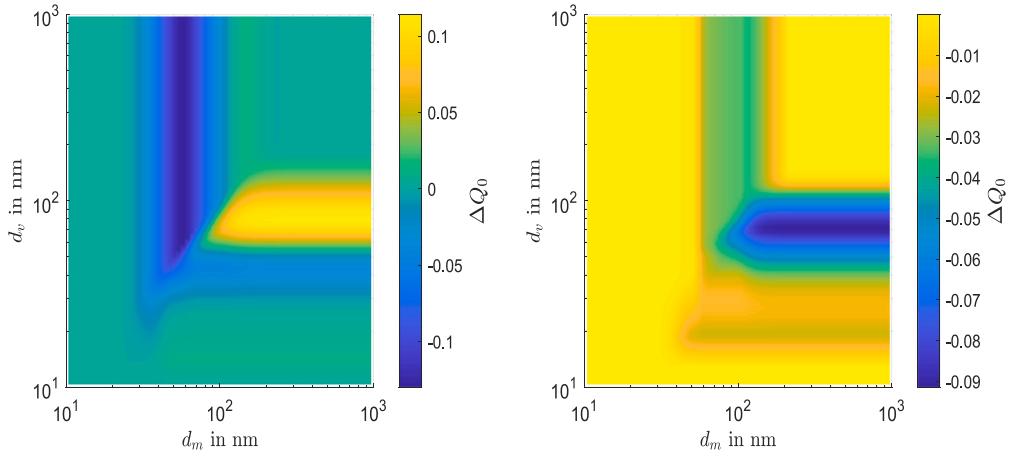

(a) Ideal particle collective of spherical particles with a mean diameter of 68 nm (c.f. figure 4a).

(b) Real measurement data of round silver particles.

Fig. 17. Difference of the sum distribution, from solving to d_m/d_{st} and conversion to the d_m/d_v distribution compared to directly solving to d_m/d_v distribution.

However, there is still some room for improvement. For example the influence of the tolerated error margins in case of soft-linear boundary conditions could be investigated in detail. So far the have to be adjusted manually as they depend on the number of measurement points and the resolution of the distribution. However an automatic or parameterized determination of these error margins would be superior, like it is done for other inversion methods (Sipkens et al., 2020b).

Also, a valid termination criterion for the iteration must be defined in order to ensure a fully converged solution at any time. In addition, data inversion of bimodal distributions is currently problematic, as the algorithm falsely creates additional spurious modes. This can be improved by additionally using a Faraday Cup Electrometer, which will provide further data helping to increase the available information and therefore increasing accuracy when complex 2D distributions are analyzed. In future research, the algorithm presented in this study should be systematically compared with existing data inversion methods, following the approach of previous work by Sipkens et al. (2020a), in which various inversion routines were evaluated. Such a comparison should be conducted under standardized conditions using identical datasets to enable a meaningful and objective assessment of performance. By analyzing key performance metrics such as accuracy, convergence behavior, and computational efficiency, a clearer understanding of the strengths and limitations of the POCS algorithm in relation to established methods can be achieved. Building upon these findings, the most suitable algorithm for the data inversion of a CDMA system can then be identified, ensuring optimal reconstruction accuracy and methodological robustness. This step would provide valuable guidance for future applications and contribute to the refinement of inversion techniques in this field.

CRediT authorship contribution statement

Torben N. Rüther: Writing – original draft, Visualization, Validation, Software, Resources, Formal analysis, Data curation, Conceptualization. **David B. Rasche:** Writing – original draft, Visualization, Validation, Software, Resources, Methodology, Investigation, Funding acquisition, Formal analysis, Data curation, Conceptualization. **Hans-Joachim Schmid:** Writing – review & editing, Visualization, Validation, Supervision, Resources, Project administration, Methodology, Investigation, Funding acquisition, Conceptualization.

Declaration of competing interest

The authors declare that they have no known competing financial interests or personal relationships that could have appeared to influence the work reported in this paper.

Acknowledgments

This research has been supported by the Deutsche Forschungsgemeinschaft (grant no. SPP2045).

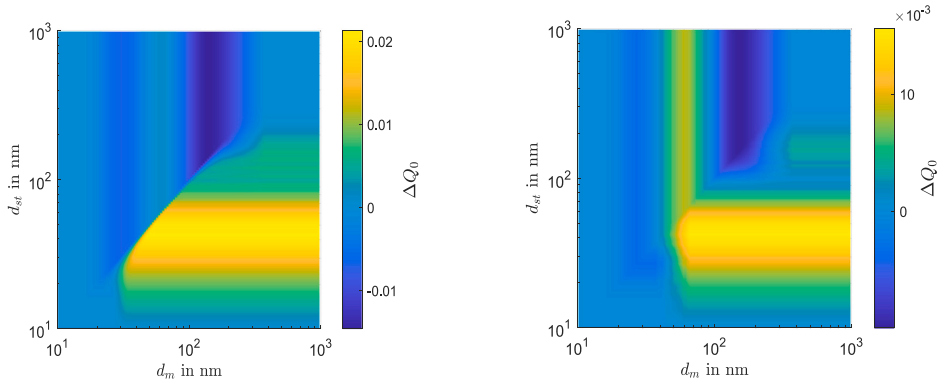

(a) Initial Condition: Array of zeros. (b) Initial Condition: Correct particle size distribution

Fig. B.18. Calculated results of the POCS-algorithm for round silver particles with a mean diameter at 68 nm for different initial conditions.

Appendix A. Calculation of the normalized mobility and particle relaxation time and the interval limits

In order to normalize τ and Z, the mean paths, τ^* and Z^*, are employed. These variables are solely contingent upon the underlying geometry and volume flows (c.f. Table 1).

$$Z^* = \frac{Q_{sh}}{2 \cdot \pi LU} \cdot \ln\left(\frac{r_{\text{out}}}{r_{\text{in}}}\right) \tag{A.1}$$

$$\tau^* = \frac{2 \cdot Q_{sh}}{\pi\omega^2(r_{\text{in}} + r_{\text{out}})^2 L} \tag{A.2}$$

The calculation of the interval limits can be achieved by entering the specified interval limits of the designated particle size class into either Eq. (A.4) or Eq. (A.3), as applicable.

$$\tau = \frac{\rho \cdot d_v^3 \cdot Cu(d_m)}{18\eta d_m} = \frac{\rho \cdot d_{st}^2 \cdot Cu(d_m)}{18\eta} \tag{A.3}$$

$$Z = \frac{Q_P \cdot Cu(d_m)}{3\pi \cdot \eta \cdot d_m} \tag{A.4}$$

Subsequently, the resulting interval limit is divided by the mean values (A.5), thereby yielding $\widetilde{\tau}_{\text{low}}$, $\widetilde{\tau}_{\text{up}}$, $\widetilde{Z}_{\text{low}}$ or $\widetilde{Z}_{\text{up}}$.

$$\widetilde{Z} = Z/Z^* \quad ; \quad \widetilde{\tau} = \tau/\tau^* \tag{A.5}$$

For further information see Rüther et al. (2024).

Appendix B. Additional results of the POCS-algorithm using ideal data

See Figs. B.18–B.20.

Data availability

https://git.uni-paderborn.de/pvt/cdma.

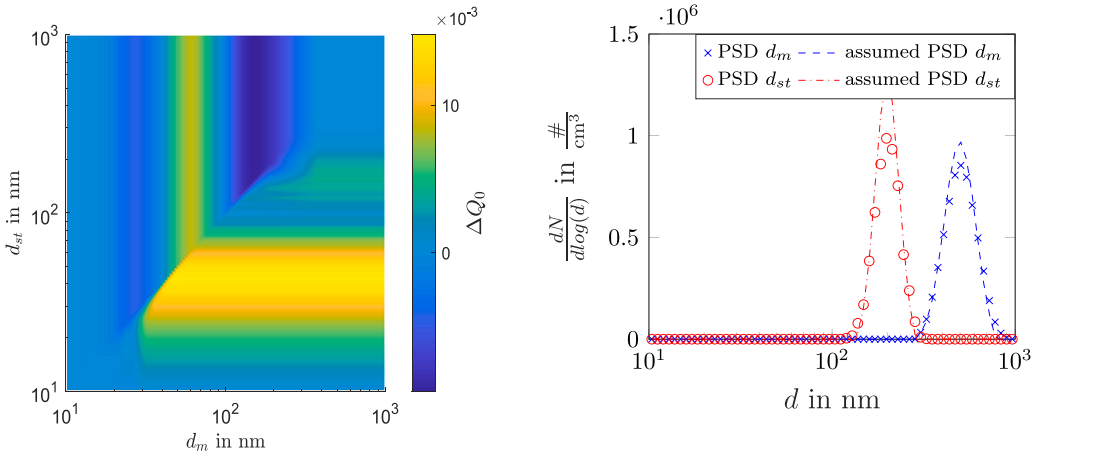

(a) Calculated results for round silver particles after 100,000 iterations of the POCS-algorithm.

(b) Results of one-dimensional data inversion with a mean mobility diameter of 500 nm and mean Stokes equivalent diameter of 200 nm.

Fig. B.19. Two-dimensional PSD for 100,000 iterations of the POCS-algorithm and one-dimensional data inversion results.

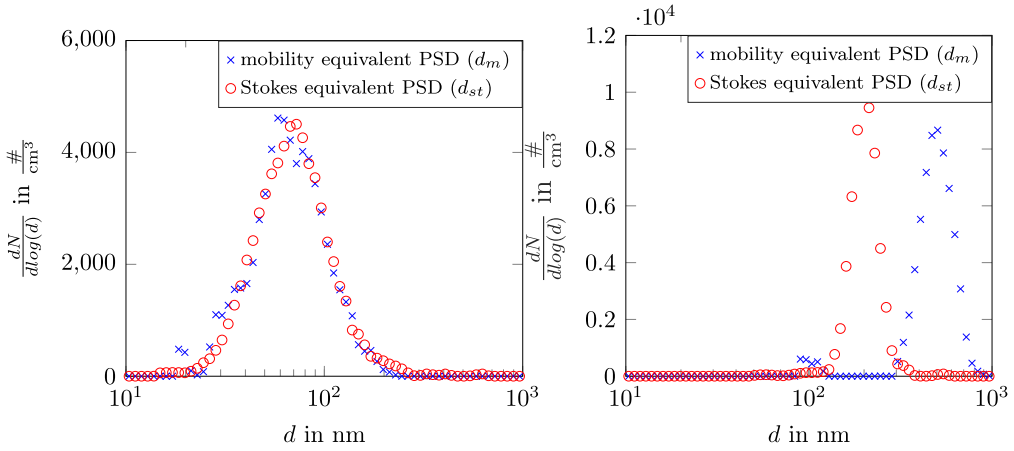

(a) Particle collective of 4b.

(b) Particle collective of 4a.

Fig. B.20. Results of the common one-dimensional inversion schemes for different constructed noise-laden measurement signals.

References

Adler, J., & Öktem, O. (2017). Solving ill-posed inverse problems using iterative deep neural networks. *Inverse Problems*, *33*(12), Article 124007. http://dx.doi.org/10.1088/1361-6420/aa9581.

Baron, P. A., Kulkarni, P., & Willeke, K. (2011). *Aerosol measurement: Principles, techniques, and applications* (3rd ed.). Hoboken N.J.: Wiley.

Broda, K. N., Olfert, J. S., Irwin, M., Schill, G. P., McMeeking, G. R., Schnitzler, E. G., & Jäger, W. (2018). A novel inversion method to determine the mass distribution of non-refractory coatings on refractory black carbon using a centrifugal particle mass analyzer and single particle soot photometer. *Aerosol Science and Technology*, *52*(5), 567–578. http://dx.doi.org/10.1080/02786826.2018.1433812.

Buckley, D. T., Kimoto, S., Lee, M.-H., Fukushima, N., & Hogan, C. J. (2017). Technical note: A corrected two dimensional data inversion routine for tandem mobility-mass measurements. *Journal of Aerosol Science*, *114*, 157–168. http://dx.doi.org/10.1016/j.jaerosci.2017.09.012.

Chen, X., Ghosh, S., Buckley, D. T., Mohan Sankaran, R., & Hogan, C. J. (2018). Characterization of the state of nanoparticle aggregation in non-equilibrium plasma synthesis systems. *Journal of Physics D (Applied Physics)*, *51*(33), Article 335203. http://dx.doi.org/10.1088/1361-6463/aad26f.

Colbeck, I. (2013). *Aerosol science: Technology and applications* (2. ed.). Hoboken: Wiley.

DeCarlo, P. F., Slowik, J. G., Worsnop, D. R., Davidovits, P., & Jimenez, J. L. (2004). Particle morphology and density characterization by combined mobility and aerodynamic diameter measurements. Part 1: Theory. *Aerosol Science and Technology*, *38*(12), 1185–1205. http://dx.doi.org/10.1080/027868290903907.

Gubin, L. G., Polyak, B. T., & Raik, E. V. (1967). The method of projections for finding the common point of convex sets. *USSR Computational Mathematics and Mathematical Physics*, *7*(6), 1–24. http://dx.doi.org/10.1016/0041-5553(67)90113-9.

Hocker, T., Aranovich, G. L., & Donohue, M. D. (2001). Adsorption-energy distribution of heterogeneous surfaces predicted by projections onto convex sets. *Journal of Colloid and Interface Science*, *238*(1), 167–176. http://dx.doi.org/10.1006/jcis.2001.7496.

Jindal, A. B. (2017). The effect of particle shape on cellular interaction and drug delivery applications of micro- and nanoparticles. *International Journal of Pharmaceutics*, *532*(1), 450–465. http://dx.doi.org/10.1016/j.ijpharm.2017.09.028.

Kenneth Wolfenbarger, J., & Seinfeld, J. H. (1990). Inversion of aerosol size distribution data. *Journal of Aerosol Science*, *21*(2), 227–247. http://dx.doi.org/10.1016/0021-8502(90)90007-K.

Knutson, E. O., & Whitby, K. T. (1975). Aerosol classification by electric mobility: apparatus, theory, and applications. *Journal of Aerosol Science*, *6*(6), 443–451. http://dx.doi.org/10.1016/0021-8502(75)90060-9.

Lienert, B. R., Porter, J. N., & Sharma, S. K. (2003). Aerosol size distributions from genetic inversion of polar nephelometer data*. *Journal of Atmospheric and Oceanic Technology*, *20*(10), 1403–1410. http://dx.doi.org/10.1175/1520-0426(2003)020{\T1\textless}1403:ASDFGI{\T1\textgreater}2.0.CO;2.

Markowski, G. R. (1987). Improving twomey's algorithm for inversion of aerosol measurement data. *Aerosol Science and Technology*, *7*(2), 127–141. http://dx.doi.org/10.1080/02786828708959153.

Masuhr, M., & Kruis, F. E. (2024). Fractionation of aerosols by particle size and material composition using a classifying aerodynamic lens. *Powders*, *3*(3), 392–415. http://dx.doi.org/10.3390/powders3030022.

Mehler, C., Klamt, A., & Peukert, W. (2002). Use of COSMO–RS for the prediction of adsorption equilibria. *AIChE Journal*, *48*(5), 1093–1099. http://dx.doi.org/10.1002/aic.690480518.

Morán, J., Li, L., Ouyang, H., Qiao, Y., Olson, B. A., & Hogan, C. J. (2023). Characterization of the bidimensional size and charge distribution of sub- and supermicrometer particles in an electrostatic precipitator. *Powder Technology*, *425*, Article 118578. http://dx.doi.org/10.1016/j.powtec.2023.118578.

Naseri, A., Sipkens, T. A., Rogak, S. N., & Olfert, J. S. (2021). An improved inversion method for determining two-dimensional mass distributions of non-refractory materials on refractory black carbon. *Aerosol Science and Technology*, *55*(1), 104–118. http://dx.doi.org/10.1080/02786826.2020.1825615.

Papula, L. (2011). *Mathematik für Ingenieure und Naturwissenschaftler Band 3: Vektoranalysis, Wahrscheinlichkeitsrechnung, Mathematische Statistik, Fehler- und Ausgleichsrechnung* (6., überarb. und erw. Auflage). Wiesbaden: Vieweg+Teubner Verlag / Springer Fachmedien Wiesbaden GmbH Wiesbaden, http://dx.doi.org/10.1007/978-3-8348-8133-5.

Park, K., Cao, F., Kittelson, D. B., & McMurry, P. H. (2003). Relationship between particle mass and mobility for diesel exhaust particles. *Environmental Science and Technology*, *37*(3), 577–583. http://dx.doi.org/10.1021/es025960v.

Park, K., Dutcher, D., Emery, M., Pagels, J., Sakurai, H., Scheckman, J., Qian, S., Stolzenburg, M. R., Wang, X., Yang, J., & McMurry, P. H. (2008). Tandem measurements of aerosol properties—A review of mobility techniques with extensions. *Aerosol Science and Technology*, *42*(10), 801–816. http://dx.doi.org/10.1080/02786820802339561.

Raasch, J., & Umhauer, H. (1984). Errors in the determination of particle size distributions caused by coincidences in optical particle counters. *Particle & Particle Systems Characterization*, *1*(1–4), 53–58. http://dx.doi.org/10.1002/ppsc.19840010109.

Rawat, V. K., Buckley, D. T., Kimoto, S., Lee, M.-H., Fukushima, N., & Hogan, C. J. (2016). Two dimensional size–mass distribution function inversion from differential mobility analyzer–aerosol particle mass analyzer (DMA–APM) measurements. *Journal of Aerosol Science*, *92*, 70–82. http://dx.doi.org/10.1016/j.jaerosci.2015.11.001.

Reist, P. C. (1993). *Aerosol science and technology* (2. ed.). New York: McGraw-Hill.

Rhein, F., Scholl, F., & Nirschl, H. (2019). Magnetic seeded filtration for the separation of fine polymer particles from dilute suspensions: Microplastics. *Chemical Engineering Science*, *207*, 1278–1287. http://dx.doi.org/10.1016/j.ces.2019.07.052.

Rüther, T. N., Rasche, D. B., & Schmid, H.-J. (2024). The centrifugal differential mobility analyser – a new device for determination of two-dimensional property distributions. *Aerosol Research*, *3*(1), 65–79. http://dx.doi.org/10.5194/ar-3-65-2025.

Sandmann, K., & Fritsching, U. (2023). Acoustic separation and fractionation of property-distributed particles from the gas phase. *Advanced Powder Technology*, *34*(12), Article 104270. http://dx.doi.org/10.1016/j.apt.2023.104270.

Schürer, G., & Peukert, W. (2005). Prediction of adsorption equilibria from physical properties of the pure components. *Adsorption*, *11*(S1), 43–47. http://dx.doi.org/10.1007/s10450-005-5896-5.

Shapiro, M., Vainshtein, P., Dutcher, D., Emery, M., Stolzenburg, M., Kittelson, D. B., & McMurry, P. H. (2012). Characterization of agglomerates by simultaneous measurement of mobility, vacuum aerodynamic diameter and mass. *Journal of Aerosol Science*, *44*, 24–45. http://dx.doi.org/10.1016/j.jaerosci.2011.08.004.

Sipkens, T. A., Boies, A., Corbin, J. C., Chakrabarty, R. K., Olfert, J., & Rogak, S. N. (2023). Overview of methods to characterize the mass, size, and morphology of soot. *Journal of Aerosol Science*, *173*, Article 106211. http://dx.doi.org/10.1016/j.jaerosci.2023.106211.

Sipkens, T. A., Olfert, J. S., & Rogak, S. N. (2020a). Inversion methods to determine two-dimensional aerosol mass-mobility distributions: A critical comparison of established methods. *Journal of Aerosol Science*, *140*, Article 105484. http://dx.doi.org/10.1016/j.jaerosci.2019.105484.

Sipkens, T. A., Olfert, J. S., & Rogak, S. N. (2020b). Inversion methods to determine two-dimensional aerosol mass-mobility distributions II: Existing and novel Bayesian methods. *Journal of Aerosol Science*, *146*, Article 105565. http://dx.doi.org/10.1016/j.jaerosci.2020.105565.

Slowik, J. G., Stainken, K., Davidovits, P., Williams, L. R., Jayne, J. T., Kolb, C. E., Worsnop, D. R., Rudich, Y., DeCarlo, P. F., & Jimenez, J. L. (2004). Particle morphology and density characterization by combined mobility and aerodynamic diameter measurements. Part 2: Application to combustion-generated soot aerosols as a function of fuel equivalence ratio. *Aerosol Science and Technology*, *38*(12), 1206–1222. http://dx.doi.org/10.1080/027868290903916.

Stark, H., & Olsen, E. T. (1992). Projection-based image restoration. *Journal of the Optical Society of America A*, *9*(11), 1914. http://dx.doi.org/10.1364/JOSAA.9.001914.

Stark, H., & Yang, Y. (1998). Vector space projections: A numerical approach to signal and image processing, neural nets, and optics. In *A wiley-interscience publication*, ISBN: 0471241407.

Stolzenburg, M. R. (1988). *An ultrafine aerosol size distribution system* (Ph.D. thesis), Minnesota: University of Minnesota.

Tavakoli, F., & Olfert, J. S. (2014). Determination of particle mass, effective density, mass–mobility exponent, and dynamic shape factor using an aerodynamic aerosol classifier and a differential mobility analyzer in tandem. *Journal of Aerosol Science*, *75*, 35–42. http://dx.doi.org/10.1016/j.jaerosci.2014.04.010.

Tigges, L., Jain, A., & Schmid, H.-J. (2015). On the bipolar charge distribution used for mobility particle sizing: Theoretical considerations. *Journal of Aerosol Science*, *88*, 119–134. http://dx.doi.org/10.1016/j.jaerosci.2015.05.010.

Toy, R., Peiris, P. M., Ghaghada, K. B., & Karathanasis, E. (2014). Shaping cancer nanomedicine: the effect of particle shape on the in vivo journey of nanoparticles. *Nanomedicine (London, England)*, *9*(1), 121–134. http://dx.doi.org/10.2217/nnm.13.191.

Twomey, S. (1975). Comparison of constrained linear inversion and an iterative nonlinear algorithm applied to the indirect estimation of particle size distributions. *Journal of Computational Physics*, *18*(2), 188–200. http://dx.doi.org/10.1016/0021-9991(75)90028-5.

Voutilainen, A., Kolehmainen, V., & Kaipio, J. P. (2001). Statistical inversion of aerosol size measurement data. *Inverse Problems in Engineering*, *9*(1), 67–94. http://dx.doi.org/10.1080/174159701088027753.

Wang, Y. (2008). An efficient gradient method for maximum entropy regularizing retrieval of atmospheric aerosol particle size distribution function. *Journal of Aerosol Science*, *39*(4), 305–322. http://dx.doi.org/10.1016/j.jaerosci.2007.11.008.

Wang, Y., Fan, S., Feng, X., Yan, G., & Guan, Y. (2006). Regularized inversion method for retrieval of aerosol particle size distribution function in w(1,2) space. *Applied Optics*, *45*(28), 7456–7467. http://dx.doi.org/10.1364/ao.45.007456.

Wiedensohler, A. (1988). An approximation of the bipolar charge distribution for particles in the submicron size range. *Journal of Aerosol Science*, *19*(3), 387–389. http://dx.doi.org/10.1016/0021-8502(88)90278-9.

Worlitschek, J., Hocker, T., & Mazzotti, M. (2005). Restoration of PSD from chord length distribution data using the method of projections onto convex sets. *Particle & Particle Systems Characterization*, *22*(2), 81–98. http://dx.doi.org/10.1002/ppsc.200400872.

Yee, E. (1989). On the interpretation of diffusion battery data. *Journal of Aerosol Science*, *20*(7), 797–811. http://dx.doi.org/10.1016/0021-8502(89)90091-8.

Zhang, J., Qiao, J., Sun, K., & Wang, Z. (2022). Balancing particle properties for practical lithium-ion batteries. *Particuology*, *61*, 18–29. http://dx.doi.org/10.1016/j.partic.2021.05.006.

4.4 Centrifugal Differential Mobility Analyzer - Validation and First Two-dimensional Measurements

Torben N. Rüther, Hans-Joachim Schmid, Sebastian Gröne, Christopher Dechert
Powders, 4, (2025), https://doi.org/10.3390/powders4020011
Nachdruck aus Powders (2025) mit Erlaubnis vom MDPI.

Der Autor dieser Dissertation betreute zusammen mit Christopher Dechert Sebastian Gröne bei der Durchführung der Strömungssimulation sowie der Berechnung der Transferfunktionen anhand der Strömungsdaten [GRD23]. Die Durchführung, Analyse und Auswertung der Messreihen sowie die Messung und Auswertung eines Silberaerosols bei verschienden Sinterstufen wurden ebenfalls von dem Autor dieser Arbeit durchgeführt. Prof. Hans-Joachim Schmid hat den Autor während der gesamten Arbeit betreut. Er, Christopher Dechert und Sebastian Gröne haben an der Revision des Manuskripts mitgewirkt.

powders

MDPI

Article

Centrifugal Differential Mobility Analysis—Validation and First Two-Dimensional Measurements

Torben Norbert Rüther, Sebastian Gröne, Christopher Dechert and Hans-Joachim Schmid *

Particle Technology Group, Department Mechanical Engineering, Paderborn University, Warburger Straße 100, 33098 Paderborn, Germany; torben.ruether@uni-paderborn.de (T.N.R.); sebgr@mail.uni-paderborn.de (S.G.); christopher.dechert@uni-paderborn.de (C.D.)
* Correspondence: hans-joachim.schmid@uni-paderborn.de

Abstract: To obtain a more comprehensive understanding of the specific properties of complex-shaped technical aerosols—such as partially sintered aggregates formed in combustion processes or structured particles resulting from complex synthesis processes—it is essential to measure more than a single equivalent size. This study examines a novel method for determining a two-dimensional distribution of two distinct particle properties within the size range from 50 nm to 1000 nm: the Centrifugal Differential Mobility Analyzer (CDMA). The CDMA enables the simultaneous measurement of both mobility and Stokes equivalent diameters, providing a detailed two-dimensional particle property distribution. This, in turn, allows for the extraction of shape-related information, which is essential for characterizing particles in terms of their chemical composition, reactivity, and other physicochemical properties. This paper presents a detailed evaluation of a first CDMA prototype. First, CFD simulations of the flow field within the classifier are presented in order to assess and understand non-idealities arising from the exact geometry. Subsequently, the transfer function is evaluated by particle trajectory calculations based on the simulated flow field. It can be demonstrated that the simulated transfer functions agree quite well with transfer functions derived from streamlines of an ideal flow field, indicating that the non-idealities in the classifying region are almost negligible in their effect on the classification result. An experimental determination of the transfer function shows additional effects not covered by the previous simulations, like broadening by diffusion and losses due to diffusion and precipitation within the in- and outlet of the classifier. Finally, the determined transfer functions are used to determine the full two-dimensional distribution with regard to the mobility and Stokes equivalent diameter of real aerosols, like spherical particles and aggregates at different sintering stages, respectively.

Keywords: centrifugal differential mobility analysis; 2D-measurement; particle characterization; moving reference frame CFD-simulation; transfer function

Academic Editor: Massimo Poletto

Received: 4 January 2025
Revised: 12 March 2025
Accepted: 26 March 2025
Published: 2 April 2025

Citation: Rüther, T.N.; Gröne, S.; Dechert, C.; Schmid, H.-J. Centrifugal Differential Mobility Analysis—Validation and First Two-Dimensional Measurements. *Powders* **2025**, *4*, 11. https://doi.org/10.3390/powders4020011

1. Introduction

Technical aerosols often exhibit complex behavior influenced by particle size, structure and shape. Characterizing such ensembles, particularly in the case of nanoscale aerosols, presents significant challenges, as their small dimensions severely limit the investigation through conventional light scattering techniques [1,2]. For aggregates with highly intricate and irregular morphologies, defining a single representative particle size becomes even more difficult [2,3]. Consequently, in most cases, an equivalent property is introduced as a practical means of characterization.

An equivalent diameter is defined as the diameter of a spherical particle that exhibits the same specific property (such as electrical mobility, inertial behavior, or settling velocity) as the particle under consideration. However, relying solely on a single equivalent diameter is inherently insufficient for a comprehensive characterization of complex particle properties, as it does not capture variations in shape, structure, or composition. To achieve a more detailed and accurate characterization, it is essential to assess multiple properties or equivalent diameters. One approach to obtaining such information is through electron microscopy, which provides structural insights, at least in the form of a projection area. This allows for a more refined analysis of particle morphology and enables a better understanding of their physical and chemical behavior.

Furthermore, so-called tandem configurations enable the measurement of two-dimensional distributions of different equivalent particle sizes, providing a more detailed characterization of aerosol properties. These setups consist of a sequential arrangement of two instruments: the first serves as a classifier, selectively isolating a specific fraction of particles based on one equivalent size, while the second either measures an additional property of the classified aerosol or performs a secondary classification based on a different equivalent size. By combining these two measurement stages, tandem configurations offer deeper insights into particle characteristics, allowing for a more comprehensive analysis of their morphology, composition, and dynamic behavior. Park et al. [4] employed a DMA-APM (Dynamic Mobility Analyzer-Aerosol Particle Mass Analyzer) configuration to simultaneously measure two different equivalent diameters. This approach was later utilized by Rawat et al. [5] to calculate a two-dimensional distribution. Since then, data inversion models for 2D distributions have been widely adopted and applied to various tandem measurement configurations [6,7]. Broda et al. [8], for instance, implemented a Twomey algorithm to derive a 2D distribution function for the mass concentration of carbon black using a CPMA-SP2-CPC (Centrifugal Particle Mass Analyzer–Single Particle Soot Photometer–Condensation Particle Counter) setup. Moreover, Sipkens et al. [9] published a comprehensive review discussing various measurement techniques for carbon black and their applications in tandem configurations.

However, these tandem methods are inherently complex. Specifically, they necessitate at least two separate devices, which increases the overall cost of the setup. Furthermore, such configurations demand a high level of specialized knowledge and technical proficiency to conduct and evaluate such measurements. The complexity arises from the unique nature of these setups, which require users to possess a deep understanding of the underlying principles and operational intricacies. Additionally, for each specific setup, the data inversion process must either be developed from scratch or adapted by the user, adding another layer of technical demand. This combination of cost, complexity and user expertise highlights the challenges associated with utilizing tandem measurement methods in aerosol characterization. Furthermore, when using two classifiers in tandem, the resulting particle concentration at the exit is typically very low. This is due to the convolution of both transfer functions, which leads to a significant reduction in the number of particles that pass through both classifiers. As a consequence, the statistics of the resulting size distributions may be poor, often requiring either significantly longer measurement times or resulting in unreliable data. To address these limitations and enable the simultaneous measurement of multiple particle properties, the CDMA (Centrifugal Differential Mobility Analyzer) was developed. The CDMA integrates the principle of classification of an Aerodynamic Aerosol Classifier (AAC) [10] with that of a Differential Mobility Analyzer (DMA) [11] in one single instrument. This allows for the measurement of a true two-dimensional distribution of both the equivalent mobility diameter and the equivalent Stokes diameter. Furthermore, additional parameters, such as effective density and fractal dimension, can

be derived from this approach, providing valuable insights into particle shape and structure [4,12,13]. These additional characteristics further enhance the comprehensiveness of the analysis, enabling a more detailed analysis of aerosol particles in terms of their physical and morphological attributes.

The principle of the CDMA, the design of a first prototype and an idealized transfer function, alongside a method for measuring the transfer function that facilitates the determination of its parameters have been published recently in a first paper [14]. Building upon this, a second paper thoroughly examined the theoretical transfer functions of the CDMA. Various alternative approaches were compared, while the influence of diffusion and applied boundary conditions on the system's behavior was also investigated [15]. A third paper focused on the application of the Projection Onto Convex Sets (POCS) algorithm for data inversion. The algorithm which had not been used before in the context of particle characterization was tested with both experimental and idealized datasets, and its performance was critically assessed [16].

The present work now substantially extends the findings from these previous publications. In particular, results from a flow-field simulation inside the classifier are presented and non-idealities in the flow field are discussed in detail. Subsequently, a method to simulate the transfer function based on particle trajectory simulations using the simulated flow fields is presented. Furthermore, the resulting transfer functions are compared to results from a much simpler streamline approach based on an idealized flow field. This reveals the influence of the flow non-idealities on the classification result. Furthermore, a methodology to measure the overall transfer function of the CDMA prototype is applied and the resulting transfer functions dependent on particle size and the flow ratio are extensively studied. Finally, the CDMA is used to characterize real aerosols of silver nanoparticles. In particular, aggregates of different structures resulting from different sintering stages are characterized by their full 2D structures to comprehensively characterize complex particles.

2. Theoretical Fundamentals

As extensively described in Rüther et al. [14], the CDMA shares key similarities with both the DMA and the AAC. Therefore, the CDMA is composed of two concentric cylinders that form a cylindrical gap, through which a sheath airflow is directed (see cross-section of the CDMA in Figure 1). These cylinders are electrically isolated from one another, enabling a voltage to be applied between them, in line with the operational principle of the DMA. Additionally, both cylinders can be rotated at the same angular velocity, following the operational principle of the AAC. This design integrates the core features of both instruments, enabling the simultaneous measurement of multiple particle properties. When an aerosol volume flow is applied to the inner cylinder (c.f. Figure 1, detail A), the particles are moved through the sheath air towards the outer cylinder by electrical and/or centrifugal forces. At the end of the classification chamber, (c.f. Figure 1, detail B), the particles are sampled, so that particles matching the predetermined properties are extracted as sample volume flow for subsequent particle counting.

Assuming Stokes' drag force and neglecting inertia, the force equilibrium results in:

$$Q_P \cdot E + m_P \cdot a_c = 3\pi\eta d_m w_{Dr} \cdot \frac{1}{Cu(d_m)} \tag{1}$$

Q_P represents the particle charge, $E = -\frac{U}{r \cdot \ln(r_o/r_i)}$ denotes the electric field strength in a radial direction, m_P is the particle mass, $a_c = \omega^2 \cdot r$ represents the centrifugal acceleration, η denotes the dynamic viscosity, d_m is the mobility diameter, w_{Dr} denotes the radial particle drift velocity, and Cu is the Cunningham slip correction factor [17]. The deterministic de-

scription of the particle path neglecting diffusion is achieved by rearranging and integrating Equation (1).

$$r(x) = \sqrt{\frac{\left(\tau \cdot \omega^2 \cdot r_{in}^2 + \frac{Z \cdot U}{\ln\left(\frac{r_o}{r_i}\right)}\right) \cdot \exp\left\{2 \cdot \tau \cdot \omega^2 \cdot x \cdot \frac{\pi \cdot \left(r_o^2 - r_i^2\right)}{Q_{sh} + Q_a}\right\} - \frac{Z \cdot U}{\ln\left(\frac{r_o}{r_i}\right)}}{\tau \cdot \omega^2}} \tag{2}$$

U represents the voltage applied to the outer cylinder, ω denotes the rotational velocity of both cylinders, r_o and r_i are the outer and inner radii, r_{in} is the radius at which the particle enters into the classification gap, x is the position of the particle in the axial direction, Q_{sh} is the sheath air volume flow, Q_a is the aerosol volume flow, τ is the particle relaxation time and Z is the particle mobility. With

$$\tau = \frac{\rho \cdot d_v^3 \cdot Cu(d_m)}{18 \cdot d_m \cdot \eta} = \frac{\rho \cdot d_{st}^2 \cdot Cu(d_m)}{18\eta} \tag{3}$$

and

$$Z = \frac{n \cdot e \cdot Cu(d_m)}{3\pi \cdot \eta \cdot d_m} \tag{4}$$

with ρ as the particle density, d_v as the volume equivalent diameter, d_{st} as the Stokes equivalent diameter, n as the number of charges carried by a particle, and e as the elementary charge. Please note that n and U might be positive or negative depending on the polarity and charge, respectively. Also note that, according to Rüther et al. [14], the argument of the Cunningham slip correction factor is d_m.

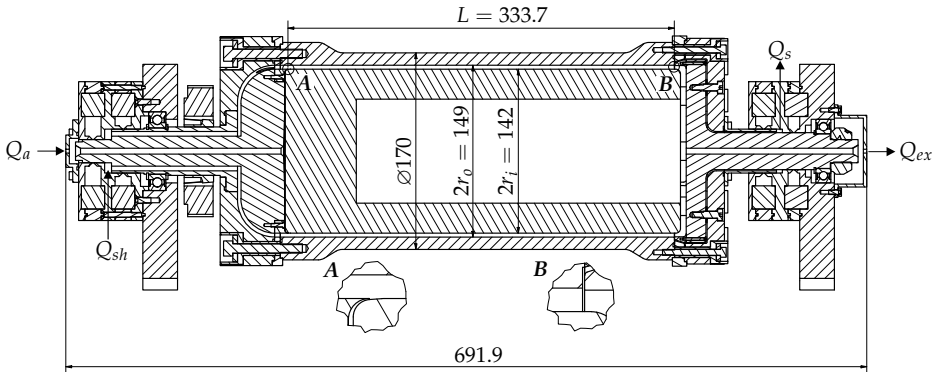

Figure 1. Cross-section of the CDMA prototype [14].

Therefore, the trajectory of a particle with given properties d_m and d_{st} can be calculated from the volume flow ratio and the applied rotational velocity and voltage.

Z^* is the mobility required for a particle entering at the center of the aerosol inlet to be sampled exactly at the center of the outlet for a given set of operational parameters [18]. τ^* describes the same behavior but for the relaxation time [10].

$$Z^* = \frac{Q_{sh} + Q_{ex}}{4 \cdot \pi L U} \cdot \ln\left(\frac{r_o}{r_i}\right) \tag{5}$$

$$\tau^* = \frac{Q_{sh} + Q_{ex}}{\pi \omega^2 (r_i + r_o)^2 L} \tag{6}$$

with Q_{ex} being the excess volume flow and L the length of the classifying gap. Relating the particle properties Z and τ to the characteristic values at the actual operation point Z^* and τ^* lead to the normalized mobility or the normalized particle relaxation time, respectively.

$$\widetilde{Z} = Z/Z^* \quad ; \quad \widetilde{\tau} = \tau/\tau^* \tag{7}$$

3. Design

Figure 1 shows the cross-section of a first prototype of the CDMA. The aerosol is fed from the left side, enters through the center bore, and flows through a small gap to the inlet of the classification region A. The sheath air is fed between two ferrofluidic seals on the left side. Then, it passes through eight axial holes into the CDMA. After a flow deflection, the sheath air also enters into the classification gap at A. Together the flows pass through the classification zone. At point B, the excess volume flow continues the inner cylinder, flows to the center and exits through a center bore on the right side. The sample air is extracted in the radial direction at point B. Then, the sample flows through small channels until it leaves the CDMA through a small hole between the ferrofluidic seals on the right side. Voltage can be applied through a carbon-sliding contact on the outer cylinder, the rotational speed is applied by a belt drive mounted on the left side. For more details about the design of the CDMA prototype, see also [14].

4. Numerical Flow Simulations

CFD simulations were performed in order to verify the flow profile in the classification gap and to identify potential non-ideal flow patterns. A simulation was performed using the OpenFOAM Version 8 framework under the assumptions of incompressible and isothermal flow, employing the $k-\omega$ SST turbulence model [19]. Although the results indicated laminar flow within the classifying gap, this turbulence model was selected to ensure an accurate representation of potential turbulence in the inlet and outlet regions. Moreover, due to the presence of narrow gaps, the $k-\omega$ SST model was preferred over the $k-\epsilon$ model, as it exhibits superior performance in wall-bounded flows, particularly within the viscous sublayer. Although the $k-\omega$ model tends to overestimate shear stress in fluid flows, the $k-\omega$ SST model mitigates this by incorporating the $k-\epsilon$ model in regions away from the walls. By analyzing the turbulent kinetic energy, critical regions can be identified and subsequently examined for the presence of micro-vortices in potential future studies using Large Eddy Simulation (LES) or Direct Numerical Simulation (DNS). Surface roughness is not considered in this work due to the surface being highly polished and the predominant laminar flow characteristics.

In the simulation, pure particle-free air under standard conditions is used as the working fluid. The sheath air is introduced through eight symmetrically arranged inlet tubes (indicated by the green dot in Figure 2) and is subsequently distributed uniformly along the entire circumference. Within the computational model, these inlets are represented as laminar flow profiles entering the simulation domain. To optimize computational efficiency, the flow domain is reduced to a representative angular section of 45° in the circumferential direction, as illustrated in Figure 2. This reduction is justified by the symmetry of the system, allowing for an accurate representation of the overall flow behavior while minimizing computational cost.

At the symmetry interfaces, periodic boundary conditions are applied, so that fluxes across the interfaces are admitted. The boundary condition at the walls is a zero-slip boundary condition (Dirichlet boundary condition for the velocity). The aerosol inlet, sheath air inlet, and excess air outlet are also set to a defined volumetric flow rate. A plug flow profile is assumed at the aerosol inlet and the excess air outlet, while a fully developed

Powders **2025**, *4*, 11

laminar tube flow is applied at the inlet of the sheath air. The sample outlet is defined by the Neumann condition; thus, the mass balance is always maintained.

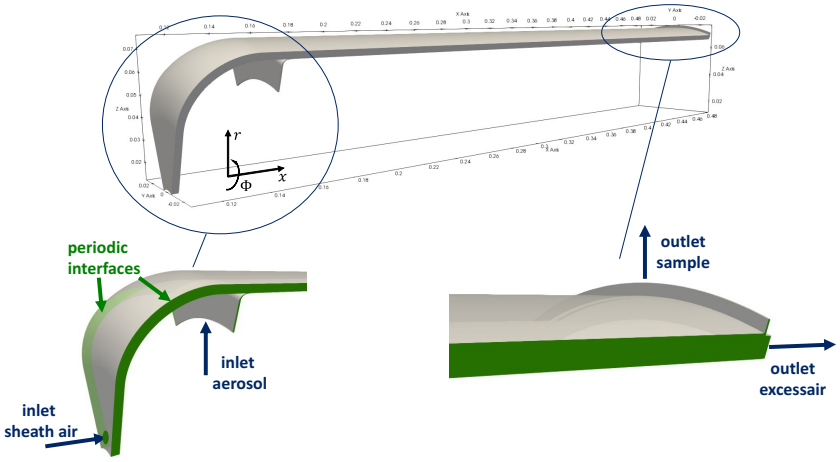

Figure 2. A 45 ° section of the flow domain used for the calculations, including the boundary conditions.

The rotation is implemented by a single rotating frame approach, using the 'SRF-SimpleFoam' solver to calculate the velocity fields. The computational grid consists of 70 elements in the radial direction, 50 elements in the circumferential direction, and 550 elements along the flow direction, with a logarithmically increasing resolution towards the boundary layers. A mesh independence study confirmed the adequacy of this resolution, as doubling the mesh density resulted in deviations of less than 0.4% in the pressure drop across the prototype. Additionally, critical regions, such as the aerosol inlet and sample outlet, as well as edge areas, were refined to enhance the accuracy of the flow representation in these zones. This ensures a more precise depiction of localized flow phenomena and potential gradients.

The following simulation results are based on a flow ratio $\beta = Q_a/Q_{sh} = 0.2$ ($Q_a = Q_s = 0.3\,\mathrm{l/min}$, $Q_{sh} = Q_{ex} = 1.5\,\mathrm{l/min}$). The flow ratio β directly influences the width of the transfer function, with smaller β-values resulting in a narrower transfer function. Consequently, a lower β leads to an improved resolution, as it enhances the system's ability to distinguish between closely spaced particle sizes. This relationship is crucial in optimizing measurement precision and ensuring accurate characterization of the aerosol properties. The chosen parameter set was identified by Rüther et al. [14] in preliminary tests as the standard operating conditions for the current prototype and was also employed in the experimental measurements.

4.1. Flow Behavior Without Rotation

To investigate the radial symmetry of the flow, Figure 3 shows the flow pattern at different positions. Here, x is the absolute position in axial direction, where the inlet of the sheath air is at $x = 0\,\mathrm{m}$. For reasons of clarity, the velocities in the axial direction in the highlighted planes are color coded. At the axial coordinate $x = 0.14\,\mathrm{m}$, the deflection of the sheath air is completed. The plane at $x = 0.151\,\mathrm{m}$ is located directly before the aerosol joins the sheath air. It can be observed that the flow profile is symmetrical across the gap width, with no significant deviations in the circumferential direction.

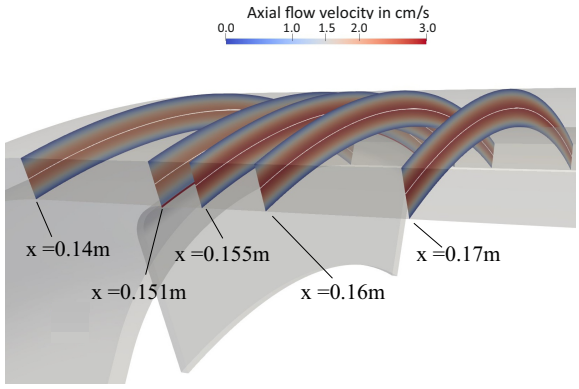

Figure 3. Cross-sections of the axial flow velocity at different axial coordinates in the proximity of the aerosol inlet. White lines within the displayed planes represent the sources for the plots in Figure 4. The red line at $x = 0.151$ m indicates the position of the aerosol inlet, which, in this context, represents the region where the aerosol enters the measurement slit.

Figure 4 provides a more detailed representation of the axial velocity. On the left, the axial velocity is plotted against the radial coordinate for $\phi = 0°$. It can be observed that a uniform velocity profile is quickly established. At $x = 0.155$ m, which is only 4 mm downstream from the point where the aerosol volume flow merges with the sheath air flow, no deviations from the subsequent flow profiles are evident. The right side of Figure 4 further investigates this by showing the velocity profiles along the center of the gap, enabling a more precise analysis of the circumferential direction (indicated by the white lines in Figure 3). In this region, the values across the circumferential direction show only slight variations, which can be attributed to the eight inlet flows. Moreover, it is observed that this small difference (less than $\pm 0.5\%$) diminishes further as the axial coordinate x increases. This observation suggests that there are no significant variations in the flow profile along the circumferential direction. Therefore, it can be assumed that the flow profile in the middle plane ($\phi = 0°$) is representative of the overall flow profile within the CDMA. As a result, only the flow profile in this middle plane is presented and utilized in the subsequent analyses and calculations.

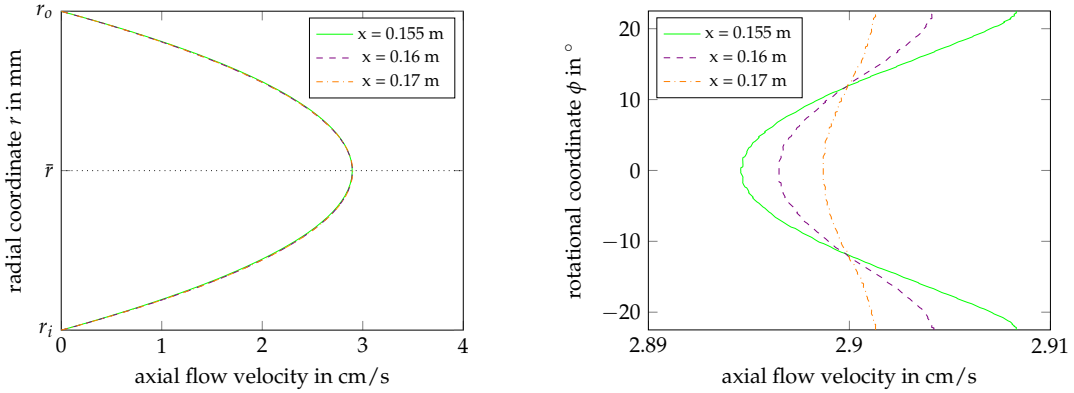

Figure 4. Plots of the axial velocities for 0 RPM. (**Left**): at $\phi = 0$ with respect to radial coordinate r. (**Right**): at the middle of the classification gap ($\bar{r} = 72.6$ mm, see also dotted line left).

Powders **2025**, *4*, 11

Figure 5 shows the streamlines at 0 RPM for this middle plane at $\phi = 0°$. As the streamlines in this region are exceptionally smooth, showing no indication of vortex formation or interaction with the surrounding airflow, it can be reasonably assumed that neither cross-mixing nor backflow occurs. However, a significant expansion of the aerosol flow is observed, which can be attributed to two primary factors: First, the CDMA has been designed so that, for $\beta = 0.1$, the inlet cross section and the sheath air cross section correspond to the respective flow rates. At $\beta = 0.2$, the higher aerosol flow Q_a needs to occupy more space. Second, the non-slip boundary condition at the wall leads to a reduction in the flow velocity near the walls, and therefore, the streamlines must expand towards the center of the gap.

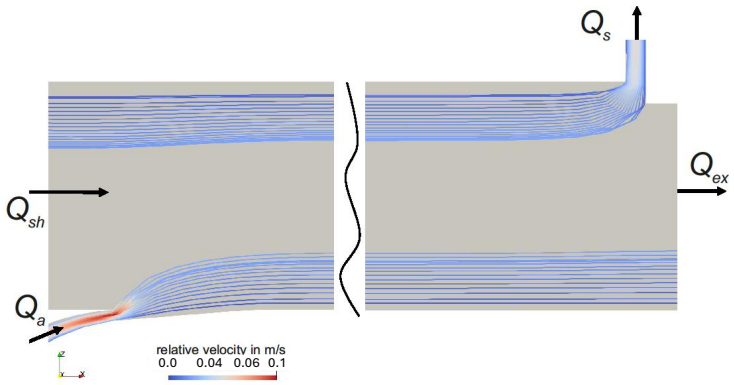

Figure 5. Streamlines in the plane at $\phi = 0°$ of the flow domain, for $Q_a = 0.3$ l/min and $Q_{sh} = 1.5$ l/min. The bottom set of streamlines starts from the aerosol inlet while the upper one ends at the sample outlet.

4.2. Flow Behavior with Rotation

Figure 6 shows the angular distribution of the axial velocity at different positions in axial direction analogous to Figure 4, but now for different rotational velocities. It can be observed that the flow profile shifts inward, particularly at higher speeds, and exhibits a higher maximum velocity. However, this effect diminishes as the x-coordinate increases. The velocity profile in the circumferential direction at the center of the classification gap (c.f. Figure 6, right) is also less uniform compared to the non-rotating case, with deviations of up to $\pm 5\%$. Despite these deviations, the profile tends to converge towards the ideal profile as the flow progresses. While these deviations are noteworthy, it is important to consider that they primarily occur at very high speeds and that the deviations decrease with increasing x-coordinates. Therefore, when analyzing the flow with rotation, here only the middle plane ($\phi = 0°$) will be considered moving forward.

In Figure 7, axial velocity fields of the cases for 0, 475, and 2000 RPM are compared. It can be observed that for increasing rotational speed, the velocity profile increasingly shifts toward the inner wall of the transfer domain and shows higher peak velocities. Downstream in the axial direction, the effective cross-section widens up to the geometrically available cross-section. This results in a more symmetric profile for the axial velocity.

Upon examining the inlet region, it becomes evident that a significantly higher flow velocity is observed here compared to other regions. However, even in this region, the flow characteristics do not indicate the formation of vortices. It is important to note that this conclusion is based on the current simulation model, which lacks the capability to accurately capture such detailed flow phenomena. To investigate vortex formation and accurately

Powders **2025**, *4*, 11

resolve the flow field, more advanced simulation techniques such as Large Eddy Simulation (LES) or Direct Numerical Simulation (DNS) would be required. These methods would enable a more precise representation of the flow dynamics, particularly in the critical areas where vortices may form.

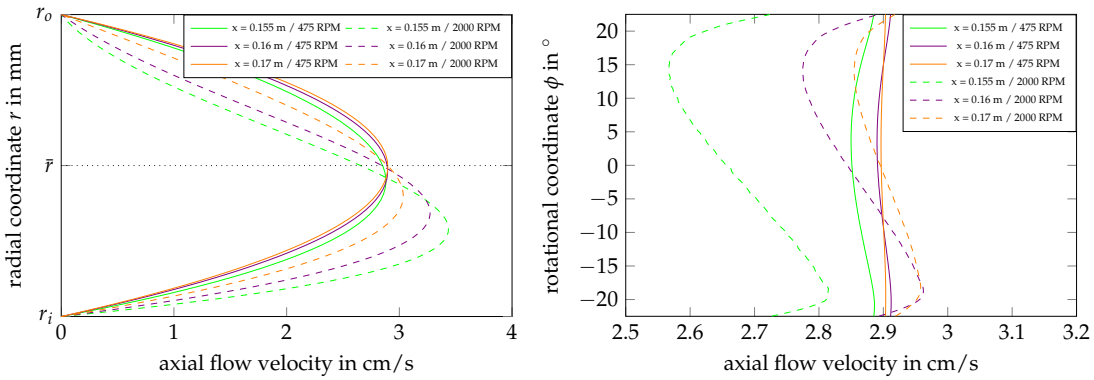

Figure 6. Plots of the axial velocities for 475 RPM and 2000 RPM. (**Left**): at $\phi = 0\,^\circ$ with respect to radial coordinate r. (**Right**): at the middle of the classification gap ($\bar{r} = 72.6$ mm, see also dotted line left).

In general, the presence of turbulence would lead to cross-mixing between adjacent streamlines, resulting in a broadening of the flow profile. This broadening would cause a significant deterioration in the resolution of the transfer function, as it would blur the distinctions between different particle size classes. Thus, turbulence is considered prohibitive in this context, as it would compromise the accuracy and performance of the system.

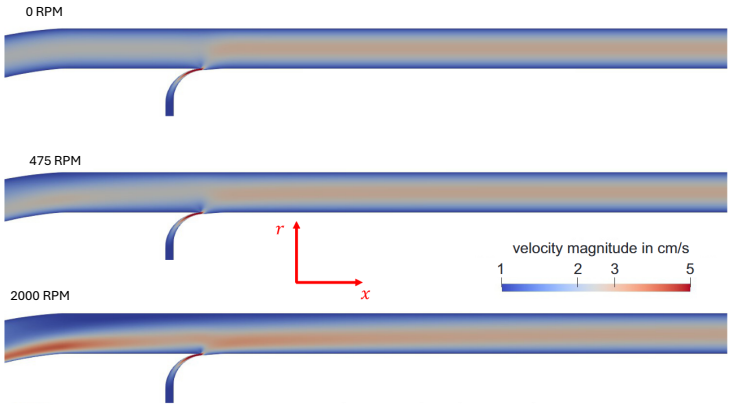

Figure 7. Axial velocity magnitude in the middle plane ($\phi = 0°$) for different rotational speeds.

Figure 8 illustrates the relative tangential velocity, i.e., the deviation of the tangential velocity from solid body rotation. It is evident that the air is unable to immediately match the rotational speed, particularly when there is a flow in the radial direction. This effect can be attributed to the low viscosity of the fluid and the relatively large gap width, which hinder the immediate transmission of rotational speed. As the flow velocity increases, the difference between the rotational and axial velocities also becomes more pronounced, but this disparity is eventually compensated over time.

Powders **2025**, *4*, 11

This phenomenon also highlights that the velocity profile initially stabilizes near the wall before propagating inward. However, since particles are introduced near the wall, where the flow stabilizes relatively quickly (c.f. Figures 7 and 8), the influence of these variations on the particle trajectories is somewhat minimized.

Therefore, the impact of the actual flow field on the transfer function will be explored in more detail in the subsequent chapter, where the relationship between the flow dynamics and particle behavior is examined comprehensively.

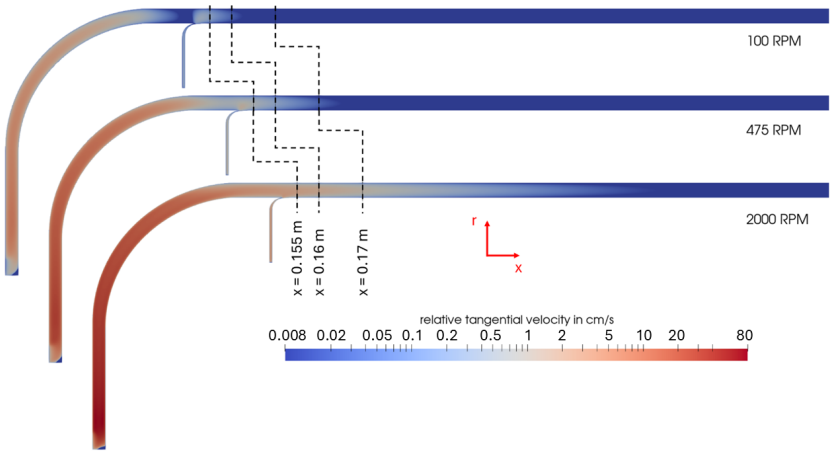

Figure 8. Relative tangential velocity in the middle plane ($\phi = 0°$) for different rotational speeds.

5. Transfer Function of the CDMA

5.1. Transfer Function Based on CFD Simulations

To investigate the influence of the flow profile on the classification, the transfer function was derived directly from CFD data. The determination of a transfer function for specific CDMA operating parameters (at fixed voltage and velocity) is a stepwise process. For each considered particle size, multiple trajectories are calculated while changing the radial particle starting point in the inlet cross section. For singly charged, spherical particles, the transfer probability for one particle size is then given by the number of successfully traversed particles N_{sampled} divided by the total number of simulated particles N_{tot}:

$$\Omega(d_p) = \frac{N_{\text{sampled}}}{N_{\text{tot}}} \tag{8}$$

The particle size can then be converted into the mobility Z, particle relaxation time τ or their normalized values ($\widetilde{Z}, \widetilde{\tau}$), respectively.

A particle trajectory is calculated using CFD data of the flow simulations. For calculating trajectories, the travelled distance in the radial and axial direction is determined for every calculated time step. The developed algorithm obtains the velocity data of the current particle location. Besides flow velocity data, additional forces are considered to act on the particle in the radial direction. The resulting radial velocity component is calculated using the fluid velocity component in the radial direction, particle size and CDMA operating parameters (c.f. Equation (2)) while neglecting the diffusion and inertia of the particle.

Figure 9 shows trajectories of successfully sampled particles (green) and deposited ones. It is obvious that the resolution of the simulation depends on the number of trajectories, the duration of the virtual time steps and the number of particle sizes investigated.

However, these quantities increase only with high computational costs; thus, a compromise must be made.

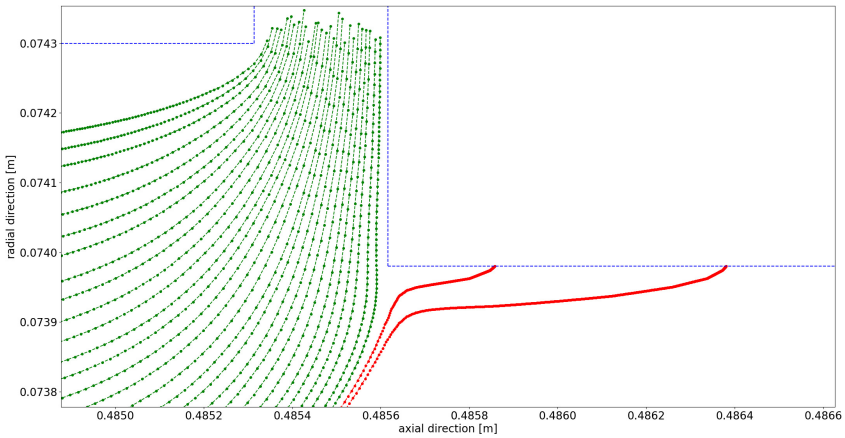

Figure 9. Representative particle trajectories at the sample outlet. Trajectories labeled in green are successfully sampled. The trajectories labeled in red are not classified.

5.2. Ideal Transfer Function Based on Streamline Approach

To compare the simulated results with theoretical values, we use an ideal transfer function. The ideal two-dimensional transfer function was derived from streamline functions assuming ideal flow profiles and neglecting diffusion. Details for derivation are given in [15].

$$\Omega = \frac{1}{2\beta(1+A)} \cdot \left[-\left|-1-\frac{\beta+\kappa^2}{\kappa^2-1}\cdot A+\frac{\widetilde{Z}}{\widetilde{\tau}}\cdot\frac{1+\beta}{2\widetilde{h}}\cdot A\right| + \left|-1-\beta-\frac{\kappa^2+\beta\kappa^2}{\kappa^2-1}\cdot A+\frac{\widetilde{Z}}{\widetilde{\tau}}\cdot\frac{1+\beta}{2\widetilde{h}}\cdot A\right| \right. \\ \left. + \left|-1+\beta-\frac{\beta+\kappa^2}{\kappa^2-1}\cdot A+\frac{\widetilde{Z}}{\widetilde{\tau}}\cdot\frac{1+\beta}{2\widetilde{h}}\cdot A\right| - \left|-1-\frac{\kappa^2+\beta\kappa^2}{\kappa^2-1}\cdot A+\frac{\widetilde{Z}}{\widetilde{\tau}}\cdot\frac{1+\beta}{2\widetilde{h}}\cdot A\right| \right] \tag{9}$$

β is the ratio of aerosol volume flow Q_a to sheath air volume flow Q_{sh}, $\widetilde{h}$ is the ratio of the gap width to the mean radius, κ is the ratio of the inner radius r_i to the outer radius r_o and A is a substitution to facilitate reading.

$$\widetilde{h} = 2 \cdot \frac{r_o - r_i}{r_o + r_i} \tag{10}$$

$$\kappa = \frac{r_i}{r_o} = \frac{1-\widetilde{h}/2}{1+\widetilde{h}/2} \tag{11}$$

$$A = \exp\left\{\widetilde{\tau}\cdot\frac{2\widetilde{h}}{1+\beta}\right\} - 1 \tag{12}$$

This results in a two-dimensional transfer function, as displayed in Figure 10.

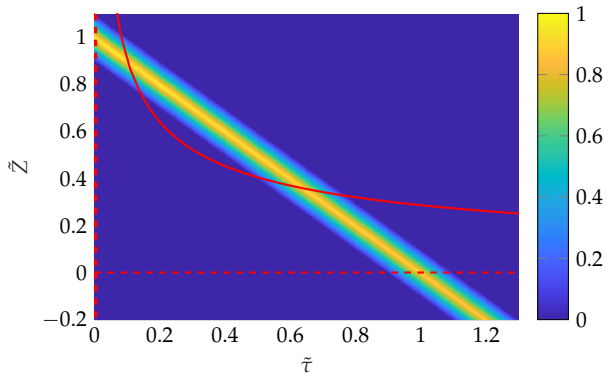

Figure 10. Ideal two-dimensional transfer function with $\beta = 0.1$ and $\widetilde{h} = 0.05$. Operating conditions are taken into account by normalization of $\widetilde{Z}$ and $\widetilde{\tau}$ by Z^* and τ^*, respectively. The dashed red lines represent transfer functions for $\widetilde{\tau} = 0$ and $\widetilde{Z} = 0$, respectively. The solid red line represents the transfer function of singly charged spherical particles at fixed operating parameters (ω, U).

5.3. Comparison of Transfer Functions

In the following, we intend to compare the idealized transfer function based on the streamline approach (cf. Section 5.2) with the particle trajectory simulations based on CFD simulations (cf. Section 5.1). However, a quantitative comparison of 2D functions is difficult to visualize. Moreover, the computational effort for determining the 2D transfer function from the particle trajectory simulations would be immense. Therefore, we will compare the transfer functions for $\widetilde{\tau} = 0$ and $\widetilde{Z} = 0$ (red, dashed lines, cf. Figure 10) in Figure 11 and the transfer function for spherical particles (red solid line, c.f. Figure 10) in Figure 12.

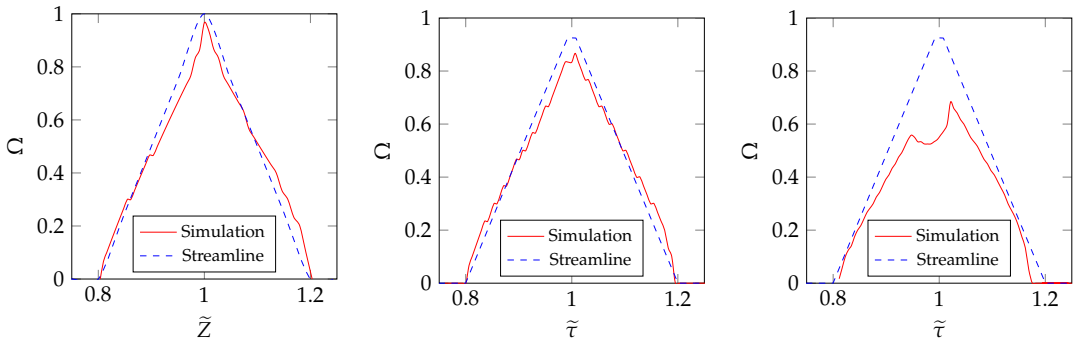

(**a**) $n = 0$ RPM, $U = 20.99$ V

(**b**) $n = 475$ RPM, $U = 0$ V, $\rho = 10490\,\mathrm{kg/m^3}$

(**c**) $n = 2000$ RPM, $U = 0$ V, $\rho = 580\,\mathrm{kg/m^3}$

Figure 11. Comparison of transfer functions of spherical particles at $\widetilde{Z} = 0$ and $\widetilde{\tau} = 0$ determined by streamline and particle trajectory simulation approaches, respectively. With $\beta = 0.2$ and a modal particle size of 100 nm.

The operational parameters for determining the transfer functions for $\widetilde{\tau} = 0$ and $\widetilde{Z} = 0$ as illustrated in Figure 11 were selected so that $\widetilde{\tau} = 1$ or $\widetilde{Z} = 1$ results for a particle size of 100 nm. In order to test for different centrifugal conditions, two different densities were chosen in Figure 11b and Figure 11c, respectively. It is evident that the resolution of the simulation results is limited because of the restricted number of calculated particle trajectories per particle size. An investigation of the pure electrical mode (see Figure 11a) reveals a high degree of agreement between the transfer functions. The minor discrepancies

can be attributed to the flow field and the limited resolution. Figure 11b,c illustrate the transfer functions at different speeds in purely rotational mode. The transfer functions exhibit a high degree of agreement for the case of 475 RPM (see Figure 11b). The simulated transfer function is slightly lower, indicating a slightly reduced probability of classification around $\widetilde{\tau} = 0$. As the speed increases (cf. Figure 11c), the relative position of the transfer function remains consistent, while the height of the transfer function is reduced significantly. This can be attributed to the increasing distortion of the flow field especially at the edges of the aerosol inlet and sample outlet. It is likely that small flow deviations at the edges of the inlet and outlet lead to increasing losses so that especially the tip of the transfer function, where over the whole gap all particles should be sampled, will be decreased significantly in height.

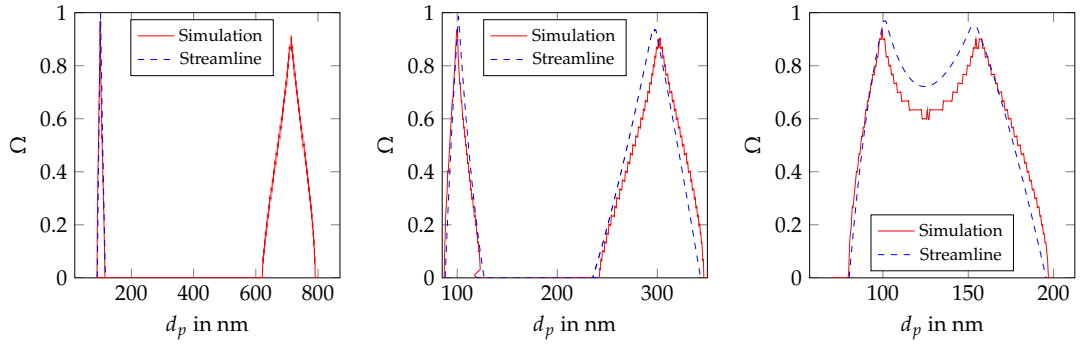

(**a**) $n = 100$ RPM, $U = 20.06$ V (**b**) $n = 200$ RPM, $U = 17.27$ V (**c**) $n = 300$ RPM, $U = 12.63$ V

Figure 12. Comparison of transfer functions at different operation modes determined by streamline and particle trajectory simulation approaches, respectively. With $\beta = 0.2$ and a particle density of 10,490 kg/m^3.

To extend the investigation of the transfer functions, the combination of applying both voltage and rotational velocity is examined, too. To simplify the two-dimensional transfer function to a one-dimensional transfer function, perfectly spherical particles carrying one elementary charge are considered (c.f. red solid line in Figure 10 as an example). In this case, small particles with high electrical mobility and low mass and larger particles with lower mobility and high mass are classified simultaneously, resulting in two peaks of the transfer function, as shown in Figure 12.

Varying the operating parameters results in a shift of the two peaks until they merge and eventually diminish. The simulated transfer functions are again very close to the ideal transfer functions but show a slightly smaller height at higher centrifugal forces.

This indicates that the transfer functions derived from the simulation are accurately represented by the theoretical streamline calculation. Furthermore, the results demonstrate that the flow profile within the CDMA has no significant impact on the transfer behavior as long as it stays laminar. At higher speeds, a small distortion of the transfer function occurs when the circumferential speed is not yet fully developed at the inlet of the classification gap. The absence of a shift in the transfer function serves to substantiate the assertions outlined in Section 4.2, which posits that the flow profile exerts no essential influence in this particular context.

It should be pointed out that the boundary condition at the aerosol inlet has a much more severe influence on the transfer function: A previous study [15] showed that the assumption of a constant particle concentration and a laminar flow profile at the aerosol inlet may lead to significantly different transfer functions if compared to the assumption of

a constant particle flux density at the aerosol inlet as typically assumed and as applied in this study.

6. Measurement of Transfer Functions

In order to validate the theory and the experimental CDMA prototype, the real transfer function has been investigated experimentally.

6.1. Theory

As shown in Ruther et al. [14], a tandem setup comprising a DMA and a CDMA is employed to determine the transfer functions Ω (c.f. Figure 13). Following the assumption of a broad distribution of the test aerosol, the ratio of the number concentrations (n_1 and n_2 before and after the CDMA classification) can be described as follows [20]:

$$n_2/n_1 = \frac{\int_{-\infty}^{+\infty} \Omega_1\left(\widetilde{Z}\right) \cdot \Omega_2\left(\widetilde{Z}\right) \mathrm{d}\widetilde{Z}}{\int_{-\infty}^{+\infty} \Omega_1\left(\widetilde{Z}\right) \mathrm{d}\widetilde{Z}} \tag{13}$$

The transfer functions in general are well described by Gaussian functions [15]. Therefore, the transfer function Ω_1 of the pre-classifying DMA and the transfer function Ω_2 of the CDMA at zero rotation can be described using the parameters of the Gaussian function $\Omega_{1,\max}, \Omega_{2,\max}, \widetilde{\mu}_{1,\widetilde{Z}}, \widetilde{\mu}_2, \sigma_{1,\widetilde{Z}}, \sigma_2$ as follows:

$$\Omega_1 = \Omega_{1,\max} \cdot \exp\left\{-\frac{(\widetilde{Z} - \widetilde{\mu}_{1,\widetilde{Z}})^2}{\sigma_{1,\widetilde{Z}}^2}\right\} \quad ; \quad \Omega_2 = \Omega_{2,\max} \cdot \exp\left\{-\frac{(\widetilde{Z} - \widetilde{\mu}_2)^2}{\sigma_2^2}\right\} \tag{14}$$

Inserting Equation (14) in Equation (13) leads to [14]:

$$n_2/n_1 = \Omega_{1,\max} \cdot \Omega_{2,\max} \cdot \sqrt{\frac{1}{\sigma_{1,\widetilde{Z}}^2 + \sigma_2^2}} \cdot \exp\left\{-\frac{(\widetilde{\mu}_2 - \widetilde{\mu}_{1,\widetilde{Z}})^2}{\sigma_{1,\widetilde{Z}}^2 + \sigma_2^2}\right\} \tag{15}$$

This means that measuring the ratio n_2/n_1 for a fixed voltage applied to the upstream DMA (i.e., $\mu_{1,\widetilde{Z}}$ fixed) while varying the voltage of the CDMA (i.e., varying the $\widetilde{\mu}_2$), makes it possible to determine the transfer function by simply fitting a Gaussian function to the measured $n_2/n_1(\widetilde{\mu}_2)$, if the transfer function of the pre-classifying DMA is known [14].

The exact approach to determine these parameters with high accuracy is described in Appendix B, so that $c_{\widetilde{Z}}$ and $\widetilde{\mu}_{1,\widetilde{Z}}$ are determined as follows:

$$\sigma_{1,\widetilde{Z}} = 0.5732 \cdot \beta \tag{16}$$

$$\widetilde{\mu}_{1,\widetilde{Z}} = 1.0154 \tag{17}$$

This procedure for determining the transfer function of a DMA-DMA setup can be applied to a DMA-AAC setup (or in this case a DMA-CDMA setup with the CDMA operated at $U = 0V$) as well. In the case of spherical particles, the mobility of the first DMA can be converted into the particle relaxation time.

Defining the transfer functions as follows:

$$\Omega_1 = \Omega_{1,\max} \cdot \exp\left\{-\frac{(\widetilde{\tau} - \widetilde{\mu}_{1,\widetilde{\tau}})^2}{\sigma_{1,\widetilde{\tau}}^2}\right\} \quad ; \quad \Omega_2 = \Omega_{2,\max} \cdot \exp\left\{-\frac{(\widetilde{\tau} - \widetilde{\mu}_2)^2}{\sigma_2^2}\right\} \tag{18}$$

Powders **2025**, *4*, 11

Because of the charge distribution, other particle sizes can pass the pre-classifying DMA as well. Therefore, the particle number is quite different for the considered particle size interval. This must be corrected, as shown in Rüther et al. [14]. The following parameters can then be determined by applying Equation (A1).

$$\sigma_{1,\tilde{\tau}} = 0.6369 \cdot \beta \tag{19}$$

$$\tilde{\mu}_{1,\tilde{\tau}} = -0.99477 \tag{20}$$

These values can be used to calculate the transfer functions for the CDMA corresponding to Equation (15), i.e., replacing $\sigma_{1,\tilde{Z}}$ and $\mu_{1,\tilde{Z}}$ by $\sigma_{1,\tilde{\tau}}$ and $\mu_{1,\tilde{\tau}}$, respectively.

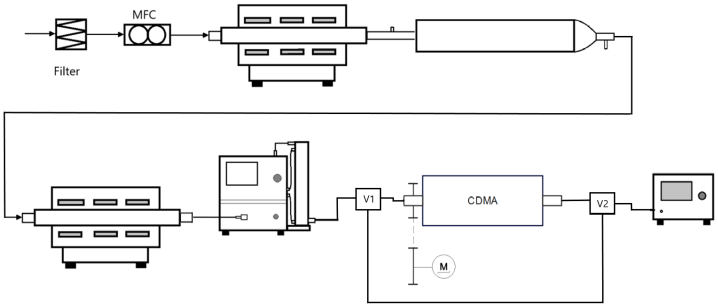

Figure 13. Schematic of the entire experimental setup: test aerosol production with two tube furnaces (Nabertherm) and an agglomeration tube, as well as the consecutive setup for the measurement of a transfer function consisting of a classifier (TSI 3080) with a DMA (TSI 3081), CDMA and CPC (TSI 3775) [14].

6.2. Production of the Test Aerosol and Measurement Setup

A method for producing an aerosol of a relatively immutable, broad particle size distribution for a large time period was developed using a setup comprising two hot-wall reactors with an agglomeration tube ($V = 10\,\mathrm{l}$) positioned between them (see Figure 13). An air flow rate of (2 l/min) controlled by a mass flow controller (MFC) is introduced into the setup. Silver is melted and evaporated at a temperature of 1150 °C within the upstream hot-wall reactor. Upon cooling towards the exit of the first furnace, the vapor becomes supersaturated, resulting in the immediate formation of silver particles. Subsequently, larger agglomerates are formed in the agglomeration tube, which are ultimately sintered into spherical particles in the second hot-wall reactor at 750 °C.

Subsequently, the spherical particles are pre-classified in a DMA, which is set to a specific mobility value. The valves $V1$ and $V2$ allow to bypass the CDMA completely, allowing to directly determine the number concentration n_1 by the CPC. Alternatively, by closing the bypass route, the aerosol will be classified by the CDMA. In this case, the CDMA was programmed to run sweeps for the voltage or the rotational velocity, respectively. Consequently, the CPC will determine the number concentration n_2 as a function of the operating parameter $n_2 = f(U, \omega)$.

6.3. Experimental Determination of the CDMA Transfer Function for $\tilde{\tau} = 0$ and $\tilde{Z} = 0$ at Different β-Values

Transfer functions of the CDMA prototype have been determined as described in the previous section. However, these transfer functions are not only affected by the deterministic particle trajectories in the classification gap. In the case of the CDMA prototype geometry where the gap width is quite small, diffusion strongly influences the transfer function. This

Powders **2025**, *4*, 11

leads to a broader transfer function with reduced height. However, the change in the transfer functions can be theoretically predicted pretty well [15]. Additionally, Rüther et al. [14] demonstrated that in the CDMA prototype, increased losses occur in the sample outlet due to still-existing electric and centrifugal fields. Nevertheless, as shown in Rüther et al. [14], such losses can be predicted by particle trajectory simulation based on the respective electrical and centrifugal fields. Such predicted losses can be used to correct the measured transfer functions accordingly. In the following, all presented parameters of the transfer functions have been adapted after performing corresponding corrections to the measured transfer functions [14]. Therefore, the presented results should describe the transfer function of the deterministic classification process in the CDMA gap.

Figure 14 illustrates the parameters of this CDMA transfer function over a range of operational parameters in 'DMA mode', i.e., for $\widetilde{\tau} = 0$. When considering the height of the transfer function $\Omega_{\max}$ in Figure 14a, it is noticeable that there are obviously additional losses not covered by the above-mentioned simulations. Moreover, these additional losses in the aerosol inlet and outlet are particularly present in the case of reduced aerosol volume rates due to increased residence times. It is noteworthy that values exceeding 1 were observed in a few cases, which can be attributed to potential measurement errors or inaccuracies in the determination of the transfer function of the pre-classifying DMA.

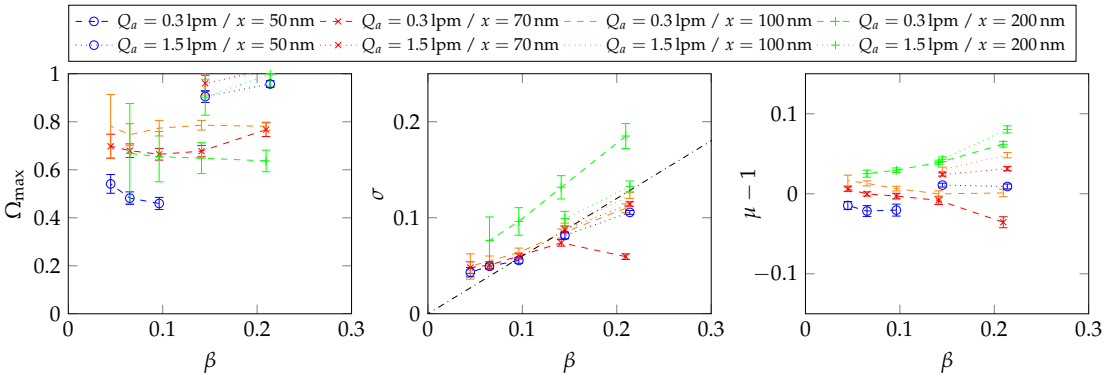

(**a**) Maximum Height (**b**) Width (**c**) Shift

Figure 14. Measured transfer function parameters of the CDMA in 'DMA mode' (i.e. for $\widetilde{\tau} = 0$) with 95% confidence interval derived out of three independent measurements, corrected for simulated diffusion in the measurement gap, electrical and centrifugal losses.

However, the width of the transfer function is nearly identical to the calculated ideal width (cf. Figure 14b). This indicates, that the broadening according to diffusion is well captured by the simulation so that the width of the corrected transfer function agrees very well with the expectations. Only the measurement series for 0.3 l/min exhibits a slight elevation for 200 nm particles, which most likely can be attributed to measurement errors. This is due to poor statistics because only a very small number of particles were counted at 200 nm, as this was at the edge of the particle size distribution of the test aerosol.

The shift of the transfer function (Figure 14c) is small and comparable to the results obtained for standard DMA instruments, which are presented in Figures A2–A7 in Appendix B.

The transfer functions for $\widetilde{Z} = 0$, i.e., operating the CDMA in AAC mode, are illustrated in Figure 15. It is important to note that for $\beta < 0.1$, there is no measurable transfer

function. This is due to massive particle losses occurring at the outlet due to the prevailing centrifugal forces. Thus, each measurement series comprises only two data points [14].

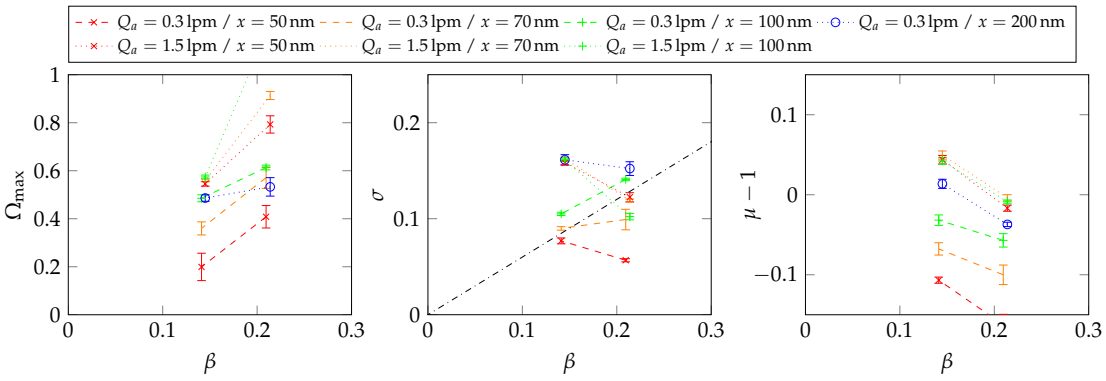

(**a**) Maximum Height (**b**) Width (**c**) Shift

Figure 15. Measured transfer function parameters of the CDMA operated in 'AAC mode' (i.e., for $\widetilde{Z} = 0$) with 95% confidence interval derived out of three independent measurements, corrected for simulated diffusion in the measurement gap, electrical and centrifugal losses.

Figure 15a illustrates the maximum height of the transfer functions. Despite the corrections, the transfer function remains dependent on the particle size and the prevailing flow conditions. This finding is particularly relevant in the context of rotational operation, because even small imperfections, such as deviations in production, a non-concentric alignment of both cylinders, and similar factors have a greater impact on the flow field, generating this dependency. The measurement was conducted over the entire CDMA (including transport to and from the measurement gap), thus precluding the possibility of correcting all undetermined losses. However, no direct correlation could be established between the corrected measurement values and further diffusion in the inlet and outlet. A number of other loss mechanisms occur here that cannot simply be separated. Thus, no equivalent loss length for diffusion, as would be present when flowing through a pipe, could be determined.

Figure 15b illustrates the width of the transfer function. The measured values displayed do not exhibit a correlation with the beta values as the range of variation is too big. This can be attributed to the inaccuracies and the considerable losses of the CDMA system. In comparison to $\widetilde{\tau} = 0$, a non-negligible shift in the transfer function (c.f. Figure 15c) is also present. This indicates a dependency on particle size, volume flows or rotational speed.

6.4. Experimental Determination of the Transfer Function for $\widetilde{\tau} = 0$ and $\widetilde{Z} = 0$ at $\beta = 0.2$

In this section, we will focus on the targeted operating conditions of the CDMA ($Q_a = 0.3\,\mathrm{l/min}$ at $\beta = 0.2$). As part of this investigation, the transfer functions for particles of varying sizes are measured once more under these conditions. The resulting data are presented in Figure 16.

After the correction of simulated modification by diffusion in the measurement gap and simulated losses due to electrical and centrifugal forces in the outlet, it can be observed that the heights of the transfer functions (see Figure 16a) are only weakly depending on particle size in the examined size range from 50 nm to 200 nm. Even for operation in 'DMA mode' or 'AAC mode' the heights of the transfer functions are in a similar range. It is notable that the widths of the transfer functions exhibit a slight upward deviation for larger

particles, which again can be attributed to the poor statistics due to a relatively low particle number of particles exceeding 150 nm.

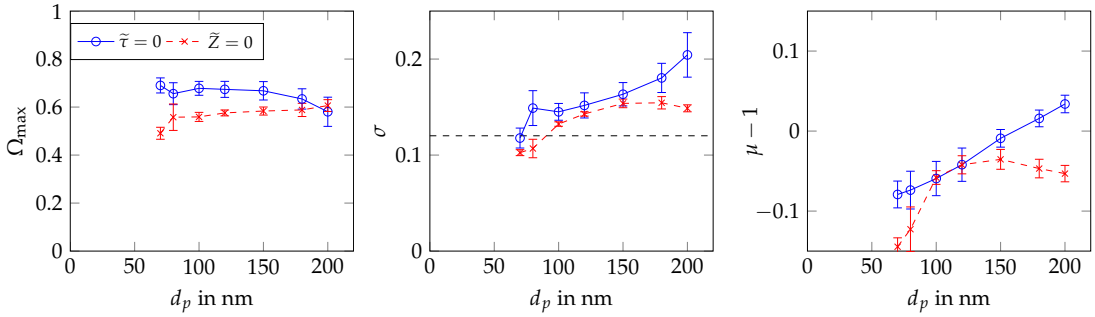

(**a**) Maximum Height (**b**) Width (**c**) Shift

Figure 16. Measured transfer function parameters of the CDMA for $\beta = 0.2$ with $Q_a = 0.3$ lpm at different particle sizes d_p with 95% confidence interval derived from three independent measurements, corrected for simulated diffusion in the measurement gap, electrical and centrifugal losses.

If all applied corrections as outlined above would cover all non-idealities, the resulting height of the transfer functions shown in Figure 16a should be close to 1 for all particle sizes. However, if we determine an average value from all measured height values, we obtain a height reduction factor, $\eta_{\text{HeightRed}} = 0.61$. In fact, this $\eta_{\text{HeightRed}}$ accounts for all additional losses, e.g., diffusional losses in the inlet and outlet tubing, losses due to centrifugal forces in the inlet section, etc.

Thus, the real transfer function can be well estimated by correcting the theoretical transfer function (c.f. Section 5) with simulated modifications by diffusion as well as simulated losses in the outlet due to electrical and centrifugal forces as outlined above and subsequent scaling with $\eta_{\text{HeightRed}}$. Since the width of the transfer function does not exhibit significant variations, particularly not in a systematic manner, the width of the transfer function is adopted according to the mean width, as shown in Figure 16b. Additionally, a shift correction factor, $\epsilon_{\text{Shift}} = -0.051$, is introduced to align the theoretical transfer function with the experimentally measured one.

By assuming that these corrections are applicable not only to the transfer functions at $\widetilde{Z} = 0$ and $\widetilde{\tau} = 0$ but also to the entire two-dimensional transfer function, a generalized description of the real transfer function for any given operating condition is obtained.

7. Measurement Results and Analysis of Two-Dimensional Size Distributions for Different Sintering Stages of Silver Nanoparticles

The previous section provided a brief overview of the measurement process for determining the transfer function of the CDMA. Unlike the ideal transfer function, the measured transfer function inherently accounts for all real-world imperfections and deviations. To accurately model the system, the ideal transfer function is adjusted based on these measured values (as explained in Section 6.4). This 2D transfer function is then used to calculate the kernel matrix $\underline{\underline{\boldsymbol{K}}}_{i,j,k,l}$, which must be known in order to calculate the expected measured sample number concentrations for given operating conditions $\Delta N(U_i, \omega_j)$ for a given 2D particle size density distribution $q(d_{m,k}, d_{St,l})$ with respect to mobility diameter d_m and Stokes diameter d_{St}:

$$\frac{\Delta N(U_i, \omega_j)}{N_{\text{tot}}} = \sum_k \sum_l \underline{\boldsymbol{K}}_{i,j,k,l} \cdot q_{k,l} \cdot \Delta\log(d_{m,k}) \cdot \Delta\log(d_{St,l}) \tag{21}$$

Details on how this kernel matrix can be derived for a given 2D transfer function are given in [16].

In order to determine a 2D size distribution from measured number concentrations at the CDMA sample outlet requires an inversion of a so-called ill-posed problem. As outlined in the introduction, there are many different approaches to solving such inversion problems. As described in detail by Rüther et al. [16], the POCS (Projection onto Convex Sets) algorithm which is well established e.g., in the field of image reconstruction, was applied to a particle characterization problem for the first time. It is an iterative algorithm that allows to consider an arbitrary number of conditions, e.g., Equation (21), marginal distributions, which can be determined independently by operation of the CDMA in 'DMA mode' and 'AAC mode', respectively, and the normalization of density distribution or non-negativity of density distribution. This algorithm proved to be excellently suited to efficiently and accurately solve this inversion problem.

7.1. Production of the Aerosol and Measurement Setup for Two-Dimensional Distributions

The first measurements of a two-dimensional particle size distribution are carried out using the test aerosol setup shown in Section 6.2 but with no pre-classifying DMA. This setup is shown in Figure 17. In this study, agglomerates at different sintering stages shall be produced by controlling the temperature of the second furnace intended for controlled sintering. Here, temperatures of 20 °C, 60 °C, 100 °C, 175 °C, 250 °C, and 400 °C are used.

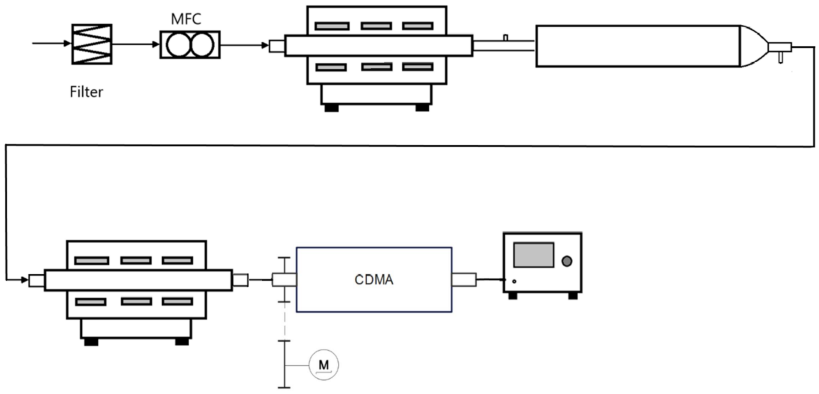

Figure 17. Schematic of the experimental setup for investigation of the two-dimensional distribution at different sintering stages: test aerosol production with a tube-furnace (Nabertherm) at 1150 C, an agglomeration tube and a sintering tube-furnace (Nabertherm) at 20 °C, 60 °C, 100 °C, 175 °C, 250 °C and 400 °C. Followed by the CDMA with a classifier (TSI 3080) providing the voltage and sheath air, and a CPC (TSI 3775).

7.2. Derivation of Further Properties

From the two-dimensional distribution of the mobility and Stokes diameter, it is possible to derive other quantities characterizing the particle shape like the aerodynamic d_{ae} and volume d_v equivalent diameters, the effective density ρ_{eff} or the shape factor χ [21].

$$d_{ae} = d_{st} \cdot \sqrt{\rho/\rho_0} \tag{22}$$

$$d_v = (d_{st}^2 \cdot d_m)^{1/3} \tag{23}$$

$$\rho_{eff}/\rho = (d_v/d_m)^3 \tag{24}$$

$$\chi = d_m/d_v \tag{25}$$

Since a sphere experiences a smaller drag force than any other particle of the same volume, the following relations are valid:

$$\rho \geq \rho_{eff} \quad ; \quad \chi \geq 1 \quad ; \quad d_m \geq d_v \geq d_{St} \tag{26}$$

7.3. Measurement Results

Figure 18 shows the two-dimensional distributions of the aforementioned quantities at different sintering temperatures. The measurement comprises 29 voltages, which are logarithmically distributed between 0 and 250 V, and 14 speeds, which are logarithmically distributed between 0 RPM and 1500 RPM. This results in a total measurement time of about 12 h. We are aware that such a measurement time is not acceptable for many applications. However, we expect to reduce this measurement time by a factor 10–20 by continuously scanning the voltage instead of increasing it stepwise. Furthermore, after the marginal distributions are measured right at the beginning by running scans in 'DMA mode' and 'AAC mode', respectively, an intelligent, automatic determination of the relevant range for U and ω will further reduce the required measuring time.

At high sintering temperatures (for example, 400 °C, as shown in Figure 18), the agglomerates are supposed to be completely sintered forming almost perfect spherical particles. This can be clearly seen from all representations of the measured 2D distributions: the relative effective density ρ_{eff}/ρ and shape factor χ for all particles are close to 1 and, therefore, the $\rho_{eff}/\rho - d_m$-distribution and the $\chi - d_m$-distribution are becoming more or less 1D-distributions of d_m, with the other value being constant. The d_{st}/d_m-distribution shows a bi-sectional distribution since for spherical particles, $d_m = d_{st}$.

For lower sintering temperatures, more irregularly shaped agglomerates are produced, and therefore, the relative effective density becomes lower than 1, and the shape factor becomes larger than 1. Consequently, true 2D distributions can be determined giving detailed information about the size and structure of the agglomerates (c.f. Figures A8–A10 in the Appendix C for more sintering stages in between). Since the Stokes diameter is always less or equal to the mobility diameter, the corresponding 2D distribution is more skewed towards d_m for less sintered agglomerates. It can be clearly seen that for a sintering temperature of 175 °C, there are still a few almost spherical particles while only agglomerate particles with quite diverse mobility shape factor larger than 1 are present if the second furnace is set to 20 °C, i.e., no sintering occurs at all.

It is clearly demonstrated that the new measurement technique provides a powerful means to determine valuable information about the size and structural properties of the agglomerates. This can be used to obtain a deeper understanding of aerosol synthesis if applied to corresponding processes. In particular, relevant particle properties can be determined by directly enabling, for example, the optimization of the synthesis conditions for generating particles more efficiently.

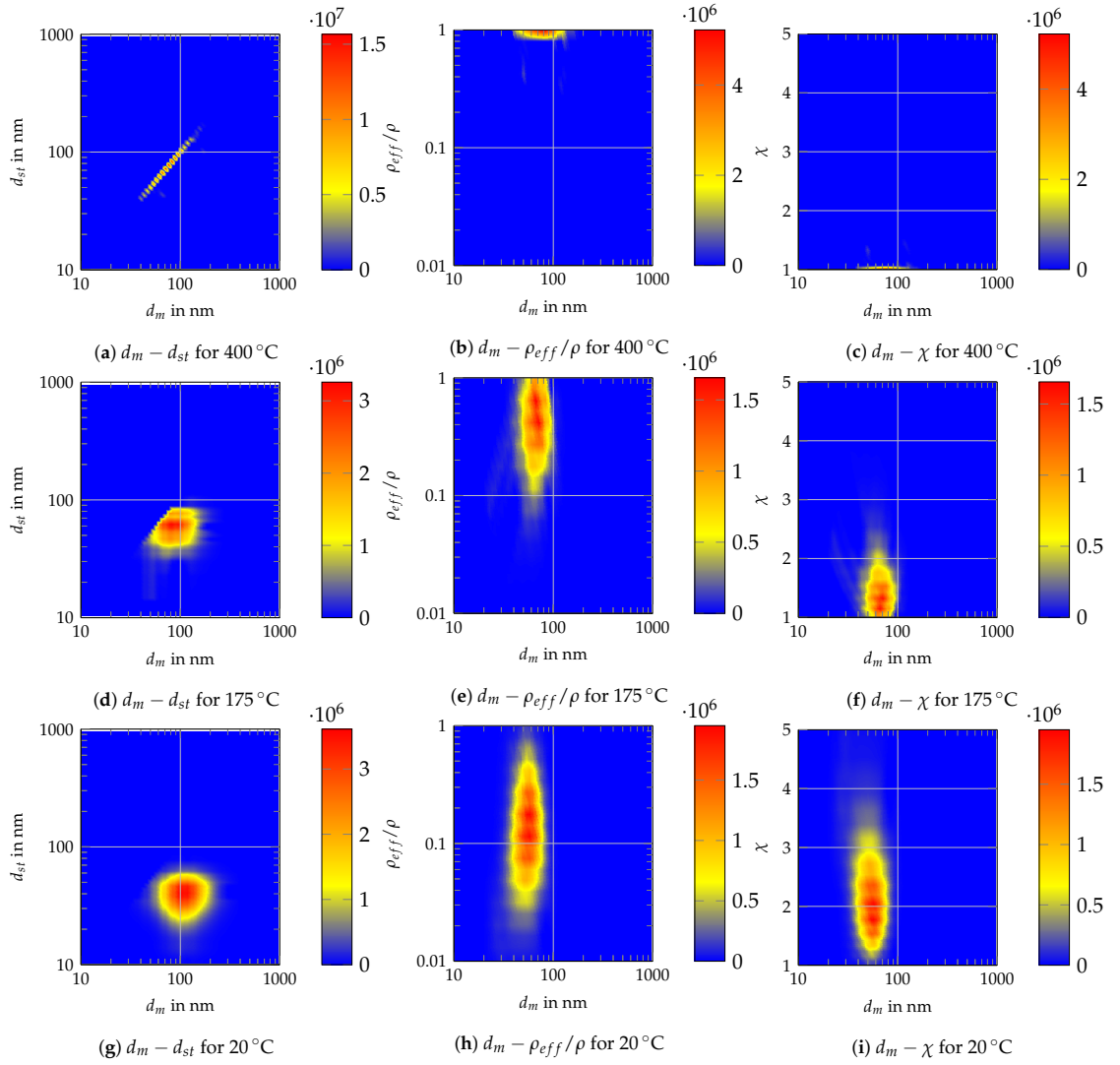

Figure 18. Measurement results for silver particles at different sintering temperatures.

8. Conclusions

The proposed methodology for determining two-dimensional property distributions has significant potential for both research and industrial processes. With these additional insights, the behavior of complex particle systems can be more comprehensively understood.

The Centrifugal Differential Mobility Analyzer can measure two-dimensional distributions, e.g., regarding the mobility and Stokes diameter, thus enabling the investigation of the distribution of different other characteristic property values. The new approach has the advantage that the measurement can be performed with one single instrument and be evaluated with an established inversion algorithm. Moreover, avoiding the tandem set-up provides much better statistical significance due to higher particle concentrations at the sample outlet. The functionality of the prototype was validated and then meticulously characterized to identify potentials for further improvements. Even though a

number of weaknesses in the first prototype were identified, it is feasible to determine the actual transfer functions with good accuracy, thereby enabling data inversion on this basis. The data inversion is highly robust and yields plausible results [16], which can be converted into further property distributions. In comparison with one-dimensional measurement techniques, the CDMA offers a substantial increase in the amount of information obtained.

As the next step, the design of the CDMA prototype will be comprehensively revised to significantly reduce losses in the inlet and outlet regions, thereby improving measurement accuracy [14]. This optimization can be further enhanced by employing more advanced CFD simulations, particularly including the complete inlet and outlet regions and attached tubings, to resolve all flow non-idealities accurately. Simulating particle trajectories based on these flow simulations should then allow to predict all losses more accurately. Additionally, diffusion can be minimized by increasing the gap width [15], while the flow field within the CDMA can be optimized for higher rotational speeds. Furthermore, the implementation of a scanning mode for the voltage, as applied in SMPS systems, will enable a substantial reduction in the measurement time, thereby rendering the entire measurement process less susceptible to errors, i.e., fluctuations of the aerosol generation process. At that stage, it will become considerably more straightforward to examine other particulate systems and assess the performance of the CDMA across a range of materials and particle sizes. Subsequent investigations should also cover the further validation of results, such as the actual particle sizes and effective density, using electron microscopy images or a comparison with tandem setups, e.g., a DMA-AAC setup. Furthermore, combining the CPC with a Faraday-Cup-electrometer would result in more information and thus in an improvement in the data inversion quality. Additionally, the introduction of sensitivity analyses concerning operating parameters and diffusion effects could contribute to a more comprehensive understanding of the CDMA.

Moreover, the CDMA set-up is not only useful for determining size and shape. If the particle shape of a test aerosol can be considered as known, it is feasible to determine the charge distribution or the Cunningham slip correction, thereby establishing a novel methodology for determining these properties, particularly for non-spherical particles. Since the presented study focuses on the determination of particle shape by including centrifugal forces, it is essential to know the particle material density with a high degree of precision. However, in the case of unknown particle systems, only the aerodynamic diameter can be determined, giving no direct information on the actual particle shape. However, if particle shape is known (e.g., compact, almost spherical), the 2D size-density-distribution could be determined instead. Moreover, integration with additional measurement systems could enable access to a three-dimensional distribution of properties. For instance, it may be feasible to examine the scattered light behavior of particles to integrate mass spectrometry or low-pressure impaction of the sample aerosol.

Author Contributions: Conceptualization, T.N.R. and H.-J.S.; methodology, T.N.R. and H.-J.S.; software, T.N.R., S.G. and C.D.; validation, T.N.R., S.G. and C.D.; formal analysis, T.N.R.; investigation, T.N.R. and H.-J.S.; resources, T.N.R. and H.-J.S.; data curation, T.N.R. and S.G.; writing—original draft preparation, T.N.R.; writing—review and editing, H.-J.S., S.G. and C.D.; visualization, T.N.R. and S.G.; supervision, H.-J.S.; project administration, H.-J.S.; funding acquisition, H.-J.S. All authors have read and agreed to the published version of the manuscript.

Funding: This work was supported by the German Research Foundation under the SPP 20245 MehrDimPart (GZ: SCHM 1429/19-1).

Data Availability Statement: Code availability is given under: https://git.uni-paderborn.de/pvt/cdma, reference number 11577 (CDMA, 2025).

Conflicts of Interest: The authors declare no conflicts of interest.

Abbreviations

The following abbreviations are used in this manuscript:

CDMA	Centrifugal Differential Mobility Analyzer
DMA	Differential Mobility Analyzer
AAC	Aerodynamic Aerosol Classifier
CPC	Condensation Particle Counter
lpm	Standard liters per minute
RPM	Revolutions per minute
MFC	Mass-flow Controller

Nomenclature

κ	ratio of r_i to r_o	–
β	ratio of Q_a to Q_{sh}	–
χ	shape factor	–
η	dynamic viscosity	Pas
Ω	transfer function of classifier	–
Ω	transfer function	–
ω	angular speed $\omega = 2\pi \cdot n$	1/s
ρ	particle density	kg/m^3
ρ_0	assumed reference density of $1000\,kg/m^3$	kg/m^3
ρ_{eff}	effective density	kg/m^3
σ	standard deviation of Gaussian shaped transfer function	–
σ	width of the transfer function	–
τ	particle relaxation time	s
τ^*	nominal particle relaxation time	s
$\underline{\boldsymbol{K}}$	Kernel matrix	–
$\widetilde{\mu}_2, \widetilde{\mu}_1$	fit parameters for the shift of a Gaussian function	–
$\widetilde{\tau}$	normalized particle relaxation time	–
$\widetilde{h}$	ratio of the gap width to the mean radius	–
$\widetilde{Z}$	normalized particle mobility	–
a_c	centrifugal acceleration	m/s^2
Cu	Cunningham slip correction factor	–
d_m	mobility equivalent diameter	m
d_v	volume equivalent diameter	m
d_{ae}	aerodynamic equivalent diameter	m
d_p	diameter of a spherical particle	m
d_{st}	stokes equivalent diameter	m
E	electric field	V/m
L	length of the CDMA classification gap	m
m_p	particle mass	kg
n	number of particle charges	–
N_{tot}	total number of simulated streamlines	#
$N_{\text{traversed}}$	number of successfully traversed streamlines	#
q	particle density distribution	–
Q_a	aerosol volume flow	m^3/s
Q_p	particle charge	As

Q_s	sample volume flow	m^3/s
Q_{ex}	excess air volume flow	m^3/s
Q_{sh}	sheath air volume flow	m^3/s
r_i	inner radius	m
r_o	outer radius	m
r_{ae}	outer radius of the aerosol air streamlines	m
r_s	inner radius of the sampling air streamlines	m
U	voltage	V
w_{Dr}	particle drift velocity	m/s
x	length coordinate in axial direction	m
Z^*	nominal particle mobility	$m^2/(Vs)$
Z_p	particle mobility	$m^2/(Vs)$

Appendix A. Further Illustration of the CFD Simulation

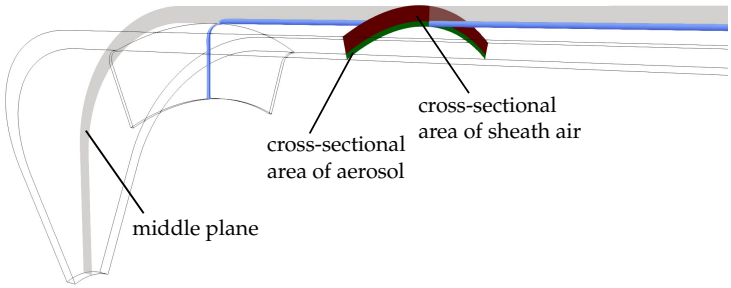

Figure A1. Schematic drawing of the flow sections and the middle plane.

Appendix B. Transfer Function Parameter Determination

As it is very important to know the transfer function of the pre-classifying DMA precisely when measuring the transfer function of the CDMA via a tandem setup (see Equation (13)), this section describes how this DMA transfer function can be determined precisely in advance.

For this purpose, three identical DMAs (Long DMA TSI 3081) were measured in each possible tandem setup arrangement. The aerosol used was a silver aerosol, which was produced as in Section 3. Please keep in mind that Equation (13) is only applicable for broad particle size distributions at the inlet of the first DMA, i.e., the particle density distribution can be considered constant over a classification window of the DMA. Otherwise, the distribution must be included in the calculation. We now assume that all DMAs are identical and consequently have the same transfer function, which can be well described by a Gaussian function [15], i.e., $c = e$ and $\widetilde{\mu}_1 = \widetilde{\mu}_2$. Since $\widetilde{\mu}_2$ is the varied parameter for the data points to fit on, in this special case, $\widetilde{\mu}_1$ is fixed and must be set to one, and the resulting shift then is twice as high. Thus, Equation (15) for two identical DMA's results in:

$$n_2/n_1 = \sqrt{\frac{1}{2}} \cdot d \cdot \exp\left\{-\frac{(\widetilde{\mu}_2/2-1)^2}{2 \cdot e^2}\right\} \tag{A1}$$

To obtain comparative values that were as valid as possible, the aerosol volume flow rate was varied to 0.3 and 1.5 l/min, and the sheath air volume flow rate was varied to different values. This was done to ensure the most accurate and valid results possible. This method

enabled the analysis of different beta values. The series of measurements were conducted at particle sizes of 50, 70, 100, and 200 nm. For every measuring point, the mean value was calculated from three individual measurements, resulting in a measured parameter set for every setting (see Figure A2). To determine the characteristic parameters of every DMA, the mean value of $\widetilde{\mu}$ was first determined for every DMA–DMA combination. The c has a linear dependency to β so that a linear regression is applied to obtain a regression constant for every combination, so that $c = k \cdot \beta$. Table A1 lists the values for k^2 and $\widetilde{\mu}_2$ for the assumption that the tandem setup consists of two identical DMAs. It can be seen that the values for the combinations differ from each other, but there is some regularity, i.e., all combinations show a significantly broader transfer function since k^2 is considerably larger.

Table A1. Values for k^2 and $\widetilde{\mu}_2$ assuming two identical DMA's in a tandem setup.

DMA Combination	1-2	1-3	2-1	2-3	3-1	3-2
k^2	0.6778	1.0173	0.6964	1.0443	0.8622	0.8950
$\widetilde{\mu}_2$	1.0282	1.0568	1.0261	1.0504	0.9900	0.9891

In order to remove the assumption of identical transfer functions for all DMAs and to obtain individual parameters for every DMA, a system of equations is required. For the widths of the transfer function, we follow by comparing the coefficients of Equations (A1) and (15):

$$2 \cdot e^2_{\text{identical}} = c^2 + e^2 \tag{A2}$$

Therefore:

$$2 \cdot \beta^2 \cdot k^2_{\text{identical}} = (k^2_{\text{DMA1}} + k^2_{\text{DMA2}}) \cdot \beta^2 \tag{A3}$$

Thus, it is possible to set up a system of equations, where $2 \cdot k^2_{\text{identical}}$ is the solution vector for each combination, while k^2_{DMA1} and k^2_{DMA2} are the unknown variables.

The same can be done for $\widetilde{\mu}_2$:

$$(\widetilde{\mu}_{2,\text{identical}} - 1)/2 = \widetilde{\mu}_{\text{DMA2}} - \widetilde{\mu}_{\text{DMA1}} \tag{A4}$$

Here, $(\widetilde{\mu}_{2,\text{identical}} - 1)/2$ is the solution vector. Since the DMA's were interchanged in every direction, the system of equations was overdetermined, so the solution can be determined by least squares regression.

The height a of the transfer function for the pre-classifying DMA is not important, because it cancels out from Equation (15). This yields the parameters resulting for the DMAs, as shown in Table A2.

Table A2. Parameters of the analysed DMA's.

DMA	1	2	3
k	0.5732	0.5988	0.7818
$\widetilde{\mu}$	1.0154	1.0117	1.0080

Here, it is shown that DMA1 and DMA2 are very similar, but DMA3 has a much higher value for k, which yields a broader transfer function. This is also proved in Figures A2–A7, where it can be seen that for the figures where DMA3 is the second DMA, β is much higher, while for the other diagrams, the width β is around the theoretically ideal line (black dashed line).

Moreover, the maximum height of the transfer functions is decreasing with decreasing values for β. This is because for more narrow transfer functions, the influence of diffusion

is increasing. There is also a clear tendency from small to large particles at the maximum height, which is caused by diffusion. For some measurement points, the maximum height exceeds one. Here, DMA3 is the pre-classifying DMA. This indicates that there are discrepancies in the determination of the parameters or measurement errors.

The shift does not seem to have major dependencies on the β-values but seems to be influenced by the particle size or the volume flows itself. This is caused by deviations in the applied voltage of the system.

DMA1 appears to have the best properties; thus, it was selected as the pre-classifying DMA for the CDMA transfer function measurements.

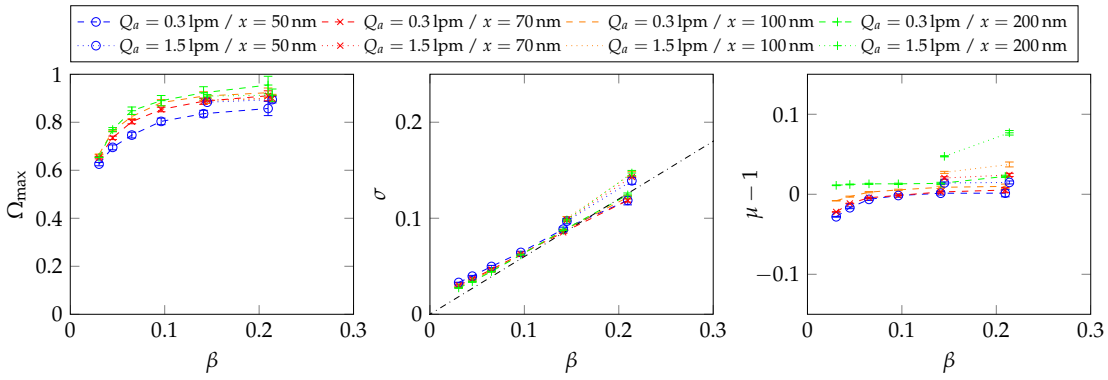

(**a**) Maximum Height (**b**) Width (**c**) Shift

Figure A2. Measured transfer function parameters of the the DMA combination 1-2, with 95% confidence interval derived out of three samples.

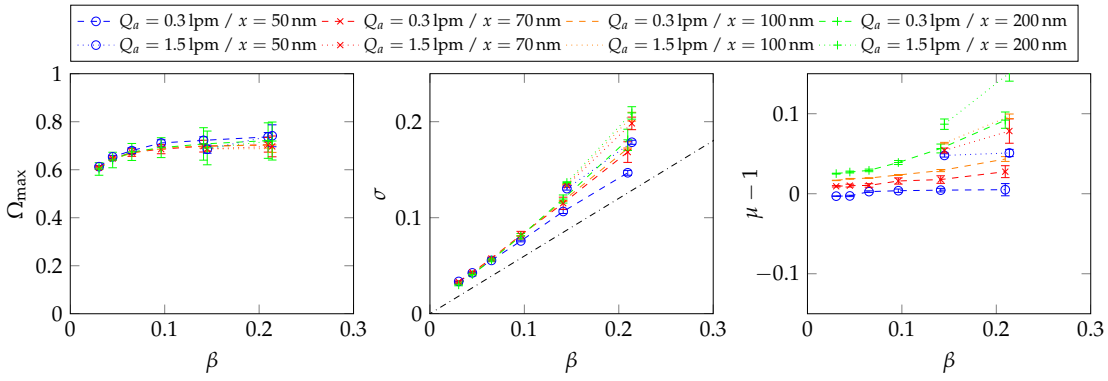

(**a**) Maximum Height (**b**) Width (**c**) Shift

Figure A3. Measured transfer function parameters of the the DMA combination 1-3, with 95% confidence interval derived out of three samples.

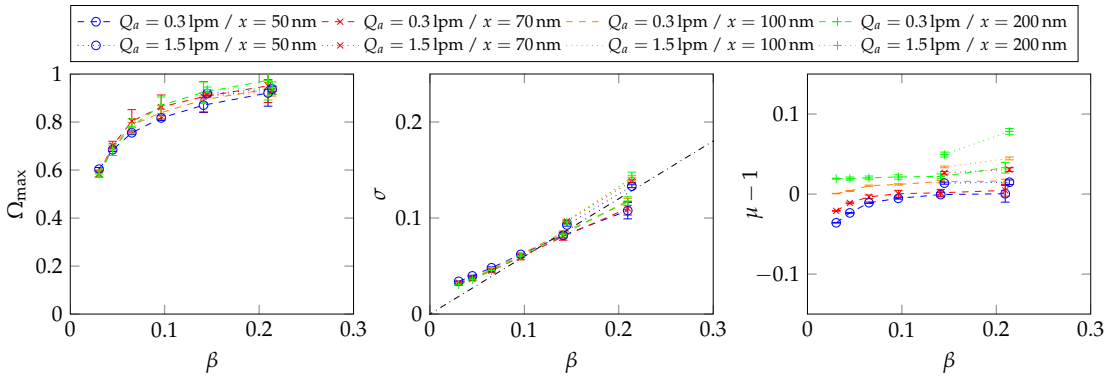

(**a**) Maximum Height (**b**) Width (**c**) Shift

Figure A4. Measured transfer function parameters of the the DMA combination 2-1, with 95% confidence interval derived out of three samples.

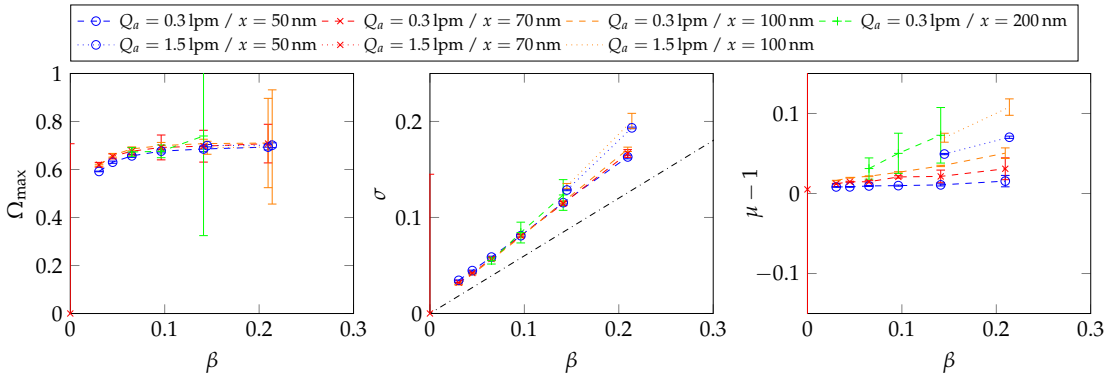

(**a**) Maximum Height (**b**) Width (**c**) Shift

Figure A5. Measured transfer function parameters of the the DMA combination 2-3, with 95% confidence interval derived out of three samples.

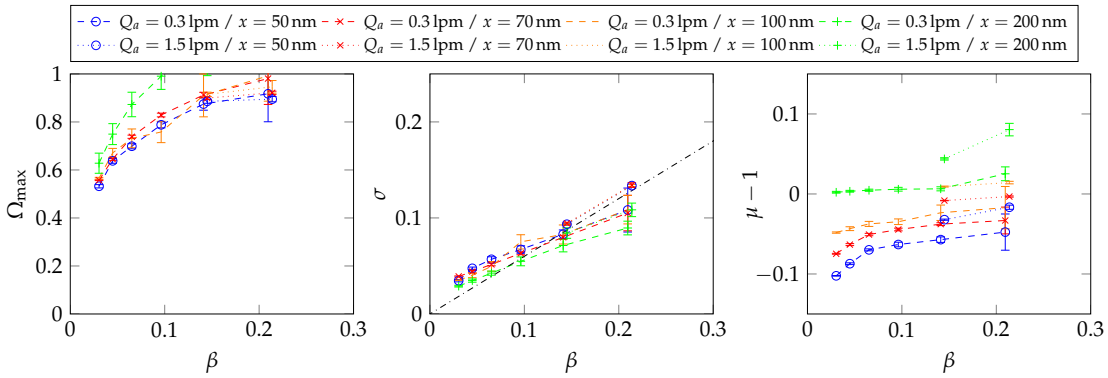

(**a**) Maximum Height (**b**) Width (**c**) Shift

Figure A6. Measured transfer function parameters of the the DMA combination 3-1, with 95% confidence interval derived out of three samples.

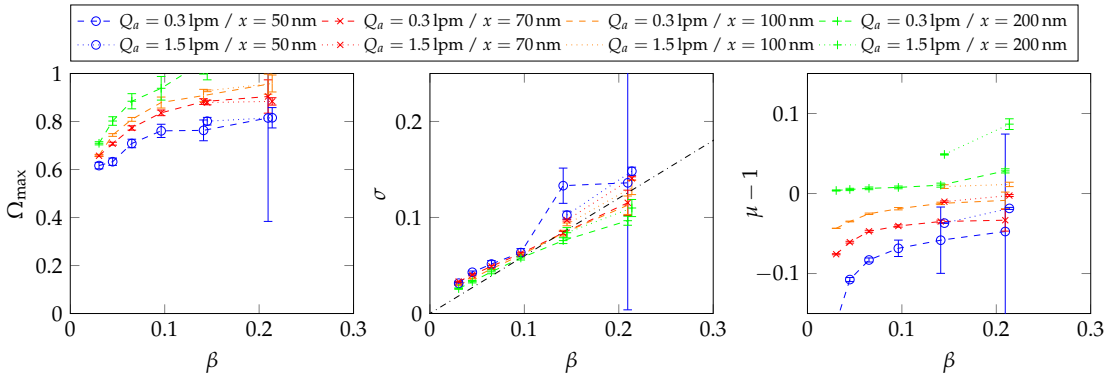

(**a**) Maximum Height (**b**) Width (**c**) Shift

Figure A7. Measured transfer function parameters of the the DMA combination 3-2, with 95% confidence interval derived out of three samples.

Appendix C. Two-Dimensional Property Distribution for Agglomerated Silver Particles Treated at Different Sintering Temperatures

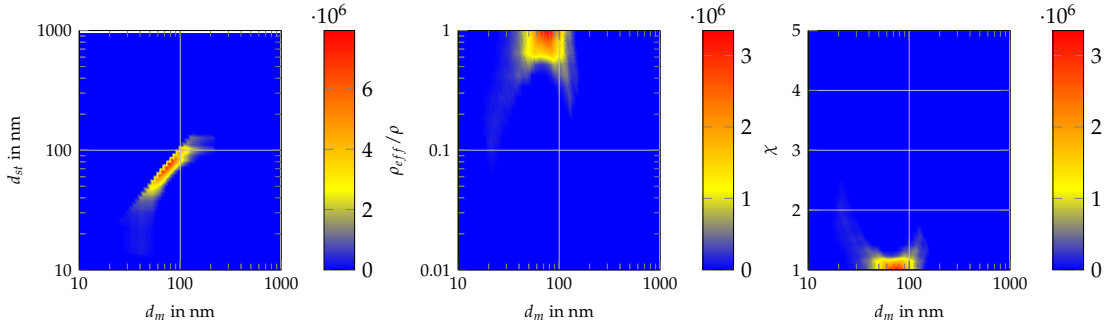

(**a**) Mobility diameter - Stokes diameter (**b**) Mobility diameter - effective density (**c**) Mobility diameter - shape factor

Figure A8. Measurement results for silver particles at a sintering temperature of 250 °C.

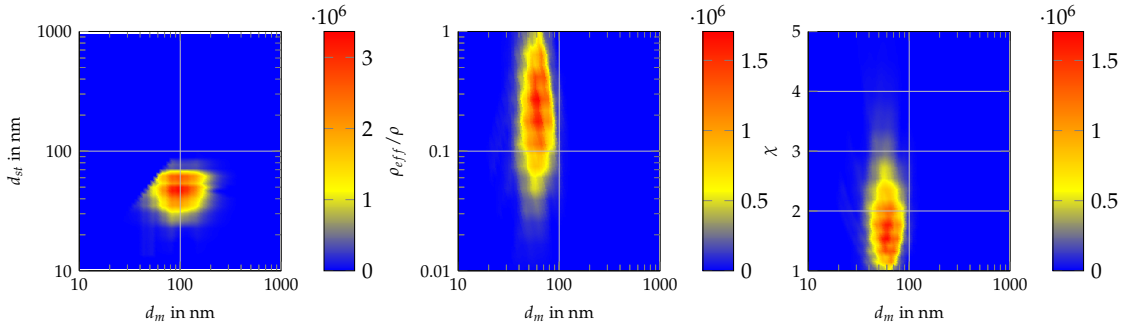

(**a**) Mobility diameter - Stokes diameter (**b**) Mobility diameter - effective density (**c**) Mobility diameter - shape factor

Figure A9. Measurement results for silver particles at a sintering temperature of 100 °C.

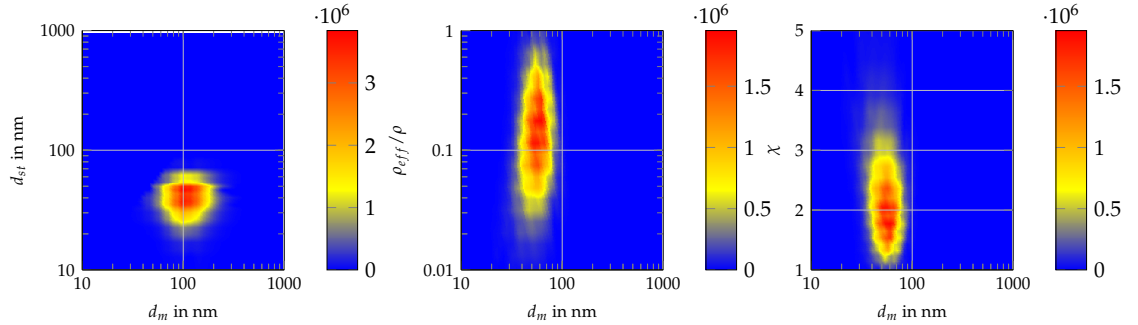

(**a**) Mobility diameter - Stokes diameter (**b**) Mobility diameter - effective density (**c**) Mobility diameter - shape factor

Figure A10. Measurement results for silver particles at a sintering temperature of 60 °C.

References

1. Baron, P.A.; Kulkarni, P.; Willeke, K. *Aerosol Measurement: Principles, Techniques, and Applications*, 3rd ed.; Wiley: Hoboken, NJ, USA, 2011.
2. Friedlander, S.K. *Smoke, Dust, and Haze: Fundamentals of Aerosol Dynamics*, 2nd ed.; Topics in Chemical Engineering; Oxford University Press: New York, NY, USA, 2000.
3. Colbeck, I. *Aerosol Science: Technology and Applications*, 2nd ed.; Wiley: Hoboken, NJ, USA, 2013.
4. Park, K.; Dutcher, D.; Emery, M.; Pagels, J.; Sakurai, H.; Scheckman, J.; Qian, S.; Stolzenburg, M.R.; Wang, X.; Yang, J.; et al. Tandem Measurements of Aerosol Properties—A Review of Mobility Techniques with Extensions. *Aerosol Sci. Technol.* **2008**, *42*, 801–816. [CrossRef]
5. Rawat, V.K.; Buckley, D.T.; Kimoto, S.; Lee, M.H.; Fukushima, N.; Hogan, C.J. Two dimensional size–mass distribution function inversion from differential mobility analyzer–aerosol particle mass analyzer (DMA–APM) measurements. *J. Aerosol Sci.* **2016**, *92*, 70–82. [CrossRef]
6. Buckley, D.T.; Kimoto, S.; Lee, M.H.; Fukushima, N.; Hogan, C.J. Technical note: A corrected two dimensional data inversion routine for tandem mobility-mass measurements. *J. Aerosol Sci.* **2017**, *114*, 157–168. [CrossRef]
7. Sipkens, T.A.; Olfert, J.S.; Rogak, S.N. Inversion methods to determine two-dimensional aerosol mass-mobility distributions II: Existing and novel Bayesian methods. *J. Aerosol Sci.* **2020**, *146*, 105565. [CrossRef]
8. Broda, K.N.; Olfert, J.S.; Irwin, M.; Schill, G.P.; McMeeking, G.R.; Schnitzler, E.G.; Jäger, W. A novel inversion method to determine the mass distribution of non-refractory coatings on refractory black carbon using a centrifugal particle mass analyzer and single particle soot photometer. *Aerosol Sci. Technol.* **2018**, *52*, 567–578. [CrossRef]
9. Sipkens, T.A.; Boies, A.; Corbin, J.C.; Chakrabarty, R.K.; Olfert, J.; Rogak, S.N. Overview of methods to characterize the mass, size, and morphology of soot. *J. Aerosol Sci.* **2023**, *173*, 106211. [CrossRef]
10. Tavakoli, F.; Olfert, J.S. Determination of particle mass, effective density, mass–mobility exponent, and dynamic shape factor using an aerodynamic aerosol classifier and a differential mobility analyzer in tandem. *J. Aerosol Sci.* **2014**, *75*, 35–42. [CrossRef]
11. Knutson, E.O.; Whitby, K.T. Aerosol classification by electric mobility: Apparatus, theory, and applications. *J. Aerosol Sci.* **1975**, *6*, 443–451. [CrossRef]
12. Slowik, J.G.; Stainken, K.; Davidovits, P.; Williams, L.R.; Jayne, J.T.; Kolb, C.E.; Worsnop, D.R.; Rudich, Y.; DeCarlo, P.F.; Jimenez, J.L. Particle Morphology and Density Characterization by Combined Mobility and Aerodynamic Diameter Measurements. Part 2: Application to Combustion-Generated Soot Aerosols as a Function of Fuel Equivalence Ratio. *Aerosol Sci. Technol.* **2004**, *38*, 1206–1222. [CrossRef]
13. Tavakoli, F.; Olfert, J.S. An Instrument for the Classification of Aerosols by Particle Relaxation Time: Theoretical Models of the Aerodynamic Aerosol Classifier. *Aerosol Sci. Technol.* **2013**, *47*, 916–926. [CrossRef]
14. Rüther, T.N.; Rasche, D.B.; Schmid, H.J. The Centrifugal Differential Mobility Analyser—A New Device for Determination of Two-Dimensional Property Distributions. *Aerosol Res.* **2025**, *3*, 65–79. [CrossRef]
15. Rüther, T.N.; Schmid, H.J. Prediction of the transfer function for a Centrifugal Differential Mobility Analyzer by Streamline functions. *Aerosol Sci. Technol.* 2025, *submitted*.
16. Rüther, T.N.; Rasche, D.B.; Schmid, H.J. The POCS-Algorithm—An effective tool for calculating 2D particle property distributions via Data Inversion of exemplary CDMA measurement data. *Aerosol Sci.* 2025, *submitted*.
17. Allen, M.D.; Raabe, O.G. Slip correction measurements for aerosol particles of doublet and triangular triplet aggregates of spheres. *J. Aerosol Sci.* **1985**, *16*, 57–67. [CrossRef]

18. Stolzenburg, M.R. An Ultrafine Aerosol Size Distribution System. Ph.D. Thesis, University of Minnesota, Minneapolis, MN, USA, 1988.
19. Könözsy, L., The $k-\omega$ Shear-Stress Transport (SST) Turbulence Model. In *A New Hypothesis on the Anisotropic Reynolds Stress Tensor for Turbulent Flows: Volume I: Theoretical Background and Development of an Anisotropic Hybrid $k-\omega$ Shear-Stress Transport/Stochastic Turbulence Model*; Springer International Publishing: Cham, Switzerland, 2019; pp. 57–66. [CrossRef]
20. Li, W.; Li, L.; Chen, D.R. Technical Note: A New Deconvolution Scheme for the Retrieval of True DMA Transfer Function from Tandem DMA Data. *Aerosol Sci. Technol.* **2006**, *40*, 1052–1057. [CrossRef]
21. DeCarlo, P.F.; Slowik, J.G.; Worsnop, D.R.; Davidovits, P.; Jimenez, J.L. Particle Morphology and Density Characterization by Combined Mobility and Aerodynamic Diameter Measurements. Part 1: Theory. *Aerosol Sci. Technol.* **2004**, *38*, 1185–1205. [CrossRef]

5 Zusammenfassung

Der Centrifugal Differential Mobility Analyzer (CDMA) stellt eine innovative Methode zur simultanen Bestimmung zweidimensionaler Partikelgrößenverteilungen dar. Das von Rasche entwickelte Konzept wurde genutzt, um einen Prototypen zu entwerfen, zu konstruieren, zu fertigen und aufzubauen. Dabei sind neben der präzisen Konstruktion der Einzelteile und der Programmierung des Zusammenspiels aller Systemkomponenten insbesondere auch methodische Aspekte der Evaluierung des Messaufbaus von zentraler Bedeutung. So konnte beispielsweise eine reibungsfreie Dichtung zwischen der rotierenden Welle und dem Lager durch eine eigens konstruierte Ferrofluid-Dichtung realisiert werden. Darüber hinaus wurde ein neuartiger Ansatz entwickelt, bei dem die Transferfunktion des CDMA über ein Tandem-DMA-CDMA-Setup vergleichsweise einfach bestimmt werden kann. Diese Methodik wurde anschließend auf reale Messungen angewendet, wobei erste Transferfunktionen erfolgreich ermittelt wurden. Dies untermauerte sowohl die Validität der Methode als auch die Funktionstüchtigkeit des Messaufbaus.
Die Messungen zeigten jedoch insbesondere bei schmalen Transferfunktionen eine erhebliche Partikelabscheidung. Weitere Untersuchungen, darunter Simulationen des elektrischen Feldes, verdeutlichten, dass sowohl das elektrische Feld als auch die Zentrifugalkräfte maßgeblich zu einer erhöhten Partikelabscheidung im Einlass- und Auslassbereich des CDMA beitragen. Ein weiteres experimentelles Problem bestand darin, ein konstantes Aerosol mit gleichbleibenden Eigenschaften bereitzustellen. Dies wurde durch den Einsatz von Heißwandreaktoren gelöst, in denen Silber verdampft, die rekondensierten Silberpartikel zur Agglomeration gebracht und anschließend zu nahezu kugelförmigen Partikeln gesintert wurden.
Die Theorie zur Berechnung der Transferfunktion anhand von Partikeltrajektorien wurde ebenfalls erweitert, sodass die Annahme einer konstanten Zentrifugalkraft über den gesamten Klassierspalt nicht länger erforderlich ist. Dies ist insbesondere im AAC-Betriebsfall bei einem großen Verhältnis der Spaltbreite zum mittleren Spaltradius $\widetilde{h}$ von Bedeutung. Darüber hinaus konnte gezeigt werden, dass die Ergebnisse des Partikeltrajektoriemodells äquivalent über das Streamline-Modell hergeleitet werden können. Letzteres bietet den Vorteil, dass Einflüsse wie Diffusion oder ein laminare Strömungsprofil analytisch leichter berücksichtigt werden können.
Letzteres bietet den Vorteil, dass Einflüsse wie Diffusion oder ein laminare Strömungsprofil analytisch leichter berücksichtigt werden können. In Analogie zu Stolzenburg [Sto88] konnte gezeigt werden, dass Diffusion iinsbesondere bei kleinen Partikeln zu einer signifikanten Verbreiterung der Transferfunktion führt, während ein laminares Strömungsprofil in der Hüllluft nur einen geringen Einfluss auf das Klassierergebnis besitzt. Besonders hervorzuheben ist jedoch, dass der Einfluss eines laminarer Strömungsprofils im Aerosolvolumenstrom nicht vernachlässigt werden sollte. Aufgrund der Wandbedingungen (Geschwindigkeit an der Wand ist gleich Null) entsteht bei Annahme einer homogenen Partikelkonzentration ein Partikelstromdichteprofil über dem Spaltradius, das der Form eines laminaren Strömungsprofils entspricht. Dies führt dazu, dass die Transferfunktion selbst für große Partikel besser

durch eine Gauß-Verteilung als durch eine Dreiecksfunktion beschrieben werden kann.
Zur vollständigen Charakterisierung des CDMA wurden zudem CFD-Simulationen der Fluidströmungen durchgeführt. Auf Grundlage der ermittelten Strömungsprofile konnten Transferfunktionen berechnet werden. Dabei zeigte sich, dass insbesondere hohe Drehzahlen das Strömungsprofil im Klassierspalt beeinflussen können. Dennoch bleibt der Einfluss auf die Transferfunktion aufgrund der Vielzahl anderer Unsicherheiten vernachlässigbar. Es empfiehlt sich jedoch, bei hohen Drehzahlen einen Strömungsgleichrichter vor dem Klassierspalt zu implementieren, um eine möglichst gleichmäßige Strömung zu gewährleisten.
Für die Dateninversion wurde der POCS-Algorithmus gewählt, ein neuartiger Ansatz, der sich insbesondere für schlecht gestellte mathematische Probleme eignet. Der von Rasche [Ras25] adaptierte Algorithmus wurde zunächst anhand künstlich erzeugter Daten getestet, sowohl mit als auch ohne Messrauschen, und anschließend auf tatsächliche Messdaten angewendet. Dabei zeigte sich eine hohe Effizienz und Robustheit des Algorithmus, selbst bei stark verrauschten Daten. Für verschiedene Sinterstufen eines Silberaerosols konnten 2D-Verteilungen bestimmt werden, wobei die Dateninversion plausibele Ergebnisse lieferte. Einschränkungen traten jedoch bei bimodalen Ursprungsverteilungen auf, da der Algorithmus zusätzliche Moden generierte, die im ursprünglichen Signal nicht vorhanden waren. Diese Problematik stellt einen Schwerpunkt für die Weiterentwicklung der Methode dar.

6 Fazit

Zusammenfassend lässt sich festhalten, dass der Centrifugal Differential Mobility Analyzer (CDMA) in Kombination mit dem POCS-Algorithmus vielversprechende Ergebnisse liefert und eine zuverlässige Messung sowie Umwandlung von zweidimensionalen Verteilungen in weitere Eigenschaftsverteilungen ermöglicht. Dies bestätigt, dass das grundlegende Funktionsprinzip des CDMA erfolgreich umgesetzt wurde. Dennoch haben die durchgeführten Untersuchungen auch Verbesserungspotenziale aufgezeigt, die für zukünftige Arbeiten entscheidend sind, um die Leistungsfähigkeit des Systems weiter zu steigern.
Ein zentraler Ansatzpunkt ist die Optimierung des Prototyp-Designs. Durch eine Reduktion der theoretischen Verluste könnten nicht nur die Messergebnisse präzisiert, sondern auch engere Transferfunktionen realisiert werden. Diese Verbesserungen wären ein entscheidender Schritt, um die Effizienz und Genauigkeit des CDMA weiter zu erhöhen. Darüber hinaus sollte das System um ein Faraday-Cup-Elektrometer ergänzt werden. Diese Erweiterung würde insbesondere die Dateninversion für komplexere Partikelkollektive erleichtern, da die aktuelle Implementierung primär für monomodale Partikeln geeignet ist. Eine präzisere Dateninversion, gestützt durch zusätzliche Messinformationen, könnte die Aussagekraft der Ergebnisse erheblich verbessern.
Ein weiterer vielversprechender Ansatz für die zukünftige Entwicklung ist die Erweiterung des Messverfahrens um eine zusätzliche Dimension. Die Erfassung des Streulichtintensitätsdurchmessers oder des aerodynamischen Durchmessers im Vakuum nach der Klassierung im CDMA würde neue Perspektiven eröffnen und die Analysemöglichkeiten des Systems erheblich erweitern.

Insgesamt hat sich der CDMA als ein innovatives und vielversprechendes Werkzeug erwiesen, dessen Potenzial durch gezielte Weiterentwicklungen noch erheblich gesteigert werden kann. Mit den vorgeschlagenen Verbesserungen und Erweiterungen könnte das System in der Zukunft nicht nur breitere Anwendungsbereiche erschließen, sondern auch als wegweisendes Instrument in der Partikelanalyse etabliert werden.

Literatur

[Ale97] Helmut Alexander. *Physikalische Grundlagen der Elektronenmikroskopie*. Angewandte Physik. Wiesbaden und s.l.: Vieweg+Teubner Verlag, 1997. ISBN: 9783663122968. DOI: 10.1007/978-3-663-12296-8.

[All+04] James D. Allan, Alice E. Delia u. a. „A generalised method for the extraction of chemically resolved mass spectra from Aerodyne aerosol mass spectrometer data“. In: *Journal of Aerosol Science* 35.7 (2004), S. 909–922. ISSN: 00218502. DOI: 10.1016/j.jaerosci.2004.02.007.

[AR85] Michael D. Allen und Otto G. Raabe. „Slip correction measurements for aerosol particles of doublet and triangular triplet aggregates of spheres“. In: *Journal of Aerosol Science* 16.1 (1985), S. 57–67. ISSN: 00218502. DOI: 10.1016/0021-8502(85)90020-5.

[BKW11] Paul A. Baron, Pramod Kulkarni und Klaus Willeke. *Aerosol measurement: Principles, techniques, and applications*. 3rd ed. Hoboken N.J.: Wiley, 2011. ISBN: 9780470387412.

[Bru07] Jürg Brunner. *Partikelmessungen (Grössenverteilung und Anzahl) mit einem SMPS: GRUNDLAGEN UND AUSWERTEVERFAHREN: TECHNISCHER BERICHT*. Zürich: Stadt Zürich, 2007.

[Col13] Ian Colbeck. *Aerosol Science: Technology and Applications*. 2. ed. Hoboken: Wiley, 2013. ISBN: 978-1-119-97792-6.

[DeC+04] Peter F. DeCarlo, Jay G. Slowik, Douglas R. Worsnop, Paul Davidovits und Jose L. Jimenez. „Particle Morphology and Density Characterization by Combined Mobility and Aerodynamic Diameter Measurements. Part 1: Theory“. In: *Aerosol Science and Technology* 38.12 (2004), S. 1185–1205. ISSN: 0278-6826. DOI: 10.1080/027868290903907.

[Fri00] Sheldon Kay Friedlander. *Smoke, dust, and haze: Fundamentals of aerosol dynamics*. 2. ed. Topics in chemical engineering. New York: Oxford Univ. Press, 2000. ISBN: 978-0195129991.

[Fur+19] Orkun Furat, Thomas Leißner, Kai Bachmann, Jens Gutzmer, Urs Peuker und Volker Schmidt. „Stochastic Modeling of Multidimensional Particle Properties Using Parametric Copulas“. In: *Microscopy and microanalysis : the official journal of Microscopy Society of America, Microbeam Analysis Society, Microscopical Society of Canada* 25.3 (2019), S. 720–734. DOI: 10.1017/S1431927619000321.

[Fur+20] Orkun Furat, Matthias Masuhr, Frank Einar Kruis und Volker Schmidt. „Stochastic modeling of classifying aerodynamic lenses for separation of airborne particles by material and size“. In: *Advanced Powder Technology* 31.6 (2020), S. 2215–2226. ISSN: 09218831. DOI: 10.1016/j.apt.2020.03.014.

[HFF78] Susanne V. Hering, Richard C. Flagan und Sheldon K. Friedlander. „Design and evaluation of new low-pressure impactor. I“. In: *Environmental science & technology* 12.6 (1978), S. 667–673. ISSN: 0013-936X. DOI: 10.1021/es60142a004.

[HK91] Risto E. Hillamo und Esko I. Kauppinen. „On the Performance of the Berner Low Pressure Impactor“. In: *Aerosol Science and Technology* 14.1 (1991), S. 33–47. ISSN: 0278-6826. DOI: 10.1080/02786829108959469.

[Hin99] W.C. Hinds. *Aerosol Technology: Properties, Behavior, and Measurement of Airborne Particles*. Wiley, 1999. ISBN: 9780471194101. URL: https://books.google.de/books?id=ORxSAAAAMAAJ.

[IT08] Panich Intra und Nakorn Tippayawong. „An overview of differential mobility analyzers for size classification of nanometer-sized aerosol particles.“ In: *Songklanakarin Journal of Science & Technology* 30.2 (2008).

[Jin17] Anil B. Jindal. „The effect of particle shape on cellular interaction and drug delivery applications of micro- and nanoparticles“. In: *International journal of pharmaceutics* 532.1 (2017), S. 450–465. DOI: 10.1016/j.ijpharm.2017.09.028.

[JSO13] Tyler J. Johnson, Jonathan P. R. Symonds und Jason S. Olfert. „Mass–Mobility Measurements Using a Centrifugal Particle Mass Analyzer and Differential Mobility Spectrometer“. In: *Aerosol Science and Technology* 47.11 (2013), S. 1215–1225. ISSN: 0278-6826. DOI: 10.1080/02786826.2013.830692.

[Jon99] A. R. Jones. „Light scattering for particle characterization“. In: *Progress in Energy and Combustion Science* 25.1 (1999), S. 1–53. ISSN: 03601285. DOI: 10.1016/S0360-1285(98)00017-3.

[Kel+22] Georgios A. Kelesidis, David Neubauer, Liang-Shih Fan, Ulrike Lohmann und Sotiris E. Pratsinis. „Enhanced Light Absorption and Radiative Forcing by Black Carbon Agglomerates“. In: *Environmental science and technology* 12 (2022), S. 8610–8618. ISSN: 00218502. DOI: 10.1021/acs.est.2c00428.

[KPL92] J. Keskinen, K. Pietarinen und M. Lehtimäki. „Electrical low pressure impactor“. In: *Journal of Aerosol Science* 23.4 (1992), S. 353–360. ISSN: 00218502. DOI: 10.1016/0021-8502(92)90004-F.

[KW75] E. O. Knutson und K. T. Whitby. „Aerosol classification by electric mobility: apparatus, theory, and applications“. In: *Journal of Aerosol Science* 6.6 (1975), S. 443–451. ISSN: 00218502. DOI: 10.1016/0021-8502(75)90060-9.

[Lee+13] Berto P. Lee, Yong Jie Li, Richard C. Flagan, Charles Lo und Chak K. Chan. „Sizing Characterization of the Fast-Mobility Particle Sizer (FMPS) Against SMPS and HR-ToF-AMS“. In: *Aerosol Science and Technology* 47.9 (2013), S. 1030–1037. ISSN: 0278-6826. DOI: 10.1080/02786826.2013.810809.

[LLC06] Weiling Li, Lin Li und Da-Ren Chen. „Technical Note: A New Deconvolution Scheme for the Retrieval of True DMA Transfer Function from Tandem DMA Data“. In: *Aerosol Science and Technology* 40.12 (2006), S. 1052–1057. ISSN: 0278-6826. DOI: 10.1080/02786820600944331.

[MZ11] Eckard Macherauch und Hans-Werner Zoch. *Praktikum in Werkstoffkunde: 91 ausführliche Versuche aus wichtigen Gebieten der Werkstofftechnik*. 11., vollst. überarb. und erw. Aufl. Studium Werkstofftechnik. Wiesbaden: Vieweg + Teubner, 2011. ISBN: 383480343X.

[May75] K. R. May. „An “ultimate” cascade impactor for aerosol assessment“. In: *Journal of Aerosol Science* 6.6 (1975), S. 413–419. ISSN: 00218502. DOI: 10.1016/0021-8502(75)90057-9.

[MC16] J. Moore und Eleonora Cerasoli. „Particle Light Scattering Methods and Applications“. In: Dez. 2016, S. 543–553. DOI: 10.1016/B978-0-12-803224-4.00040-6.

[OC05] J. S. Olfert und N. Collings. „New method for particle mass classification—the Couette centrifugal particle mass analyzer“. In: *Journal of Aerosol Science* 36.11 (2005), S. 1338–1352. ISSN: 00218502. DOI: 10.1016/j.jaerosci.2005.03.006.

[Olf+06] J. S. Olfert, K.StJ. Reavell, M. G. Rushton und N. Collings. „The experimental transfer function of the Couette centrifugal particle mass analyzer“. In: *Journal of Aerosol Science* 37.12 (2006), S. 1840–1852. ISSN: 00218502. DOI: 10.1016/j.jaerosci.2006.07.007.

[OSC07] J. S. Olfert, J.P.R. Symonds und N. Collings. „The effective density and fractal dimension of particles emitted from a light-duty diesel vehicle with a diesel oxidation catalyst“. In: *Journal of Aerosol Science* 38.1 (2007), S. 69–82. ISSN: 00218502. DOI: 10.1016/j.jaerosci.2006.10.002.

[Par+08] K. Park, D. Dutcher u. a. „Tandem Measurements of Aerosol Properties—A Review of Mobility Techniques with Extensions“. In: *Aerosol Science and Technology* 42.10 (2008), S. 801–816. ISSN: 0278-6826. DOI: 10.1080/02786820802339561.

[Ras25] David Benedikt Rasche. *Zur maßgeschneiderten Synthese und mehrdimensionalen Charakterisierung gasgetragener Nanopartikeln / von M.Sc. David Benedikt Rasche ; Referent: Prof. Dr.-Ing. Hans-Joachim Schmid, Korreferent: Prof. Dr.-Ing. Einar Kruis*. Universität Paderborn, 2025. DOI: 10.17619/UNIPB/1-2292.

[RSN19] Frank Rhein, Felix Scholl und Hermann Nirschl. „Magnetic seeded filtration for the separation of fine polymer particles from dilute suspensions: Microplastics“. In: *Chemical Engineering Science* 207 (2019), S. 1278–1287. ISSN: 00092509. DOI: 10.1016/j.ces.2019.07.052.

[SF23] Krischan Sandmann und Udo Fritsching. „Acoustic separation and fractionation of property-distributed particles from the gas phase“. In: *Advanced Powder Technology* 34.12 (2023), S. 104270. ISSN: 09218831. DOI: 10.1016/j.apt.2023.104270.

[Sha+12] M. Shapiro, P. Vainshtein u. a. „Characterization of agglomerates by simultaneous measurement of mobility, vacuum aerodynamic diameter and mass“. In: *Journal of Aerosol Science* 44 (2012), S. 24–45. ISSN: 00218502. DOI: 10.1016/j.jaerosci.2011.08.004.

[SOR20] T. A. Sipkens, J. S. Olfert und S. N. Rogak. „Inversion methods to determine two-dimensional aerosol mass-mobility distributions: A critical comparison of established methods“. In: *Journal of Aerosol Science* 140 (2020), S. 105484. ISSN: 00218502. DOI: 10.1016/j.jaerosci.2019.105484.

[Slo+04] Jay G. Slowik, K. Stainken u. a. „Particle Morphology and Density Characterization by Combined Mobility and Aerodynamic Diameter Measurements. Part 2: Application to Combustion-Generated Soot Aerosols as a Function of Fuel Equivalence Ratio“. In: *Aerosol Science and Technology* 38.12 (2004), S. 1206–1222. ISSN: 0278-6826. DOI: 10.1080/027868290903916.

[Sto88] Mark Richard Stolzenburg. „An Ultrafine Aerosol Size Distribution System“. Dissertation. Minnesota: University of Minnesota, 1988.

[Szy02] Wladyslaw Witold Szymanski. „Aerosol concentration measurement with multiple light scattering system and laser aerosol spectrometer“. In: *Atmospheric Research* 62.3-4 (2002), S. 255–265. ISSN: 01698095. DOI: 10.1016/S0169-8095(02)00013-3.

[Taj+11] Naoko Tajima, Nobuhiko Fukushima, Kensei Ehara und Hiromu Sakurai. „Mass Range and Optimized Operation of the Aerosol Particle Mass Analyzer“. In: *Aerosol Science and Technology* 45.2 (2011), S. 196–214. ISSN: 0278-6826. DOI: 10.1080/02786826.2010.530625.

[TO13] F. Tavakoli und J. S. Olfert. „An Instrument for the Classification of Aerosols by Particle Relaxation Time: Theoretical Models of the Aerodynamic Aerosol Classifier“. In: *Aerosol Science and Technology* 47.8 (2013), S. 916–926. ISSN: 0278-6826. DOI: 10.1080/02786826.2013.802761.

[TO14] Farzan Tavakoli und Jason S. Olfert. „Determination of particle mass, effective density, mass–mobility exponent, and dynamic shape factor using an aerodynamic aerosol classifier and a differential mobility analyzer in tandem“. In: *Journal of Aerosol Science* 75 (2014), S. 35–42. ISSN: 00218502. DOI: 10.1016/j.jaerosci.2014.04.010.

[TJS15] L. Tigges, A. Jain und H.-J. Schmid. „On the bipolar charge distribution used for mobility particle sizing: Theoretical considerations“. In: *Journal of Aerosol Science* 88 (2015), S. 119–134. ISSN: 00218502. DOI: 10.1016/j.jaerosci.2015.05.010.

[Toy+14] Randall Toy, Pubudu M. Peiris, Ketan B. Ghaghada und Efstathios Karathanasis. „Shaping cancer nanomedicine: the effect of particle shape on the in vivo journey of nanoparticles“. In: *Nanomedicine (London, England)* 9.1 (2014), S. 121–134. DOI: 10.2217/nnm.13.191.

[WJ87] Hwa-Chi Wang und Walter John. „Particle Density Correction for the Aerodynamic Particle Sizer“. In: *Aerosol Science and Technology* 6.2 (1987), S. 191–198. ISSN: 0278-6826. DOI: 10.1080/02786828708959132.

[Wie88] A. Wiedensohler. „An approximation of the bipolar charge distribution for particles in the submicron size range“. In: *Journal of Aerosol Science* 19.3 (1988), S. 387–389. ISSN: 00218502. DOI: 10.1016/0021-8502(88)90278-9.

[WC96] David B. Williams und C. Barry Carter. *Transmission electron microscopy: A textbook for materials science*. New York und New York, NY: Springer und Plenum Press anfangs, 1996. ISBN: 030645324X.

[WL80] James Charles Wilson und Benjamin Y.H. Liu. „Aerodynamic particle size measurement by laser-doppler velocimetry“. In: *Journal of Aerosol Science* 11.2 (1980), S. 139–150. ISSN: 00218502. DOI: 10.1016/0021-8502(80)90030-0.

[Zha+22] Jing Zhang, Jinshuo Qiao, Kening Sun und Zhenhua Wang. „Balancing particle properties for practical lithium-ion batteries“. In: *Particuology* 61 (2022), S. 18–29. ISSN: 16742001. DOI: 10.1016/j.partic.2021.05.006.

Studentische Arbeiten

Die nachfolgenden Referenzen sind unveröffentlichte studentische Arbeiten, welche im Rahmen der vorliegenden Dissertation erstellt und unter maßgeblicher Anleitung des Autors dieser Dissertation durchgeführt und betreut wurden. Ergebnisse dieser Arbeiten sind teilweise in die vorliegende Dissertation eingeflossen. Der Autor möchte den Studierenden für ihren motivierten Einsatz und ihre Unterstützung danken.

[GRD23] Sebastian Gröne, Torben Norbert Rüther und Christopher Dechtert. *(Betreuer T.N. Rüther): Numerical Investigations of the Flow Field and the Transfer Function inside a Centrifugal-DMA: Universiät Paderborn. Maschinenbau/Lehrstuhl für Partikelverfahrenstechnik, unveröffentlichte Masterarbeit.* 2023.

[HR22] Thomas Hesse und Torben Norbert Rüther. *(Betreuer T.N. Rüther): Herstellung stabiler Testaerosole im Heißwandreaktor: Universiät Paderborn. Maschinenbau/Lehrstuhl für Partikelverfahrenstechnik, unveröffentlichte Bachelorarbeit.* 2022.

[RR22] Lena Margret Riedemann und Torben Norbert Rüther. *(Betreuer T.N. Rüther): Untersuchung eines neuen Verfahrens zur Ermittlung der wahren Scherrate in einem Koaxialrheometer: Universiät Paderborn. Maschinenbau/Lehrstuhl für Partikelverfahrenstechnik, unveröffentlichte Studienarbeit.* 2022.

[WR24] Rabea Weigand und Torben Norbert Rüther. *(Betreuer T.N. Rüther): Analyse und Evaluation des Einflusses eines Unterstützungskurses für Maschinenbaustudierende auf ihre Überforderung und Ängstlichkeit in den ersten Semestern: Universiät Paderborn. Maschinenbau/Lehrstuhl für Partikelverfahrenstechnik, unveröffentlichte Masterarbeit.* 2024.

A Erklärung zur Zitation von Inhalten aus studentischen Arbeiten

In Ergänzung zu meinem Antrag auf Zulassung zur Promotion in der Fakultät für Maschinenbau der Universität Paderborn erkläre ich gemäß §11 der Promotionsordnung und unter Beachtung der Regelung zur Zitation studentischer Arbeiten:

Die von mir vorgelegte Dissertation habe ich selbstständig verfasst, und ich habe keine anderen als die dort angegebenen Quellen und Hilfsmittel benutzt. Es sind Inhalte studentischen Ursprungs (studentische Arbeiten) in dieser Dissertation enthalten.

Ich habe die verwendeten Arbeiten entsprechend der Regelung „Zitation aus studentischen Arbeiten in Dissertationen“ zitiert.

Brilon, den 10.09.2025

Torben Rüther

Lebenslauf wurde aus datenschutzrechtlichen Gründen entfernt.